

Applications of Granular Crystals for Nondestructive Evaluation, Structural Health Monitoring, and Mechanical Wave Control

by

Hoda Jalali

Bachelor of science, Civil Engineering, University of Tehran, 2013

Master of science, Civil Engineering – Structural Engineering, University of Tehran, 2016

Submitted to the Graduate Faculty of
Swanson School of Engineering in partial fulfillment
of the requirements for the degree of
Doctor of Philosophy

University of Pittsburgh

2022

UNIVERSITY OF PITTSBURGH
SWANSON SCHOOL OF ENGINEERING

This dissertation was presented

by

Hoda Jalali

It was defended on

March 1, 2022

and approved by

Lev Khazanovich, Ph.D. Professor, Department of Civil and Environmental Engineering

Amir H. Alavi, Ph.D. Assistant Professor, Department of Civil and Environmental Engineering

Samuel Dickerson, Ph.D. Assistant Professor, Department of Electrical and Computer Engineering

Dissertation Director: Piervincenzo Rizzo, Ph.D. Professor, Department of Civil and Environmental Engineering

Copyright © by Hoda Jalali

2022

Applications of Granular Crystals for Nondestructive Evaluation, Structural Health Monitoring, and Mechanical Wave Control

Hoda Jalali, PhD.

University of Pittsburgh, 2022

Granular crystals are a class of nonlinear periodic structures in form of arrays of elastic particles that interact nonlinearly via Hertzian contact. The structural discreteness and nonlinearity of granular crystals can be used to control the propagation of mechanical waves. In addition, their mechanical response can be tailored by adjusting their composition and loading conditions. On account of these properties, granular crystals offer several potential engineering applications like shock-absorbing, energy harvesting, acoustic switching, nondestructive evaluation (NDE), and structural health monitoring (SHM).

A 1D granular crystal composed of identical spherical particles subjected to zero or weak static compression supports the generation and propagation of highly nonlinear solitary waves (HNSWs). The interaction of HNSWs with a given material/structure of interest is affected by the mechanical properties and the geometry of the interacting material/structure. Therefore, HNSWs have gained research attention in NDE and SHM applications recently.

This dissertation investigates the application of HNSWs for the detection of localized corrosion in steel structures, and the identification and characterization of anisotropy in rocks. Numerical simulations were conducted to study the interaction of HNSWs with steel plates and rock materials of different conditions. Furthermore, the application of the HNSWs for the mentioned NDE applications was examined experimentally. The experimental data were analyzed using multivariate statistical methods to enhance the performance of the proposed NDE method. The present study provides evidence for the effectiveness

of the HNSWs-based NDE method in detecting localized corrosion in plate-like structures and in detecting anisotropy in rocks. In addition, this study investigates the long-term performance of the developed HNSW-based NDE method using video processing techniques.

Finally, this dissertation investigates the asymmetric propagation of mechanical waves in a compressed 1D granular crystal of spherical particles coupled with asymmetric intruders. A numerical analysis was conducted to investigate the dynamic response of the system subjected to small-amplitude periodic vibrations. It was shown that the proposed design can provide unidirectional transmission of low-frequency mechanical waves.

Table of Contents

Preface.....	xxiii
1.0 Introduction	1
1.1 Background	2
1.1.1 Highly Nonlinear Solitary Waves	2
1.1.2 Granular Crystals as Acoustic Metamaterials	4
1.2 Motivation and Vision.....	7
1.2.1 Detection of Localized Corrosion	7
1.2.2 Characterizing Anisotropy in Rocks	10
1.2.3 Controlling Mechanical Waves.....	11
1.3 Organization of Dissertation	14
1.4 Intellectual Merit and Broader Impact	14
2.0 Application of Granular Crystals to Detect Localized Corrosion	17
2.1 Introduction	18
2.2 Modeling	21
2.2.1 Coupled Discrete / Finite Element Model: Kirchhoff–Love Plate and Point Masses.....	21
2.2.2 Coupled Discrete / Finite Element Model: Using 3D Solid Elements.....	25
2.2.3 Analytical Modeling.....	28

2.3 Experiments.....	31
2.3.1 Solitary Wave Transducers	32
2.3.2 Magnet Experiment.....	34
2.3.3 Corrosion Experiment on the 6.3 mm-Thick Plate	36
2.3.4 Corrosion Experiment on the 4.8 mm-Thick Plate	38
2.4 Multivariate Outlier Analysis.....	41
2.5 Numerical Results	42
2.5.1 Interaction of HSNWs with Pristine and Corroded Plates	42
2.5.2 Effect of Localized Corrosion on Solitary Wave Features	47
2.5.3 Comparing Numerical and Analytical Results in Pristine Plates	49
2.5.4 Parametric Study	53
2.6 Experimental Results.....	62
2.6.1 Magnet test results.....	62
2.6.2 Corrosion Progress in the 6.3 mm-Thick Plate	65
2.6.3 Corrosion Monitoring Results of the 6.3 mm-Thick Plate.....	66
2.6.4 Outlier Analysis Results of Monitoring the 6.3 mm-Thick Plate	74
2.6.5 Corrosion Progress in the 4.8 mm-Thick Plate	77
2.6.6 Corrosion Monitoring Results of the 4.8 mm-Thick Plate.....	80
2.6.7 Outlier Analysis Results of Monitoring the 4.8 mm-Thick Plate	85
2.7 Conclusions	87

3.0	Application of Granular Crystals to Characterize Anisotropy of Rock Materials	89
3.1	Introduction	89
3.2	Materials and Experiments.....	92
3.3	Numerical Modeling	94
3.4	Results	98
3.4.1	Numerical Results	98
3.4.2	Experimental Results.....	102
3.4.3	Outlier Analysis.....	106
3.4.4	Estimating the Rocks Young’s Modulus: Using Solitary Wave Features	108
3.4.5	Parametric Study	110
3.5	Conclusions	113
4.0	The Long-term Performance of the Solitary Wave-Based Nondestructive Evaluation	114
4.1	Introduction	115
4.2	Experimental Setup	118
4.3	Discrete Element Modeling.....	119
4.4	Video Processing.....	120
4.5	Results and Discussion.....	122
4.5.1	Repeatability: Analyzing the 6-day Test Results	122
4.5.2	Estimating the Plate Young’s Modulus: Using Solitary Wave Features	127
4.5.3	Video Processing Results	129

4.6 Conclusion.....	138
5.0 Application of Granular Crystals to Control Mechanical Waves	139
5.1 Introduction	140
5.2 Acoustic Diode Design and Numerical Setup.....	144
5.3 Results and Discussion.....	150
5.4 Conclusions	163
6.0 Summary and Conclusions.....	165
6.1 Overview of the Dissertation	165
6.2 Main Novel Findings.....	167
6.3 Limitations of the Solitary Wave-based NDE.....	169
6.4 Suggestions for Future Studies.....	170
Bibliography.....	171

List of Tables

Table 2.1 – Monitoring positions, methods, and the size of localized corrosion area under each transducer.	37
Table 2.2 - The type of solitary wave transducers used on each monitoring position and the size of localized corrosion area under each transducer.	41
Table 2.3 - Density, mechanical properties, and thermal conductivity of the materials considered in this study.	57
Table 2.4 - Effect of ISW on Time of flight and amplitude ratio based on the analytical Zener Model	61
Table 2.5 –The outliers detected by each solitary wave transducers over the last 50 hours of monitoring the 4.8 mm-thick plate.	87
Table 3.1 - Properties of the rock samples.	93
Table 3.2 - Mechanical properties of sandstone and slate.....	98
Table 4.1 – Time waveforms analysis. Average value of the time of flight, amplitude ratio, correlation coefficient, ISW correlation coefficient, and PSW correlation coefficient associated with the three solitary wave transducers.	127
Table 5.1 – Static overlap and cutoff frequency of compressed monatomic granular chains.....	150
Table 5.2 – Bandwidth and efficiency of passive acoustic diodes designs available in the scientific literature.	158

List of Figures

Figure 1.1 - A one-dimensional granular crystal. (a) A monoatomic array of closely packed particles. (b) The particles in the granular crystal interacting via nonlinear contact springs. 2

Figure 1.2 – Scheme of the proposed NDE/SHM system for the detection of localized corrosion..... 9

Figure 1.3 – Design of the proposed granular crystal design to mitigate noise and vibration..... 13

Figure 2.1 – The coupled discrete element (DE) and finite element (FE) models of the interaction between the granular chain and the plate. (a) The integrated at the contact point between the granular chain and the plate. (b) Scheme of the DE model where the granular chain is simulated as a series of point masses connected by nonlinear springs and dashpots. (c) A zoom-in of the mesh refinement pattern in a 20 mm × 20 mm square in the middle of the plate. (d) The mid surface representing the plate in the FE model and © the nodes and the degrees of freedom of each plate element. 23

Figure 2.2 - Scheme of the numerical model. (a) The coupled discrete element (DE) and finite element (FE) model used in this study. One-quarter of the model is stimulated due to symmetry. (b) The DE model simulating the chain of particles as a spring-mass system, in which the point masses are connected by the nonlinear springs (defined based on the Hertzian contact law) and dashpots. (c) Graphical representation of the Hertzian contact law. The contact force between adjacent particles F is nonlinearly proportional to the deformation δ of the diameter connecting the centers of the interacting particles. (d and e) Zoom-in views of the FE model at the interface between the last particle and the plate in (d) pristine and (e) corroded conditions. Corrosion was simulated as a local thickness reduction in the plate, below the interaction point. 26

Figure 2.3 - The solitary wave transducers used in the corrosion experiment on the 4.8 mm-plate and the magnet experiment. (a) The conventional solitary wave transducer controlled by the National Instruments PXI and (b) the wireless transducer controlled by a printed circuit board attached to the transducer frame. (c) A side-by-side view of the PXI controlled transducer and the wireless transducer. 34

Figure 2.4 – The magnet test setup. (a) The steel plate monitored with four solitary wave transducers. The plate was supported by four plastic rods in the corners, and a magnet was attached to the plate. (b) The plate dimensions and the positions of the four solitary wave transducers and the magnet. The transducers were in fixed positions while the magnet position changed over the plate. 35

Figure 2.5 – The experimental setup in corrosion experiment I. (a) The accelerated corrosion test setup used to induce localized corrosion in a steel plate. (b) The steel plate dimensions, and the position of the localized corrosion areas monitored with ultrasonic (A) and solitary wave transducers (B, C, D). (c) Scheme of a HNSW transducer used in this study. 37

Figure 2.6 - The setup of corrosion experiment on the 4.8 mm-thick plate. A steel plate subjected to localized corrosion was monitored with eight solitary wave transducers of which half were wireless transducers and half were controlled with the NI PXI. 39

Figure 2.7 – The dimensions and the positions of the monitoring transducers and the supports in the corrosion experiment on the 4.8 mm-thick plate. 40

Figure 2.8 - Numerical results on the interaction of HNSWs with a steel plate in the pristine (left column) and corroded (right column) conditions. (a and b) The time history of the displacement of the mass points and (c and d) force at the mass points as a solitary wave propagates through the granular chain and interacts with the plate. (e and f) The time history of the displacement of points A, B, and C,

corresponding to the center of the last particle, the contact point in the plate, and the lowest point in the plate below the interaction point. (g and h) The time history of the contact indentation at the chain-plate interface..... 45

Figure 2.9 - Numerical (a) time of flight and (b) amplitude ratio as a function of relative corrosion depth in a granular chain interacting with a 6.3 mm-thick plate. 48

Figure 2.10 - Numerical and analytical results on the effect of plate thickness on (a) time of flight and (b) amplitude ratio in a HNSW transducer made of 19 mm particles. 50

Figure 2.11 - Numerical and analytical results on the effect of particle diameter on (a) time of flight and (b) amplitude ratio in HNSW transducers in contact with a 6.3 mm-thick plate..... 51

Figure 2.12- (a) Time of flight and (b) amplitude ratio as a function of the dimensionless ratio of particle diameter over plate thickness, predicted using the numerical and analytical methods. 53

Figure 2.13 - Effect of plate thickness on the sensitivity of the HNSW-based NDE for the detection of localized corrosion. (a) Time of flight and (b) amplitude ratio as a function of relative corrosion depth in solitary wave transducers in contact with plates with an initial thickness of 3.2 mm, 4.8 mm, 6.3 mm, 7.9 mm, and 9.5 mm. 54

Figure 2.14 - Effect of particle diameter on the sensitivity of the HNSW-based NDE for the detection of localized corrosion. (a) Time of flight and (b) amplitude ratio as a function of relative corrosion depth in solitary wave transducers composed of 13 mm, 19 mm, and 25 mm particles. 56

Figure 2.15 – Effect of particle material on the sensitivity of the HNSW-based NDE for the detection of localized corrosion. (a) Time of flight and (b) amplitude ratio as a function of relative corrosion depth in solitary wave transducers composed of aluminum, titanium, steel, silicon nitride, and tungsten particles. 58

Figure 2.16 – Effect of chain length on the sensitivity of the HNSW-based NDE for the detection of localized corrosion. (a) Time of flight and (b) amplitude ratio as a function of relative corrosion depth in solitary wave transducers composed of 9, 15, and 21 particles. 59

Figure 2.17 - Effect of sensor location on the sensitivity of the HNSW-based NDE for the detection of localized corrosion. (a) Time of flight and (b) amplitude ratio as a function of relative corrosion depth in a solitary wave transducer composed of 21 particles. The solitary wave force profiles were analyzed at particles #5, #10, and #15. 60

Figure 2.18 - The effect of the incident solitary wave amplitude on the solitary wave features: (a) time of flight, and (b) amplitude ratio. 61

Figure 2.19 – The solitary wave features, i.e., the ISW amplitude, the time of flight, and the amplitude ratio obtained from the magnet. The two columns represent the data associated with the small magnet and the large magnet test. 63

Figure 2.20 – The magnet test results. The solitary wave time of flight and amplitude ratio as a function of the distance between the magnet and the transducer. Each column represents the data associated with one transducer. The baseline data (the case without a magnet) is shown on a negative distance value... 65

Figure 2.21 - Localized corrosion defects in the thick steel plate. (a) Top surface of the steel plate with a through-thickness hole detected in the corrosion area B. (b) A zoom in of the corrosion defect in the corrosion area B. (c) Through-thickness holes detected in the corrosion area C. (d) The corroded surface of the steel plate after removing the corrosion protection tapes. (e) A zoom-in view of the corrosion area C on the corroded surface of the steel plate. 66

Figure 2.22 - Solitary wave profiles recorded by solitary wave transducers positioned on the areas (a) B, (b) C, and (c) D on the 6.3 mm-thick plate. 67

Figure 2.23 - Experimental results of monitoring corrosion in the 6.3 mm-thick plate. Time of flight, calculated by the peak-to-peak method for solitary wave transducers used to monitor areas (a) B, (b) C, and (c) D of the test object..... 69

Figure 2.24 – Experimental results of monitoring corrosion in the 6.3 mm-thick plate. Normalized amplitude of the primary reflected solitary wave measured from the areas (a) B, (b) C, and (c) D monitored with the HNSW transducer. 70

Figure 2.25 - Comparison of the numerical results and the experimental results on the effect of localized corrosion on (a) time of flight and (b) amplitude ratio in plate with a thickness of 6.3 mm. The numerical results present the feature of the reflected solitary waves in contact with plates containing a localized defect, where the defect depth varies from 0 to 80 percent of the initial plate thickness. The experimental results show the same features of the reflected solitary waves in a HNSW transducer monitoring a localized corrosion in a plate of similar properties. The dashed line presents the 2nd order regression model fitted to the experimental data. 72

Figure 2.26 - Experimental results of monitoring corrosion in the 6.3 mm-thick plate. Amplitude of the Incident Solitary Wave..... 74

Figure 2.27 – Ultrasonic testing results of monitoring corrosion in the 6.3 mm-thick plate. (a) Ultrasonic travel time in the corrosion area A (on the left axis) and the relative local plate thickness (on the right axis). (b) Plate thickness Reduction in area A obtained from the ultrasonic test results. 74

Figure 2.28 - Multivariate outlier analysis of the experimental data obtained from monitoring the 6.3 mm-thick plate. Mahalanobis distance calculated based on the five solitary wave features including time of flights calculated by the peak-to-peak method and the correlation method, amplitude ratio, autocorrelation coefficient, and area under the primary reflected solitary wave in areas (a) B, (b) C, and

(c) D. The horizontal lines represent the 99.7% confidence threshold calculated as 19.7, 17.1, and 14.4, respectively. The green background presents the baseline data. 76

Figure 2.29 – A close-up view of the through-thickness holes detected after 100 hours in the corroding areas (a) P4, (b) W3, and (c) W4 on the 4.8 mm-thick plate. The white circles indicate the interaction point between the plate and the associated solitary wave transducers. The through-thickness holes are highlighted in yellow rectangles. 77

Figure 2.30 – Localized corrosion defects in the 4.8 mm-Thick Plate after finishing the corrosion experiment. (a) The corroded face of the plate after removing the corrosion resistant tape. (b) A close-up view of the corroded areas P2, W2, P3, and P4 on the corroded face and the dry face. 79

Figure 2.31 - The amplitudes of the incident solitary waves recorded by the eight solitary wave transducers over the corrosion experiment on the 4.8 mm-thick plate. Each datapoint presents the average of 5 consecutive measurements. 80

Figure 2.32 – The time of flights of the solitary waves recorded by the eight solitary wave transducers over the corrosion experiment on the 4.8 mm-thick plate. Each datapoint presents the average of 5 consecutive measurements. 82

Figure 2.33 - The amplitude ratios of the solitary waves recorded by the eight solitary wave transducers over the corrosion experiment on the 4.8 mm-thick plate. Each datapoint presents the average of 5 consecutive measurements. 83

Figure 2.34 – The time of flights and amplitude ratios obtained from the monitoring transducers on the 4.8 mm-thick plate. Datapoints are presented at 2D amplitude ratio-time of flight space. 85

Figure 2.35 - The Mahalanobis distance calculated based on the time of flight and amplitude ratio in the 4.8 mm-thick plate. For each transducer, the baseline data included the measurements obtained by the

transducer over the first 24 hours of the experiment. The horizontal lines represent the 99.7% confidence threshold of the MSD of the baseline data..... 86

Figure 3.1 -Photos of the sandstone and slate samples (the slate samples are the two at the rightmost side of the picture). 93

Figure 3.2 – Photo of the whole experimental setup. The HNSW transducer used in the study presented here contained 9.5 mm particles and the sensor consisted of a wafer-type PZT embedded in between two half-particles. 94

Figure 3.3 – Numerical model of the interaction of solitary waves and rock samples. (a) The discrete element model, and (b) the coupled discrete element/finite element model..... 96

Figure 3.4 - Numerical solitary wave force profiles in a solitary wave transducer was in contact with (a) sandstone and (b) slate samples for different elastic modulus values. 99

Figure 3.5 – (a) Time of flight and (b) amplitude ratio of solitary waves interacting with sandstone and slate samples as function of elastic modulus. The granular chain is composed of 9.5 mm stainless-steel particles. 101

Figure 3.6 - Numerical amplitude ratio and time of flight for sandstone and slate samples. Data labels represent the corresponding elastic modulus. 102

Figure 3.7 - Experimental (a) time of flight and (b) amplitude ratio in different samples and conditions. 103

Figure 3.8 – Experimental (a, c, e) time of flight and (b, d, e) amplitude ratio at different angles around (a, b) sandstone1 and sandstone 2, (c, d) sandstone 3 and sandstone 4, and (e, f) slate1 and slate 2. 105

Figure 3.9 - Experimental data in the 2D amplitude ratio-time of flight space. The ellipses present the 99.7% confidence ellipse obtained based on the Mahalanobis distance (MSD), where the baseline data

was the measurements taken at (a, d) the first 20°, (b, e) the first 45°, and (c, f) the first 90° around the samples. The sandstone confidence ellipses were obtained considering data related to (a, b, c) sandstones 1 and 2, and (d, e, f) all sandstones. 108

Figure 3.10 - Estimation of the modulus of elasticity of the rock samples using the numerical results. 109

Figure 3.11 - (a) Time of flight and (b) amplitude ratio of solitary waves interacting with sandstone and slate samples as function of Young’s modulus. The granular chain is composed of 9.5 mm aluminum particles. 111

Figure 3.12 - (a) Time of flight and (b) amplitude ratio of solitary waves interacting with sandstone and slate samples as function of Young’s modulus. The granular chain is composed of 4.8 mm stainless-steel particles. 112

Figure 3.13 - Normalized sensitivity of (a) Time of flight and (b) amplitude ratio as function of the Young’s modulus of the inspecting media in solitary wave transducers made of particles of different sizes and materials. 112

Figure 4.1 – Schematics and photo of the solitary wave transducer for NDE/SHM applications. ... 117

Figure 4.2 – Photo of the experimental setup in which two high-speed cameras pointed at the striker and the sensor disk of transducer T2. 118

Figure 4.3 – Video processing algorithm used to track the striker. 121

Figure 4.4 - Video processing algorithm used to detect the vibration of the sensor disk. 121

Figure 4.5 – Image noise reduction using the Wiener filter with different Gaussian noise variances (σ). 122

Figure 4.6 – Experimental time waveforms obtained by averaging the single waveforms collected throughout the whole experiment. (a) Transducer 1. (b) Transducer 2. (c) Transducer 3..... 123

Figure 4.7 – The solitary wave features extracted from the time-waveforms recorded with the sensor disk. Each dot represents the average value of the ten measurements collected every 20 minutes. (Left column) Transducer 1. (Center column) Transducer 2. (Right column) Transducer 3. 126

Figure 4.8 – Numerical relationship between the elastic modulus of the plate modeled as a semi-bulky material and the time of flight associated with the primary reflected wave. (a) Striker fall equal to 4 mm and different dissipation coefficients. (b) Dissipation coefficient equal to 4.5 N/m.s and different striker falling heights..... 129

Figure 4.9 – Analysis of the sixteen videos collected with the two high-speed cameras. Solitary wave features extracted from the time waveforms collected with the sensor disk. (a) Peak amplitude of the incident wave, (b) time of flight associated with the primary reflected wave, and (c) normalized amplitude of the reflected wave. 130

Figure 4.10 - Time waveforms measured by the sensor disk associated with strikes number 7 and 8. 130

Figure 4.11 – Snapshots relative to one of the sixteen frames. The value of h indicates the relative position of the striker. 131

Figure 4.12 – Video processing analysis of the striker motion. (a) Vertical position of the striker for all 16 events for the whole duration of the motion. (b) Close-up view of the motion relative to the first and the second impacts on the chain. (c) As of (b) but relative to strikes #7 and #8. 133

Figure 4.13 – Video processing analysis of the striker motion. Peak amplitude of the incident wave recorded with the sensor disk and the corresponding (a) relative rebound height, (b) rebound height.. 134

Figure 4.14 – Video processing of the sensor disk. Individual frame and pre-processing. The edges and center lines of the sensor disk identified using the video processing algorithm adopted in this study. . 135

Figure 4.15 - Video processing of the sensor disk. (Left column) Time history of the disk vibrations. Note that the position of the sensor center line was obtained by averaging the position of 4 horizontal edges associated with the sensor disk. As such, the sensor displacements were discretized in steps of 0.25 pixel. Therefore, the minimum sensor displacement obtained from the videos is about 0.011 mm. (Right column) Close-up view of strikes 1, 8, and 10. 136

Figure 4.16 - The sensor vibrations detected in the videos in colormap format. 137

Figure 4.17 – Peak-to-peak sensor displacement as a function of the associated incident solitary wave amplitudes. 137

Figure 5.1 – (a) Design of the proposed 1-D acoustic diode. (b) Forward configuration, which allows the propagation (from left to right) of acoustic waves, since there is a gap between the particles and the intruders after applying the static compression. (C) Reverse configuration, in which the acoustic energy (propagating from left to right) is blocked by multiple reflections in the PBZ. 146

Figure 5.2 - Effect of asymmetric intruders on the interaction force acting on the i^{th} particle in the PBZ in the reverse configuration. 148

Figure 5.3 – Validation of the numerical model of the acoustic diode. (a, b) Displacement of the 1st and 40th particles when the diode made of stainless-steel particles is subjected to a sinusoidal excitation along the forward configuration at (a) 1000 Hz and (b) 8000 Hz. (c, d) Displacement of 1st and 40th PTFE particles when the diode is subjected to a sinusoidal excitation of (c) 1000 Hz and (d) 3000 Hz along the forward configuration. 152

Figure 5.4 – Dynamic response of the stainless-steel diode subjected to a 1 μm peak-to-peak, 125 Hz, 100 ms sine wave. Displacement of the particles #1, #10, #30, and #40 in the (a) forward and (b) reverse configuration. (c) close-up view of (a); (d) close-up view of (b). 154

Figure 5.5 – Dynamic response of the stainless-steel AD subjected to a 1 μm peak to peak amplitude, 125 Hz, 100 ms sine wave (a) Displacement of particle #40 as a function of time in both configurations. (b) Force of particle #40 as a function of time in both configurations. (c) Power distribution over frequency for the transmitted wave at particle #40 in both configurations(d) Energy transfer ratio as the wave propagates through the chain in both configurations..... 156

Figure 5.6 – Reverse configuration. Energy transfer ratio as a function of lattice site and frequency, where the peak-to-peak amplitude of the input signal is equal to 1 μm . (a) from 25 Hz to 1000 Hz with a frequency step of 20 Hz, and (b) from 1000 Hz to 7000 Hz with a frequency step of 40 Hz. (c) 2D map for frequencies between 25 Hz and 250 Hz. (d) 3D plot for frequencies between 25 Hz and 250 Hz... 157

Figure 5.7 – Time domain response of the stainless-steel diode at the 40th particle, under 1 μm peak-to-peak amplitude and frequency of (a) 300 Hz, and (b) 500 Hz. 159

Figure 5.8 –Energy transfer ratio as a function of lattice site and frequency in the reverse configuration, where the peak-to-peak amplitude was (a) 0.2 μm and (b) 2 μm . (c) Comparison of energy transfer ratio at particle #40 in the reverse configuration..... 160

Figure 5.9 – Reverse configuration. Energy transfer ratio as a function of lattice site and frequency, where the peak-to-peak amplitude is equal to 1 μm and the diode contains (a) 30 and (b) 50 particles. (c) Comparison of energy transfer ratio at the last particle in diodes with 30, 40, and 50 particles..... 162

Figure 5.10 – (a) Energy transfer ratio as a function of lattice site and frequency, where the peak-to-peak amplitude is equal to $1 \mu m$ in the aluminum diode. (b) Comparison of energy transfer ratio at the last particle in stainless-steel and aluminum diodes..... 163

Figure 5.11 - Time domain response of the PTFE AD in the forward and reverse configurations. Displacement of the 40th particle, when the chain is subjected to a periodic vibration with peak-to-peak amplitude of $1 \mu m$ and frequency of 125 Hz..... 163

Preface

I would like to thank my advisor, Professor Piervincenzo Rizzo, for his mentorship and support throughout my Ph.D. studies. I appreciate him for giving me this research opportunity and allowing me to grow as a researcher.

I would like to thank my dissertation committee members, Professor Lev Khazanovich, Professor Amir H. Alavi, and Professor Samuel Dickerson for their professional guidance and the time they dedicated to this work.

I acknowledge the financial support of the National Science Foundation, the American Society of Nondestructive Testing, and the University of Pittsburgh.

I would like to extend my gratitude to my colleagues at the Laboratory of Nondestructive Evaluation and Structural Health Monitoring, Dr. Amir Nasrollahi, Dr. Kaiyuan Li, Ritesh Misra, and Yuhui Zeng for their collaboration in my research. The solitary wave transducers and the discrete element model used in this study were developed based on the work of the former Ph.D. students of the group, Dr. Amir Nasrollahi and Dr. Kaiyuan Li. The wireless units used in one of the corrosion experiments were designed and assembled by Mr. Ritesh Misra. The experiments presented in Chapter 3 were designed and implemented by Mr. Yuhui Zeng. I am also sincerely grateful to Mr. Charles Hager (Scooter) for his assistance in the experiments.

I would like to extend my special thanks to my family for their love, support, and encouragement throughout my studies. This accomplishment is as much as theirs as it is mine. I am deeply thankful to Naser for his support, patience, and encouragement during my studies. None of this would happen without his support.

1.0 Introduction

Granular crystals are arrays of closely packed particles interacting via nonlinear contact forces, and a class of nonlinear periodic structures or discrete nonlinear systems. A one-dimensional (1D) monatomic granular crystal is shown in Figure 1.1a. The nonlinearity in granular crystals results from the Hertzian Contact between the particles [1, 2]. According to the Hertz law, the contact force between adjacent particles F is nonlinearly proportional to the deformation δ of the diameter connecting the centers of the interacting particles:

$$F = A\delta_+^{3/2} \quad (1.1)$$

Here, A denotes the contact stiffness coefficient, and the subscript $+$ denotes the operator $\max(\delta, 0)$. The subscript $+$ implies that granular crystals do not support tensile force between the particles when they are separated from each other (tensionless contact between the particles). If the contact area between the adjacent particles is small, granular crystals can be modeled as a system of point masses connected with nonlinear springs as shown in Figure 1.1b.

The dynamic behavior of granular arrays can be tuned to strongly nonlinear, weakly nonlinear, and linear regimes [3-5]. Strongly nonlinear arrays are uncompressed chains that support the formation and propagation of highly nonlinear solitary waves (HNSWs). In linear and weakly nonlinear regimes, where the granular chain is statically compressed, unique features like speed tunability [5] and filtering [3, 6, 7] are provided. The unique dynamic behavior of granular crystals has led to their application in numerous engineering applications including nondestructive evaluation (NDE) and structural health monitoring (SHM) [8-18], and acoustic wave controlling [6, 19-30].

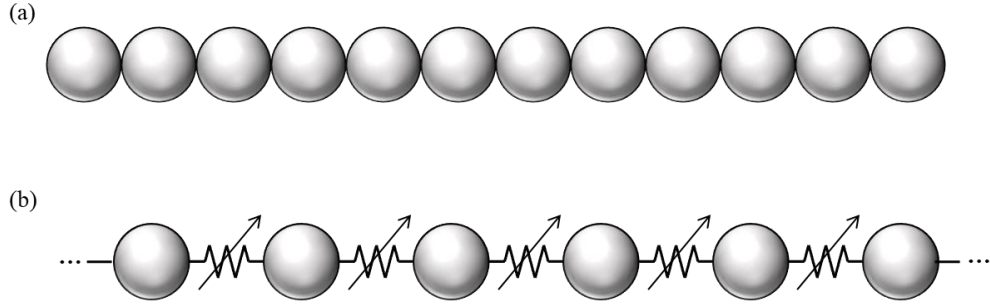


Figure 1.1 - A one-dimensional granular crystal. (a) A monoatomic array of closely packed particles. (b) The particles in the granular crystal interacting via nonlinear contact springs.

1.1 Background

1.1.1 Highly Nonlinear Solitary Waves

The propagation of HNSWs in granular crystals was first studied by Nesterenko [31]. He showed numerically, analytically, and experimentally that 1D granular crystals composed of spherical particles support the generation and propagation of HNSWs under zero or weak static compression [31, 32]. Compared to linear elastic waves in continuous media, HNSWs present unique properties. For example, they support a high level of acoustic energy within a finite spatial wavelength of five particles diameters [4, 5]. Moreover, the speed of HNSWs (V_s) depends nonlinearly on their amplitude. It is shown that the speed of solitary waves depends on the maximum force between the particles (F_m) through the following equation [5]:

$$V_s = 0.6802 \left(\frac{E}{R\rho^{3/2}(1-\nu^2)} \right)^{1/3} F_m^{1/6} \quad (1.2)$$

According to Eq. (1.2), solitary waves speed depends also on the elastic parameters (Young's modulus E and Poisson's ratio ν) and the density ρ of the particles. Thus, solitary wave speed can

be tuned by changing the system's parameters like material properties [33-35], the particles' shape and dimension [33-38], the particles' configuration and arrangement [3, 34, 35], and static precompression [4, 39].

Researchers have shown that the interaction of HNSWs with an elastic medium results in a series of reflected solitary waves which their amplitudes and arrival times depend on the mechanical and geometric properties of the adjacent medium [40, 41]. Yang *et al.* studied numerically, analytically, and experimentally the reflection of HSNWs at the interface of a large thin plate, and found that the amplitude and the arrival time of the reflected solitary waves depend on the plate thickness, the particles size, and the distance from the plate boundaries [42]. Cai *et al.* examined the interaction of HNSWs with a slender beam and reported that the geometric and mechanical properties of the beam and the thermal stress applied to the beam affect certain features of the solitary waves [43].

Kim *et al.* indicated experimentally and numerically that solitary waves are effective to detect delamination in a carbon fiber reinforced polymer composite plate [11]. A numerical study on the interaction of HNSWs with composite beams showed that solitary waves are effective to evaluate the directional elastic parameters of the composites [44]. Other researchers reported that solitary wave-based NDE method is effective in detecting subsurface voids [45], and assessing the quality of adhesive joints [8, 10], composites [11, 15, 44, 46], orthopedic and dental implants [12, 47]. Other applications include but are not limited to the measurement of internal pressure in tennis balls [48-50] and the measurement of axial stress [17, 51].

1.1.2 Granular Crystals as Acoustic Metamaterials

Section 1.1.1 presented a review on the propagation of HNSWs in uncompressed granular crystals, i.e., strongly nonlinear regime. Uncompressed granular chains cannot support the propagation of oscillatory waves, and are therefore called a sonic vacuum [4]. In this section, we focus on the dynamic response of compressed 1-D granular crystals, which support the propagation of periodic waves. The following presents a review on the application of granular crystals in wave propagation manipulation like wave filtering, localizing, and rectifying.

In the linear and weakly nonlinear regimes, a constant compressive force F_0 is applied to both ends of the chain. The initial static compression causes an initial deformation (δ_0) between the neighboring particle centers, $\delta_0 = (F_0/A)^{2/3}$, and the equation of motion of the particles is:

$$m\ddot{u}_i = A_{i-1,i}[\delta_0 + u_{i-1} - u_i]_+^{3/2} - A_{i+1,i}[\delta_0 + u_i - u_{i+1}]_+^{3/2} \quad (1.3)$$

In a chain composed of identical elastic spherical particles, the stiffness constants $A_{i-1,i}$ and $A_{i+1,i}$ are identical:

$$A = \frac{E\sqrt{2R}}{3(1-\nu^2)} \quad (1.4)$$

If the amplitude of the dynamic displacements ($u_{i-1} - u_i$ and $u_i - u_{i+1}$) is much less than the static overlap (δ_0), using the Taylor series expansion, it is shown that that the chain can be considered as a linear lattice with spring constant $K_2 = \frac{3}{2}A\delta_0^{1/2}$ [3]. The study of vibrations in a linear springs-masses system shows the presence of a cut-off frequency. Based on the Newton's law, the equation of motion of the particles in a 1D linear monoatomic chain is written as:

$$m\ddot{u}_i = K_2(u_{i-1} - u_i) - K_2(u_i - u_{i+1}) \quad (1.5)$$

or:

$$m\ddot{u}_i = K_2(u_{i-1} - 2u_i + u_{i+1}) \quad (1.6)$$

Consider the following solution in the form of a traveling wave:

$$u_n = Ue^{i(kna - \omega t)} \quad (1.7)$$

Here, k , ω , and a represent the wave number, the angular frequency, and the distance between the masses at rest. Substituting Eq. (1.7) in Eq. (1.6) yields to the dispersion relation for a linear monoatomic chain:

$$\omega = \sqrt{\frac{4K_2}{m}} \left| \sin k \frac{a}{2} \right| \quad (1.8)$$

Based on Eq. (1.8), linear monoatomic chains have an upper limit for frequency as $f_c = (\sqrt{4K_2/m})/2\pi$. In fact, linear chains act as a low-pass acoustic filter and the cutoff frequency f_c depends on the static precompression, and the geometric and the material properties of the particles.

Several theoretical and experimental studies have shown the presence of frequency bandgaps in compressed diatomic chains with alternating particles glued [29], welded [26], or statically compressed together [27, 52]. It has been also reported that a 1D diatomic granular crystal with three-particle unit cells provides two distinct finite band gaps [7]. The bandgaps can be tuned by changing the initial compression [7, 52, 53], the particles geometric and material properties [52], the particles configuration [53, 54], the amplitude of the applied vibrations [55], and by using electric [56] and magnetic fields [52, 57].

Furthermore, researchers have shown that the presence of one or a few dissimilar particles (defects) in a compressed monoatomic granular chain causes tunable defect modes above the cut-off frequency in the linear regime [58, 59]. In the weakly nonlinear regime, where the amplitude of dynamic displacements are smaller but not far smaller than the static overlap, diatomic granular

chains exhibit discrete breathers or intrinsic localized modes close to or within their bandgaps [27, 60]. The localized modes can be used as a mechanism to localize vibrational energy in space.

Recently, acoustic diodes have emerged as novel acoustic metamaterials designed to break reciprocity in the propagation of acoustic waves using nonlinearity and periodicity. The first acoustic diode was proposed by Liang *et al.*, which consisted of a superlattice of glass and water layers and a nonlinear medium (ultrasonic contrast agent made of suspension of microbubbles) acting as a frequency converter [61-63]. It was shown that the system blocks acoustic waves if it applied from the superlattice side, and the wave frequency is higher than the cut-off frequency of the superlattice. On the other hand, the system partially transmits the acoustic energy if the same acoustic wave is applied from the nonlinear medium side. The reason is that the nonlinear medium partially converts the incident wave to a secondary wave with a different frequency which lies within the pass band of the superlattice. Therefore, the designed system allows the propagation of the applied acoustic wave only in one direction.

This innovative design was followed by other researchers using granular media as frequency converters and frequency filters to achieve efficient nonreciprocal wave propagation within a broad frequency band [20, 64]. For instance, Devaux *et al.* used nonlinear granular media as the frequency converter component and a superlattice as the frequency filter [20]. Fu *et al.* used a 1-D chain of masses connected by tension-compression asymmetric bilinear springs and linear springs, acting as a frequency converter and a frequency filter, respectively [64]. Boehler *et al.* reported non-reciprocal acoustic transmission in a 1-D granular chain containing a defect particle [19], where the chain filters acoustic waves of frequencies above the chain cut-off frequency in one direction. In the opposite direction, the presence of the defect particle causes a vibrational mode localized around the defect particle, and the frequency of the generated mode lies within the

chain pass band, so vibrations propagate through the chain. Recently, Cui *et al.* demonstrated the nonreciprocal propagation of acoustic waves by breaking geometrical symmetry in a granular chain [65]. The proposed system was based on the amplitude-dependent bandgaps in a compressed granular chain coupled with a conical rod. The conical rod was used to change the amplitude of the incident wave, activating the bandgaps only in one direction.

1.2 Motivation and Vision

This dissertation investigates the applications of highly nonlinear solitary waves as a new NDE/SHM method to detect localized corrosion in plate-like structures. Additionally, this dissertation studies the application of the solitary wave-based NDE method to examine anisotropy in rock materials. Numerical and experimental methods were used in this research to examine the effectiveness and reliability of the proposed method in these applications. Furthermore, this dissertation investigates the propagation of mechanical waves in a compressed 1D granular crystal of spherical particles coupled with asymmetric intruders.

1.2.1 Detection of Localized Corrosion

Corrosion affects many engineering structures worldwide. For example, pipelines subjected to high temperatures in power plants and petrochemical industries are vulnerable to wall thinning corrosion and erosion-corrosion, which may lead to leakage and explosion. According to the U.S. PHMSA [66], in the last 20 years, nearly 6,000 incidents in pipelines have been reported in the U.S., causing more than 290 deaths and about \$10 billion in damage. Nearly 30% of these incidents

were caused by corrosion [66]. Corrosion was also a significant contributing factor in about 20% of accidents in refineries in Europe [67]. Therefore, regular inspection and maintenance of pipelines are crucial to ensure safety and prevent adverse consequences for the economy and the environment.

Several NDE/SHM methods exist for corrosion detection in pipes. The most important ones are ultrasonic testing [68-74], infrared thermography [75-77], and pulsed eddy current [78-82]. All these methods have been proved effective in detecting corrosion. However, they may be limited by the operating temperature of the pipelines and require temporary shutdowns. For example, ultrasonic testing is not applicable at high temperatures because piezoelectric transducers, used to generate and detect the ultrasounds, are depolarized at temperatures higher than the Curie temperature (about 250°C). Besides, the difference in the coefficient of thermal expansion at the interface between the transducer and the monitoring media may cause noise or false positives. Therefore, there has been an increased interest in developing NDE methods for detecting corrosion at high temperatures. Some researchers proposed using piezo materials like bismuth titanate and lithium niobite, which can operate up to 550 °C and 1000 °C [83-87], respectively. However, the use of these piezo materials leads to a lower sensitivity over time, and their attachment is sophisticated and time-consuming [88]. Furthermore, using non-contact systems such as EMATs [89] and lasers [90, 91] was proposed, but using these systems causes lower efficiency than conventional piezoelectric transducers, or they are too expensive to warrant widespread usage. A recent development was proposed by Cegla *et al.* [88], who proposed using thin waveguides separate the vulnerable piezo from the high-temperature area to be inspected [73, 88].

The vision of this research is to propose an alternative NDE approach that can also be used for the 24/7 monitoring (structural health monitoring approach) of pipes. The method relies on the

propagation of HNSWs propagating in an uncompressed 1D granular crystal [4, 28, 33, 39, 92-97]. The overall principle of the proposed NDE approach is schematized in Figure 1.2. A vertical chain of identical spheres is in dry contact with the structure to be inspected. An incident solitary wave (ISW) is generated at the top of the chain and propagates through the array toward the surface of the structure. At the interface between the chain and the structure to be inspected, most of the acoustic energy carried by the ISW is reflected, giving rise to one or two reflected solitary waves, typically referred to as the primary and the secondary reflected solitary waves (PSW and SSW).

Comparing with the ultrasonic testing, in HNSW-based NDE, the chain of particles represents the “pulse-echo” transducer that acts as a transmitter of solitary waves and as a sensor for the same waves. If the particles are made of thermally insulating material, they act as a buffer between the structure and the sensing system embedded in the array. As such, HNSW-based NDE can be used for detecting corrosion at high temperatures, and it offers several advantages over classical NDE methods, including simplicity, low cost, and portability.

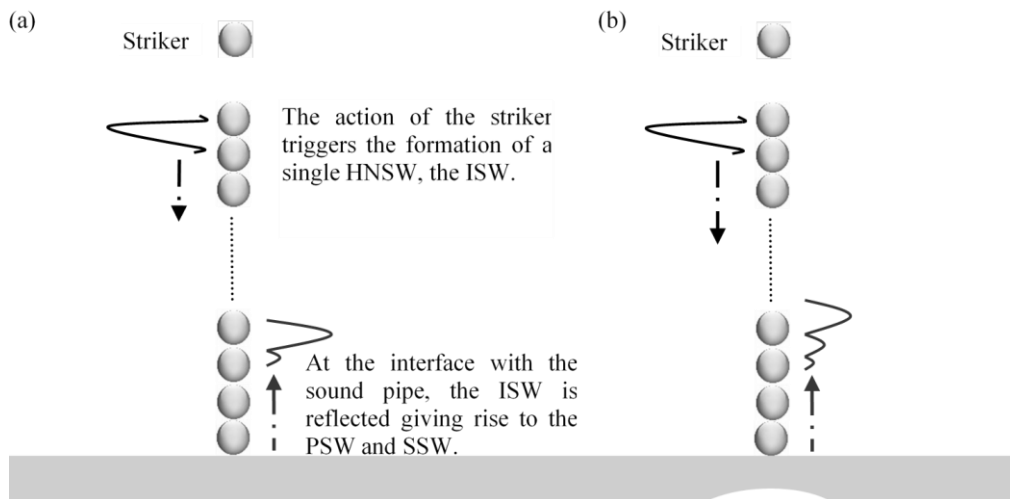


Figure 1.2 – Scheme of the proposed NDE/SHM system for the detection of localized corrosion.

1.2.2 Characterizing Anisotropy in Rocks

In oil and gas industry, elastic properties of rocks have an important impact on hydraulic fracturing development [98], wellbore stability [99, 100], seismic interpretation [101], and micro-seismic monitoring [102]. The elastic moduli of rocks vary on different orientations, due to the effect of anisotropy. Anisotropy as an inherent characteristic of rocks, is attributed to the inclusion alignment, clay orientations, pores, cracks, foliations, and/or beddings [103]. Transversely isotropic (TI) models are generally used to characterize the anisotropy of sedimentary and metamorphic rocks. The elastic moduli of TI material are symmetric about an axis that is normal to a plane of isotropy [104, 105]. For layered and/or foliated rocks, the isotropic planes are generally parallel to the layers/foliation planes [106].

While there are some practical successes associated with assuming rock to be a TI material, the reality is more complex [107]. Furthermore, in testing anisotropic properties even for an ideally TI material, there is a challenge because both static compression tests and ultrasound characterization require *a priori* identification of symmetry directions so that loading and wavepaths can be aligned accordingly. Typically, the foliation planes are determined visually, but with limited resolution for microscopic and/or visually-subtle foliations. Some nondestructive evaluation methods, like scanning-electron-microscopy (SEM) and computed-tomography (CT) provide precise measurements at the expense of costly equipment and time-consuming preparation ([108, 109]). In the absence of reliable specimen orientation from visual methods, methods based on the propagation of ultrasonic P-waves can be used. For example, [107], extracted the seismic properties of spherical rock samples by measuring the P-wave velocity along 132 directions. Other studies [110-112] demonstrated that the velocity of the P-wave propagating parallel to the foliation planes is higher than the perpendicular direction, yielding the conclusion that the orientation of

isotropic planes can be determined by mapping P-wave velocity distribution. However, ultrasonic-based characterization requires extensive sample preparation (i.e., spherical samples or many, variably oriented cylindrical or prismatic specimens) and can encounter challenges with coupling sensors to curved surfaces.

This study proposes a low cost, fast, and simple alternative NDE technique based on the generation, propagation, and detection of HNSWs for high resolution characterization of anisotropy of rocks. Similar to the description in section 1.2.1, the technique relies on the use of a short granular chain made of spherical particles placed in a point-contact with the structure to be inspected.

This dissertation presents the numerical and experimental investigation of the effectiveness of the solitary wave-based NDE for detecting anisotropy in rocks. The experiments were performed by Mr. Yuhui Zeng, while the author conducted the numerical modeling and the experimental data analysis.

1.2.3 Controlling Mechanical Waves

Controlling mechanical waves like sound and structural vibrations is of great interest in many engineering applications. For instance, extensive research has been devoted to improving the seismic behavior of civil structures. Shock and vibration control are also crucial in designing many mechanical systems. In addition, reducing environmental noise annoyance is extremely important to enhance human comfort, health, and efficiency. For this purpose, several passive and active methods including hydraulic dampers, tuned mass dampers, and electronic sensor-actuator loops have been developed.

Over the past three decades, acoustic metamaterials or phononic crystals have emerged as artificial structures designed and engineered to control mechanical waves [3, 113]. They are mostly designed based on using periodicity and discreteness [3, 113]. Therefore, most of the proposed acoustic metamaterials are composed of repeating small units called unit cells or meta-atoms. It is shown that periodic structures can strongly affect the propagation of waves through Bragg scattering, i.e. the scattering of waves with a wavelength in the order of the dimension of the periodic unit [3, 114, 115].

Granular crystals, described in section 1, are a class of nonlinear periodic structures and the focus of this research. Nonlinearity in granular crystals provides unique properties like frequency conversion, localization, and tuning the dynamic behavior of the system [3]. These features have led to proposing various applications of granular crystal for the control of wave propagation including impact mitigation and energy harvesting [116, 117], acoustic lenses [118], acoustic switches and logic gates [119], and acoustic diodes [19, 20, 64, 93].

The vision of this study is to propose a novel design of granular crystals for controlling noise, structural vibrations, and impacts. The proposed design uses periodicity, discreteness, nonlinearity, and spatial asymmetry to control the propagation of mechanical waves. Figure 1.3 presents the proposed design, which is a statically compressed 1D chain of spherical particles. The chain consists of two neutral zones (NZs) and one potential barrier zone (PBZ). In the PBZ, particles are in contact with asymmetric intruders attached to the supporting frame.

This design follows the work of Li and Rizzo, in which asymmetric intruders in a chain of particles were used to achieve unidirectional propagation of solitary waves [23]. It was shown that the asymmetric intruders prevent the propagation of solitary waves by restraining the displacement of particles along one direction (forward configuration). However, the system allows the

propagation of solitary waves along the opposite direction (reverse configuration). Although the system was proven effective under impact loading, its performance under periodic loadings was not considered.

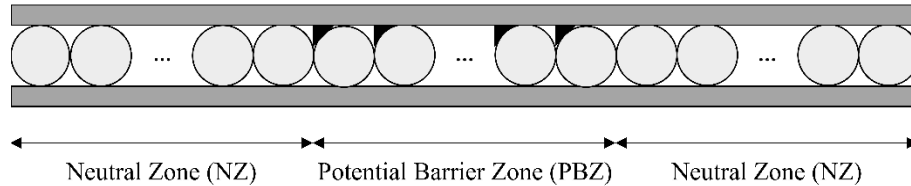


Figure 1.3 – Design of the proposed granular crystal design to mitigate noise and vibration.

In the present dissertation, we studied the propagation of periodic waves in the forward and reverse configurations. In the forward configuration, the actuator is positioned on the left side of the chain, and the initial compression and vibrations are applied to the first particle on the left side of the chain. In this configuration, applying initial compression causes the particles to move slightly toward right, leading to a gap between the particles and the intruders in the PBZ. The amplitude of the applied dynamic vibrations is smaller than the initial static deformation. So, periodic vibrations transmit through the chain by the oscillation of the particles with no interaction between the particles and the intruders in the PBZ. On the contrary, in the reverse configuration, the actuator is positioned on the right side of the chain. The initial compression, applied to the right side of the chain, causes the particles to move slightly toward left. As a result, the particles in the PBZ are pressed to the intruders, and their dynamic oscillations are restrained by the intruders. Consequently, the proposed design transmits the applied acoustic energy in the forward direction but partially blocks it in the reverse direction.

1.3 Organization of Dissertation

This dissertation is organized as follows: Chapter 2.0 presents the study on the application of HNSWs for the detection of localized corrosion. Coupled discrete element/finite element models were used to study the dynamic interaction between solitary waves and steel plates in pristine and corroded conditions. In addition, two experiments were conducted to monitor localized corrosion in two steel plates of different thicknesses using the solitary wave transducers. Chapter 3.0 investigates the application of HNSWs to characterize transversely isotropic geo-materials. Similarly, numerical and experimental methods were used to examine the interaction of solitary waves with sandstone and slate samples in different conditions. In chapter 4.0, the long-term performance of the developed solitary wave transducers is studied in a one-week-long test using vision-based methods. Finally, chapter 5.0 presents a numerical investigation of the dynamic response of a compressed 1D granular crystal coupled with asymmetric rigid intruders at shielding mechanical vibrations. All chapters are extracted from peer-reviewed journal publications, listed at the beginning of each chapter. Chapter 6.0 concludes this dissertation with a summary of the research and a list of main novel findings and recommendations for future research.

1.4 Intellectual Merit and Broader Impact

The present study will aid in the development of granular crystal-based engineering devices. Part of the present study will contribute to the development of a new NDE method for detecting localized corrosion using HNSWs and characterizing anisotropy in rock materials. This study

demonstrates that the HNSW-based NDE method is effective for localized NDE applications. In addition, the study provides new insights into the behavior of solitary waves and their interaction with boundaries. The dissertation also investigates the reliability of the HNSW-based NDE in long-term applications and provides insight into the potential modifications for the design of HNSW transducers. This research also investigates the application of a novel design of granular crystals coupled with asymmetric intruders for controlling mechanical waves like noise and structural vibrations.

The body of this work takes the form of several peer-review articles that are at various stages of publication during the final writing herein:

Refereed journal articles:

Jalali, H., Rizzo, P. “Numerical investigation of the interaction of highly nonlinear solitary waves with corroded steel plates.” *International Journal of Mechanical Sciences* 208, 2021.

Jalali, H., Zeng, Y., Rizzo, P., and Bungler. A. “Highly Nonlinear Solitary Waves to Characterize Anisotropy of Rock Materials.” *Materials Evaluation* 79(10) 2021.

Jalali, H., Rizzo, P. “Highly nonlinear solitary waves for the detection of localized corrosion.” *Smart Materials and Structures*, 29(8), 2020.

Jalali, H., Rizzo, P., Nasrollahi, A., “Asymmetric propagation of low-frequency acoustic waves in a granular chain using asymmetric intruders.” *Journal of Applied Physics*, 126(7), 2019.

Manuscripts under review:

Jalali, H., Misra, R., Dickerson, S., and Rizzo, P. “Remote Monitoring of Localized Corrosion using Solitary Waves.” Under review in *Structural Health Monitoring*.

Jalali, H., and Rizzo, P. “On the long-term performance of solitary wave-based transducers for nondestructive evaluation applications.” Under review in *ASME Journal of Nondestructive Evaluation*.

Additionally, auxiliary publications resulted from this study are:

Misra, R., Jalali, H., Dickerson, S. and Rizzo, P. “Wireless Module for Nondestructive Testing/Structural Health Monitoring Applications Based on Solitary Waves.” *Sensors*, 20(11), 2020.

Misra, R., Jalali, H., Dickerson, S. and Rizzo, P. “Wireless Node for Highly Nonlinear Solitary Wave Transducers.” *IEEE Sensors Journal*, 2021.

And the related conference proceedings are:

Jalali, Hoda, and Piervincenzo Rizzo. "A Remote Solitary Wave-based Technique for Monitoring Corrosion in Steel Structures: Numerical Analysis and Experimental Validation." In *Quantitative Nondestructive Evaluation*, vol. 85529, p. V001T09A004. American Society of Mechanical Engineers, 2021.

Jalali, H., Nasrollahi, A., Rizzo, P. “Monitoring local impedance changes with solitary waves.” In *European Workshop on Structural Health Monitoring*, pp. 669-678. Springer, Cham, 2020.

2.0 Application of Granular Crystals to Detect Localized Corrosion

This chapter investigates the application of HNSWs traveling through a 1D granular crystal as an NDE method to detect localized corrosion in steel structures. The present study involves numerical modeling and experimental investigation of the interaction of HNSWs with a steel plate in pristine and corroded condition. Coupled discrete/finite element models were developed to predict the time of flight and the relative amplitudes of the reflected solitary waves as localized corrosion progresses in the plate. Numerical models were used to examine the sensitivity of the method in terms of different parameters such as plate initial thickness, chain length, and particles' mechanical and geometric properties. Furthermore, a few experimental studies were conducted by using chains of monoperiodic particles in contact with a steel plate subjected to localized accelerated corrosion. A few damage-sensitive features were extracted from the time waveforms and fed into a multivariate statistical analysis to enhance the sensitivity of the proposed non-invasive monitoring approach. Machine learning techniques were implemented to improve the sensitivity of the HNSW-based NDE to localized corrosion.

This chapter is written based on the following peer-reviewed articles:

Jala Jalali, H., Misra, R., Dickerson, S., and Rizzo, P. "Remote Monitoring of Localized Corrosion using Solitary Waves." Under review in *Structural Health Monitoring*.

Jalali, H., Rizzo, P. "Numerical investigation of the interaction of highly nonlinear solitary waves with corroded steel plates." *International Journal of Mechanical Sciences* 208, 2021.

Jalali, H., Rizzo, P. "Highly nonlinear solitary waves for the detection of localized corrosion." *Smart Materials and Structures*, 29(8), 2020.

2.1 Introduction

Solitary waves are compact nonlinear stress waves that can travel through uncompressed or weakly compressed chains of particles where adjacent particles are in contact with each other [4, 32, 33, 39, 120-123]. The discreteness and the nonlinear contact between the particles result in unique characteristics [4, 32, 33, 39, 120-123]. For instance, the traveling speed depends nonlinearly on their amplitude and is significantly lower than the speed of sound in the material composing the particles in the chain.

Several research groups demonstrated that the interaction of solitary waves with an interface can be used to draw inferences about the mechanical properties and geometry of the adjacent medium. For instance, numerical studies showed that solitary waves can be used to detect impurities in granular chains [124, 125]. Yang *et al.* [126] demonstrated experimentally and analytically that the magnitudes and traveling times of the waves reflected from the interface with any linear elastic homogeneous medium depend on the mechanical and geometric properties of the medium. The above principles represent the ground foundation of the application of solitary waves for NDE and SHM applications. To this end, the use of HNSWs has been proved effective at identifying the mechanical properties of linear elastic media [43, 126, 127], composites [44, 128], and geomaterials [129, 130], measuring thickness [42-44], monitoring cement and concrete hydration [8, 131, 132], detecting defects in elastic solids and composites [11, 15, 133-137], assessing adhesive joints [10], orthopedic and dental implants [138] and bone microstructure [139, 140], inferring axial stress [9, 17, 43, 49], and measuring intraocular pressure [141].

Compared to some traditional NDE/SHM techniques, the solitary wave-based technique provides some unique advantages like simplicity and low cost. The setup includes a granular chain

composed of identical spheres in contact with the object to be inspected/monitored. The impact of a striker on the chain creates an incident solitary wave (ISW) traveling through the chain toward the surface of the inspection medium. The interaction of the ISW with the inspection medium causes the formation of one or few reflected solitary waves. The first and the second (if any) reflected solitary waves are typically referred to as the primary reflected solitary wave (PSW) and the secondary reflected solitary wave (SSW). The major parameters used in solitary wave-based NDE/SHM applications are the time of flight and the normalized amplitude. The former is defined as the time interval between the ISW and the PSW while the latter is the ratio of the amplitude of the PSW to the amplitude of the incident wave.

The goal of this study is to develop a new NDE method based on the propagation of HNSWs propagating in an uncompressed 1D granular crystal. The method can also be used for the 24/7 monitoring (SHM approach) corrosion monitoring. In order to establish the proposed HNSW-based method for detecting and monitoring localized corrosion in metallic structures, it is essential to understand how these waves interact with pristine and corroded plates. Although there is a limited number of studies about the interaction of HNSWs with pristine plates, the interaction of HNSWs with damaged plates has not been investigated before.

This study aims to fill this gap of knowledge by presenting numerical and experimental studies on thin plates subjected to localized corrosion. For this purpose, two coupled discrete element (DE) and finite element (FE) models were developed on the interaction between granular chains and plates. In one model, the plate was simulated using the Kirchhoff–Love theory of plates, and all the particles were simulated as point masses interacting with nonlinear spring. In the other model, the interacting particle and the plate were modeled as 3D deformable solid parts.

The numerical models were used to examine the interaction of solitary waves with plates in pristine and corroded conditions, respectively. Furthermore, the numerical models were used to examine the effects of parameters such as size, number, and material of the particles on the sensitivity of the proposed method at detecting the onset and growth of localized corrosion. The scope of the study is to identify the optimal parameters of the HNSW transducer that are applicable at high temperature or radioactive environments and show maximum sensitivity to localized corrosion.

Moreover, two experiments were conducted to monitor localized corrosion in two different steel plates (6.3 mm and 4.8 mm in thickness) using HNSW transducers. Multivariate outlier detection was implemented to analyze the experimental solitary wave data and improve the sensitivity of the NDE method to localized corrosion. This anomaly detection technique has been widely applied in SHM for detecting structural damages in vibration analysis [142-146], ultrasonic guided waves [147-151], and HNSWs-based NDE [152].

This chapter is organized as follows: Section 2.2 presents the numerical and numerical methods implemented to study the interaction of HNSWs with plates in pristine and corroded conditions. Section 2.3 describes the solitary wave transducers and the two corrosion experiments in which two, corroding plates were monitored using solitary wave transducers. Section 0 presents the statistical analysis performed to analyze the data obtained from the corrosion experiments. Section 2.5 presents the numerical and analytical predictions on the effect of different parameters like initial plate thickness, particle size, particle material properties, and chain length on the reflected solitary wave features. The results obtained from the experimental studies are presented and discussed in Section 2.6. Finally, this chapter concludes with a summary of the main conclusions drawn from the present work.

2.2 Modeling

2.2.1 Coupled Discrete / Finite Element Model: Kirchhoff–Love Plate and Point Masses

This research numerically investigates the interaction of HNSWs with a thin plate using a DE/FE analysis, all implemented in MATLAB®. The two models are integrated at the contact point between the last particle of the granular array and the plate, as shown in Figure 2.1a.

The DE model simulates the chain of particles as a series of point masses connected by nonlinear springs and dashpots as shown in Figure 2.1b. The interaction between two adjacent particles is modeled based on the Hertzian contact law. (Eq. (1.1)) For a chain of N identical spheres, the equation of motion of each particle is as follows:

$$\begin{aligned}
 m\ddot{u}_i &= A_{i-1,i}[u_{i-1} - u_i]_+^{3/2} - A_{i+1,i}[u_i - u_{i+1}]_+^{3/2} \\
 &+ \gamma_{i-1,i}[\dot{u}_{i-1} - \dot{u}_i][u_{i-1} - u_i]_+ - \gamma_{i+1,i}[\dot{u}_i - \dot{u}_{i+1}][u_i - u_{i+1}]_+ \\
 &+ mg
 \end{aligned} \tag{2.1}$$

where m is the particle's mass, g is the gravitational acceleration, and u_i and \dot{u}_i represent the displacement and the velocity of the i^{th} particle, respectively. As shown in Figure 2.1b, u_{N+1} represents the displacement of the plate at the contact point. The coefficient $A_{i,i+1}$ is the contact stiffness between the i^{th} and the $i+1^{\text{th}}$ particles defined as [2]:

$$A_{i,i+1} = \begin{cases} \frac{E_b \sqrt{2R}}{3(1 - \nu_b^2)} & i = 1:N - 1 \\ \frac{4\sqrt{R}}{3} \left[\frac{(1 - \nu_b^2)}{E_b} + \frac{(1 - \nu_p^2)}{E_p} \right] & i = N \end{cases} \tag{2.2}$$

According to Eq. (2.2), the stiffness constant is a function of particles radius R , Poisson's ratio ν , and elastic modulus E of the particles and the plate. The subscript b indicates the properties

associated with the beads, whereas the subscript p indicates the plate. Dissipation was introduced with the coefficient, $\gamma_{i,i+1}$ ($i=1:N-1$) and set equal to 4.5 N.s.m^{-1} in agreement with previous studies [40, 153]. Also, the energy dissipation coefficient at the chain-plate interface ($\gamma_{N,N+1}$) was set to 34.05 N.s.m^{-1} as reported in [40].

The FE model simulates the wave propagation in the plate based on the classical plate theory. The plate was meshed into 9216 elements (96 elements along each edge). As shown in Figure 2.1a, the mesh was refined near the interaction area between the plate and the granular chain to enhance the accuracy of the numerical results. However, coarser elements were used at further distances from the interaction point to save computational time. The mesh refinement pattern was determined based on a preliminary convergence test, where it was shown that further increase of the mesh density does not cause a significant change in the properties of solitary waves and the plate deformations. A similar refinement pattern was used in a numerical study on the detection of delamination in composite beams using HNSWs [11]. Figure 2.1c shows a zoom-in of the meshing refinement pattern in a square of size $20 \text{ mm} \times 20 \text{ mm}$, located in the middle of the plate around the interaction point of the plate and the chain. The FE analysis was based on the Reissner-Mindlin plate theory in which the plate is represented by its mid surface (Figure 2.1d). As depicted in Figure 2.1e, each element of the mesh consisted of four nodes, and each node had three degrees of freedom: transverse deflection w , rotation about the x-axis θ_x , and rotation about the y-axis θ_y .

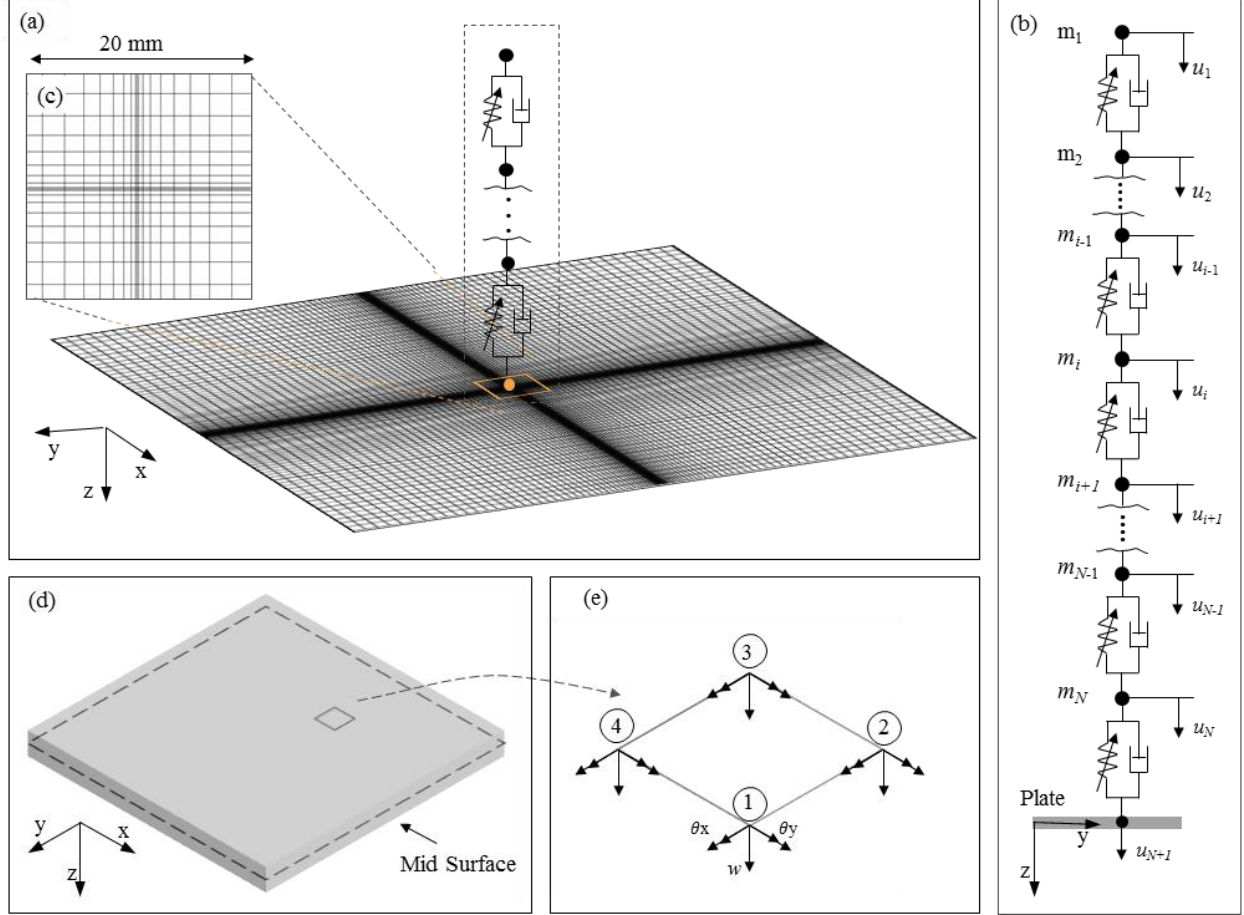


Figure 2.1 – The coupled discrete element (DE) and finite element (FE) models of the interaction between the granular chain and the plate. (a) The integrated at the contact point between the granular chain and the plate. (b) Scheme of the DE model where the granular chain is simulated as a series of point masses connected by nonlinear springs and dashpots. (c) A zoom-in of the mesh refinement pattern in a 20 mm × 20 mm square in the middle of the plate. (d) The mid surface representing the plate in the FE model and © the nodes and the degrees of freedom of each plate element.

With h representing plate thickness, the stiffness matrix \mathbf{k}_e of each element is given as [154]:

$$\mathbf{k}_e = \int_A \frac{h^3}{12} [\mathbf{B}^I]^T \mathbf{c} \mathbf{B}^I dA + \int_A \kappa h [\mathbf{B}^O]^T \mathbf{c}_s \mathbf{B}^O dA \quad (2.3)$$

The first and second terms in Eq. (5) represent the bending and shear stiffness, respectively. The strain matrices \mathbf{B}^I and \mathbf{B}^O depend on the element shape functions and their derivatives [154]. The

parameter κ represents the shear correction factor for rectangular cross-sections equal to 5/6. The material matrices \mathbf{c} and \mathbf{c}_s are defined as:

$$\mathbf{c} = \frac{E_p}{1-\nu_p^2} \begin{bmatrix} 1 & \nu_p & 0 \\ \nu_p & 1 & 0 \\ 0 & 0 & (1-\nu_p)/2 \end{bmatrix} \quad \mathbf{c}_s = \frac{E_p}{1+\nu_p} \begin{bmatrix} 1 & 0 \\ 0 & 1 \end{bmatrix} \quad (2.4)$$

In this study, the plate element stiffness matrix, \mathbf{k}_e , was calculated by integrating Eq. (2.4) numerically using 5×5 Gauss points of integrations. Similarly, the element mass matrix, \mathbf{m}_e , is calculated by numerically integrating:

$$\mathbf{m}_e = \int_A \mathbf{N}^T \mathbf{I} \mathbf{N} dA \quad (2.5)$$

where \mathbf{N} represents the shape function matrix as presented in [154]. With ρ_p representing the density of the steel plate, the matrix \mathbf{I} is given by:

$$\mathbf{I} = \begin{bmatrix} \rho_p h & 0 & 0 \\ 0 & \rho_p h^3/12 & 0 \\ 0 & 0 & \rho_p h^3/12 \end{bmatrix} \quad (2.6)$$

In the numerical simulation, the plate was simply supported along the four edges, and the elastic properties of the steel plate and particles were as $E = 200$ Gpa, $\nu = 0.3$, and $\rho = 7800$ kg.m⁻³. The localized corrosion defect was modeled at the midpoint of the plate by changing the thickness of plate elements, h , from the baseline value of 6.3 mm to smaller values. The dynamic response of the system was analyzed by solving the nonlinear equations of equilibrium in MATLAB solver ode45. The solitary wave profile at the sensor particle was obtained by averaging the interaction forces between the sensor particle and its adjacent particles [44, 94].

2.2.2 Coupled Discrete / Finite Element Model: Using 3D Solid Elements

The interaction of HNSWs with pristine and corroded plates was also investigated using a DE/FE analysis implemented in ABAQUS/Standard. Figure 2.2 presents the scheme of the model. Due to the two symmetry planes in the problem, only one quarter of the geometry was modeled. Here, the DE model simulated the propagation of the solitary waves along the chain of particles whereas the FE model simulated the dynamic interaction between the particle in contact with the plate and the plate.

A granular chain composed of nine particles was simulated to comply with the experimental studies explained in section 02.3.3. In the DE model, the top eight particles, m_1 - m_8 , were modeled as a series of point masses connected with nonlinear axial springs and linear dampers (Figure 2.2b). The nonlinear connectors were defined such to resemble the Hertzian contact law (Figure 2.2c and Eq. (1.1)). Since only one quarter of the geometry was considered in this model, the mass points were $m/4$ in mass, and the stiffness coefficients of the connectors were equal to $A_{i,i+1}/4$ for $i = 1: N - 1$ in Eq. (2.2). The linear damping coefficient was equal to 4.5 N.s.m^{-1} as proposed by previous studies [126].

The last particle of the chain and the plate were modeled as deformable solids made of linear elastic material with no material damping. The interaction between the last particle and the plate was modeled as frictionless hard contact. Figure 2.2d and Figure 2.2e show zoom-in views of the FE model at the interface between the last particle and the plate in the pristine and corroded conditions, respectively. As shown in Figure 2.2e, localized corrosion was simulated as a local thickness reduction (mass loss) in a finite area. The localized corrosion defects were $25.4 \text{ mm} \times 25.4 \text{ mm}$, positioned below the chain-plate interaction point, and the defect depth varied from 0 to 80 percent of the initial plate thickness.

Both the plate and the 3D particle were meshed using 3D 8-node linear isoparametric elements (C3D8 in ABAQUS). The mesh size decreased gradually near the interface of the particle and the plate to improve the accuracy of deformations and stresses calculated at the interface ((Figure 2.2d and (Figure 2.2e). The mesh size was 0.4 mm in areas close the chain-plate interaction, and a preliminary mesh sensitivity analysis showed that further mesh refinement (e.g. using an element size of 0.2 mm close to the interaction area) does not change the properties of the solitary waves and the plate deformations significantly.

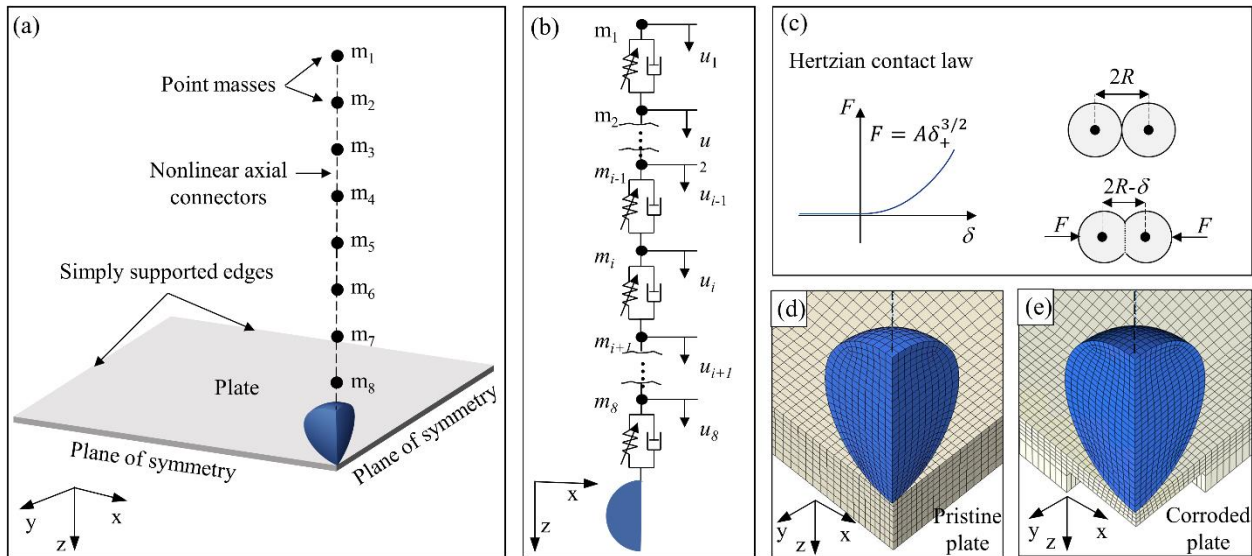


Figure 2.2 - Scheme of the numerical model. (a) The coupled discrete element (DE) and finite element (FE) model used in this study. One-quarter of the model is stimulated due to symmetry. (b) The DE model simulating the chain of particles as a spring-mass system, in which the point masses are connected by the nonlinear springs (defined based on the Hertzian contact law) and dashpots. (c) Graphical representation of the Hertzian contact law. The contact force between adjacent particles F is nonlinearly proportional to the deformation δ of the diameter connecting the centers of the interacting particles. (d and e) Zoom-in views of the FE model at the interface between the last particle and the plate in (d) pristine and (e) corroded conditions. Corrosion was simulated as a local thickness reduction in the plate, below the interaction point.

The DE and the FE models were coupled by connecting the last point mass in the DE model (m_8) to the uppermost node of the 3D particle using the nonlinear connectors described earlier. Concentrated loads equal to one-quarter of the weight of the particles were applied on the mass points, resulting in an initial static compression in the chain. Moreover, body forces were applied to model the effect of gravity. The plate was assumed simply supported along the external edges. Symmetry boundary conditions were applied to the planes of symmetry.

To generate solitary waves in the model, an impact velocity of $V_{imp} = 0.31 \text{ m}\cdot\text{s}^{-1}$ was applied to the first mass point in the chain (m_1). This initial velocity is equivalent to the falling of the striker from a height of 5 mm in the experimental studies presented in section 02.3.3. The interaction of HNSWs with the plate in pristine and corroded conditions was solved using Abaqus\Standard using implicit numerical algorithms. In each case, the time history of the displacement of the mass points and different nodes in the FE parts were extracted. The solitary wave profiles at the sensor particle (positioned in the middle of the granular chain) were then calculated by averaging the interaction force between this particle and its upper and lower adjacent particles. The results were used to analyze the effect of localized corrosion on the interaction between HNSWs and plates.

Furthermore, this model was used to perform a parametric study on the effect of several chain parameters on the sensitivity of the HNSW-based NDE for corrosion detection. The parametric study considers the effect of the granular chain length, particles' size, particles' material, and the sensor location. The present study also investigated the effect of the initial plate size and thickness on the sensitivity of the solitary wave transducers to corrosion.

2.2.3 Analytical Modeling

The time of flight and the normalized amplitude of the reflected solitary waves at the chain-plate interface of a thin plate were also predicted analytically by using the Zener model, which describes the normal impact of a single spherical particle on a large thin plate [155]. This model assumes that the impact is not perfectly elastic and part of the kinetic energy of the impact is dispersed by the propagation of flexural elastic waves in the plate [155-157]. A coefficient of restitution e , comprised between 0 and 1, is introduced and defined as the ratio of the reflected to the incident velocity. The model also assumes that the impact is over before the flexural waves are reflected from the boundaries. In fact, the model assumes that the duration of the impact between the plate and the interacting particle is so short that the reflected flexural waves from the plate boundaries may be neglected. It should be noted that this analytical model is more reliable in thick plates where the local contact stresses in the plate are not disturbed by the plate boundaries.

The Zener model combines the equations of motion of the plate and the particle, yielding to the following nonlinear differential equation:

$$\frac{d^2\sigma}{d\tau^2} + \left(1 + \lambda \frac{d}{d\tau}\right) \sigma^{\frac{3}{2}} = 0 \quad (2.7)$$
$$\left. \begin{array}{l} \sigma = 0 \\ d\sigma/d\tau = 1 \end{array} \right\} \text{at } \tau = 0$$

where τ is the dimensionless time, σ represents the dimensionless approach, and λ is a dimensionless inelasticity parameter that accounts for the energy dissipation during the impact, and defined as:

$$\lambda = \frac{\pi^{3/5}}{4\sqrt{3}} \left(\frac{2R}{h}\right)^2 \left(\frac{\rho_b}{\rho_p}\right)^{3/5} \left[\frac{v_m^2 \rho_p (1 - v_p^2)}{E_p} \right]^{1/10} \left[1 + \frac{E_p (1 - v_b^2)}{E_b (1 - v_p^2)} \right]^{-2/5} \quad (2.8)$$

In Eq. (2.8), h is the plate thickness, ρ is the density, and the subscripts b and p denote the bead and the plate, respectively.

This coefficient of restitution can be obtained as a function of λ by solving Eq. (2.7) for a given λ . Boettcher *et al.* proposed the following analytical approximation equation for the coefficient of restitution [157]:

$$e = \exp\left(-\pi(0.54975\lambda - 0.08507\lambda^2 + 0.08559\lambda^3 - 0.01163\lambda^4)\right) \quad (2.9)$$

When the plate thickness is much larger than the particle diameter ($h \gg 2R$) or the plate is considerably stiffer than the bead ($E_p \gg E_b$), the inelasticity parameter is nearly zero ($\lambda \approx 0$) and the restitution factor approaches one ($e \approx 1$). This implies that the particle does not lose kinematic energy during the impact due to the propagation of stress waves in the plate, i.e. the plate behaves like a rigid body. During an inelastic impact ($\lambda > 0$), part of the kinematic energy of the particle is transferred to the plate ($e < 1$), causing flexural elastic waves propagating radially in the plate.

Owing to the relationship between amplitude and speed of the HNSWs ($F_m \propto v_m^{6/5}$), the coefficient of restitution e can be associated with the normalized amplitude (AR) of the solitary waves, defined as ratio of the amplitude of PSW to the amplitude of the ISW, as follows:

$$AR = \frac{F_{m,PSW}}{F_{m,ISW}} = \left(\frac{v_{m,PSW}}{v_{m,ISW}}\right)^{6/5} = e^{6/5} \quad (2.10)$$

In addition, the time of flight of the PSW, defined as the time difference between the arrival of the ISW and the PSW at a given particle location, hereinafter indicated as the sensor particle, can be expressed as [42]:

$$ToF = T_{ti} + T_c + T_{tr} \quad (2.11)$$

Here, T_{ti} represents the traveling time of the ISW between the sensor particle and the plate interface, T_c represents the contact time between the last particle in the chain and the plate, and T_{tr} is the traveling time of the PSW from the plate interface to the sensor particle.

The traveling times of the ISW and the PSW (T_{ti} and T_{tr} respectively) can be calculated based on the distance between the sensor particle and the plate and their propagation speed. If there are N particles of diameter D between the sensor and the plate, the traveling times of the ISW and PSW is expressed as:

$$T_{ti} = ND/V_i \quad (2.12)$$

$$T_{tr} = ND/V_r \quad (2.13)$$

where V_i and V_r denote the speed of the propagation of the ISW and PSW, respectively. The speed of HNSWs propagation (V_s) in an uncompressed granular chain is given by [4]:

$$V_s = 0.9146 D v_m^{1/5} A^{2/5} m^{-2/5} \quad (2.14)$$

According to Eq. (2.14), HNSWs speed (V_s) depends on the diameter (D) and the mass (m) of the particles, the stiffness coefficient of the contact between the particles (A), and the maximum particle velocity (v_m). Chatterjee [121] showed numerically that the maximum particle velocity (v_m) under the propagation of HNSWs is related to the striker velocity (v_{imp}) as: $v_m \approx 0.682v_{imp}$. Therefore, the traveling times of the ISW and the PSW can be estimated as:

$$T_{ti} = 1.18Nv_{imp}^{-1/5}A^{-2/5}m^{2/5} \quad (2.15)$$

$$T_{tr} = 1.18Ne^{-1/5}v_{imp}^{-1/5}A^{-2/5}m^{2/5} \quad (2.16)$$

Additionally, the solution of Eq. (2.7) provides the dimensionless contact time as a function of the inelasticity parameter, λ [157]:

$$\tau_c = 2.762 + 0.4568 \exp(1.27\lambda) \quad (2.17)$$

And the interaction time (T_c) is given by:

$$T_c = m^{2/5}v_m^{-1/5}A_p^{-2/5}\tau_c \quad (2.18)$$

where A_p represents the Hertzian stiffness constant at the particle-plate presented in Eq. (2.2).

The above analytical model only accounts for energy dissipation at the impact by the generation of flexural wave which propagate radially in the plate from the interaction point. However, the model neglects shear deformations in the plate, and energy loss during the impact caused by friction, plastic deformations, and viscous damping at the contact area. Moreover, the analytical model predicts the traveling times of the ISW and the PSW neglecting the initial compression in the chain caused by the weight of the particles in the chain.

2.3 Experiments

This section presents the experiments conducted to evaluate the effectiveness of solitary waves for detecting corrosion. Section 2.3.1 presents a brief description of the solitary wave transducers used in this study. Wired and wireless transducers were used for corrosion monitoring as explained

in section 2.3.1. Then, sections 2.3.2, 2.3.3, and 2.3.4 present the setup of the three experiments used in this study: one magnet experiment and two corrosion monitoring experiments on two different plates.

In the magnet experiment, “damage” was simulated in terms of variation of the local mechanical impedance by moving a permanent magnet at different locations on a steel plate. Four transducers were used to detect the impurity created by the presence of the magnet. This experiment aimed at validating the repeatability and the identical manufacturing of transducers. The experiment results can also help to determine the region of influence of the proposed setup empirically.

In each corrosion experiments, a corroding steel plate was monitored using several solitary wave transducers. The steel plates were $609.6 \text{ mm} \times 609.6 \text{ mm} \times 6.3 \text{ mm}$ and $609.6 \text{ mm} \times 1219.2 \text{ mm} \times 4.8 \text{ mm}$. Solitary wave transducers with different lengths (number of particles) were used for monitoring the corroding plate.

2.3.1 Solitary Wave Transducers

Figure 2.3 shows the solitary wave transducers used in the magnet experiment and the corrosion monitoring on the 4.8 mm-thick plate, presented in sections 2.3.2 and 0, respectively. A conventional solitary wave transducer controlled by the National Instruments PXI is shown in Figure 2.3a. In addition, Figure 2.3b shows a wireless transducer. In the wireless transducer, a Printed Circuit Board (PCB) is mounted on the transducer frame which enables actuating the transducer and recording the solitary waves without any wired connection to electronic equipment.

As shown in Figure 2.3a and Figure 2.3b, both the PXI controlled transducer and the wireless transducers consisted of a vertical chain of 14 spherical particles and 1 sensor disk. The particles

were 19.05 mm in diameter, and 28.2 g in mass. All the particles except the top one (striker) were made of non-ferromagnetic stainless-steel. A commercial electromagnet was used on the top of the chain to lift and release the striker (made of ferromagnetic stainless-steel) from a height of 4 mm. The impact of the striker results in the generation and propagation of solitary waves in the chain. Sensor disks were used to measure the solitary waves as they propagate through the granular chain. The sensor disks were made of a lead zirconate titanate (PZT) wafer, embedded between two 19.05 mm diameter, 6.05 mm thick stainless-steel disks. The PZT was insulated from the metal using Kapton tape.

Figure 2.3c shows a side-by-side view of the PXI controlled transducer and the wireless transducer. In the PXI controlled transducer, the PXI wave generator sends square waves to a MOSFET also connected to a DC power supply. The MOSFET acts as a switch to activate the electromagnet periodically. In addition, the solitary wave force profiles are sampled and recorded using the PXI digitizer. In the wireless transducer, the PCB includes a driver circuit that provides current to the electromagnet, an analog to digital converter (ADC) chip electronic that samples the solitary waves, filters to remove noise and provide anti-aliasing, and a wireless module that allows the unit to transmit data to mobile devices. All the components are connected to and controlled by a microcontroller (MCU). In addition, the bulky DC power supply is replaced by a portable battery connected to the PCB.

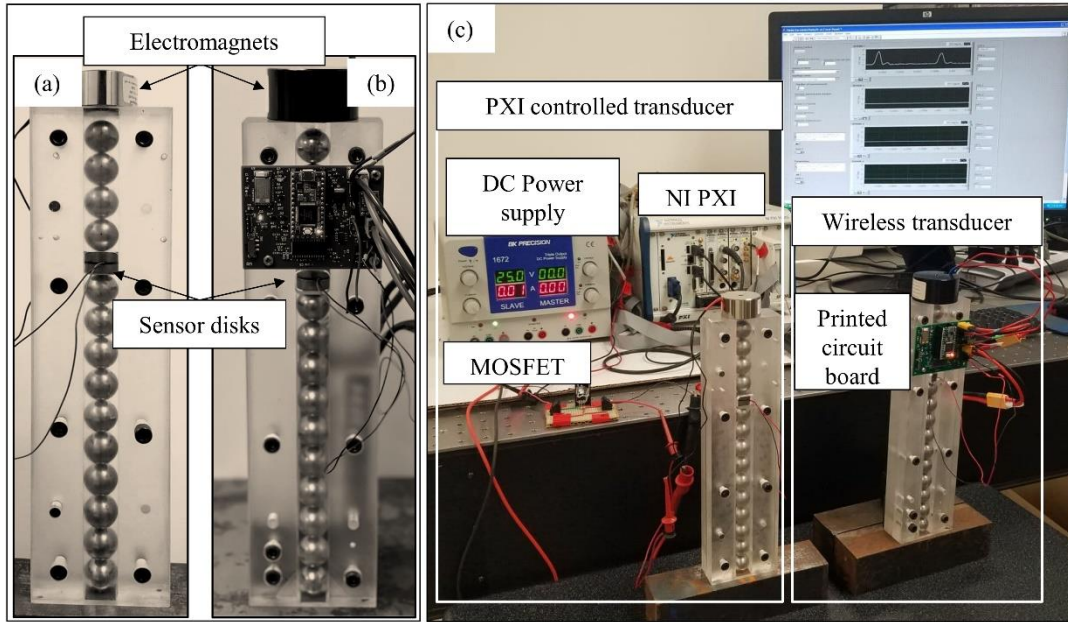


Figure 2.3 - The solitary wave transducers used in the corrosion experiment on the 4.8 mm-plate and the magnet experiment. (a) The conventional solitary wave transducer controlled by the National Instruments PXI and (b) the wireless transducer controlled by a printed circuit board attached to the transducer frame. (c) A side-by-side view of the PXI controlled transducer and the wireless transducer.

The corrosion monitoring experiment on the 6.3 mm-thick plate, presented in section 2.3.3, was conducted using only wired transducers. In this experiment, shorter solitary wave transducers were used, where the granular chains were composed of eight 19.05 mm steel spheres and one sensor disk. Further details are presented in section 2.3.3.

2.3.2 Magnet Experiment

In this experiment, “damage” was simulated in terms of variation of local mechanical impedance. To achieve the scope without causing permanent damage, a U-shaped magnet was located at different positions over a 609.6 mm × 1219.2 mm × 4.8 mm steel plate. The plate was

supported by four 50.8 mm × 101.6 mm plastic rods located underneath the plate corners. The photo and the scheme of the setup are shown in Figure 2.4a and Figure 2.4b, respectively. Four long wired transducers (as described in section 2.3.1) were used to detect the impurity created by the presence of the magnet. The transducers were at 243.8 mm center to center distances from each other and from one of the plate long edges.

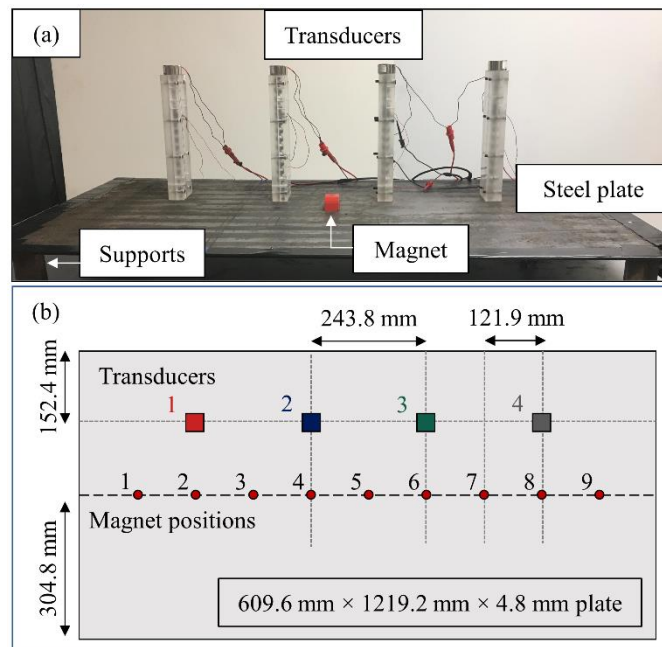


Figure 2.4 – The magnet test setup. (a) The steel plate monitored with four solitary wave transducers. The plate was supported by four plastic rods in the corners, and a magnet was attached to the plate. (b) The plate dimensions and the positions of the four solitary wave transducers and the magnet. The transducers were in fixed positions while the magnet position changed over the plate.

The test was performed twice using a 52.1-gr. and a 199-gr. magnet, respectively, hereinafter referred to as the small magnet and the large magnet, respectively. Each time, the magnet was attached to the plate’s upper surface at nine discrete positions along the plate centerline (Figure 2.4b). The distance between two consecutive positions was 121.9 mm. Position 1 and position 9

were 121.9 mm away from the opposite short edges of the plate. For convenience, position 0 indicate the baseline, i.e., the plate without any magnet. For each position (including the baseline), 10 solitary wave measurements were recorded using each solitary wave transducer at a sampling rate of 8 MHz.

2.3.3 Corrosion Experiment on the 6.3 mm-Thick Plate

In this experiment, a 609.6 mm × 609.6 mm × 6.3 mm steel plate was half immersed in a 3.5% NaCl solution to induce accelerated corrosion through a conventional electrochemical corrosion process [68, 88, 158]. The overall experimental setup is shown in Figure 2.5a. A copper sheet (electrode) was immersed in the solution and 10 V was applied between the steel and the copper plates using a DC power supply. The test specimen and the electrode were connected to the positive and the negative poles of the power supply, respectively. An oxygen diffuser was placed in the solution to increase the corrosion rate.

To induce localized corrosion, the wet face of the steel plate was covered in advance with corrosion-resistant tape, and three square-shaped tape cores were removed with a cutter to expose the metal to the NaCl solution. The locations of these areas are labeled as A, B, and C in Figure 2.5b. Two solitary wave transducers and one pulse-echo ultrasonic transducer (model Olympus DHC713) were placed on the dry side of the test specimen right above the areas B, C, and A, respectively, as summarized in Table 2.1. Ultrasonic testing was added to the experiment to compare corrosion monitoring results obtained from the HNSW-based method and conventional bulk ultrasonic testing. A third HNSW transducer was positioned on a part of the plate, protected by the tape. The position of this control HNSW transducer is labeled with the letter D in Figure 2.5b and listed in in Table 2.1.

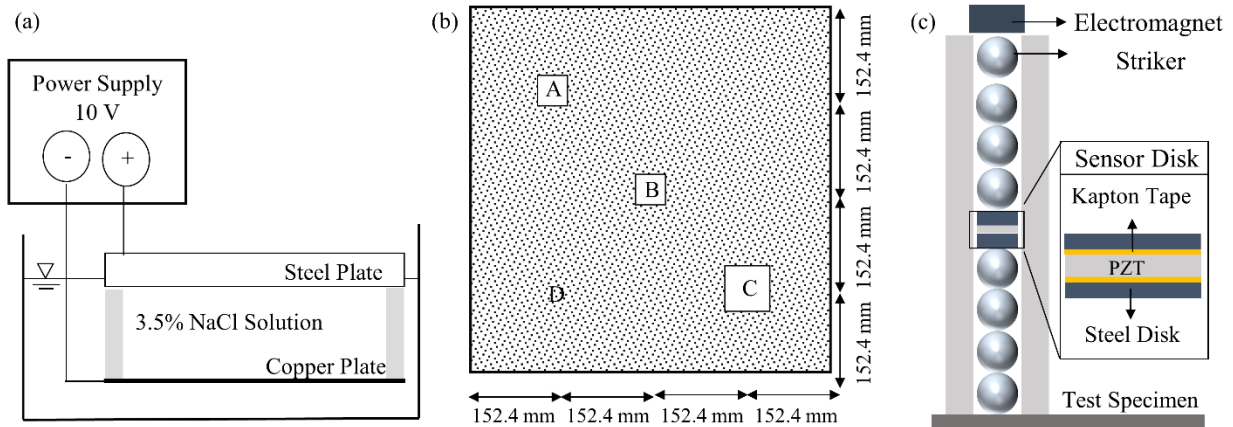


Figure 2.5 – The experimental setup in corrosion experiment I. (a) The accelerated corrosion test setup used to induce localized corrosion in a steel plate. (b) The steel plate dimensions, and the position of the localized corrosion areas monitored with ultrasonic (A) and solitary wave transducers (B, C, D). (c) Scheme of a HNSW transducer used in this study.

Table 2.1 – Monitoring positions, methods, and the size of localized corrosion area under each transducer.

Monitoring Position	Monitoring Method	Corrosion Size (mm)
A	Ultrasonic transducer	25.4×25.4
B	HNSW transducer	25.4×25.4
C	HNSW transducer	50.8×50.8
D	HNSW transducer	Pristine

Each HNSW transducer (Figure 2.5c) consisted of an array of eight 19.05 mm spheres. All the particles except the top one (striker) were made of non-ferromagnetic stainless-steel. A commercial solenoid was used to lift and release the ferromagnetic striker from a height of 5 mm. The solenoids were connected to and controlled by a National Instruments PXI running in LabVIEW. The solitary wave force profiles were recorded by a sensor disk positioned in the middle of the chain between the fourth and the fifth particles. The sensor disk was made of a lead zirconate titanate PZT wafer, embedded between two 19.05 mm diameter, 6.05 mm thick disks. The PZT was insulated from the metal using Kapton tape.

The steel plate was monitored for about 350 hours, and the areas subjected to localized corrosion were inspected on average every hour. The monitoring intervals were shorter (30 min) at the beginning to provide a large baseline dataset for the statistical analysis. Each set of measurements included one ultrasonic signal recorded with the commercial ultrasonic transducer and ten solitary wave signals taken with each HNSW transducer. The HNSW waveforms were sampled at 10 MHz. The experimental HNSWs results were analyzed using outlier analysis to improve the efficiency of HNSW-based NDE for detecting localized corrosion. This technique has been applied for detecting structural damages in vibration analysis [142-146], ultrasonic guided waves [147-151], and HNSWs-based NDE [152].

2.3.4 Corrosion Experiment on the 4.8 mm-Thick Plate

In this experiment, a 609.6 mm × 1219.2 mm × 4.8 mm subjected to localized corrosion was monitored using solitary wave transducers (Figure 2.6). Accelerated corrosion test based on the electrochemical corrosion process was employed in this test to make corrosion in the plate. For this purpose, the steel plate was half-immersed in 3.5% sodium chloride (NaCl) solution. In addition, a copper sheet was immersed in the solution and 20 V was applied between the steel (anode) and the copper (cathode) plates using a DC power supply. The test specimen and the electrode were connected to the positive and the negative pole of the power supply, respectively. An oxygen diffuser was also placed in the solution to increase the corrosion rate.

To induce localized corrosion, the wet face of the steel plate was covered in advance with corrosion-resistant tape. Then, six square-shaped tape cores were removed with a cutter to expose the metal to the NaCl solution. The plate was monitored using eight solitary wave transducers of which half were wireless transducers and half were controlled with the National Instruments PXI.

Figure 2.6 shows the positions of the monitoring transducers and the plate supports in this experiment. Two solitary wave transducers, i.e., P1 and W1 were used to monitor pristine parts of a plate, while the rest of the transducers were positioned on the corroding areas in the plate. Figure 2.6 lists the monitoring positions, the type of solitary wave transducers used on each position, and the size of the localized corrosion area under each transducer.

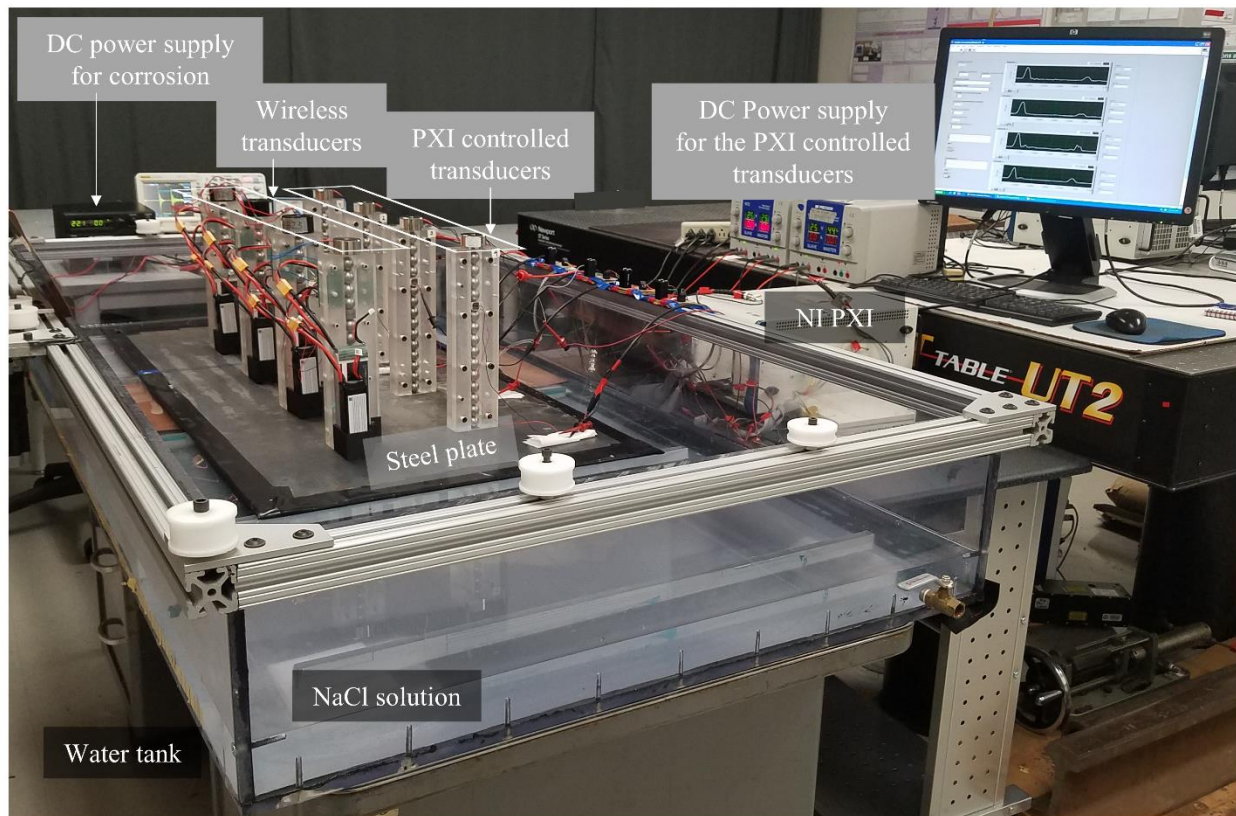


Figure 2.6 - The setup of corrosion experiment on the 4.8 mm-thick plate. A steel plate subjected to localized corrosion was monitored with eight solitary wave transducers of which half were wireless transducers and half were controlled with the NI PXI.

The plate was monitored using the solitary wave transducers for 270 hours. For some corroding areas, monitoring was stopped earlier as through-thickness holes were detected in the related area.

Each transducer was programmed to make 5 measurements every 10 minutes at a sampling rate of 8 MHz. Overall, more than 42000 solitary wave measurements were taken using the eight transducers.

The setup was completed by an ultrasonic commercial transducer to monitor a 25.4 mm × 25.4 mm corroding area located on the midpoint between areas P3 and W3 for 100 hours. After monitoring this area was terminated, the same ultrasonic transducer was used to examine the remaining plate thickness at the monitoring point of each solitary wave transducer.

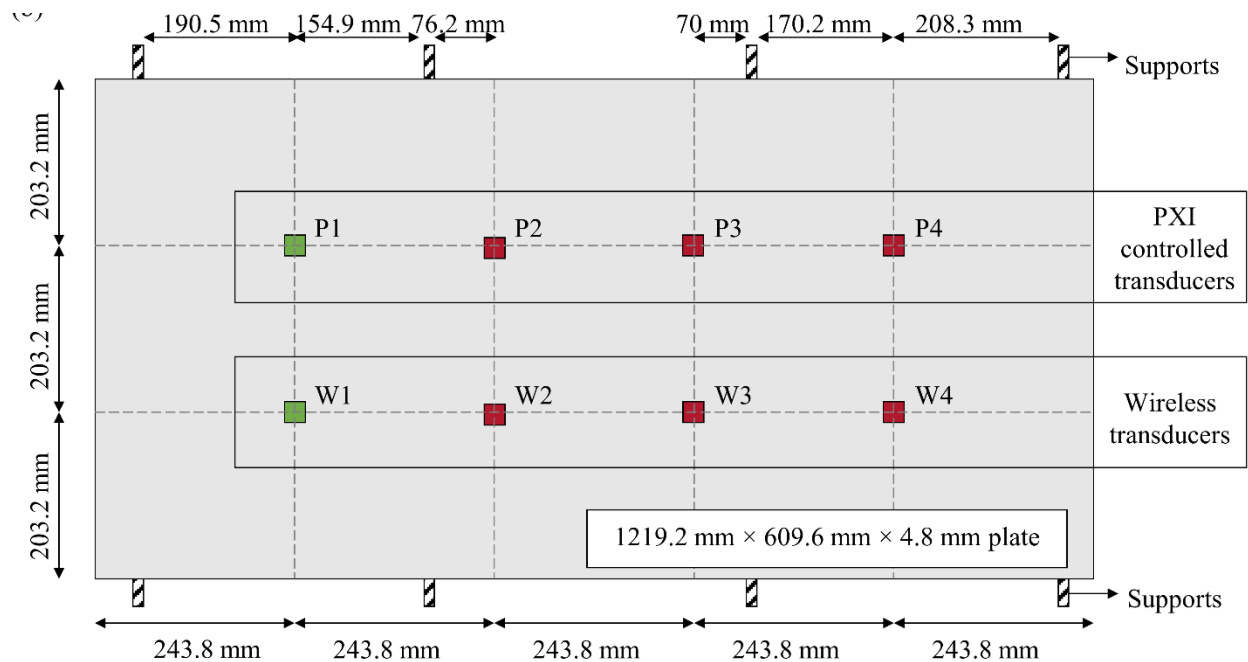


Figure 2.7 – The dimensions and the positions of the monitoring transducers and the supports in the corrosion experiment on the 4.8 mm-thick plate.

Table 2.2 - The type of solitary wave transducers used on each monitoring position and the size of localized corrosion area under each transducer.

Monitoring position	Monitoring transducer	Corroded (C) or Pristine (P)	Corrosion defect size (mm)
P1	PXI controlled	P	-
P2	PXI controlled	C	25.4 mm × 25.4 mm
P3	PXI controlled	C	50.8 mm × 50.8 mm
P4	PXI controlled	C	12.7 mm × 12.7 mm
W1	Wireless	P	-
W2	Wireless	C	25.4 mm × 25.4 mm
W3	Wireless	C	50.8 mm × 50.8 mm
W4	Wireless	C	12.7 mm × 12.7 mm

2.4 Multivariate Outlier Analysis

Multivariate outlier analysis was implemented to consider the effect of multiple parameters in detecting defects using HNSWs and improve the sensitivity of the HNSW-based NDE to corrosion. This unsupervised learning algorithm establishes whether a new configuration of the system is discordant or inconsistent from the baseline configuration which consists of an existing set of data (or patterns) that describes the normal operative conditions. For each measurement set, the MSD (D_{ζ}) was calculated as:

$$D_{\zeta} = (\{x_{\zeta}\} - \{\bar{x}\})^T [K]^{-1} (\{x_{\zeta}\} - \{\bar{x}\}) \quad (2.19)$$

where $\{x_{\zeta}\}$ represents the potential outlier vector, $\{\bar{x}\}$ is the mean vector of the baseline, and $[K]$ is the covariance matrix of the baseline. In comparison to the Euclidian distance, the MSD takes into account the correlation between variables using the covariance matrix $[K]$.

Equation 1 resembles the equation of a hyper-ellipse centered at \bar{x} in multidimensional space. When the input vector is formed by two parameters such as the solitary wave normalized amplitude and the time of flight, the concept of MSD can be used to generate confidence ellipses. If experimental data is normally distributed, the MSD follows a χ^2 distribution. This is because the distribution of the positive square root of the sum of squares of a set of normally distributed data follows a χ^2 distribution. Therefore, the threshold for MSD-based confidence ellipses was extracted from the χ^2 distribution so that it separates the 99.7% lower MSDs from the 0.3% higher MSDs. The confidence ellipses were used to detect outliers or anomalies whose MSDs from the dataset means are higher than the threshold value.

2.5 Numerical Results

2.5.1 Interaction of HSNWs with Pristine and Corroded Plates

This section presents a comparison of the numerical results relative to a pristine and a corroded steel plate obtained from the coupled DE/FE model using the 3D solid elements. The plate was 609.6 mm \times 609.6 mm \times 6.3 mm while the metamaterial supporting the propagation of the wave was composed of nine stainless steel spheres. The plate and the chain particles were made of stainless steel, with the elastic modulus and the Poisson's ratio were $E = 200$ GPa and $\nu = 0.3$, respectively. The corrosion defect was was 25.4 mm \times 25.4 mm \times 5.08 mm coupon below the point of contact between the plate and the chain. Each particle was 19.05 mm in diameter and 28.2 g in mass.

The results are presented in Figure 2.8. The left and the right columns refer to the pristine and the corroded plate, respectively. The time history of the displacement of the mass points m_1 to m_8 is shown in Figure 2.8a and Figure 2.8b. The incident solitary wave was triggered in the chain by applying an initial downward velocity of 0.31 m/s (corresponding to a falling height of 5 mm) to the first particle in the chain (m_1). Consequently, the particles m_1 to m_8 move downward (negative displacement) sequentially as the incident solitary wave propagates through the chain toward the plate interface. Once the wave is reflected back from the chain-plate interface, each particle bounces back to its original rest position. Note that at time equal to 0 ms, each particle exhibits a negative displacement due to the static deformation induced by the weight of the chain.

In the corroded plate, this initial deformation and the maximum displacement of the particles m_7 and m_8 are larger than in the pristine plate. Moreover, the time interval between the downward and upward movement of all particles is longer in the corroded plate, i.e., longer impact time and larger time of flight. These differences are caused by the lower contact stiffness at the particle-plate interaction point in the corroded plate.

Figure 2.8c and Figure 2.8d present the dynamic force at each mass point as the solitary wave propagates through the chain. The force at each particle was calculated by averaging the interaction forces between the particle and the upper and lower adjacent particles, and the contact forces were determined based on the Hertzian contact law and the displacements of the particles, presented in Figure 2.8a and Figure 2.8b. The averaged interaction forces presented in Figure 2.8c and Figure 2.8d would be identical to the forces measured by a sensor particle (with embedded PZT) in experiments. The first pulse at each particle represents the ISW and the subsequent pulses represent the PSW and the SSW traveling upward from the chain-plate interface. It should be noted that the crossing of the ISW and PSW at each particle is simultaneous with the movement of the particle

downward and upward, respectively. The wave reflected from the corroded plate (Figure 2.8d) is weaker and delayed with respect to the wave associated with the pristine plate. This effect can be explained by the lower contact stiffness at the chain-plate interface and larger deflections in the corroded plate (shown in Figure 2.8a). The reflected solitary wave is weaker in the corroded plate since more energy is transferred to the plate during the interaction between the last particle and the plate due to the larger deflections in the plate. Furthermore, the corrosion delays the solitary wave because it takes longer for each particle to bounce back to its original position in the corroded plate due to the larger deflections.

The displacements predicted with the FE analysis, including the center of the last particle, the contact point in the plate, and the lowest point (points A, B, and C) in the plate below the interaction point are shown in Figure 2.8e and Figure 2.8f. The magnitude of the maximum displacements in the last particle and the contact area in the plate are considerably larger in the corroded plate compared to the pristine plate since the contact stiffness decreases significantly in the corroded plate. According to Figure 2.8f, as the last particle and the interaction area in the plate reach their maximum displacement ($Time \approx 0.43$ ms in the corroded plate), the plate begins to rebound elastically, and the contacting particle is pushed back towards the rest of the chain until it collides with particle m_8 ($Time \approx 0.600$ ms in the corroded plate). Consequently, the PSW is induced in the granular chain. Meanwhile, the collision between the contacting particle and m_8 causes the contacting particle and the contact area in the plate to move downward again. Then, the second rebound occurs in the plate ($Time \approx 0.68$ ms in the corroded plates) causing the formation of the SSW in the granular chain. Figure 2.8e and Figure 2.8f confirm that the lower contact stiffness and the larger deformations in the corroded plate lead to longer delays between the ISW and the PSW.

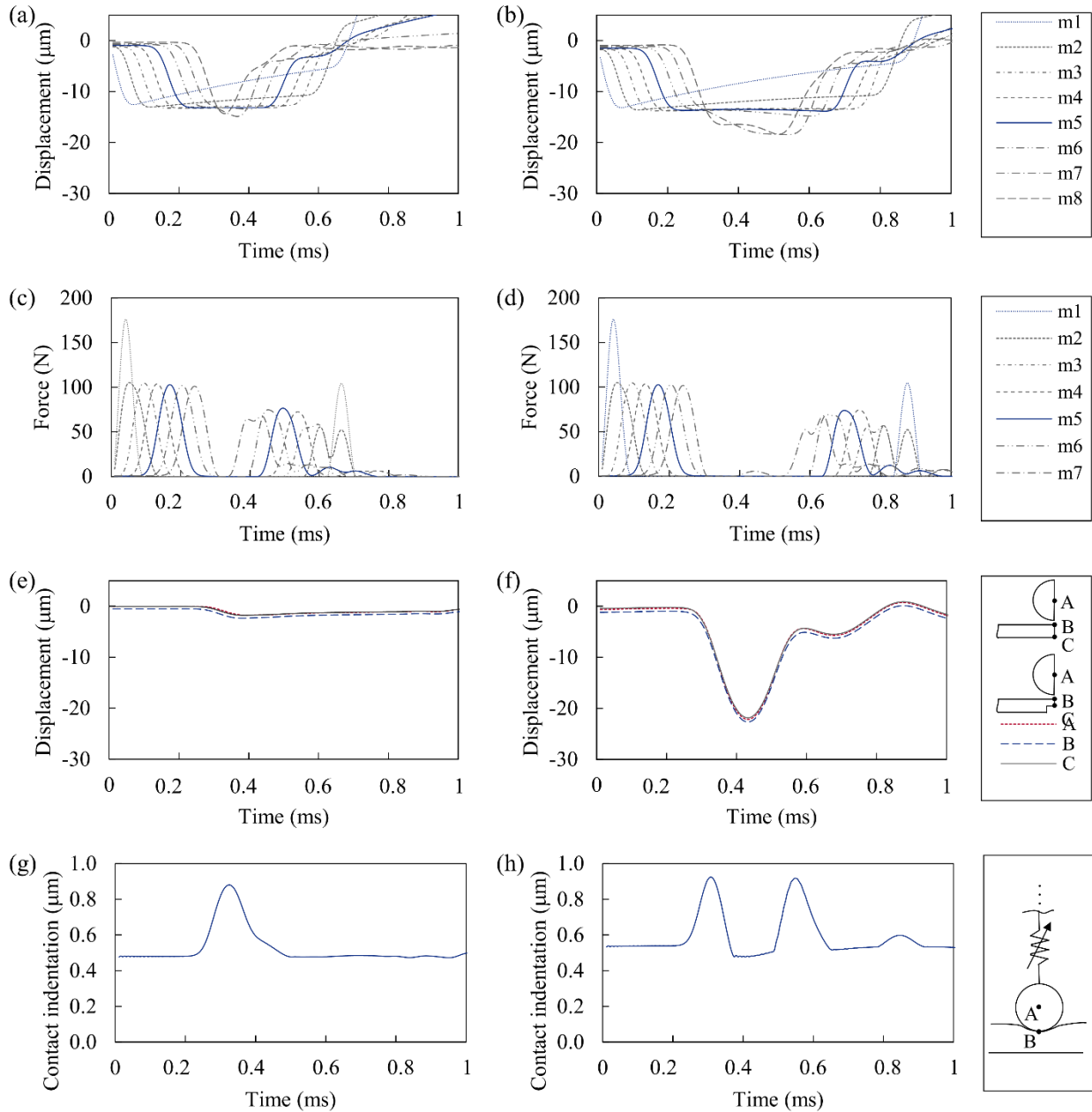


Figure 2.8 - Numerical results on the interaction of HNSWs with a steel plate in the pristine (left column) and corroded (right column) conditions. (a and b) The time history of the displacement of the mass points and (c and d) force at the mass points as a solitary wave propagates through the granular chain and interacts with the plate. (e and f) The time history of the displacement of points A, B, and C, corresponding to the center of the last particle, the contact point in the plate, and the lowest point in the plate below the interaction point. (g and h) The time history of the contact indentation at the chain-plate interface.

The contact indentation at the chain-plate interface is also presented in Figure 2.8g and Figure 2.8h. The contact indentation was obtained by subtracting displacements of point B from the displacement of point A (shown in Figure 2.8e and Figure 2.8f). In other words, the contact indentation is defined as the difference of the displacements of the contact point in the plate and the center of the interacting particle. According to Figure 2.8g, in the pristine plate, the initial elastic indentation caused by the weight of the chain is $0.48\ \mu\text{m}$. After $0.22\ \text{ms}$, the incident solitary wave arrives at the interacting particle and presses the particle down toward the plate (refer to Figure 2.8e and Figure 2.8g). Consequently, the contact indentation increases to a maximum of $0.88\ \mu\text{m}$ at time equal to $0.325\ \text{ms}$ (Figure 2.8g). Then, the particle and the plate are bounced back to the original position and the contact indentation decreases to its initial level, i.e., constant at $0.48\ \mu\text{m}$.

The contact indentation at the interaction of the corroded plate and the particle is shown in Figure 2.8h. In this case, the initial elastic indentation due to the chain weight is $0.53\ \mu\text{m}$. The initial indentation is higher in the corroded plate than the pristine plate since the contact stiffness between the plate and the interacting particle is lower in the corroded condition. It is shown in Figure 2.8f and Figure 2.8h that the incident solitary wave arrives at the interacting particle after $0.22\ \text{ms}$. As the interacting particle is pressed down toward the plate, the contact indentation increases to $0.92\ \mu\text{m}$ at time equal to $0.31\ \text{ms}$. Then, the particle and the particle's motion slow down as the impact energy is transferred to the plate. As a result, the contact indentation decreases to $0.48\ \mu\text{m}$ at time equal to $0.370\ \text{ms}$. At time equal to $0.43\ \text{ms}$, the plate and the interacting particle start to rebound (Figure 2.8f), which causes the second phase of contact indentation increasing. The second peak in the contact indentation represent the origin of the PSW created the chain-plate interface.

In brief, the displacements of the interacting particle and the impact area in the plate are small in the pristine condition (Figure 2.8e). Therefore, the chain-plate interaction is fast, and the plate and the particles rebound in a short time (Figure 2.8a and Figure 2.8g). In contrast, the lower contact stiffness at the chain-plate interface in the corroded condition causes larger displacements in the interacting particle and the impact area in the plate (Figure 2.8f). Consequently, the interaction between the chain and plate lasts longer, i.e., the plate and the particles rebound later in the corroded plate. In this case, the extended chain-plate interaction causes two distinct peaks in the contact indentation associated with the ISW and the PSW, respectively.

2.5.2 Effect of Localized Corrosion on Solitary Wave Features

To quantify the variation of certain solitary wave features, let assume that the sensor particle is in the middle of the chain, i.e., particle #5 in a chain composed of 9 particles, and mass m_5 in the scheme shown in Figure 2.2. The time of flight of the PSW was calculated as the difference between the ISW and the PSW peaks. Figure 2.9 presents the numerical predictions for the interaction of HNSWs with a steel plate similar to the plate used in the corrosion experiment I and containing a corrosion-like defect of size $25.4 \text{ mm} \times 25.4 \text{ mm}$ at the plate center. The corrosion depth varies from 0 (pristine plate) to 80% of the thickness.

According to Figure 2.9a, the coupled DE/FE model using the Kirchhoff–Love Plate and Point Masses suggests that time of flight increases from 0.319 ms to 0.355 ms as the corrosion propagates in the plate. This is in excellent agreement with the experimental results presented in section 2.6.3. Furthermore, the results of the coupled DE/FE model using 3D solid elements demonstrate that time of flight increases from 0.328 ms to 0.378 ms as the corrosion defect penetrates in the plate. Overall, both the models show that the traveling time of solitary waves are affected by corrosion

defects. A nonlinear increase in time of flight is shown as a function of corrosion depth. In fact, the numerical results suggest that the sensitivity of time of flight to localized corrosion increases as the relative depth of localized corrosion is higher than 0.5.

In addition, Figure 2.9b shows that the amplitude ratio or the normalized amplitude of the reflected wave, i.e., the ratio of the PSW amplitude to the ISW amplitude, decreases from 0.74 to 0.57 (coupled DE/FE model using 3D solid elements) and 0.84 to 0.76 (coupled DE/FE model using the Kirchhoff–Love Plate and Point Masses) as the relative corrosion depth increases. As presented in section 2.6.3, the experimental results show an amplitude ratio changing from around 0.49 to around 0.35 as the localized corrosion penetrates in the plate. The overestimation of the amplitude ratio in is likely due to underestimating the energy dissipation in the chain in the models. The amplitude ratios obtained from the coupled DE/FE model using 3D solid elements is closer to the experimental data, since the 3D modeling of the impact between the last particle and the plate, allows capturing energy dissipation during the impact.

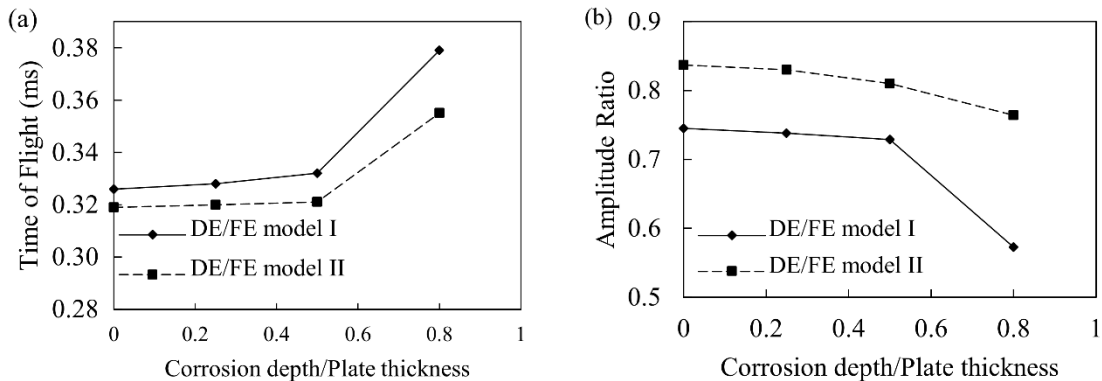


Figure 2.9 - Numerical (a) time of flight and (b) amplitude ratio as a function of relative corrosion depth in a granular chain interacting with a 6.3 mm-thick plate.

2.5.3 Comparing Numerical and Analytical Results in Pristine Plates

To quantify the effect of different setup parameters on the propagation of the solitary waves, the numerical and the analytical models described in sections 2.2.2 and 2.2.3 were used to predict the time of flight and the normalized amplitude of the solitary waves as a function of the plate thickness and particles diameter. Figure 2.10 shows the two features relative to a chain of nine 19 mm stainless steel particles in contact with plates of different thicknesses. Regardless of the approach, the results show that the time of flight is inversely proportional to the thickness whereas the normalized amplitude is proportional to the thickness. This implies that the dynamic interaction of the last particle in the chain with thinner plates results in a longer contact time and higher energy transfer from the particle to the plate because of the lower contact stiffness at particle-plate interface. For thinner plates, there is a significant difference between the analytical model and the numerical prediction. This difference is because the analytical model does not consider the effect of the plate boundaries on the local contact stresses during the chain-plate interaction. The boundary effects on the local stresses are more significant in thin plates. Therefore, the analytical model is less accurate in thin plates. In addition, the analytical model neglects the pre-compression in the chain due to the weight of the particles.

It can be concluded that the numerical model is more comprehensive because it accounts for the effect of the initial compression due to the weight of particles and the effect of plate boundaries in the chain-plate interaction. When compared to the experimental results presented in section 2.6.3, the numerical model is closer to the experimental time of flight. As discussed later, the numerical model overestimates amplitude ratio, presumably because the energy dissipation coefficient in the simulated chain was set lower than the actual value.

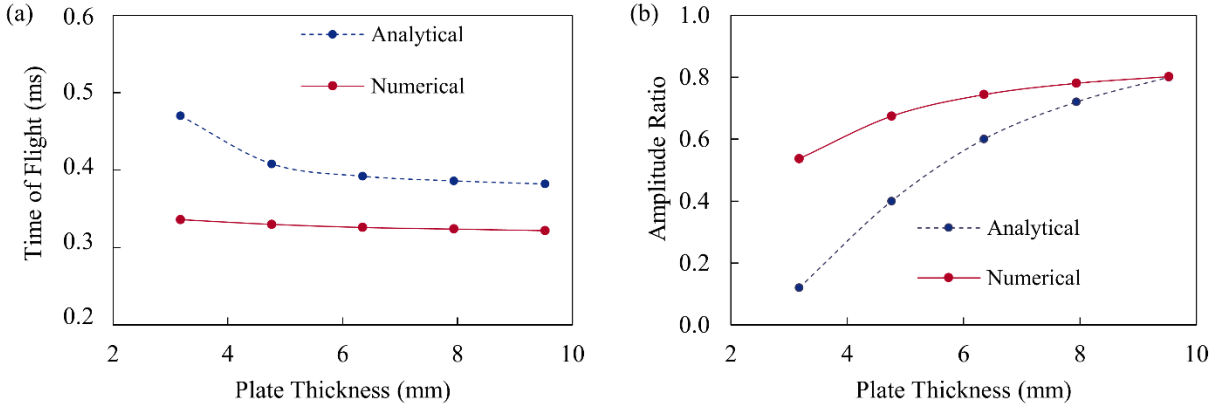


Figure 2.10 - Numerical and analytical results on the effect of plate thickness on (a) time of flight and (b) amplitude ratio in a HNSW transducer made of 19 mm particles.

The effect of the particles' diameter on the time of flight and the normalized amplitude measured at the sensors bead for a 6.3 mm-thick plate is shown in Figure 2.11. It is shown that the use of larger particles increases the time of flight because of the increase of the distance traveled by the waves. The normalized amplitude (Figure 2.11b) decreases instead with the increase in diameter because of the dependence of the inelasticity parameter on the particles radius. According to Eq. (2.8), the use of larger particles increases the inelasticity parameter and therefore, energy loss at the chain-plate interface. It should be noted that based on Eq. (2.14), the solitary wave traveling speed increases as the particle size (D) increases, as the stiffness coefficient of the contact between the particles (A) increases, and as the particles mass (m) decreases. Based on Eq. (2.2), the stiffness coefficient of the contact between the particles (A) is proportional with $D^{-1/2}$. Also, the particles mass is proportional to D^3 . Taking all these parameters into account, the solitary wave propagation speed does not depend on the particles size. The fact that time of flight increases as the particle size increases can also be explained based on Eq. (2.15) and Eq. (2.16), which show that the traveling times of the ISW and the PSW are proportional to $A^{-2/5}m^{2/5}$ and $e^{-1/5}A^{-2/5}m^{2/5}$,

respectively. It can be shown that as the particle size (D) increases, the stiffness coefficient of the contact between the particles (A) increases (Eq. (2.2)), the particles mass (m) increase, and the inelasticity parameter (λ) increases (Eq. (2.8)). Consequently, the restitution coefficient (e) decreases (Eq. (2.9)), and therefore, the traveling times of the ISW and the PSW increases.

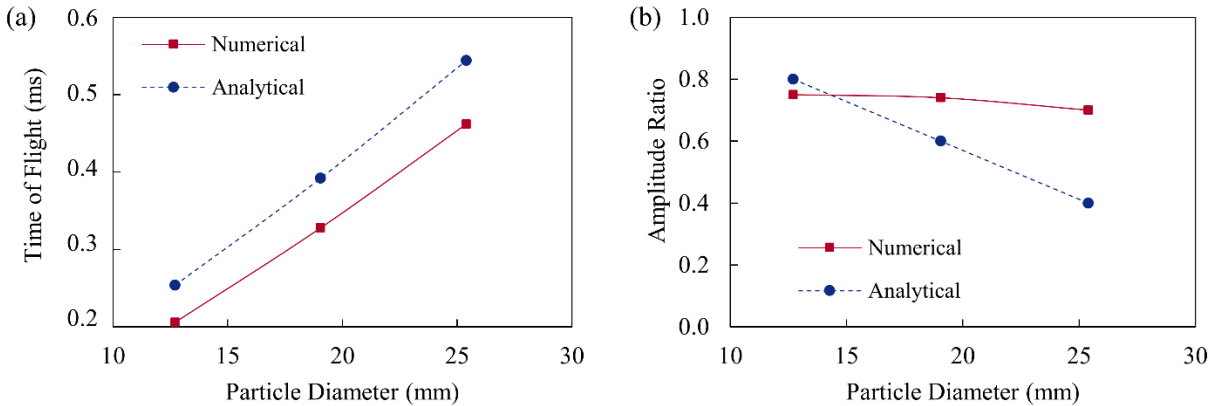


Figure 2.11 - Numerical and analytical results on the effect of particle diameter on (a) time of flight and (b) amplitude ratio in HNSW transducers in contact with a 6.3 mm-thick plate.

As shown in Figure 2.11b, the analytical and the numerical models predict different rates of change in amplitude ratio as the particle diameter varies, causing the two lines to cross each other in the lower diameter region. The difference in slope is likely because of the dissimilarities in modeling the particle-plate interaction in these two methods. As discussed previously, the analytical model neglects local deformations and changes in plate thickness during the particle impact on the plate. In fact, it only takes into account the global bending deformations in the plate. As the particle diameter increases, the bending deformations in the plate increase. Thus, the analytical model predicts that energy restitution factor and amplitude ratio decrease as the particle diameter increase. On the other hand, the numerical model accounts for both the global and local

elastic deformation at the chain-plate interface. In other words, the impact energy is partially converted to the kinetic energy of flexural waves propagating in the plate and the strain energy due to local deformations in the plate. As the particle rebounds, the strain energy is converted back to the kinetic energy of the impacting particle leading to higher amplitudes of the reflected solitary waves.

Figure 2.12 presents the time of flight and the normalized amplitude measured at the sensor bead as a function of the dimensionless diameter to thickness (D/th) ratio. Two cases of constant diameter and constant thickness were considered. The former includes the results of a solitary wave transducer made of 19 mm spheres in contact with 9.5 mm, 7.9 mm, 6.3 mm, 4.8 mm, and 3.2 mm thick plates (corresponding to a D/th ratio of 2, 2.4, 3, 4, and 6, respectively), and the latter includes the results of solitary wave transducers made of 13 mm, 19 mm, and 25 mm particles in contact with a 6.3 mm-thick plate (corresponding to a D/th ratio of 2, 3, and 4, respectively).

Figure 2.12a shows that the time of flight increases with the increase of D/th . The increase is sharper when the diameter increases, and the thickness is kept constant. This suggests that this wave parameter is more influenced by the particles diameter than by the plate thickness. Moreover, Figure 2.12b shows that the normalized amplitude decreases with the increase of the dimensionless D/th ratio. In this case, the decrease rate is almost equally affected by either the thickness or the diameter, and the analytical results of the two cases of constant diameter and constant thickness overlap each other perfectly. This is because the inelasticity parameter is non-linearly proportional to D/th ratio (Eq. (2.8)), and the normalized amplitude depends only on the inelasticity parameter (Eq. (2.9) and Eq. (2.10)).

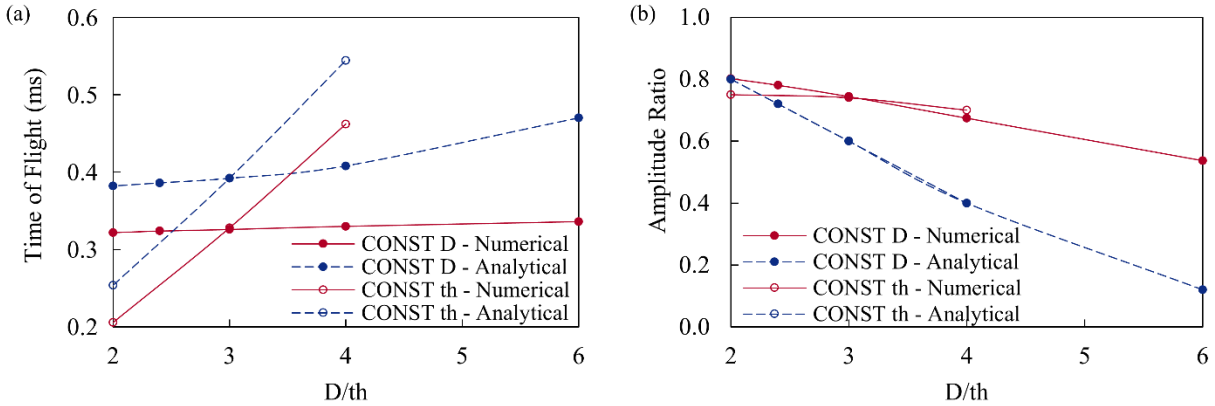


Figure 2.12- (a) Time of flight and (b) amplitude ratio as a function of the dimensionless ratio of particle diameter over plate thickness, predicted using the numerical and analytical methods.

2.5.4 Parametric Study

To enhance the sensitivity of the proposed NDE method at detecting corrosion at earlier stages, a parametric study was performed using the numerical model described in section 2.2.2. Several simulations were performed to quantify how the features of the reflected solitary waves change because a localized $25.4 \text{ mm} \times 25.4 \text{ mm}$ corrosion thins the plate underneath the chain. The following variables were considered individually or simultaneously: initial plate thickness, particles diameter, particles Young's modulus, chain length, sensor bead location, and the striker falling height.

First, the sensitivity to localized corrosion for different pristine plate thicknesses was investigated and the results are presented in Figure 2.13 for five different initial thicknesses, namely 3.2 mm, 4.8 mm, 6.3 mm, 7.9 mm, and 9.5 mm and 20%, 40%, 60% and 80% corrosion depth. Figure 2.13 shows that the time of flight increases and the amplitude ratio decreases as corrosion progresses. Also, according to Figure 2.13a, the thinner the plate, the higher is the rate of change, i.e. the sensitivity of the proposed NDE method. This effect complies with the analytical

model as the inelasticity parameter is inversely proportional to the square of plate thickness (Eq. (2.8)), i.e. energy transfer during the impact increases at a growing rate as the plate thickness decreases. Furthermore, the contact time increases exponentially as the inelasticity parameter increases (Eq. (2.17)).

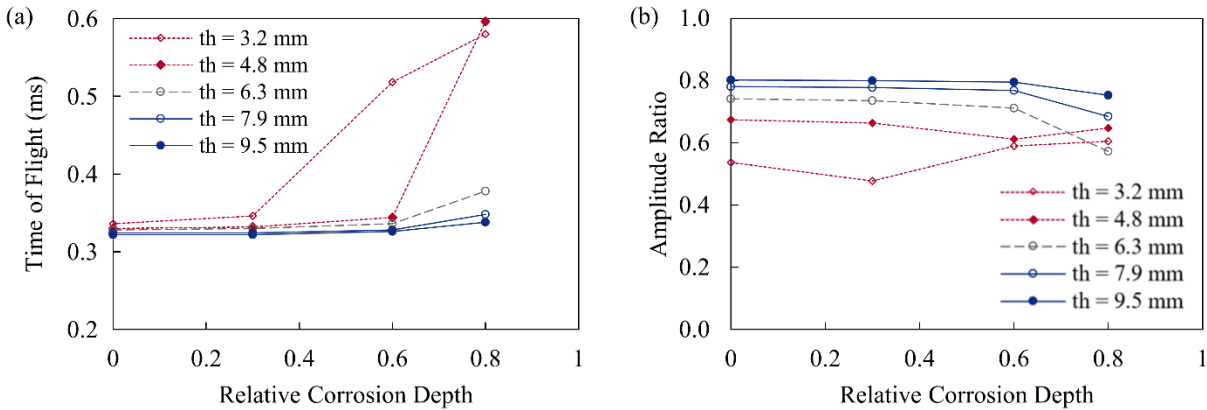


Figure 2.13 - Effect of plate thickness on the sensitivity of the HNSW-based NDE for the detection of localized corrosion. (a) Time of flight and (b) amplitude ratio as a function of relative corrosion depth in solitary wave transducers in contact with plates with an initial thickness of 3.2 mm, 4.8 mm, 6.3 mm, 7.9 mm, and 9.5 mm.

For the two thinnest plates the trend of the amplitude ratio is not monotonic whereas it becomes monotonic for plates 6.3 mm thick or more. For these latter cases, the largest change is observed when corrosion has thinned the plate by more than 60% of the initial thickness. Figure 2.13b demonstrates that the amplitude ratio increases in the two thinnest plates as the corrosion relative depth gets higher than 60% or 30%. These data points are related to the case with a remaining thickness of less than 1.3 mm at the monitoring location, i.e., a low contact stiffness at the chain-plate interface. Also, Figure 2.13a shows that time of flight increases significantly for these cases, implying a considerably longer contact time between the last particle and the plate. The longer

contact time results in the simultaneous upward movement of the plate due to the propagation of flexural waves and the initiation of the reflected solitary waves. Consequently, the kinetic energy of the flexural wave contributes to pushing the last particle back harder and thus causing stronger reflected solitary waves. In brief, the nonmonotonic trend of amplitude ratio in thinner plates can be explained by the propagation of guided waves in the plate.

The effect of the particles diameter on the rate of change of the wave features as a function of corrosion progression is presented in Figure 2.14. Three cases were considered, namely solitary wave transducers composed of 13 mm, 19 mm, and 25 mm stainless steel particles in contact with a 6.3 mm-thick plate. Monotonic trends were observed for both features and all three diameters: the time of flight increases and the normalized amplitude ratio decreases as corrosion progresses. The largest change is observed between 60 and 80 percent of the corrosion depth. The numerical results show that as a localized corrosion defect progresses in the plate, time of flight increases from 206 ms to 252 ms, from 328 ms to 378 ms, and from 462 ms to 562 ms in solitary wave transducers made of 13 mm, 19 mm, and 25 mm diameter particles, respectively. Therefore, reflected solitary waves are more sensitive to localized corrosion as the particle diameter increases. Besides higher sensitivity, the use of larger particles is advantageous because it creates a larger buffer between the sensor bead and the material to be inspected that could be operating at very high temperature, which would make the use of contact piezoelectric transducers detrimental or impossible.

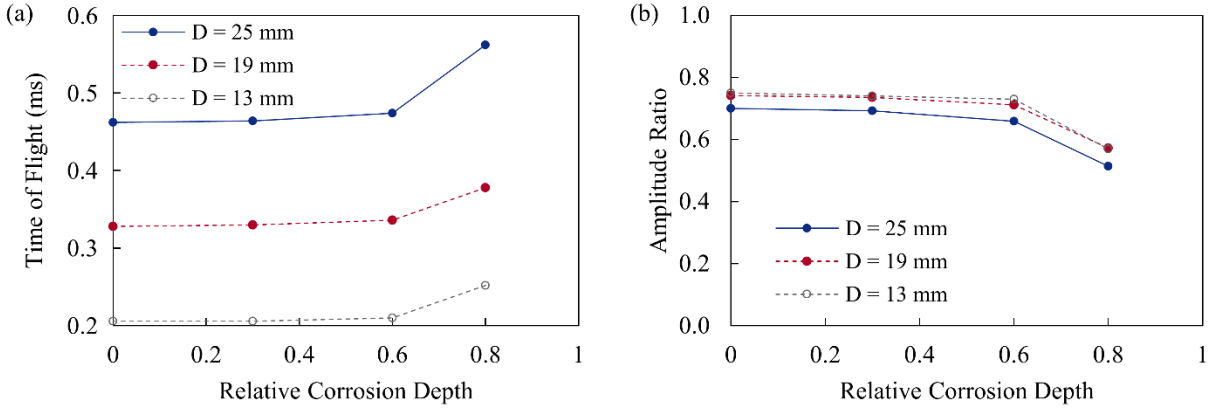


Figure 2.14 - Effect of particle diameter on the sensitivity of the HNSW-based NDE for the detection of localized corrosion. (a) Time of flight and (b) amplitude ratio as a function of relative corrosion depth in solitary wave transducers composed of 13 mm, 19 mm, and 25 mm particles.

The sensitivity of the HNSW-based NDE to localized corrosion was also studied in terms of the Young modulus of the beads. Specifically, individual 9-particles chains composed of aluminum, titanium, steel, silicon nitride, and tungsten particles, and in contact with a 609.6 mm \times 609.6 mm \times 6.3 mm steel plate were considered. Table 2.3 presents the density, mechanical properties, and thermal conductivity of these materials. The results are presented in Figure 2.15a and Figure 2.15b for the time of flight and the normalized amplitude, respectively. Figure 2.15a shows that time of flight is inversely proportional to the stiffness of the particles. This effect can be explained by observing that the stiffness constant A is proportional to the Young's modulus (Eq. (2.2)). Therefore, Eq. (2.14) suggests that the speed of HNSW propagation increases and the traveling times of the ISW and the PSW decrease. Besides, according to Eq. (2.2), as the elastic modulus of the last particle increase, the Hertzian stiffness constant at the particle-plate interface increases, and interaction time (T_c) decreases (Eq. (2.18)). Although the density and the Poisson ratio of the materials also affect the speed of HNSW propagation and the inelasticity parameter,

their effect is small when compared to the effect of the Young’s modulus. Regardless of the material used, the largest variation of the wave feature is observed after 60% of corrosion. Interestingly, the analysis of the normalized ratio suggests that the heaviest particles significantly enhance the proposed NDE method as both the rate of change is significantly higher than the ones associated with the other four materials taken into consideration in this study. The motivation of such response is associated with the relationship between particles stiffness and inelasticity parameter of the impact, which describes the energy transfer at the impact. If the proposed NDE method is to be employed at high-temperature conditions, chains made of particles with lower thermal conductivity like silicon nitride and titanium should be preferred, as they constitute a thermal buffer that would protect the sensor embedded in the chain.

Table 2.3 - Density, mechanical properties, and thermal conductivity of the materials considered in this study.

Material	Material Properties			
	Density (kg/m ³)	Young Modulus (GPa)	Poisson Ratio	Thermal Conductivity (W/mk)
Aluminum	2700	70	0.33	205
Titanium	4500	120	0.35	17
Steel	7800	200	0.3	45
Silicon Nitride	3200	280	0.2	10
Tungsten	19600	411	0.27	173

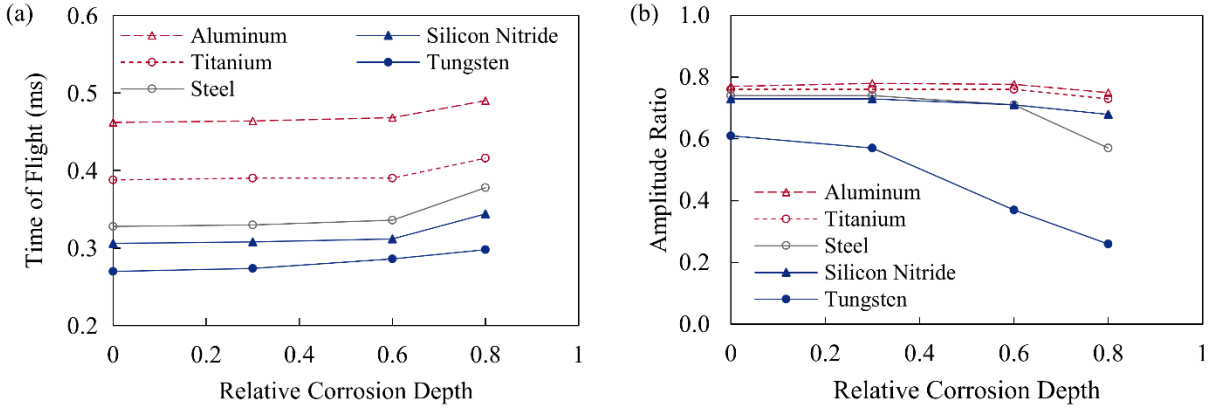


Figure 2.15 – Effect of particle material on the sensitivity of the HNSW-based NDE for the detection of localized corrosion. (a) Time of flight and (b) amplitude ratio as a function of relative corrosion depth in solitary wave transducers composed of aluminum, titanium, steel, silicon nitride, and tungsten particles.

Another parametric study examined the solitary wave propagation in chains made of 9, 15, and 21 stainless steel 19-mm in diameter particles with the sensor bead located five particles away from the chain-plate interface. The thickness of the plate was 6.3 mm. The results of this analysis are presented in Figure 2.16. The numerical data indicate that the length of the granular chain does not affect the features of the reflected solitary wave considerably. Longer chains induce a slightly shorter time of flight (Figure 2.16a). This agrees with the fact that more particles induce higher static pre-compression in the chain, which in turn induces higher amplitudes and faster waves. Additionally, according to Figure 2.16b, amplitude ratio is slightly higher in longer solitary wave transducers. The reason is that the higher initial static compression in longer chains (due to the particles weight) increases the inelasticity parameter of the impact. Therefore, based on Eq. (2.9) and Eq. (2.10), the coefficient of restitution and the amplitude ratio decreases in longer granular chains. Figure 2.16 shows that the effect of the chain length on time of flight and amplitude ratio is insignificant; however, using longer granular chains is advantageous in high-temperature environments since they allow the isolation of the sensor particle from hot zones.

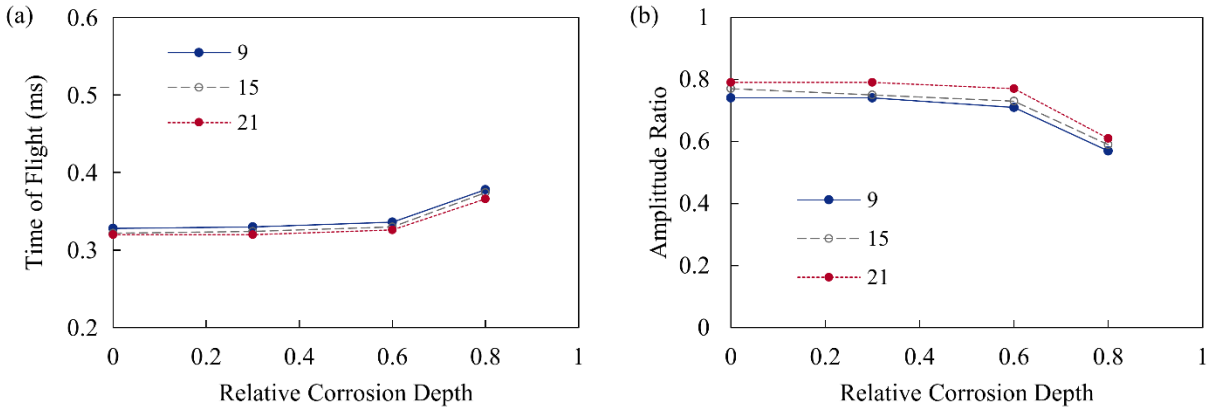


Figure 2.16 – Effect of chain length on the sensitivity of the HNSW-based NDE for the detection of localized corrosion. (a) Time of flight and (b) amplitude ratio as a function of relative corrosion depth in solitary wave transducers composed of 9, 15, and 21 particles.

Figure 2.17 shows time of flight and amplitude ratio as a function of relative corrosion depth in a solitary wave transducer composed of 21 particles, where the sensor particle was the 5th, 10th, and 15th particle from the chain-plate interface. As shown in this figure, time of flight decreases if the sensor particle is closer to the inspection medium since the ISW and the PSW travel a shorter distance. On the other hand, amplitude ratio increases if the sensor particle is closer to the inspection medium since a shorter traveling distance of the ISW and PSW causes less energy dissipation of the waves through the chain. Regarding the sensitivity to localized corrosion, numerical results show that the position of the sensor particle does not have a significant effect on the variation rate of time flight and amplitude ratio with respect to the relative depth of the localized corrosion. However, placing the sensor particle further in high-temperature environments is advantageous as it helps to keep the sensor particle away from high-temperature zones.

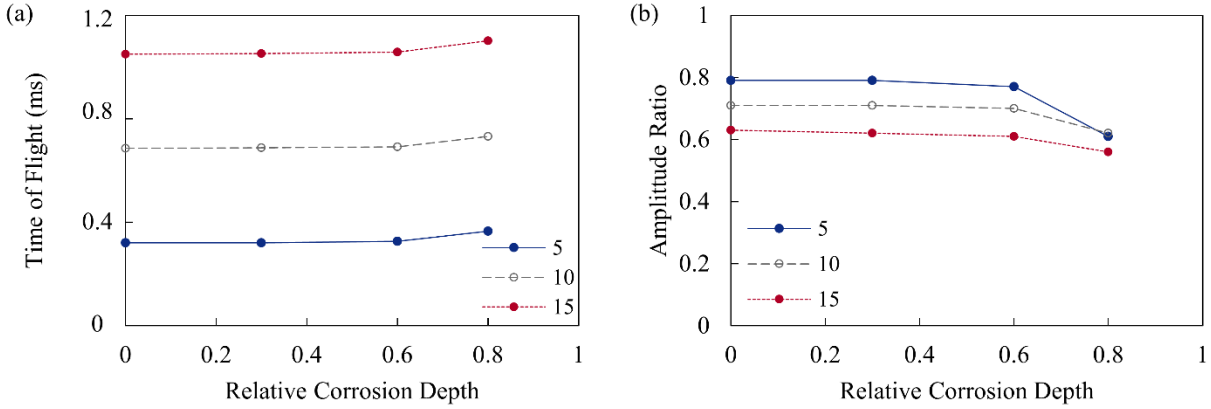


Figure 2.17 - Effect of sensor location on the sensitivity of the HNSW-based NDE for the detection of localized corrosion. (a) Time of flight and (b) amplitude ratio as a function of relative corrosion depth in a solitary wave transducer composed of 21 particles. The solitary wave force profiles were analyzed at particles #5, #10, and #15.

Finally, the effect of the striker falling height and the ISW amplitude on the time of flight and normalized amplitude of the PSW was investigated. For this purpose, the analytical Zener model presented in section 2.2.3 and the numerical model using the Kirchhoff–Love Plate and Point Masses presented in section 2.2.1 were applied for two case scenarios in which the amplitude of the ISW is increased and decreased by 20%. The results are presented in Figure 2.18 and show that the $\pm 20\%$ change in the ISW amplitude yields to $\pm 2.5\%$ in time of flight and $\pm 1.5\%$ in amplitude ratio. Therefore, both the numerical and analytical results show that the amplitude of the ISW has little effect on the wave features associated with the primary reflected wave

Figure 2.18 also presents such effect using the analytical Zener model in dashed lines. Table 2.4 summarizes the calculations of *time* of flight and amplitude ratio in the analytical model for cases of different striker falling heights (h_s). The striker velocities (v_{imp}) calculated as $\sqrt{2gh_s}$ is presented in the third column, and the maximum velocity of the particles in the chain ($v_m \approx$

$0.682v_{imp}$ [121]) is presented in the fourth column. The normalized ISW amplitude with respect to case #3 (the case of $h_s = 5$ mm) was calculated using $F_i/F_3 = (v_{m,i}/v_{m,3})^{6/5}$. The equations used to calculate other parameters are specified on the same table.

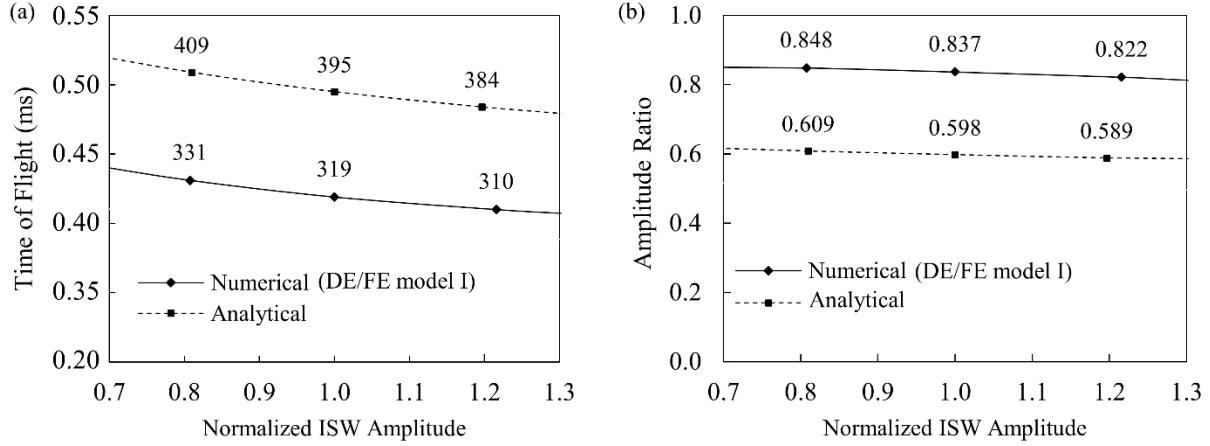


Figure 2.18 - The effect of the incident solitary wave amplitude on the solitary wave features: (a) time of flight, and (b) amplitude ratio.

Table 2.4 - Effect of ISW on Time of flight and amplitude ratio based on the analytical Zener Model

Case #	h_s (mm)	v_{imp} (m/s)	v_m (m/s)	AR w.r.t. case 3	λ (Eq. (2.8))	e (Eq. (2.8))	Amplitude ratio (Eq. (2.10))	τ_c (Eq. (2.17))	Time of flight (ms) (Eq. (2.11))
1	2.0	0.20	0.14	0.59	0.237	0.68	0.62	3.38	0.430
2	3.5	0.26	0.18	0.81	0.249	0.66	0.61	3.39	0.409
3	5.0	0.31	0.21	1.00	0.258	0.65	0.60	3.40	0.395
4	6.5	0.36	0.25	1.20	0.266	0.64	0.59	3.40	0.384
5	8.0	0.40	0.27	1.36	0.273	0.64	0.58	3.41	0.377

*Legend. h_s : striker falling height; v_{imp} : striker velocity; v_m : maximum particle velocity; λ : inelasticity parameter; e : coefficient of restitution; τ_c : dimensionless Contact Time.

2.6 Experimental Results

2.6.1 Magnet test results

Figure 2.19 presents the amplitude of the ISW, the time of flight, and the amplitude ratio obtained from the magnet test. The data associated with the small magnet and the large magnet are shown in the left column and the right column, respectively. Data from different transducers are displayed with different colors. Each dot and its corresponding bar represent the average and two standard deviations of the ten recordings. The amplitude of the incident wave at the baseline are consistent, i.e., nearly identical, for transducers 2 and 4, whereas they are different in transducers 1 and 3. However, for the other two features, namely the time of flight and the normalized amplitude, i.e., the ratio of the amplitude of the reflected wave over the amplitude of the incident wave, the values at the baseline are overall consistent with the only exception given by the normalized amplitude of transducer 3.

The comparison of the ISW baseline amplitudes within the same test shows that the value of transducer 1 is higher than the others. This is likely due to differences in the striker falling heights, energy loss due to contact forces between the striker and the inner wall of the frame, and dielectric constants of the piezo wafer embedded in the sensor disk. Nevertheless, the time of flights and the amplitude ratios associated with the four transducers are fairly similar to each other. This observation agrees with a previous research findings presented in section 2.5.4, which proved that the differences in the ISW amplitude do not significantly affect the time of flight and the amplitude ratio. Therefore, it can be assumed that the four transducers were identically manufactured and assembled. The experimental results also show acceptable repeatability over the experiment as the solitary wave features are quite constant in each transducer over the experiment.

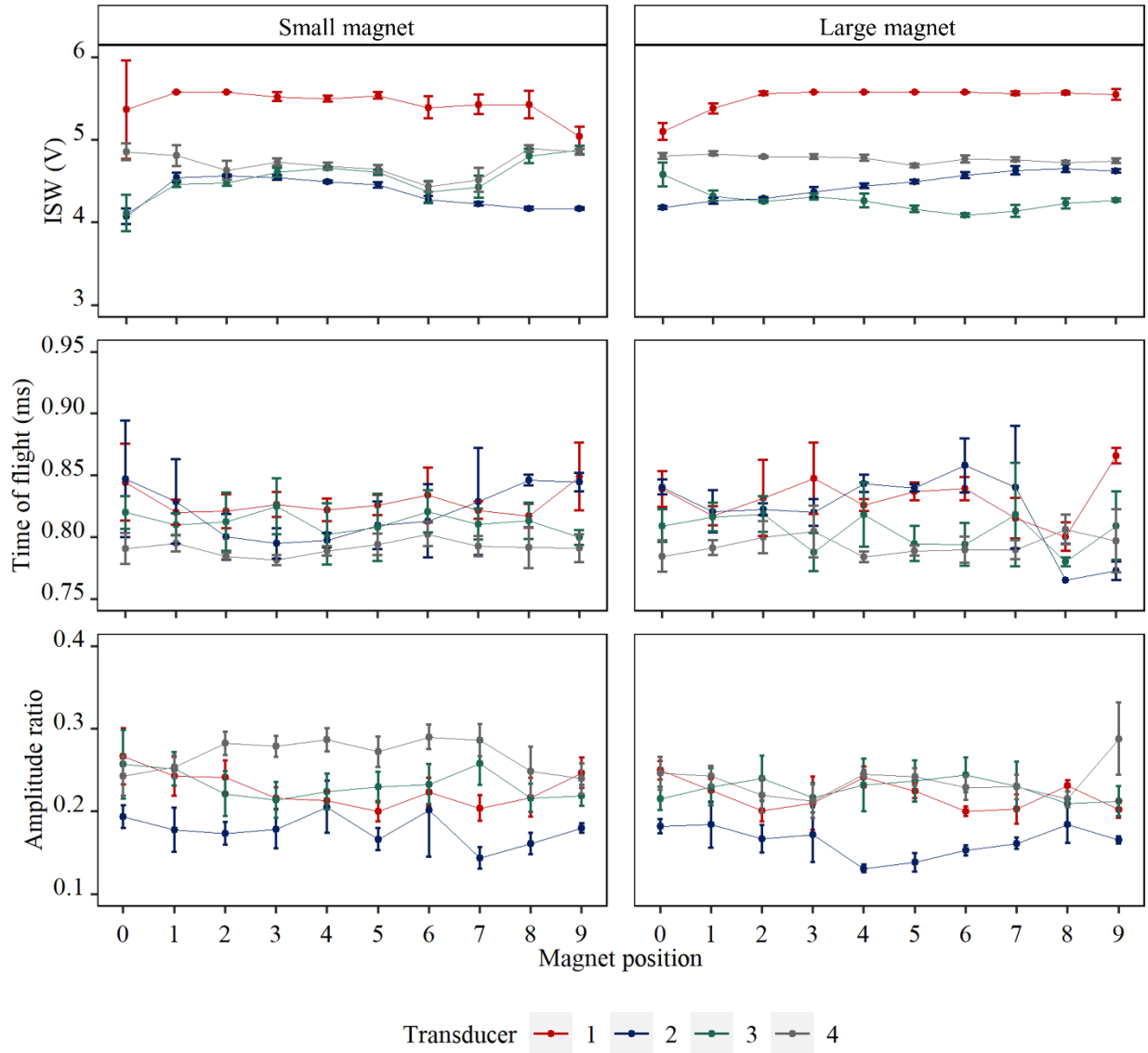


Figure 2.19 – The solitary wave features, i.e., the ISW amplitude, the time of flight, and the amplitude ratio obtained from the magnet. The two columns represent the data associated with the small magnet and the large magnet test.

The values of the ISW amplitudes were expected to be constant throughout the experiment as the presence of the magnet is expected to be irrelevant to the mechanism that generates the solitary waves. However, the experimental data show that within the same transducer, the amplitude of the ISW can vary as much as 20%. The motivation for such large variations will be discussed in

Chapter 4.0 The graphs relative to the other two features show some variations at certain localized magnet positions. However, the findings presented in Figure 2.19 are of difficult interpretation because the position of the magnets with respect to the four transducers are not the same.

As such, in order to further investigate the effect of the presence of the magnet on the reflected solitary waves, Figure 2.20 shows the average time of flight and amplitude ratio as a function of the distance between the magnet and the transducer. Each column represents the data associated with one transducer. For convenience, the baseline is displayed as a negative value. The results show that with a very few exceptions, namely the normalized ratio in devices 2 and 3, the baseline data relative to the two tests are nearly identical. The cross-comparison among different transducers cannot be performed due to transducer-to-transducer differences. This implies that the dynamic interaction between the plate and the waves did change when there was a local mechanical impedance 150 mm away from the contact point. However, the same features values did not tend back monotonically to the baseline value as the magnets were moved away. Although the results may appear detrimental, it must be noted that the mass ratios of each magnet to the plate were 0.2% and 0.8%, respectively and therefore the effect of these masses on the flexural stiffness of the plate could have been overall irrelevant. Further studies may investigate whether solitary waves are sensitive to stronger structural anomalies positioned at a significant distance from their monitoring point.

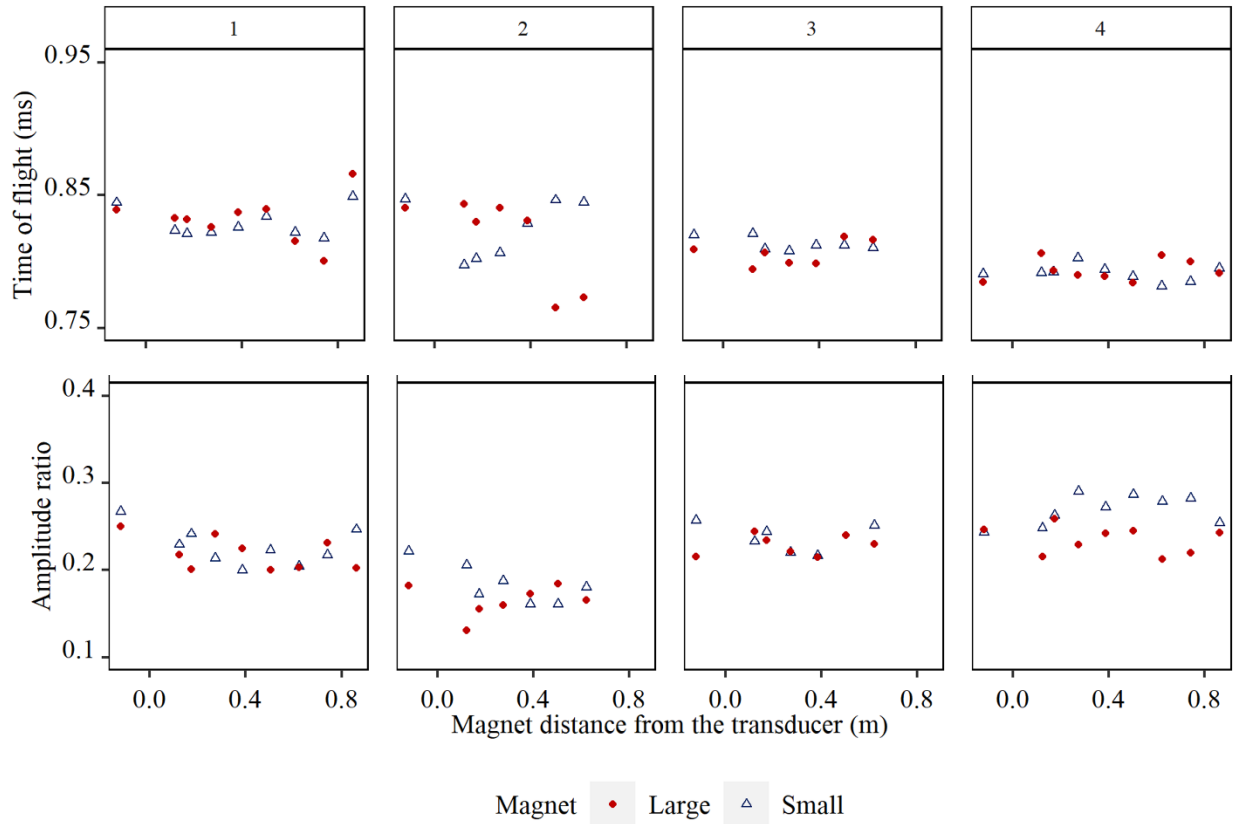


Figure 2.20 – The magnet test results. The solitary wave time of flight and amplitude ratio as a function of the distance between the magnet and the transducer. Each column represents the data associated with one transducer. The baseline data (the case without a magnet) is shown on a negative distance value.

2.6.2 Corrosion Progress in the 6.3 mm-Thick Plate

After about 270 hours, a through-thickness hole was detected at B, i.e., at the center of the plate (Figure 2.21a). A close-up view of such defect is shown in Figure 2.21b. To prevent the free fall of the particles, the monitoring of this defect was terminated after 270 hours, but the experiment continued until a new through-thickness hole appeared close to location C (Figure 2.21c). At the end of the experiment, the plate was removed from the tank and the protection tape was removed. Figure 2.21d presents the immersed face of the specimen: the presence of three pits is evident. For convenience, a close-up view of area C is shown in Figure 2.21e.

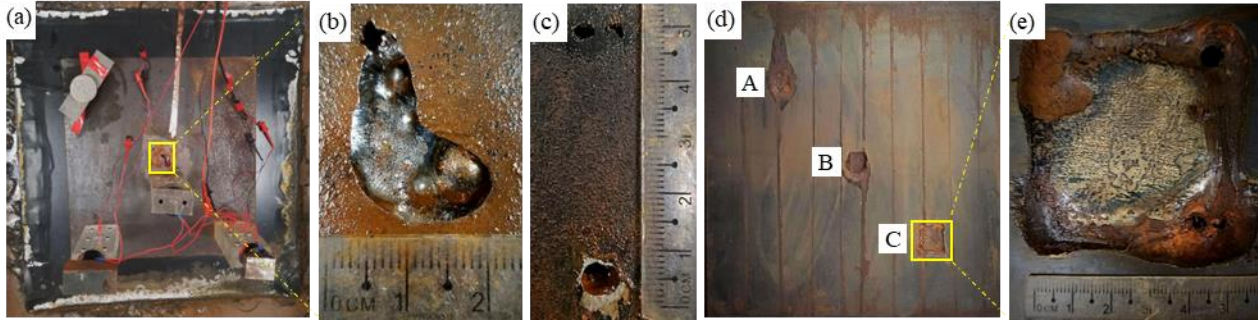


Figure 2.21 - Localized corrosion defects in the thick steel plate. (a) Top surface of the steel plate with a through-thickness hole detected in the corrosion area B. (b) A zoom in of the corrosion defect in the corrosion area B. (c) Through-thickness holes detected in the corrosion area C. (d) The corroded surface of the steel plate after removing the corrosion protection tapes. (e) A zoom-in view of the corrosion area C on the corroded surface of the steel plate.

2.6.3 Corrosion Monitoring Results of the 6.3 mm-Thick Plate

Figure 2.22 displays the experimental solitary waves recorded by the HNSW transducers positioned above the areas B, C, and D in corrosion experiment I (refer to section 2.3.3). Each waveform is the average of the ten measurements taken at a given instant. The first pulse around 0.15 ms is the ISW traveling towards the chain-plate interface. The amplitude of this pulse is expected to remain constant regardless of the conditions of the plate. The subsequent pulses represent the PSW and SSW, respectively. For clarity, the arrival of the SSWs is boxed in red rectangles. Figure 2.22a and Figure 2.22b are relative to the corroded areas B and C, respectively. They show a shift in the time of arrival and a decrease in amplitude of the PSW after measurement 150, i.e. about 75 hours within the experiment. For convenience, these sets are emphasized with the red circles in Figure 2.22.

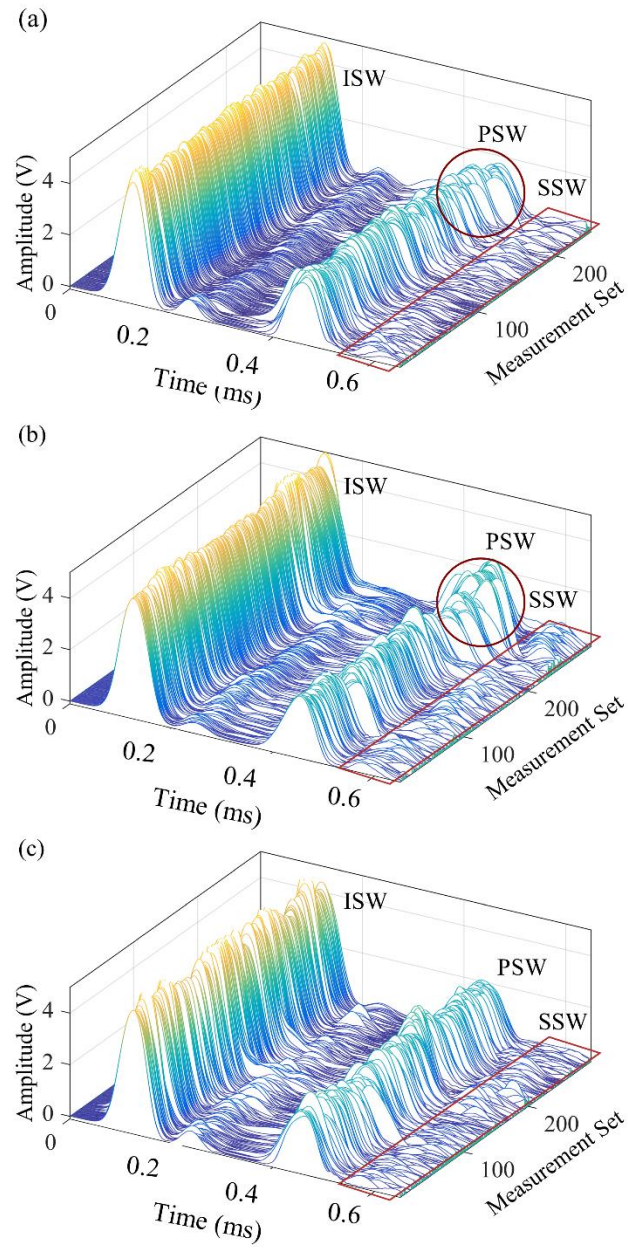


Figure 2.22 - Solitary wave profiles recorded by solitary wave transducers positioned on the areas (a) B, (b) C, and (c) D on the 6.3 mm-thick plate.

The time of flight of the PSW was calculated as the difference between the ISW and the PSW peaks. The results are presented in Figure 2.23. The graphs relative to the corroded area (Figure 2.23a and Figure 2.23b) show a moderate increase of the feature with the progression of corrosion. On the other hand, Figure 2.23c shows that the time of flight measured above the pristine area D remains relatively constant throughout the experiment. While the time of flight associated with the pristine area was about 0.325 ms, the same feature measured under extensive corrosion increased by about 10% (Figure 2.23a and Figure 2.23b).

To quantify a trend between time of flight and the time, a 2nd order polynomial regression was fitted to the experimental data (dashed lines in Figure 2.23). The 2nd order was used since the numerical results (discussed in section 2.5.2) show a nonlinear trend of the time of flight with respect to the progression of the corrosion. The coefficients of the regressions are similar for the two transducers placed above the corroding areas (Figure 2.23a and Figure 2.23b). Moreover, all regressions display that time of flight at the beginning of the experiment (*Time* = 0 hr.) was about 0.325 ms. This indicates little if no variation in the fabrication and assembly of the solitary wave transducers.

The normalized amplitude of the PSW with respect to the amplitude of the ISW (also referred to as amplitude ratio) was computed, and the results are presented in Figure 2.24. The graphs show a 30% decrease of this solitary wave feature as localized corrosion propagates in areas B and C. As the normalized amplitude relative to area D remained mostly constant (Figure 2.24), it can be concluded that this feature is significantly affected by the presence of localized corrosion. The results show that at *Time* = 0 hr, about half of the incident acoustic energy is reflected back as a PSW and this is consistent for all three transducers.

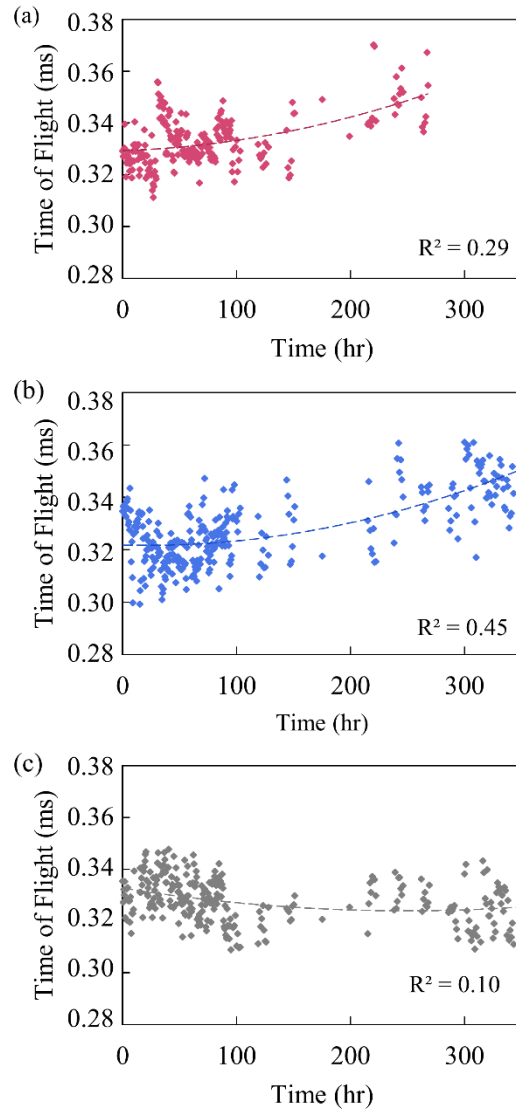


Figure 2.23 - Experimental results of monitoring corrosion in the 6.3 mm-thick plate. Time of flight, calculated by the peak-to-peak method for solitary wave transducers used to monitor areas (a) B, (b) C, and (c) D of the test object.

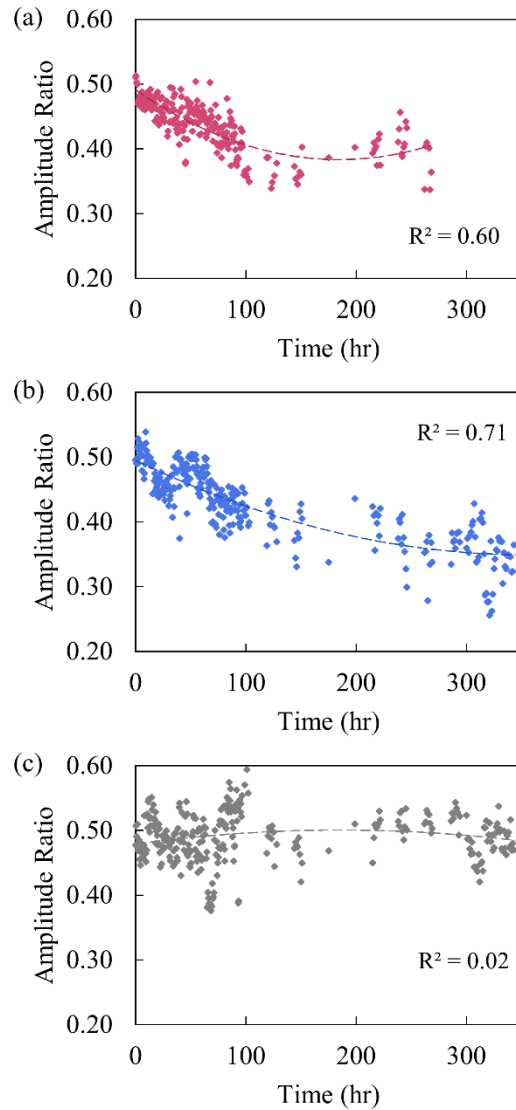


Figure 2.24 – Experimental results of monitoring corrosion in the 6.3 mm-thick plate. Normalized amplitude of the primary reflected solitary wave measured from the areas (a) B, (b) C, and (c) D monitored with the HNSW transducer.

The effect of localized corrosion on the solitary wave features can be explained by the analytical model described in section 2.2.3. This model delved with plates of uniform thickness. However, the concept of inelasticity parameter can be adopted at large in this study to explain the effect of localized corrosion on the solitary wave features. Under such approximation, it can be argued that

the progress of localized corrosion increases the value of the inelasticity parameter λ locally. According to Eq. (2.9) and Eq. (2.10), the increase of the inelasticity parameter yields to a local decrease in the coefficient of restitution and amplitude ratio, i.e., higher energy dissipation in the chain-plate interaction. Furthermore, according to Eq. (2.17) and Eq. (2.18), as the inelasticity parameter increases, the dimensionless contact time τ_c and the time of flight increase. Therefore, using the concept of the inelasticity parameter in the analytical model shows that the progress of a localized corrosion defect under the chain-plate interface is expected to increase the time of flight and decrease the amplitude ratio, as observed in Figure 2.23 and Figure 2.24.

Figure 2.25 compares the numerical results presented in section 2.5.2 with the experimental results obtained from monitoring areas B and C. The numerical results present the time of flight and the normalized amplitude of the reflected solitary wave in a plate containing a localized defect. In this case, the time of flight and the amplitude ratio are plotted as a function of the normalized corrosion depth, defined as the depth of the corrosion defect divided by the initial plate thickness. The normalized corrosion depth varies from 0 to 0.8, i.e., the defect depth varies from 0% to 80% of the initial plate thickness. The experimental results are plotted as a function of the normalized time, which is calculated as the ratio of the time spent from the start of the corrosion experiment to the related recording time to the final corrosion time when through-thickness holes were detected. Moreover, the dashed lines present a 2nd order regression model fitted to the experimental data.

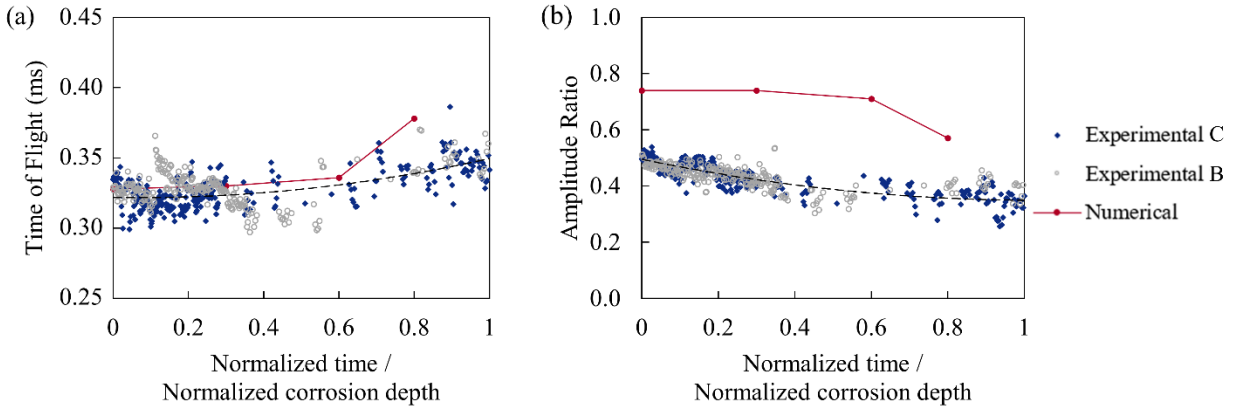


Figure 2.25 - Comparison of the numerical results and the experimental results on the effect of localized corrosion on (a) time of flight and (b) amplitude ratio in plate with a thickness of 6.3 mm. The numerical results present the feature of the reflected solitary waves in contact with plates containing a localized defect, where the defect depth varies from 0 to 80 percent of the initial plate thickness. The experimental results show the same features of the reflected solitary waves in a HNSW transducer monitoring a localized corrosion in a plate of similar properties. The dashed line presents the 2nd order regression model fitted to the experimental data.

According to Figure 2.25a, the numerical results show a 0.328 ms time of flight in the pristine condition, i.e., corrosion depth equal to zero. Also, the 2nd order regression model fitted to the experimental data predicts a 0.320 ms time of flight at the beginning of the test. The experimental observations (scattered data points) show about ± 0.02 ms error in time of flight around the fitted model due to occasional tilting/vibrations of the sensor disk and stochastic nature of the striker collision. However, both the numerical and experimental results show 10-15% increase of time of flight as a localized corrosion progresses in the plate. According to Figure 2.25b, the numerical results overestimate the experimental normalized amplitude but both numerical prediction and experimental results estimate about 25% amplitude reduction as corrosion progresses. The overestimation of the numerical amplitude is likely due to an underestimation of energy dissipation in the chain and at the chain-plate interface in the numerical model.

Figure 2.26 shows the amplitude of the ISW as a function of time, for all the three transducers. Each dot represents the average of the ten measurements. The graphs show no trend of ISW amplitude for the three transducers, and the regression suggests that the fabrication and assembly of the transducers were consistent. The random variability of the ISW amplitude can be therefore attributed to the inherent stochastic nature of the striker collision and occasional tilting and vibrations of the sensor disk. Furthermore, according to the discussion in section 2.5.4, both the numerical and analytical results show that the amplitude of the ISW has little effect on the solitary wave features when compared to the 10% and 30% change observed empirically in Figure 2.23 and Figure 2.24. Therefore, the variations observed in time of flight and amplitude ratios were truly related to the localized corrosion.

Figure 2.27 shows the ultrasonic time of flight measured by the pulse-echo transducer located above the corroding area A. The corresponding plate thickness reduction (Δth) and the remaining plate thickness (th) was estimated as:

$$\Delta th = \frac{UT_0 - UT}{UT_0 - D} th_0, \quad th = th_0 - \Delta th \quad (2.20)$$

where th_0 denotes the initial plate thickness equal to 6.3 mm, UT_0 and UT denote the initial and the current ultrasonic travel time obtained from the correlation method, and D represents the dual transducer delay. The estimated values of the remaining plate thickness and the plate thickness reduction in the area A are shown in Figure 2.27a (on the left axis) and Figure 2.27b, respectively. The graphs show an overall linear trend of the corrosion with respect to the time of the experiment. According to the estimate from the ultrasonic transducer, after 300 hours the plate under probe was about 4.2 mm, i.e. about 36% thinner. At the end of the experiments, this area A was cored to forensically quantify the true thickness. It was found that the corrosion was not uniform and the real thickness varied between 2 mm and 5 mm.

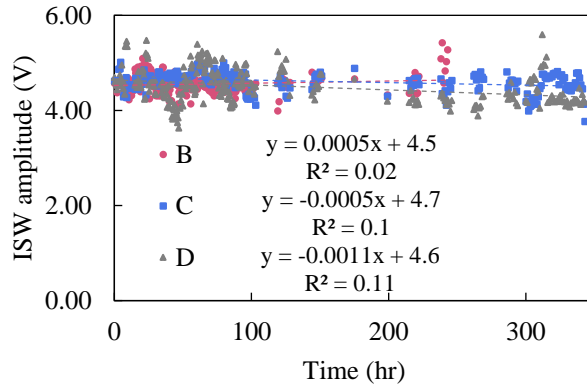


Figure 2.26 - Experimental results of monitoring corrosion in the 6.3 mm-thick plate. Amplitude of the Incident Solitary Wave.

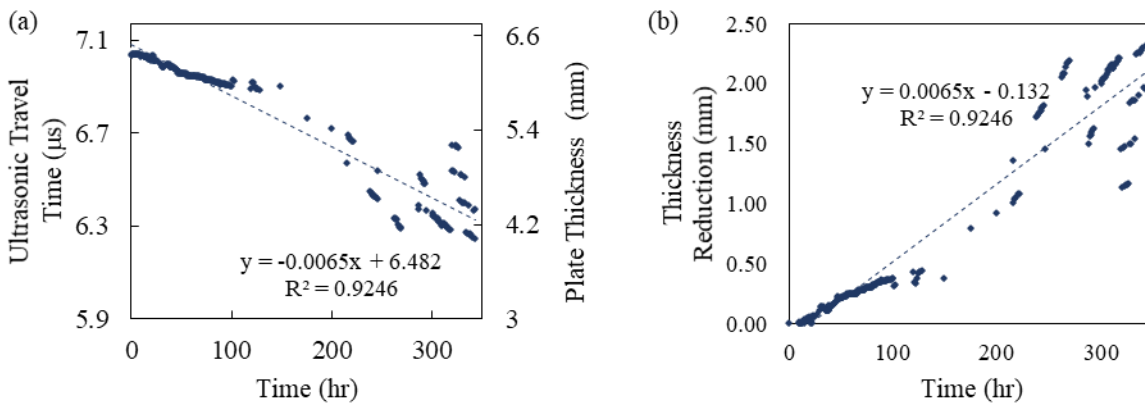


Figure 2.27 – Ultrasonic testing results of monitoring corrosion in the 6.3 mm-thick plate. (a) Ultrasonic travel time in the corrosion area A (on the left axis) and the relative local plate thickness (on the right axis). (b) Plate thickness Reduction in area A obtained from the ultrasonic test results.

2.6.4 Outlier Analysis Results of Monitoring the 6.3 mm-Thick Plate

Multivariate outlier analysis based on the Mahalanobis squared distance (MSD) was performed for the HNSW measurements obtained from the corrosion test I. The Mahalanobis distance (MD) was calculated based on Eq. (2.19) and considering five parameters, including the time of flight

calculated with the peak-to-peak method and the correlation method, the normalized amplitude of the PSW, the autocorrelation coefficient, and the area under PSW. For each transducer, the baseline consisted of the measurements taken during the first 24 hours of the experiment. The calculated MSD values are presented in Figure 2.28 and the baseline data is highlighted in the green background. The threshold corresponding to the 99.73% confidence interval is shown by the horizontal dashed lines. The threshold values were calculated as the upper value of 3σ of the baseline and is equal to 21.9, 15.4, and 13.7 in Figure 2.28a, Figure 2.28b, and Figure 2.28c, respectively. A value of the distance higher than the threshold represents an outlier, implying anomalies in the recorded data with respect to the database.

The effectiveness of the outlier analysis in detecting localized corrosion is evaluated based on the HNSWs features recorded after 100 hours (highlighted in the red background on Figure 2.28). According to Figure 2.28a and Figure 2.28b, 80% and 92% of the points in the red box show outliers in the recorded data of the corroding areas B and C, respectively. Sensitivity improves to 100% after 230 hours, as the localized corrosion progress in area C (Figure 2.28b). On the other hand, MSD calculated using the data recorded at the pristine area D (presented in Figure 2.28c) shows only 8% outliers after 100 hours (false positives). As shown in Figure 2.28c, those points are slightly higher than the threshold line, and they present false positives in the test. It can be concluded that using the multivariate outlier analysis is effective in detecting anomalies in the HNSW-based corrosion detection.

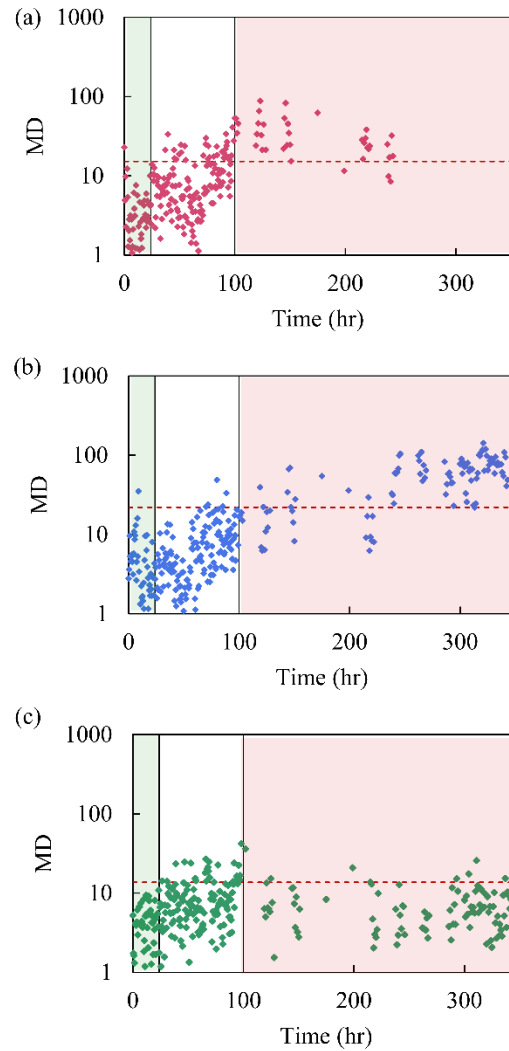


Figure 2.28 - Multivariate outlier analysis of the experimental data obtained from monitoring the 6.3 mm-thick plate. Mahalanobis distance calculated based on the five solitary wave features including time of flights calculated by the peak-to-peak method and the correlation method, amplitude ratio, autocorrelation coefficient, and area under the primary reflected solitary wave in areas (a) B, (b) C, and (c) D. The horizontal lines represent the 99.7% confidence threshold calculated as 19.7, 17.1, and 14.4, respectively. The green background presents the baseline data.

2.6.5 Corrosion Progress in the 4.8 mm-Thick Plate

After around 100 hours from the start of the corrosion experiment II, through-thickness holes were detected around 3 corroding areas, namely P4, W3, and W4. Consequently, monitoring these areas was terminated and the associated transducers were removed from the top of the plate. Figure 2.29 shows a close-up view of the through-thickness holes detected after 100 hours in the corroding areas P4, W3, and W4. The white circles indicate the interaction points between the plate and the associated solitary wave transducers. The through-thickness holes are highlighted in yellow rectangles. Based on Figure 2.29a and Figure 2.29c, in the corroding areas P4 and W4, i.e., the 12.7 mm × 12.7 mm corroding areas, the holes were detected close to the plate-transducer interaction points. On the contrary, in the corroding areas W3, which is a 50.8 mm × 50.8 mm corroding area, the corrosion-induced hole was observed at a further distance from the plate-transducer interaction point (Figure 2.29b).

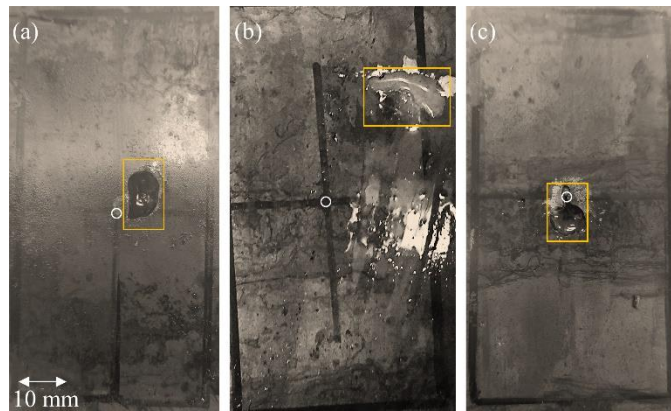


Figure 2.29 – A close-up view of the through-thickness holes detected after 100 hours in the corroding areas (a) P4, (b) W3, and (c) W4 on the 4.8 mm-thick plate. The white circles indicate the interaction point between the plate and the associated solitary wave transducers. The through-thickness holes are highlighted in yellow rectangles.

The photos reveal that the corrosion depth was not uniform and pitting corrosion occurred. This is considered one of the most dangerous and difficult to detect forms of corrosion and is caused by inhomogeneities of the composition of the steel plate, or inhomogeneities of the environment like local loss of protective oxide coating and concentration of aggressive chemicals [159]. The visual inspection of the damaged areas reveals that corrosion was deeper around the edges, i.e., corrosion seemed to have occurred at a faster rate in the proximity of the tape. This conforms with the available research findings showing that pitting corrosion is most severe at regions with disbonded coating; not regions completely free from protection [160]. It is known that concentration cells are formed because of the differences in oxygen or metal ion concentrations near the coating defect that may change local chemistry and lead to severe localized corrosion. Therefore, the presence of the plastic tape on the surface of the plate in the present experiment caused inhomogeneity in the environment and led to pitting corrosion near the edges of the corroding areas.

The use of P3 was also terminated shortly after 100 hours due to safety concerns although through-thickness holes were not detected. As a matter of fact, given that size of the exposed plate to the corroding environment under P3 was equal to the size of the part under W3, it was decided to remove the wired transducer 3 in abundance of caution. A pulse-echo ultrasonic transducer was used to monitor plate thickness at the center of area P3 at this time, and the results showed no thickness reduction in the plate-chain interaction point after 100 hours from the start of the corrosion process.

The experiment was concluded when a fourth hole around P2 after 270 hours. Then, the plate was removed from the tank, dried, the protection tape was removed, and the surface was cleaned with a cloth. Figure 2.30a shows the immersed face of the plate after removing the corrosion-resistant tape. The presence of localized corrosion is evident. The figure also reveals that the tape

protected effectively the rest of the plate. Figure 2.30b presents a close-up view of the corroded areas P2, W2, P3, W3, P4, and W4 on both faces of the plate. There was no through-thickness hole was detected around area W2. Small holes were seen around the edges of P2 and P3, whereas areas W3, P4, and W4 were extremely corroded. The deeper corrosion defects around the edges in areas P2, W2, and P3 are in agreement with the non-uniform corrosion observations discussed earlier. The pulse-echo ultrasonic testing performed after the experiment showed that the thickness of the center of areas P2, P3, and W2 decreased between 0.7 mm and 1.3 mm.

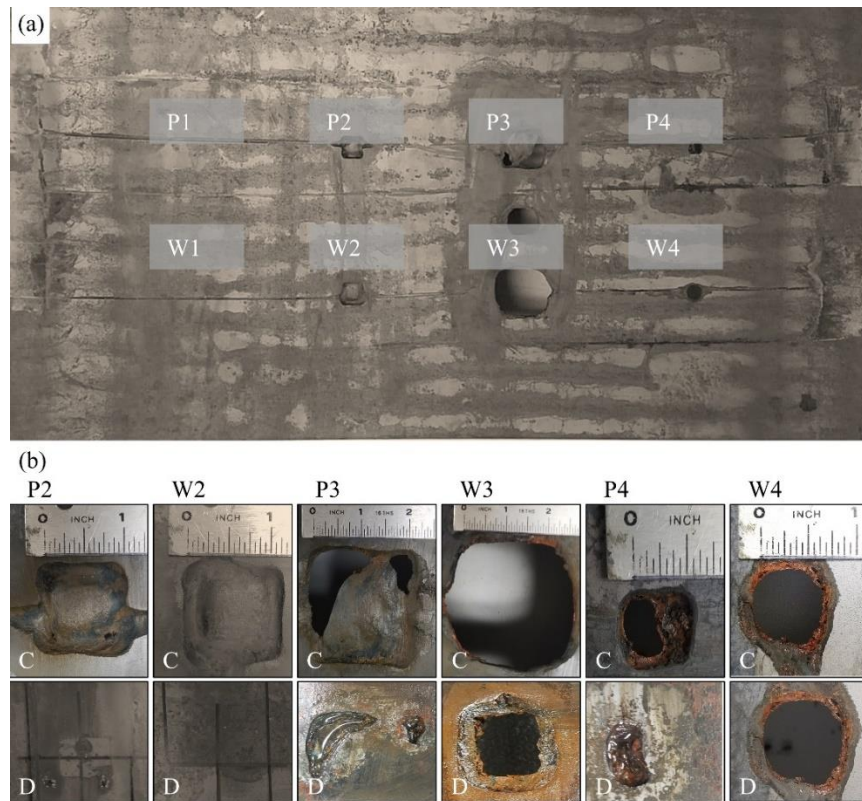


Figure 2.30 – Localized corrosion defects in the 4.8 mm-Thick Plate after finishing the corrosion experiment. (a) The corroded face of the plate after removing the corrosion resistant tape. (b) A close-up view of the corroded areas P2, W2, P3, and P4 on the corroded face and the dry face.

2.6.6 Corrosion Monitoring Results of the 4.8 mm-Thick Plate

The solitary wave features, i.e., the ISW amplitude, the time of flight, and the amplitude ratio obtained from the corrosion test II are presented in Figure 2.31, Figure 2.32, and Figure 2.33. Here, each data point presents the average of five consecutive measurements. Since monitoring areas P3, W3, P4, and W4 was terminated after 100 hours, the associated data spans from the start of the test to 100 hours. There are small gaps in the data associated with the transducers monitoring P1 and P2. In these cases, monitoring was paused manually due to improper wire connection. Data gaps seen in W1 shows were instead caused by microcontroller issues that required the manual replacement of the PCB. Notably, the removal and then the reinstallation of W1 did not alter the measurements and the data collected with the new PCB were highly comparable to the data collected with the old microcontroller.

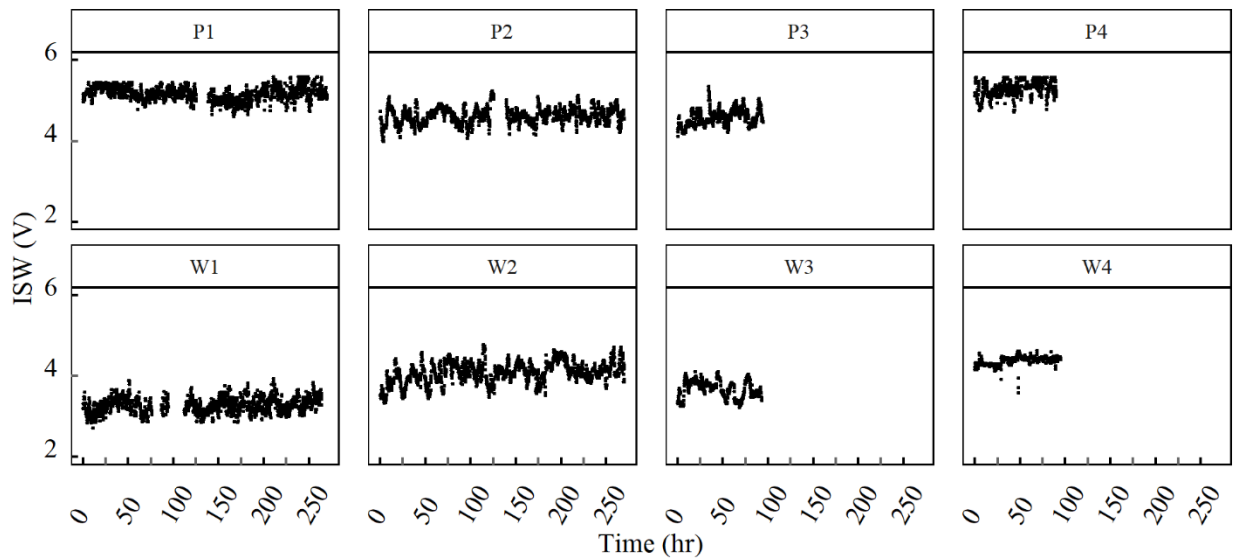


Figure 2.31 - The amplitudes of the incident solitary waves recorded by the eight solitary wave transducers over the corrosion experiment on the 4.8 mm-thick plate. Each datapoint presents the average of 5 consecutive measurements.

According to Figure 2.31, although the ISW amplitudes are slightly scattered, they do not show any increasing or decreasing trend over the experiment. This is expected as the amplitude of the generated signal should not be affected by the boundary conditions at the opposite edge of the chain. Figure 8 confirms what observed in the previous experiment, i.e., that the amplitude of the ISW among the four wired transducers is not the same. The comparison between the wired and the wireless transducers reveals that the amplitude of the incident wave detected by all four wireless transducer is mostly lower than the wired ones. This small reduction in amplitude is expected since the input stage of the wireless transducer's PCB is a passive low-pass filter whereas the PXI chassis input channels have a significantly higher electrical input impedance.

Based on Figure 2.32 and Figure 2.33, the time of flights and the amplitude ratios measured by transducers P1 and W1 did not change significantly over the experiment as they were monitoring pristine areas. In addition, the data associated with area P3 does not indicate a significant variation of the time of flights or the amplitude ratios during the monitoring period. This is because monitoring area P3 was terminated due to safety concerns before a corrosion defect progresses significantly in this area.

The data obtained from monitoring area P2 shows a significant increase in time of flight after 70 hours. In addition, the results show that the amplitude ratio decreased after around 70 hours and then increased after around 250 hours. The nonmonotonic trend in the amplitude ratio observed in this test is in agreement with the numerical predictions, reported in section 2.5.4. The numerical results showed a nonmonotonic trend in amplitude ratio as a localized corrosion defect penetrates in the plate. It was shown that the amplitude ratio increases as the remaining plate thickness gets less than 1.3 mm because of the propagation flexural waves in the plate. This effect is attributed to the propagation of flexural waves in the plate. As the plate gets very thin at the chain-plate

interface, the contact stiffness between the chain and the plate decreases. As a result, time of flight increases significantly, i.e., longer contact time between the last particle and the plate. The long contact time yields to the simultaneous initiation of the reflected solitary waves and the plate's rebound due to the propagation of flexural waves. Consequently, the kinetic energy of the flexural wave contributes to pushing the last particle back harder and thus causing stronger reflected solitary waves. This non-monotonic trend is also present, but less visible, within the first few hours of P4 and W4 before the amplitude ratio increased significantly and steadily due to the progression of the severe damage. The same can be said about the third wireless transducer.

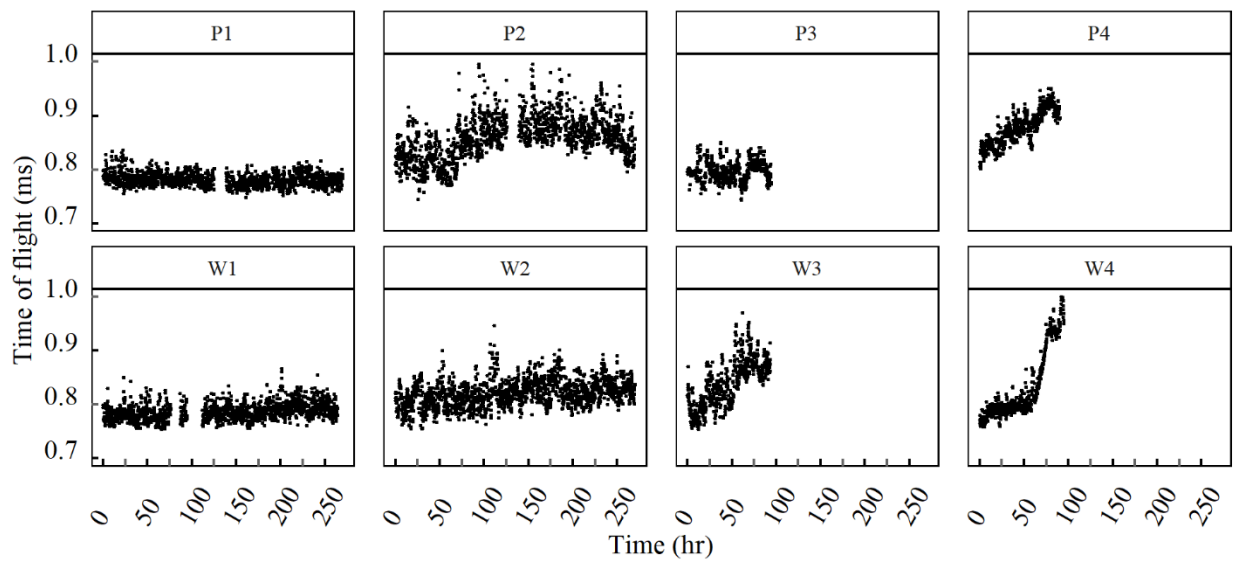


Figure 2.32 – The time of flights of the solitary waves recorded by the eight solitary wave transducers over the corrosion experiment on the 4.8 mm-thick plate. Each datapoint presents the average of 5 consecutive measurements.

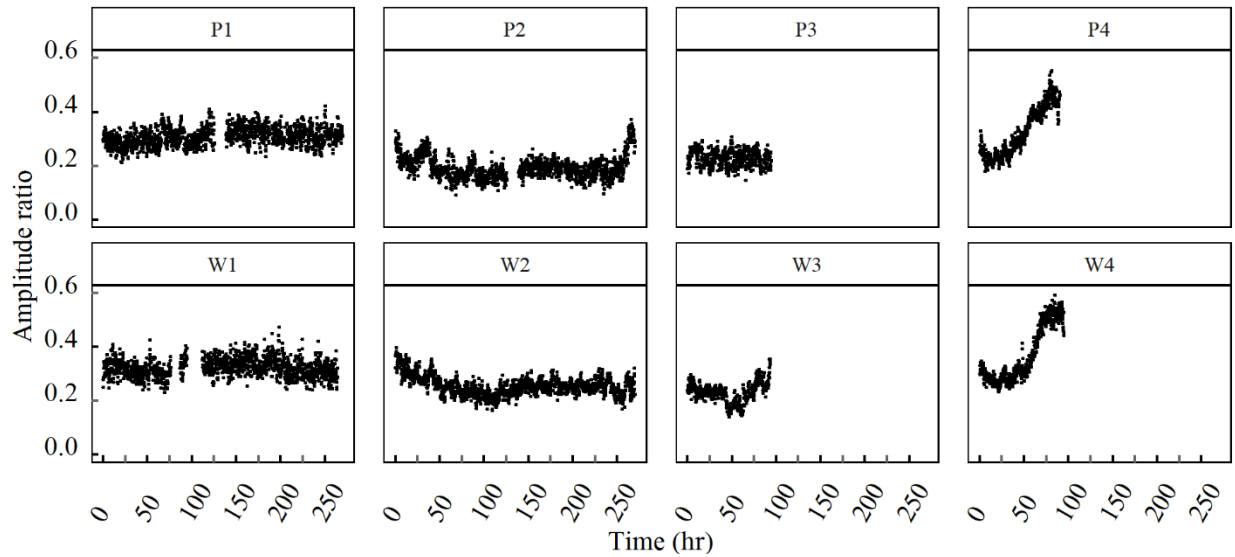


Figure 2.33 - The amplitude ratios of the solitary waves recorded by the eight solitary wave transducers over the corrosion experiment on the 4.8 mm-thick plate. Each datapoint presents the average of 5 consecutive measurements.

The data obtained from monitoring area W2 shows that the amplitude ratio decreased gradually over the corrosion experiment. In addition, the time of flight slightly increased in this area. However, the difference is not significant since this monitored area did not corrode considerably over the experiment. As discussed in section 2.6.5, no through-thickness hole was detected in area W2. In addition, thickness monitoring of the plate using the ultrasonic method at the center of this area showed that only 0.7 mm of the plate thickness was reduced, i.e., around 15% of the plate thickness. It can be concluded that the solitary wave features were affected by the progress of the localized corrosion in this area, although the corrosion defect was not substantially deep. The trend of the solitary wave features related to areas P2 and W2 are slightly different as the corrosion depth in these areas was different.

The experimental data associated with areas P3, W4, and P4 indicate a significant increase in time of flight as a result of localized corrosion defect progressed in these areas. Furthermore, Figure 2.33 shows that the amplitude ratio decreased and then increased in these areas (a nonmonotonic trend in the amplitude ratio). As discussed earlier these observations agree with the previous numerical predictions. The shift in the time of flight and the amplitude ratio is more noticeable in areas P4 and W4 than in area P3. This is associated with the observation that the through-thickness holes detected in areas P4 and W4 were close to the plate-transducer interaction point while the detected hole in area P3 was far from the inspection point (refer to Figure 2.29). In fact, after 100 hours from the start of the test, the corrosion defects were deeper at the inspection points of P4 and W4 compared with P3.

The data presented in Figure 2.32 and Figure 2.33 are clustered in Figure 2.34, where the time of flight is presented against its corresponding amplitude ratio, and the colormap identifies time. The two pristine areas form a cluster. At the opposite end, the presence of the severe corrosion skewed the data points toward the upper right corner of the plot. The comparison between wired and wireless transducers proves that W1 and W4 behaved as P1 and P4. Transducer W4 outperformed P4, whereas P2 and W2 were similar but not identical.

Overall, the results show that the time of flight and the amplitude ratio of solitary waves were affected by the presence and propagation of localized corrosion defects in the plate. It can be concluded that solitary waves are an effective localized method for the detection of defects. Furthermore, the experimental observations were in good agreement with the numerical modeling results previously reported by the authors.

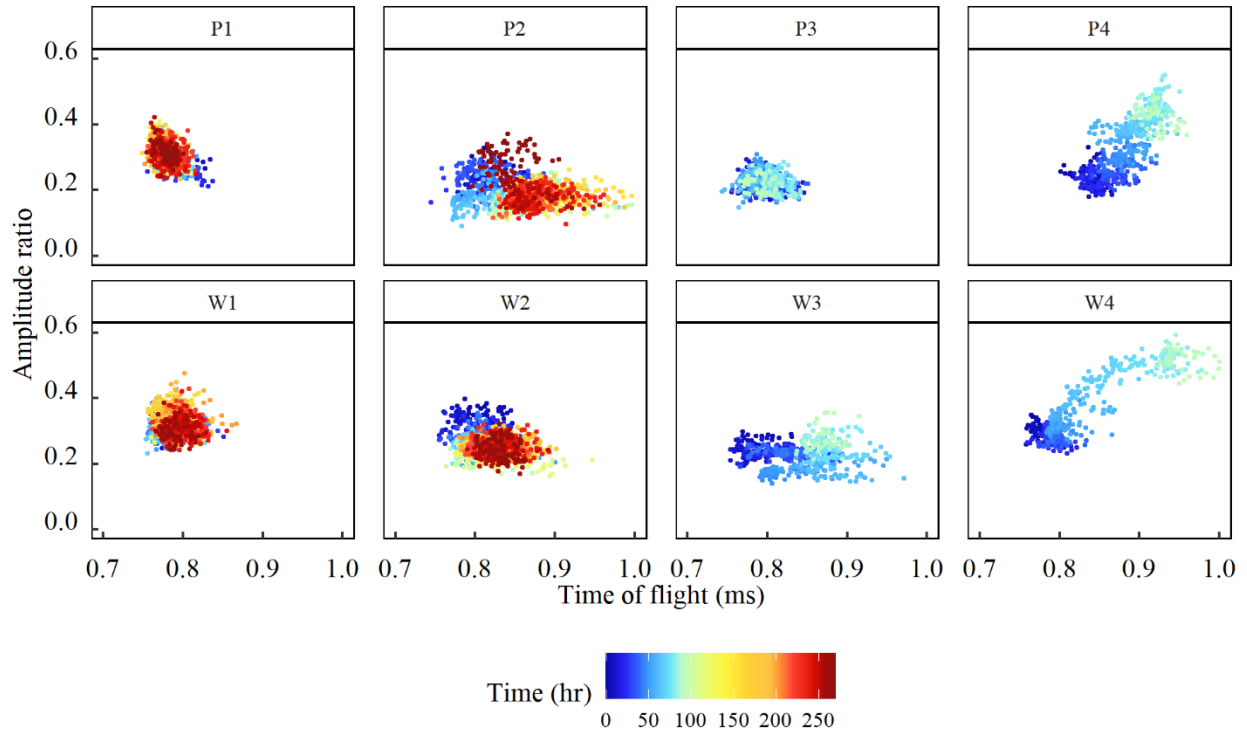


Figure 2.34 – The time of flights and amplitude ratios obtained from the monitoring transducers on the 4.8 mm-thick plate. Datapoints are presented at 2D amplitude ratio-time of flight space.

2.6.7 Outlier Analysis Results of Monitoring the 4.8 mm-Thick Plate

Figure 2.35 shows the MSD calculated based on the time of flight and amplitude ratio. In this analysis, the baseline data included the measurements obtained by each transducer within the first 24 hours. The horizontal lines represent the 99.7% confidence threshold of the MSD, calculated as the upper value of 3σ of MSD of the baseline. An MSD value higher than the threshold represents an outlier, implying anomalies in the recorded data with respect to the baseline data. Figure 12 reveals a few isolated outliers detected by W1, which in this case were false positives. The MSD computed from P2 and W2 contained several proper outliers but also many inliers that were false negatives. The MSD relative to P3, P4, and W4 show a multi-fold increase that unequivocally suggests the presence of a defect nearby the detectors.

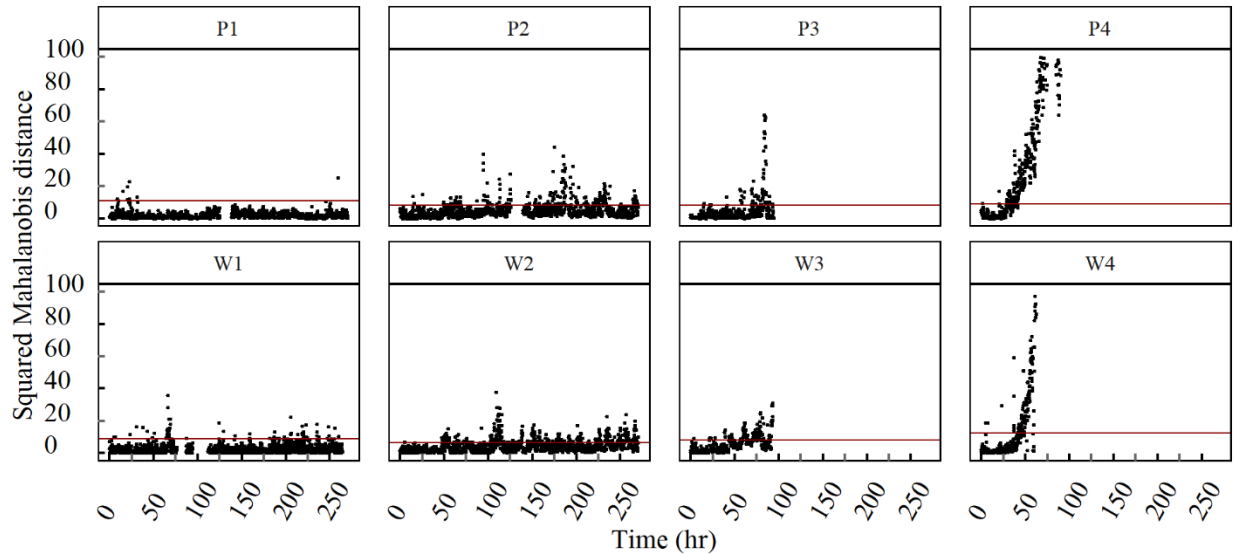


Figure 2.35 - The Mahalanobis distance calculated based on the time of flight and amplitude ratio in the 4.8 mm-thick plate. For each transducer, the baseline data included the measurements obtained by the transducer over the first 24 hours of the experiment. The horizontal lines represent the 99.7% confidence threshold of the MSD of the baseline data.

To quantify the outcomes of Figure 2.35, Table 2.5 presents the number of outliers detected in each solitary wave transducer over the last 50 hours prior to their removal. According to the results, over 90% of the observations in P4 and W4 were properly labeled as outliers. On the other hand, only 0.1% and 6.3% of data relative to P1 and W1 were (erroneously) labeled as outliers during the timeframe 220 – 270 hours. Moreover, the MSD results of the P2, W2, P3, and W3 present 20-40% outliers, which is significantly higher than the percentage of outliers in P1 and W1. Therefore, it can be concluded that the MSD results indicate the presence of corrosion defects in P2, W2, P3, and W3. However, the rate of false negatives in these areas is relatively high possibly because corrosion defects were not severe in those areas, or the defects were positioned at a noticeable distance from the monitoring points.

Table 2.5 –The outliers detected by each solitary wave transducers over the last 50 hours of monitoring the 4.8 mm-thick plate.

Monitoring position	Corroded (C) or Pristine (P)	Number of outliers (percentage)
P1	P	1 (0.3%)
P2	C	63 (22.1%)
P3	C	60 (20%)
P4	C	297 (99.3%)
W1	P	18 (6.3%)
W2	C	111 (37%)
W3	C	116 (38.7%)
W4	C	275 (91.7%)

2.7 Conclusions

In the study presented in this chapter, a new NDE technique based on the propagation and detection of solitary waves and multivariate statistics is proposed to detect localized corrosion in steel structures. The technique consists of the use of a special transducer designed to trigger, sustain, and sense nonlinear solitary waves that interact dynamically with the structure to be monitored. The proposed NDE is investigated numerically and experimentally.

Coupled discrete element/finite element models were used to study the dynamic interaction between solitary waves and steel plates. The numerical results indicate that that the time of flight and normalized amplitude of the solitary waves are strongly affected when the localized corrosion depth is higher than 50% of the plate thickness. Furthermore, it was shown that the HNSW-based NDE method is more sensitive to localized corrosion in thinner plates. It was also shown that the

method sensitivity improves by using larger, heavier, and stiffer particles. The numerical results show that the granular chain length and the position of the sensor particle do not affect the properties of the reflected solitary waves significantly. However, in high-temperature environments using longer granular chains and keeping the sensor away from the monitoring object can be beneficial to isolate the vulnerable PZT wafers from hot zones. In addition, the application of granular chains made of silicon nitride particles is advantageous in high-temperature environments since they are relatively stiff and have a lower thermal conductivity that would protect the sensor embedded in the chain.

In addition, two experiments were conducted to monitor localized corrosion in two steel plates of different thicknesses using the solitary wave transducers. The recorded waveforms are then processed with multivariate statistics based on outlier analysis to label data that diverge significantly from a set of baseline data that represent the pristine structure. The results associated with the outlier analysis demonstrated that the HNSWs were able to detect corrosion as small as 0.75 mm. The experimental results are in good agreement with the numerical predictions, and overall, the results show good accuracy and sensitivity of the HNSWs technique for detecting localized corrosion.

3.0 Application of Granular Crystals to Characterize Anisotropy of Rock Materials

This chapter delves into the application of highly nonlinear solitary waves for the nondestructive identification and characterization of anisotropy in rocks. This technique uses the characteristics of solitary waves propagating in a periodic array of spherical particles in contact with the rock to be characterized. The features of the waves that bounce off the chain rock interface are used to infer some properties of the geomaterial under consideration. Numerical models and experimental validation were conducted to explore the feasibility of the method and to calibrate the methodology for future widespread applications.

This chapter is written based on the following article:

Jalali, H., Zeng, Y., Rizzo, P., and Bungler, A. “Highly Nonlinear Solitary Waves to Characterize Anisotropy of Rock Materials.” *Materials Evaluation* 79(10) 2021.

It should be noted that the dissertation author contributed to this study by numerical modeling and experimental data analysis. The experiments of this study were designed and performed by Mr. Yuhui Zeng (coauthor of the above paper). However, the experimental setup and the data are presented here for the sake of narrative coherence.

3.1 Introduction

In the study presented in this chapter, a new NDE technique based on the generation, propagation, and detection of solitary waves is proposed for high resolution characterization of

anisotropy of rocks. HNSWs are compact waves of Gaussian-like shape that have found many applications in physics and engineering [24, 28, 161-173]. The NDT technique based on HNSWs has emerged in the last ten years as a low-cost, fast, and simple technique for the local inspection/monitoring of different materials and structures. The technique relies on the use of a short granular chain made of spherical particles placed in a point-contact with the structure to be inspected. A solitary wave, hereinafter referred to as the incident solitary wave (ISW), is induced at one end, propagates along the chain, and reaches the structure. Here, owing to principles discussed in this chapter, the ISW reflects back giving rise to one or two solitary waves, the primary and the secondary reflected waves, hereinafter labeled as PSW and SSW. Many studies have found that the amplitude and time of flight of these reflected pulses are dependent on the mechanical and geometric characteristics of the structure [8-12, 15, 17, 42-44, 46, 49-51, 126, 128, 131, 133, 135, 138, 140]. The research hypothesis of this study is that HNSW can be used for characterizing anisotropy in rocks because coupling, even to curved specimen surfaces, is simple and hence measurements in many directions can be made very rapidly. Additionally, the depth of influence is small, allowing for high spatial resolution as well as interpretation that depends on local contact mechanics rather than requiring *a priori* assumptions and/or knowledge of the intrinsic material symmetries.

The study presented in this chapter is the latest application of the HNSW-based NDT technique that Rizzo and his research group at the University of Pittsburgh have developed and applied to monitoring concrete hydration [131], assessing the quality of adhesive joints [8, 10], detecting damage in composites [8], assessing the quality of orthopedic and dental implants [138], measuring the internal pressure of tennis balls [9, 49, 50], quantifying axial stress [17, 51], detecting the onset of localized corrosion [135]. Most of the above experimental studies are based on the use of the

so-called HNSW-transducers. The term indicates a mechanical device able to trigger, sustain, and sense solitary waves. The device consists of a 1-D chain of spherical particles; a frame holding the particles, an actuation system able to trigger single solitary pulses, and a sensor embedded in the chain to measure the waves.

To the best of the Author's knowledge, the use of solitary waves in geotechnical engineering was proposed for the first time only very recently by [129] who described the use of a device similar to those developed by Rizzo's group to measure the Young's modulus of geomaterials. Villacreses *et al.* demonstrated that the method in control samples of known elastic properties, rocks, and compacted soils. They also proposed a modification of the device, which consists of placing a metal cylinder between the chain and the sample to improve the measurability of the method when dealing with soft soils.

The study presented here is both numerical and experimental. The numerical setup is based on a discrete element model to predict the dynamic interaction between the solitary waves and the material in point contact with the chain. Once such interaction was established, a systematic investigation was performed to examine the effects of parameters such as size, number, and material of the particles on the sensitivity of the proposed method at detecting subtle differences in the elastic modulus of the rock material. The scope of this part of the study was to identify the optimal parameters of the HNSW transducer to maximize the sensitivity of the NDT technique. The experiments consisted of using a HNSW transducer to test two rock materials: sandstone and slate. The sandstone was nearly isotropic, while the slate was approximately transversely isotropic, but with its axis of symmetry was unknown before the experiments. Six 20 mm in diameter samples were tested. For all the specimens, the elastic modulus was calculated from the measurement of the solitary wave characteristics. The study is completed with finite element

simulations. With respect to [129], the present study presents a parametric analysis to optimize the design of the HNSW transducers to enhance the sensitivity of the NDT technique. In addition, the study provides the design and implementation of an automatic test setup to characterize the transversely isotropy of geomaterials. Last but not least, the computation of the Mahalanobis Squared Distance (MSD) is proposed as a statistical processing method to identify the directionality of strong and weak angles in TI materials.

3.2 Materials and Experiments

Four sandstone cylinder samples and two slate samples were prepared and stored at room temperature. The samples are shown in Figure 3.1, and their properties are listed in Table 3.1. The 50 mm long samples were cored from Agra Red Sandstone [174] and a building industry quarried slate using a diamond-impregnated coring bit with inner diameter of 20 mm. The coefficient of variation (CoV), i.e. the ratio of the standard deviation to the mean, associated with the samples density was equal to 0.58% for the sandstone and 0.67% for the slate. In terms of the samples diameter, the CoV relative to the sandstone and the slate were equal to 0.42% and 0.05%, respectively. Hence, for practical purposes, the samples can be considered identical. Before testing, samples were submerged in water for 48 hours to be fully saturated. Porosity was determined from the saturated and dry measurements using the equation:

$$porosity = \frac{m_{sat} - m_{dry}}{\rho_{water} V_{bulk}} \quad (3.1)$$

where m_{sat} is the mass of samples in saturated condition, m_{dry} is the mass of samples in dry condition, ρ_{water} is the density of water, and V_{bulk} is the bulk volume.



Figure 3.1 -Photos of the sandstone and slate samples (the slate samples are the two at the rightmost side of the picture).

Table 3.1 - Properties of the rock samples.

	Sandstone1	Sandstone2	Sandstone3	Sandstone4	Slate1	Slate2
Material	sandstone	sandstone	sandstone	sandstone	slate	slate
Diameter (mm)	18.92	18.74	18.94	18.90	18.90	18.92
Length (mm)	39.32	42.16	40.42	40.40	42.96	42.00
m_{dry}^* (g)	24.3	25.7	24.8	25.0	29.5	29.3
m_{sat}^* (g)	25.7	27.2	26.6	25.9	30.1	30.0
Density (g/cm ³)	2.198	2.210	2.177	2.206	2.448	2.481

* m_{dry} is the mass of oven dried sample.

* m_{sat} is the mass of saturated sample (immersed in water for 48h).

The HNSW transducer used for characterizing TI materials in this study is shown in Figure 3.2. An array of 9.5 mm monophasic particles forms the metamaterial supporting the chain. All the particles except the top one (striker) were made of non-ferromagnetic stainless-steel (type 440C, Young's modulus $E = 200$ GPa and Poisson's ratio $\nu = 0.30$). Solitary waves are generated by lifting and releasing the ferromagnetic striker from a height of ~ 4 mm. For this purpose, commercial electromagnets (Uxcell 12 V DC) are connected to and controlled by a National Instruments PXI running in LabVIEW. The solitary wave force are recorded by wafer-type PZT embedded in between two half particles of the same diameter of the particles. To minimize

interference, the PZT is insulated from the metal using Kapton tape. The sensor system was positioned in the middle of the chain between the fourth and the fifth particles.

As shown in Figure 3.2, the specimen was secured to a motorized rotary stage connected to and controlled by a NI PXIe-8108 controller. The controller was synchronized with the PXI such that it would rotate the sample by 5 degree once a series of measurements was completed. For each angle, ten measurements were collected, i.e. the striker was lifted and released 10 times at 2 seconds interval. Each sample was therefore tested in the radial direction at 73 evenly distributed angles with the 0° and 360° overlapping.

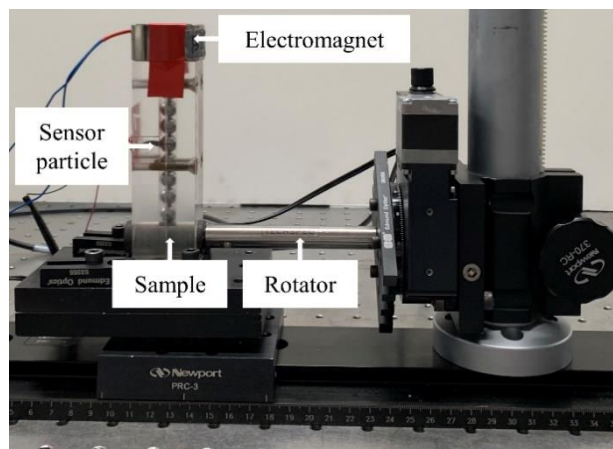


Figure 3.2 – Photo of the whole experimental setup. The HNSW transducer used in the study presented here contained 9.5 mm particles and the sensor consisted of a wafer-type PZT embedded in between two half-particles.

3.3 Numerical Modeling

The dynamic interaction between the solitary waves and the rock samples was investigated using a discrete element model based on the schematics of Figure 3.3a. The model simulates the

propagation of the waves along the chain of particles that were modeled as a series of point masses connected with a nonlinear axial spring and a dashpot. The nonlinear springs were defined based on the Hertzian contact law Eq. (1.1), which governs the mechanical interaction between adjacent particles. In addition, energy dissipation along the chain was introduced using the dashpots. Researchers have estimated the coefficient of dissipation (γ) along the chain and at the interface of a granular chain and various metallic and polymeric materials [126].

For a chain of N identical spheres, the equation of motion of each particle is as follows:

$$m\ddot{u}_i = A_{i-1,i}[u_{i-1} - u_i]_+^{3/2} - A_{i+1,i}[u_i - u_{i+1}]_+^{3/2} + \gamma_{i-1,i}[\dot{u}_{i-1} - \dot{u}_i][u_{i-1} - u_i]_+ - \gamma_{i+1,i}[\dot{u}_i - \dot{u}_{i+1}][u_i - u_{i+1}]_+ + mg \quad (3.2)$$

where m represents the particle mass, g represents the gravitational acceleration, and u_i and \dot{u}_i represent the displacement and the velocity of the i^{th} particle, respectively. As shown in Figure 3.3, u_{N+1} represents the displacement of the rock sample at the contact point. The coefficient $A_{i,i+1}$ is the contact stiffness between the i^{th} and the $i+1^{\text{th}}$ particles, defined as:

$$A_{i,i+1} = \begin{cases} \frac{E_p \sqrt{2R}}{3(1 - \nu_p^2)} & i = 1: N - 1, \\ \frac{4\sqrt{R}}{3} \left[\frac{(1 - \nu_p^2)}{E_p} + \frac{(1 - \nu_r^2)}{E_r} \right] & i = N. \end{cases} \quad (3.3)$$

According to Eq. (3.3), the stiffness constant is a function of particles radius R , the Poisson's ratio ν , and the Young's modulus E of the particles and the rock sample. The subscript p indicates the properties associated with the particles, whereas the subscript r indicates the rock sample.

The aforementioned model considers the TI as "half-infinite", i.e., it does not take into account the true geometry and boundary condition of the specimen. To overcome the approximation related with the above model, the DE approach was coupled to a finite element model implemented in ABAQUS/Standard (Figure 3.3b). The DE model simulates the propagation of the solitary waves

in the granular chain, modeled as eight point-masses (m_1 to m_8) interacting with nonlinear axial connectors. The nonlinear connectors were defined such to resemble the Hertzian contact law and the damping in the chain. The FE model simulates the interaction between the last particle in the chain and the samples, modeled as 3D deformable solids and meshed into 3D 8-node linear isoparametric elements. The sample was modeled as a 19 mm \times 41 mm isotropic cylinder. The DE and the FE models were coupled by connecting the lowest point mass in the DE model (m_8) to the uppermost node of the 3D particle using the nonlinear connectors.

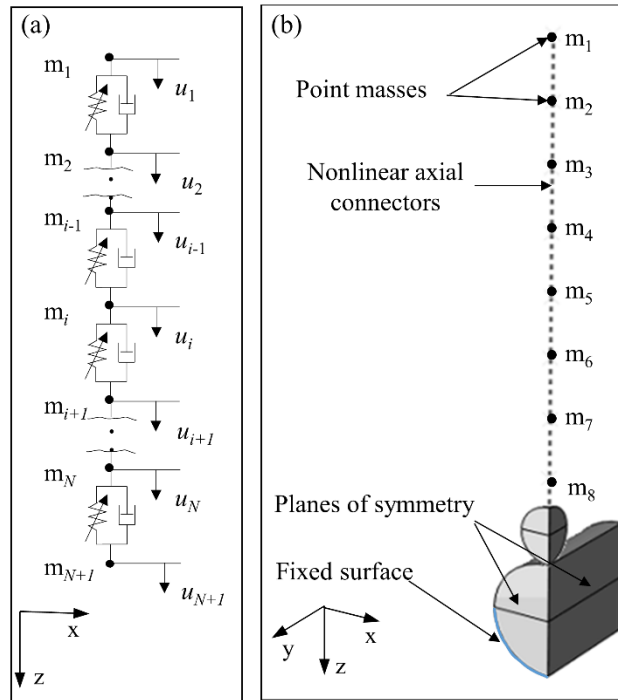


Figure 3.3 – Numerical model of the interaction of solitary waves and rock samples. (a) The discrete element model, and (b) the coupled discrete element/finite element model.

Due to the two symmetry planes in the problem, only one quarter of the geometry was simulated in the coupled DE/FE model. The contact between the last particle and the sample was modeled

as hard contact interaction with frictionless tangential behavior. Fixed boundary conditions were applied to the nodes on the lower half surface of the sample, and symmetric boundary conditions were applied to the nodes on the two planes of symmetry. Moreover, boundary conditions were imposed on the point masses so that they could move only along the chain axis. The effect of gravity was also considered by applying proper body forces and concentrated forces to the 3D parts and the point masses, respectively.

In both the DE and the coupled DE/FE model, the chain consisted 9 particles which were 9.5 mm in diameter, and their mechanical properties were as: $E = 200$ GPa and $\nu = 0.3$. Based on the properties listed in Table 3.1, the (bulk) density of the sandstone and slate samples was set to 2.2 g/cm^3 and 2.5 g/cm^3 , respectively. The interaction of HNSWs with the sandstone and slate samples was investigated within a range of the Young's modulus reported in Table 3.2. The Poisson's ratio was fixed at 0.2 and 0.25 for the sandstone and the slate, respectively. The physical impact of the striker was simulated by applying an impact velocity of 0.28 m/s to the first mass point in the chain (m_1) equivalent to striker fall from a height of 4 mm in the experiments. The nonlinear equations of equilibrium were solved using the model, and the particles displacement were extracted from the numerical results. The solitary wave profiles at the sensor particle were then calculated by averaging the interaction force between this particle and its upper and lower adjacent particles.

Table 3.2 - Mechanical properties of sandstone and slate.

Rock	Young's modulus (GPa)	Poisson's ratio
Sandstone	15 – 50 [175]	0.2 [177]
	1 – 39 [176]	
Slate	20 – 90 [175]	0.2 – 0.3 [175]
	10 -110 [176]	

3.4 Results

3.4.1 Numerical Results

Figure 3.4a and Figure 3.4b show the DE modek-generated time waveforms associated with the sandstone and slate samples, respectively, measured at the sensing location localized halfway within the chain of particles. For each inset, three different Young's moduli of the samples were considered. The first pulse is the ISW traveling towards the chain-sample interface. The subsequent pulses are the PSW and SSW, generated by the partial reflection of the ISW at the chain-sample interface. Both figures demonstrate that as the Young's modulus increases, the PSW becomes faster and stronger at the expense of the acoustic energy and speed of the secondary wave. In other words, as the Young's modulus of the samples increases the amplitude of the primary wave reflected at the interface increases, and the time interval between the ISW and the PSW arriving at the same sensing location decreases. This implies that the dynamic interaction of the last particle in the chain with softer geomaterials results in a longer contact time and higher energy transfer from the particle to the geomaterial because of the lower contact stiffness at the particle-sample interface.

When the rock is softer, the acoustic energy carried by the incident wave causes a large local deformation of the rock sample and such deformation generates the secondary pulse whose amplitude and time of flight is inversely proportional to the Young's modulus of the specimen. This higher deflection in softer geomaterials caused by the dynamic interaction between the solitary wave and the geomaterial cause separation of particles. The effect of this separation is the creation of double reflections visible in the overall time-series.

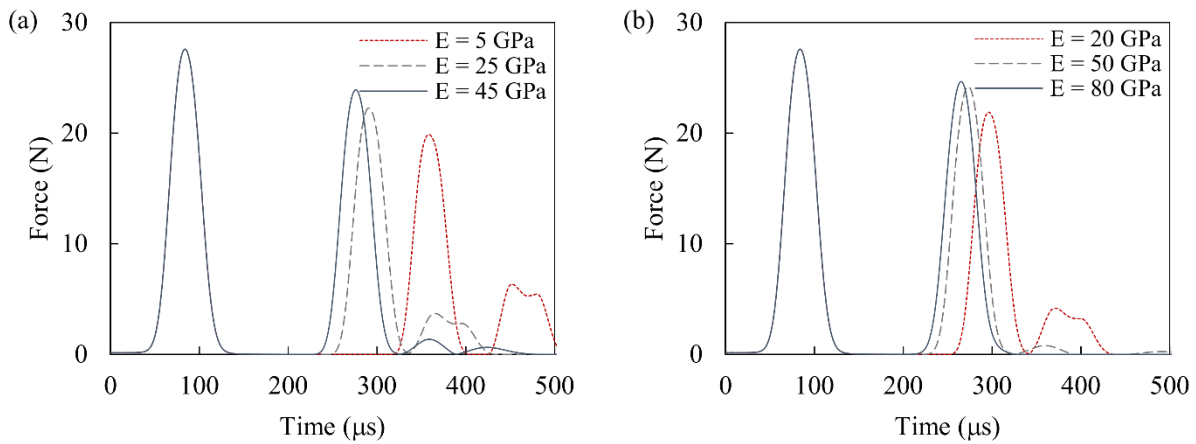


Figure 3.4 - Numerical solitary wave force profiles in a solitary wave transducer was in contact with (a) sandstone and (b) slate samples for different elastic modulus values.

Figure 3.5 presents the time of flight and the amplitude ratio of the PSW obtained from the DE and coupled DE/FE models as a function of the Young's modulus across a range of values consistent with the common geotechnical knowledge. There is an imperceptible difference between the sandstone and the slate due to differences in density and Poisson's ratio. As anticipated from Figure 3.4, the time of flight decreases, and amplitude ratio increases with the increase of the Young's modulus. Figure 3.5a shows that the slope of the curve is steeper when the rock sample is softer. Both the DE and the coupled DE/FE models predict that a slight change of Young's

modulus in the lower range of Young's modulus in sandstones results in a significant variation of solitary wave features. According to the DE model results, a small change in Young's modulus below 20 GPa induces large variation in the time of flight of the primary wave. This implies a significant sensitivity of the proposed NDT method at detecting small variations in localized stiffness of the rock. On the contrary, in the higher range of Young's modulus of slates, time of flight and amplitude ratio are not significantly affected by the variations of the Young's modulus.

Similarly, the coupled DE/FE model shows that time of flight and amplitude ratio are sensitive to the variations of Young's modulus as the Young's modulus is lower than 10 GPa. However, the variation of Young's modulus in stiffer ranges does not affect the solitary wave features. The difference between the results of the DE model and the coupled DE/FE model is because the DE model neglects the size effect of the sample and the local deformations during the particle-sample interaction. In contrast, the coupled DE/FE model considers the partial conversion of impact energy to the kinetic energy of flexural waves propagating in the sample and the strain energy due to local deformations in the sample. Therefore, the coupled DE/FE model yields to lower amplitude ratios and higher time of flight values, i.e., higher energy loss during the impacts and longer impacts.

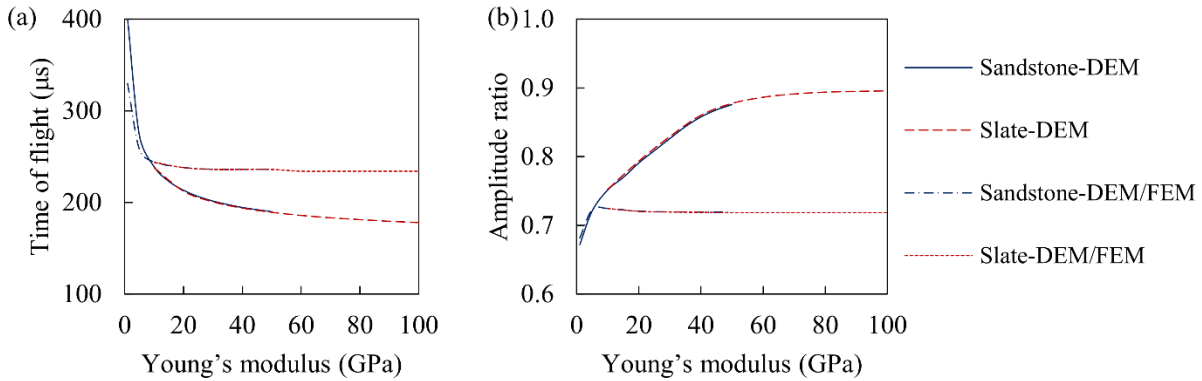


Figure 3.5 – (a) Time of flight and (b) amplitude ratio of solitary waves interacting with sandstone and slate samples as function of elastic modulus. The granular chain is composed of 9.5 mm stainless-steel particles.

Figure 3.6 shows the amplitude ratios and the corresponding time of flights for sandstone and slate samples. The labels indicate the corresponding Young's modulus in the DE model results. Graphs like this can be used to ascertain empirically the unknown Young's modulus of a geomaterial based on the amplitude ratio and the time of flight of the solitary wave test results. Figure 3.6 shows that the two solitary wave parameters are inversely proportional. In addition, soft geomaterials are typically characterized by low amplitude ratio and high time of flight, as the dynamic interaction between the last particle of the chain and the geomaterial takes a longer time and more acoustic energy is converted into the local elastic deformation of the specimen. Conversely, high amplitude ratio and low time of flight characterize stiff materials. The difference in density and Poisson's ratio between the two types of materials causes little variation at any given modulus of elasticity. The coupled DE/FE model results predict low sensitivity to variation of Young's modulus in slate and stiff sandstone samples. Furthermore, they show lower amplitude ratios at any given Young's modulus of the samples.

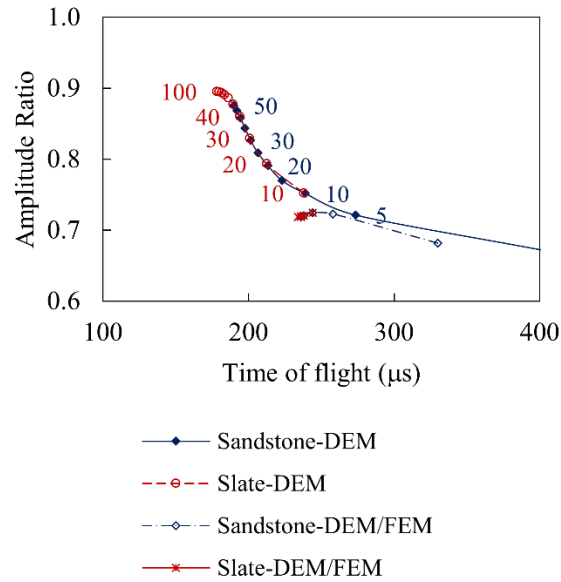


Figure 3.6 - Numerical amplitude ratio and time of flight for sandstone and slate samples. Data labels represent the corresponding elastic modulus.

3.4.2 Experimental Results

Figure 3.7 shows the time of flight (Figure 3.7a) and the amplitude ratio (Figure 3.7b) of the samples in both dry and saturated conditions. Each data point refers to the average of the seventy-three averages associated to each radial point for which ten measurements were collected. The corresponding coefficient variation (*CoV*), i.e. the ratio of the standard deviation to the mean, is shown as well. The time of flight associated with the slate samples (200 - 250 μs) is about 20% lower than the one measured in the sandstone (250 μs - 300 μs), suggesting that the slate samples were stiffer than the sandstone samples. The values are also in good agreement with the numerical predictions of Figure 3.5a. Except for sandstone 1, the dry/saturated conditions affect the experimental values of both wave parameters, but these differences are not as evident as those between the time of flight of the two different geomaterials.

Ideally, the analysis of the *CoV* may provide an indication of the isotropy of the material. Very small *CoV* suggest that the wave feature remain constant regardless the radial direction, whereas an elevated value of the *CoV* may reveal the strong dependence of the wave feature to the angle of rotation. However, **Figure 3.7** does not show a clear difference in *CoV* between the isotropic sandstone and the allegedly TI slate samples. The coefficients are approximately 3%-5% and 8%-13% for time of flights and amplitude ratios, respectively. Besides the properties of the samples, these variations could be attributed to measurement errors or slight variations in ISW amplitude, as discussed in [135].

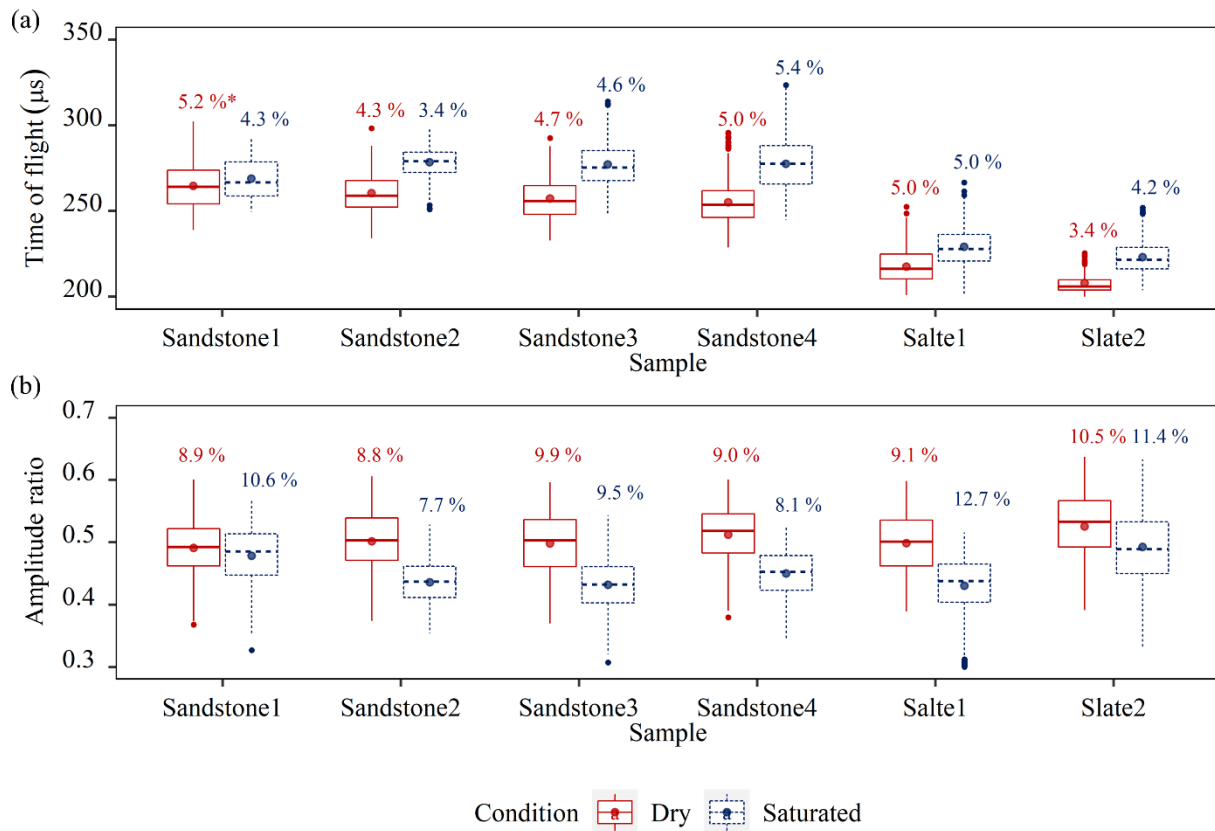


Figure 3.7 - Experimental (a) time of flight and (b) amplitude ratio in different samples and conditions.

Figure 3.7b shows that the amplitude ratios do not differ much between sandstone and slate samples. In addition, the experimental values are lower than the predicted numerical data shown in Figure 3.5b. The experimental values are likely affected with acoustic leakage between the chain and the frame supporting it, and by dissipation at the sample-chain interface. Both were not taken into account in the models, yielding to the overestimation seen in the figure.

Furthermore, Figure 3.7 shows that all the saturated samples experienced longer time of flights and lower ratios than their corresponding dry samples. This suggest that the samples stiffened once fully dry.

Figure 3.8 presents the time of flight (left column) and the amplitude ratio (right column) in polar coordinates for the dry and saturated samples. Each row presents the data obtained from 2 samples. Each data point represents the average of the ten measurements collected at each of the 73 radial points. The data are interpolated with a 4th order polynomial regression model to highlight any dependency of the wave feature on the rotation angle. The pattern relative to the time of flight of sandstone samples (Figure 3.8a and Figure 3.8c) are nearly circular with the center of the circle overlapped to the origin of the polar coordinate. The outcomes of Figure 3.8a and Figure 3.8c confirm that the isotropic nature of the sandstone did not affect the travel time of the PSW. On the other hand, Figure 3.8e shows that the fitted line has a distorted shaped and is skewed away from the origin of the polar coordinated. So, the effect of recording angle on the time of flight is significant in slate samples which are transversely isotropic materials.

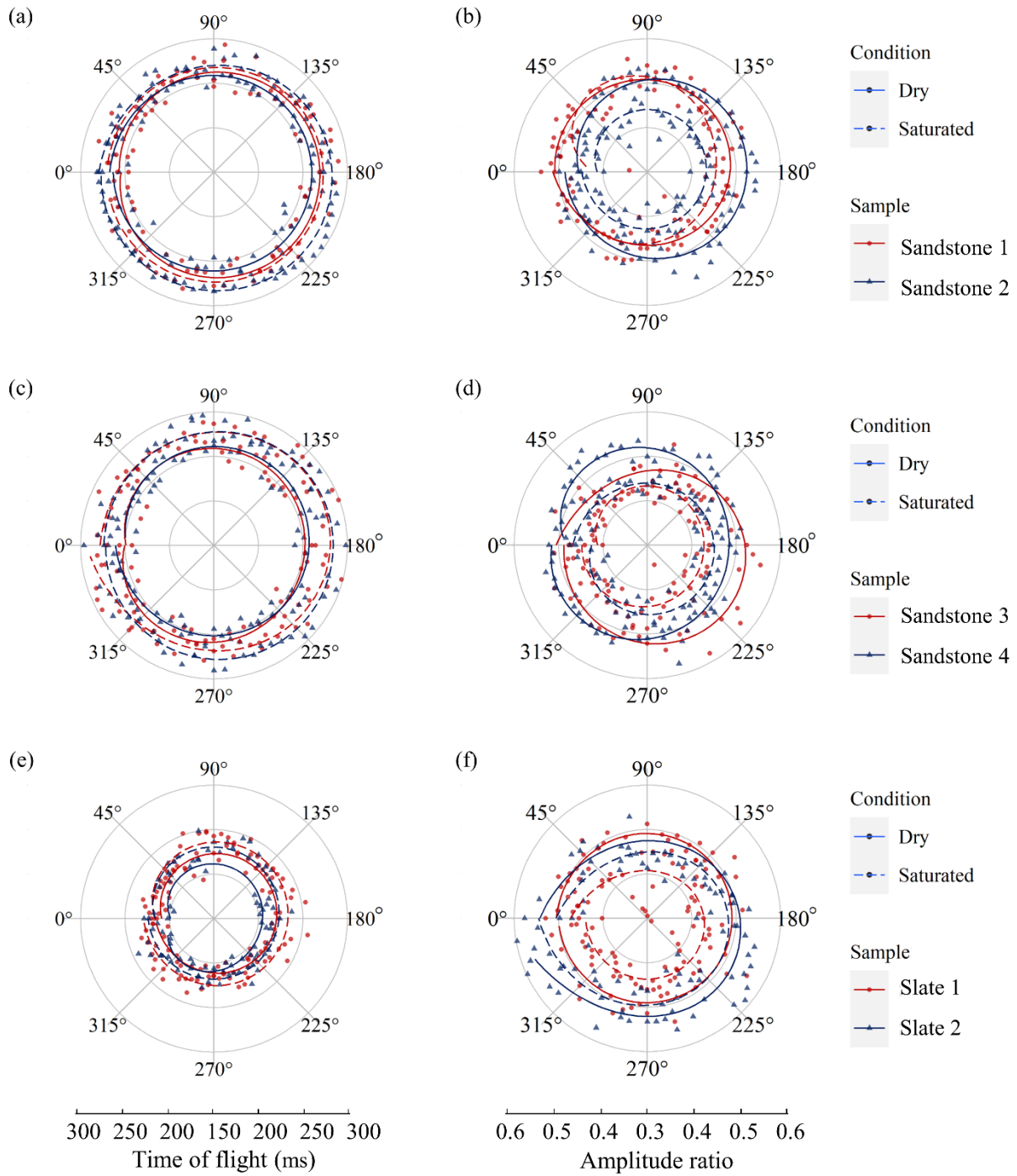


Figure 3.8 – Experimental (a, c, e) time of flight and (b, d, e) amplitude ratio at different angles around (a, b) sandstone1 and sandstone 2, (c, d) sandstone 3 and sandstone 4, and (e, f) slate1 and slate 2.

The polar graphs relative to the normalized amplitude (Figure 3.8b, Figure 3.8d, and Figure 3.8f) show a circular shape neither in sandstones nor in slates. Perhaps the variability of the experimental values, quantified in terms of the *CoV* presented in **Figure 3.7b** may have masked the effect of the angle on this solitary wave parameter. Nevertheless, there are some datapoints very close to the center of the polar graph Figure 3.8f related to slate 1. These datapoints show a low amplitude ratio of about 0.3, observed around the 45° and 225° on this sample, and they could be attributed to the weak planes in the slate sample.

3.4.3 Outlier Analysis

To further enhance the ability to identify the weak planes in TI material, a multivariate outlier detection method, based on the MSD, was implemented. This unsupervised learning algorithm establishes whether a new configuration of the system is discordant or inconsistent from the baseline configuration which consists of an existing set of data (or patterns) that describes the normal operative conditions. For each measurement set, the MSD (D_{ζ}) was calculated as:

$$D_{\zeta} = (\{x_{\zeta}\} - \{\bar{x}\})^T [K]^{-1} (\{x_{\zeta}\} - \{\bar{x}\}) \quad (3.4)$$

where $\{x_{\zeta}\}$ represents the potential outlier vector, $\{\bar{x}\}$ is the mean vector of the baseline, and $[K]$ is the covariance matrix of the baseline. In comparison to the Euclidian distance, the MSD takes into account the correlation between variables using the covariance matrix $[K]$.

Equation (3.4) resembles the equation of a hyper-ellipse centered at \bar{x} in multidimensional space. When the input vector is formed by two parameters such as the normalized amplitude and the time of flight, the concept of MSD can be used to generate confidence ellipses, such as the ones shown in Figure 3.9. Here, each point represents the average of ten measurements taken at a

specific angle in different samples and conditions. A 99.7% confidence ellipse was generated for each set of data. The ellipses are based on the assumption that the data are normally distributed and the MSD follows a χ^2 distribution. The threshold for MSD was extracted from the χ^2 distribution so that the MSD between 99.7% of the datapoints and the related centroids is smaller than the threshold. The MSD between each point positioned on the perimeter of confidence ellipses and the associated centroid is equal to the calculated threshold values. Therefore, the datapoints outside the ellipses indicate outliers whose MSD from the samples means are higher than the threshold value. The ellipses in Figure 3.9 are tilted because the time of flight and the normalized amplitude are inversely correlated. For both sandstone and slate ellipses, the baseline used to obtain the 99.7% confidence was extracted by considering the first 20° (Figure 3.9a and Figure 3.9c), 45° (Figure 3.9b and Figure 3.9d), and the first 90° (Figure 3.9e and Figure 3.9f). The graphs show that the baseline data does not affect the shape and the size of the sandstone ellipse (the blue ellipse) but significantly influences the confidence ellipse of the slate data. This demonstrates that the variance of the solitary wave features depends significantly on the range of measurement angles from TI samples.

Figure 3.9 contains a few outliers among the sandstone data and they are not located close to the extreme ends of the major axis. This small number of outliers indicates the absence of weaker/stronger planes. On the contrary, the ellipses associated with the slates and computed with baseline data within 20° and 45° show many outliers along the major axis. These outliers represent the measurements taken along the weaker planes. The red ellipses of Fig. 10c and 10f have no outliers because the baseline data (90°) is too extensive and includes data points relative to both the weak and the strong planes.

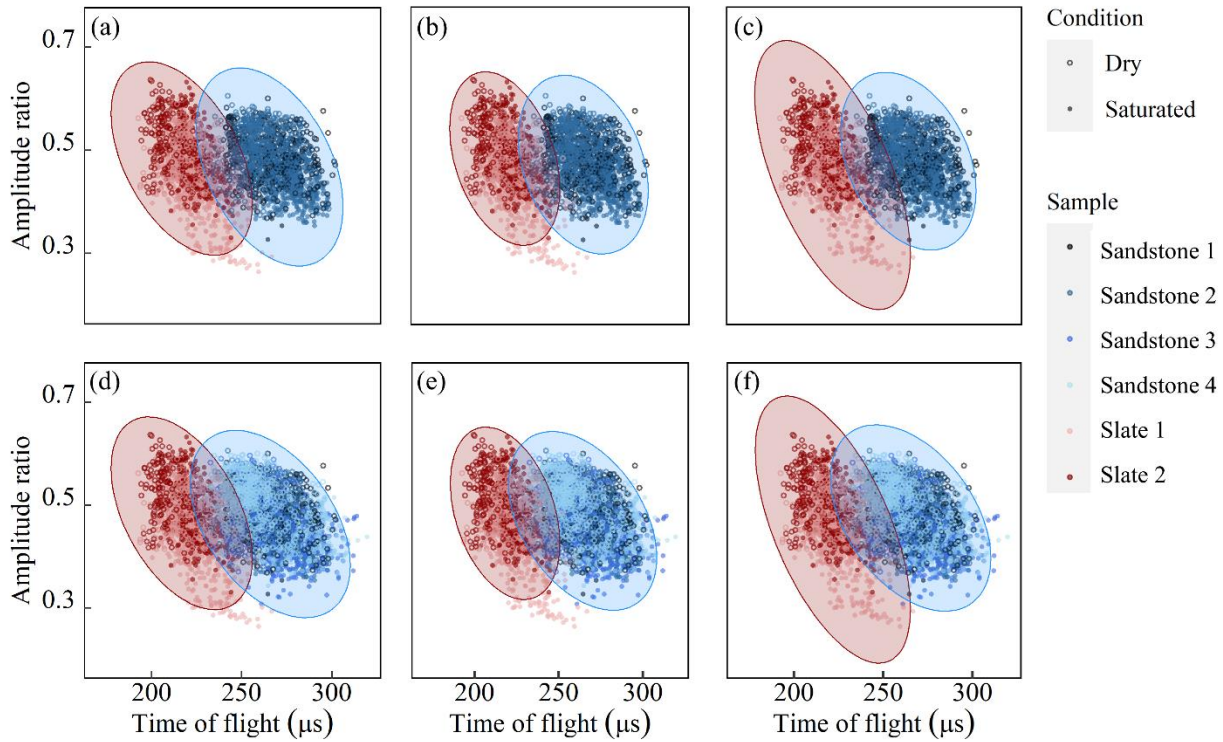


Figure 3.9 - Experimental data in the 2D amplitude ratio-time of flight space. The ellipses present the 99.7% confidence ellipse obtained based on the Mahalanobis distance (MSD), where the baseline data was the measurements taken at (a, d) the first 20°, (b, e) the first 45°, and (c, f) the first 90° around the samples. The sandstone confidence ellipses were obtained considering data related to (a, b, c) sandstones 1 and 2, and (d, e, f) all sandstones.

3.4.4 Estimating the Rocks Young's Modulus: Using Solitary Wave Features

Finally, the experimental data were used to estimate the Young's modulus of the samples by overlapping the experimental time of flight to the numerical prediction shown in Figure 3.5a. Figure 3.10a presents the numerical amplitude ratios and the corresponding time of flights for sandstone and slate samples. The square points show the experimental mean amplitude ratio and time of flight values for the samples. According to Figure 3.10a, the numerical results overestimate amplitude ratio which could be due to the underestimation of energy dissipation in the numerical

model. However, the experimental time of flights are within the range of the relative numerical predictions. Therefore, the Young's modulus of the samples was estimated based on the measured time of flights. Figure 3.10b shows the Young's modulus as a function the time of flight obtained from the numerical results in semi-logarithmic scale. The blue and red vertical lines show the mean time of flight observed empirically for the sandstones and the slates, respectively. The arrows identify the range of the estimated Young's modulus, i.e., 5 GPa and 7 GPa for the sandstone samples predicted from the coupled DE/FE model and the DE model, respectively. For the slate samples, the DE model predicts a Young's modulus of 16 GPa while the coupled DE/FE model prediction do not overlap with the related experimental results.

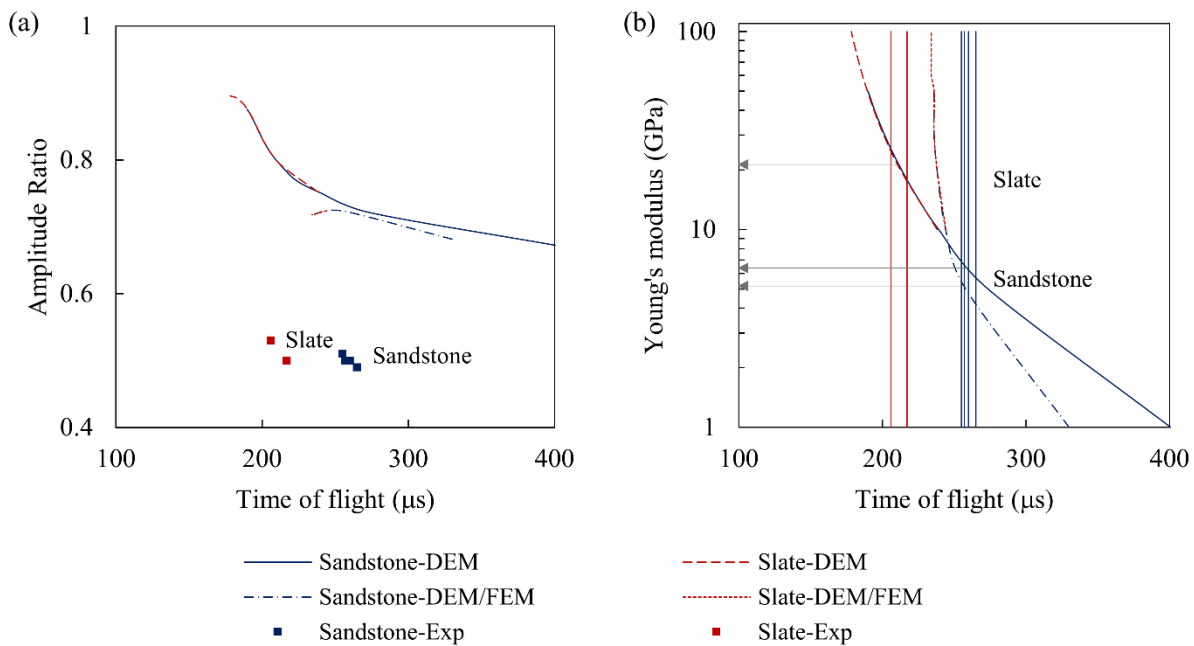


Figure 3.10 - Estimation of the modulus of elasticity of the rock samples using the numerical results.

According to [174], the Young's modulus of similar sandstone samples obtained from uniaxial compression cylindrical tests was 22 GPa. Therefore, the predicted Young's modulus values

obtained from the solitary wave method underestimate the Young's modulus of the samples. This observation is in agreement with the findings of [129] where they compared the Young's modulus of rock samples measured using ultrasonic wave velocities and solitary waves. However, the underestimation of the Young's modulus in the solitary wave-based method does not affect its effectiveness in the detection of anisotropy.

3.4.5 Parametric Study

To improve the sensitivity of the proposed NDE method in characterizing geomaterial samples, a parametric study was performed using the DE model described in section 3.2. In this study, the sensitivity to variations of the Young's modulus was investigated in granular chains composed of 9.5 mm aluminum particles and 4.8 mm steel particles. Figure 3.11 and Figure 3.12 represent the features of the solitary waves propagating in 9.5 mm aluminum and 4.8 mm steel particles and interacting with the sandstone and slate samples of different Young's modulus values. It is shown that time of flight decreases significantly over all the Youngs' modulus values in the chain made of 4.8 mm steel particles (Figure 3.13a), since the distance between the sensor disk and the inspection media is shorter in chains made of smaller particle. It is also evident that the amplitude ratio is more sensitive to the variations of the Young's modulus in the granular chains composed of 9.5 mm aluminum particles (Figure 3.11b) and 4.8 mm steel particles (Figure 3.12b) with respect to the original design, i.e., 9.5 mm steel particles (Figure 3.5b).

To further analyze the sensitivity of solitary wave features to Young's modulus variation, Figure 3.13 present a comparison of the normalized derivative of solitary wave features with respect to Young's modulus in different solitary wave transducers (studied in Figure 3.5, Figure 3.11, and Figure 3.12). According to Figure 3.13, the sensitivity of time of flight to the Young's

modulus of the inspection media is slightly higher in the solitary wave transducer made of 9.5 steel particles. On the other hand, the sensitivity of amplitude ratio to the Young's modulus variations improves significantly in the granular chains made of 9.5 mm aluminum and 4.8 mm steel particles. Overall, it can be concluded that using a solitary wave transducer made of smaller particles improves the sensitivity of solitary wave features to variation of the Young's modulus of sandstones and slates.

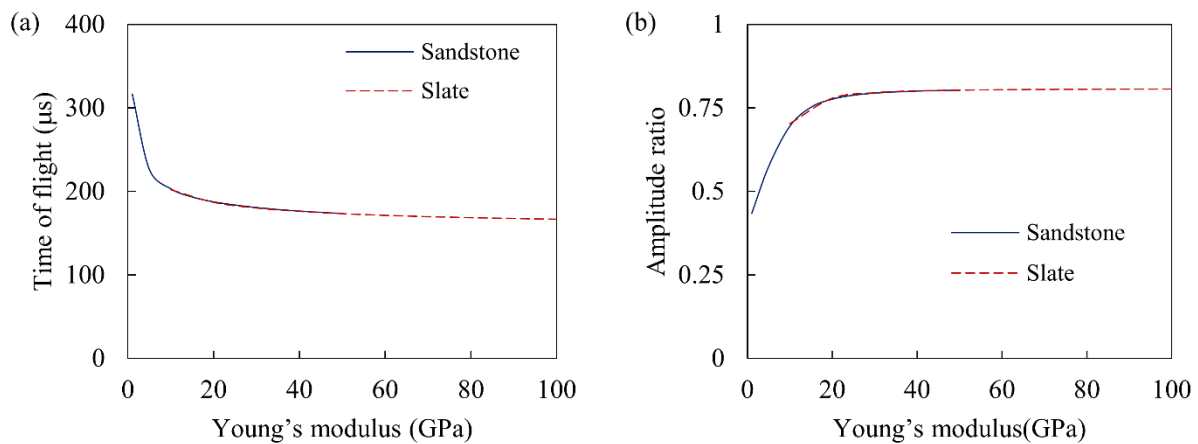


Figure 3.11 - (a) Time of flight and (b) amplitude ratio of solitary waves interacting with sandstone and slate samples as function of Young's modulus. The granular chain is composed of 9.5 mm aluminum particles.

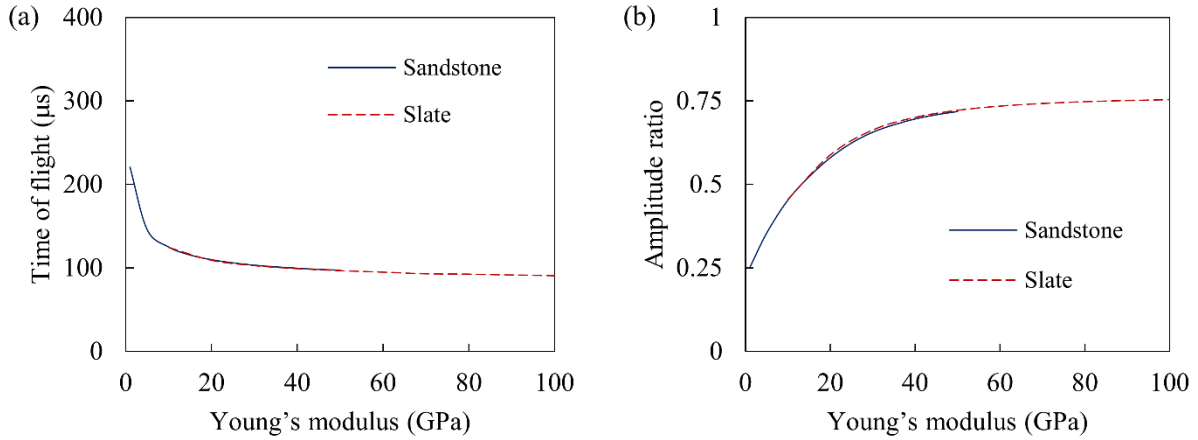


Figure 3.12 - (a) Time of flight and (b) amplitude ratio of solitary waves interacting with sandstone and slate samples as function of Young's modulus. The granular chain is composed of 4.8 mm stainless-steel particles.

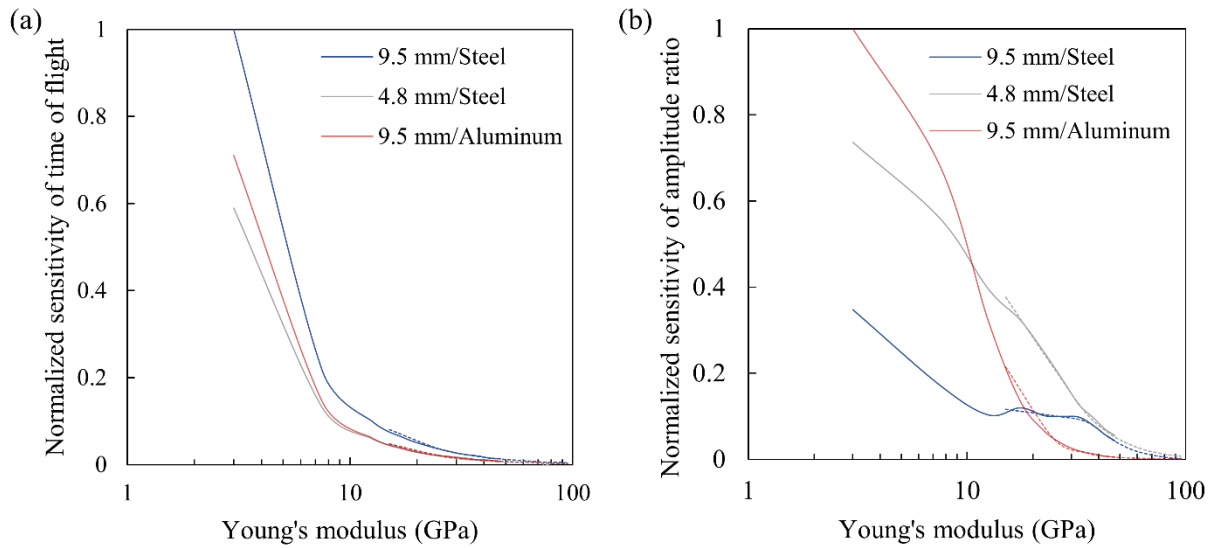


Figure 3.13 - Normalized sensitivity of (a) Time of flight and (b) amplitude ratio as function of the Young's modulus of the inspecting media in solitary wave transducers made of particles of different sizes and materials.

3.5 Conclusions

In the study presented in this chapter, an NDT technique based on the propagation and detection of solitary waves and multivariate statistics was proposed to characterize transversely isotropic geo-materials. The technique consists of the use of a special transducer designed to trigger, sustain, and sense nonlinear solitary waves that interact dynamically with the geo-material to be characterized. The recorded waveforms are then processed with multivariate statistics based on outlier analysis to identify the strongest and the weakest planes. An experimental setup was designed and implemented to demonstrate the effectiveness of the technique. The setup consists of a HNSW transducer that may embed a cylindrical sample secured to a rotary stage. At discrete radial angles, the measurement of the time-of-flight and normalized amplitude of the solitary waves was taken and input to an unsupervised learning algorithm to identify the directions of the stronger and weaker modulus. For the experiment sandstone and slate samples were considered. The study was completed with a discrete element model that depict the exact propagation of the solitary waves within the transducer, and with a discrete element model coupled to a finite element model, which takes into account the geometry and the boundary conditions of the testing samples. The numerical results associated with the time-of-flight are in good agreement with the experimental findings whereas the normalized amplitude present discrepancies likely related with dissipation and acoustic leakage, not accounted in the model.

Future studies should improve the model, test more samples of different materials, and adapt the setup to smaller samples.

4.0 The Long-term Performance of the Solitary Wave-Based Nondestructive Evaluation

In the study presented in this chapter, the long-term performance of three transducers was investigated by placing the transducers above a test object whose mechanical and geometric properties were left constant for a week while the transducers triggered and detected thousands of waves. Any variability of the waves was quantified by extracting simple features such as amplitude, time of flight, and cross-correlation coefficients. To investigate the cause of variabilities, sixteen measurements were captured with short videos at ~1,000 fps. The results of the study demonstrate that the traveling time of the solitary waves is the most reliable parameter for long-term monitoring with the lowest variability and the least susceptibility to physical changes within the array. In addition, the findings of this study allow to frame a valid strategy to improve the design of the transducers in order to make the HNSW-based technique suitable for long-term monitoring.

This chapter is written based on the following article:

Jalali, H., and Rizzo, P. “On the long-term performance of solitary wave-based transducers for nondestructive evaluation applications.” Under review in ASME Journal of Nondestructive Evaluation.

4.1 Introduction

Highly nonlinear solitary waves are lumps of acoustic energy that can propagate in nonlinear systems such as mono-periodic arrays of elastically interacting spheres, sometimes indicated as granular crystals, under zero or weak static compression [33, 120]. Compared to linear elastic waves propagating in continuous media, HNSWs present unique properties. For example, they support a high level of acoustic energy within a finite spatial wavelength of five particles diameters and their propagation speed depends nonlinearly on their amplitude [33, 178]. In addition, properties such as duration, amplitude, and speed can be tuned without electronic equipment, but by simply adding static precompression on the array or by varying the material and diameter of the particles. The tunability makes the use of HNSWs appealing in those engineering applications such as NDE and SHM.

Several studies demonstrated that the number, amplitudes, and travel time of reflected waves depend upon several factors, including the mechanical and geometric characteristics of the structure. For instance, Yang *et al.* showed numerically, analytically, and experimentally that the amplitude and the arrival time of the reflected waves from the interface of a large thin plate depend on the plate thickness, particles size, and the distance from the plate boundaries [42]. Cai *et al.* reported that the geometric and mechanical properties of a slender beam and the thermal stress applied to the beam affect the reflected solitary wave features [43]. Kim *et al.* showed numerically and experimentally that solitary waves can be used to detect delamination in a carbon fiber reinforced polymer composite plate [11]. A numerical study by Schiffer *et al.* showed that solitary waves are effective in evaluating the directional elastic parameters of composites [44]. This solitary wave-based NDE technique was proposed to assess the quality of adhesive joints [10],

monitor cement hydration [131], detect subsurface voids [133], estimate the modulus of elasticity of materials [127], infer the internal pressure of tennis balls [9, 49], just to mention a few. Recently, the authors applied the technique to monitor localized corrosion in steel plates [135, 136]. They showed numerically and experimentally that the amplitude and the time of flight of the reflected solitary waves at the interface between the chain and the plate are dependent on the presence of corrosion.

The assembly of the 1-D array shown in Figure 4.1 embraced by a rigid frame, surmounted by an electromagnet designed to lift and release the top particle (the striker), and completed by a sensing element within an array, can be denoted as the solitary-wave based transducer, hereinafter simply the transducer. The effectiveness of the design of this transducer was proven by Rizzo and collaborators in several NDE/SHM based applications [9, 49, 51, 135, 136, 179], and was recently augmented by the development of a wireless module that enables the remote implementation of the method [180]. However, the long-term performance in terms of repeatability and sensitivity of the transducer was never investigated. To fill this gap, the scope of the study presented in this chapter is to examine long-term repeatability. Three transducers were assembled and placed in contact with a bilayer system made of metallic plate and an optical table. The transducers were activated continuously for nearly a week during which over 4,000 measurements were taken. To investigate any variability intrinsic to the design of the transducers, the characteristics of the plate were left identical. In addition, a few measurements were observed with the aid of two high-speed cameras operating at 960 fps. The videos were processed using computer vision techniques to identify possible vibration/tilting in the components that might affect the repeatability of the measurements. The findings of the study will help the future development of transducers for NDE and SHM applications based on solitary waves.

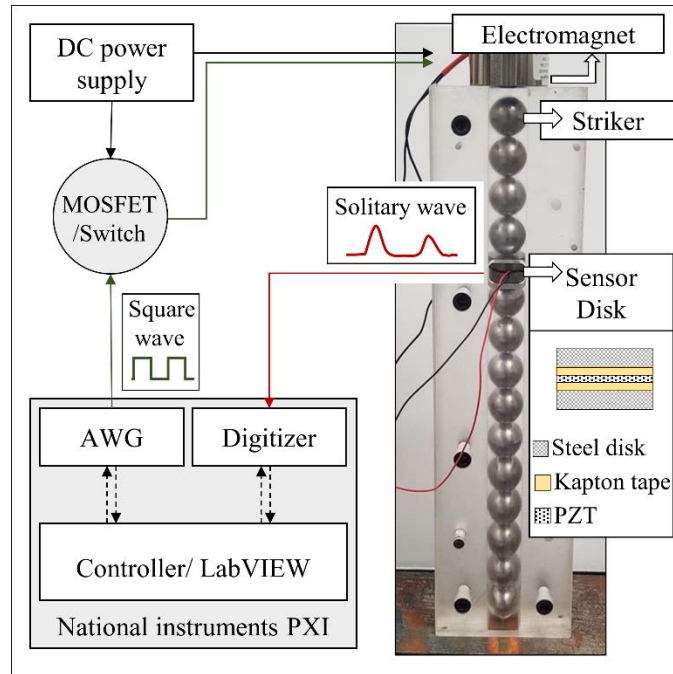


Figure 4.1 – Schematics and photo of the solitary wave transducer for NDE/SHM applications.

This chapter is organized as follows. Section 4.2 presents the setup of the experiment. Section 4.3 describes the discrete element modeling, developed by the authors, to predict the characteristics of solitary waves in monoperiodic arrays of particles of any size and any material. Section 4.4 describes the algorithms implemented to process the high-speed videos collected during the experiments. Section 4.5 discusses the results of the experiment and compares them to the numerical prediction. Section 4.6 ends the chapter with some concluding remarks and suggestions for refining the design of the transducers.

4.2 Experimental Setup

Three identical solitary wave transducers, T1, T2, and T3 were assembled in laboratory. They are shown in Figure 4.2. Each transducer contained 14 spheres, 1 sensor disk, and a commercial electromagnet. The steel spheres were 19.05 mm in diameter, and 28.2 g in mass. The electromagnet was placed 4 mm above the ferromagnetic striker. Each sensor disk was the assembly of a lead zirconate titanate (PZT) wafer in between two 19.05 mm diameter, 6.05 mm thick stainless-steel disks. The PZT was insulated from the metal using Kapton tape. The mass of each disk was 29 g (in T1 and T3) and 30 g (in T2). As noted in past studies, particles with different mass than the beads of the array give rise to spurious pulses and reflections that may be detrimental for NDE applications.

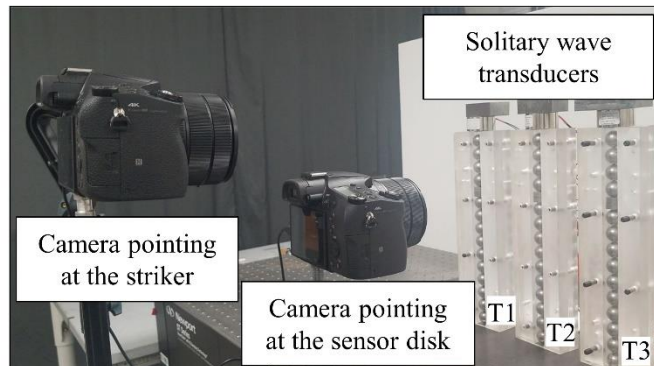


Figure 4.2 – Photo of the experimental setup in which two high-speed cameras pointed at the striker and the sensor disk of transducer T2.

A National Instruments PXI running under LabView was used to control the transducers. The function generator of the PXI sent square waves to a MOSFET also connected to a DC power supply. The MOSFET acted as a switch to power the electromagnet at intervals selected by the

user. When active, the electromagnet lifted the striker that was then released once the electromagnet was powered off. The free fall of the striker caused the mechanical impact that triggered the generation of the incident wave. The ISW propagated through the chain, interacted with the semi-bulky material in point contact with the chain and was reflected back. Both the ISW and the PSW were detected by the sensor disk positioned five particles away from the top of the chain. The disk was connected to the digitizer of the PXI. The waves were digitized and stored at a sampling rate of 8 MHz.

The three transducers were positioned on a $609.6 \text{ mm} \times 609.6 \text{ mm} \times 6.3 \text{ mm}$ steel plate, located above an optical table. The plate was monitored continuously for nearly a week. Ten measurements were taken every 20 minutes for a total of 4320 measurements. Shorter intervals would have been possible. However, the commercial electromagnets could have suffered from overheating. As the plate was not subjected to any type of damage, the setup was instrumental to study the long-term performance of the transducers.

The experimental setup was completed with two high-speed cameras operating at 960 fps. The cameras were pointed at the striker and at the sensor disk of transducer T2, respectively, as shown in Figure 4.2. The primary scope was to observe the physical movement of the striker and to detect any oscillation of the sensor disk. Sixteen strikes were recorded using a remote shutter.

4.3 Discrete Element Modeling

To interpret the experimental results, a discrete element model previously discussed in section 2.2.1 was used. The model simulates the propagation of solitary waves in granular chains and their

interactions with adjacent media. The granular chain was simulated as a series of point masses connected by nonlinear axial connectors. The connectors were defined based on the Hertzian contact law. Energy dissipation was introduced in the model with different dissipation coefficients. The impact of the striker was simulated by setting the initial velocity v_0 of the first particle to a value equal to $v_0 = (2gh)^{1/2}$, where g is the gravity and $h = 4$ mm. The dynamic response of the system was obtained by solving the nonlinear equations of motion in MATLAB using the solver ode45. The solitary wave profile at the sensor particle was obtained by averaging the interaction forces between the sensor particle and its adjacent particles.

4.4 Video Processing

The motion of the striker and the sensor disk embedded in T2 was analyzed using two video processing algorithms implemented in MATLAB. The flowchart of the two algorithms is shown in Figure 4.3 and Figure 4.4, respectively. For the striker (Figure 4.3), each video was fragmented into individual frames. Each frame was de-noised with the Wiener filter [181] using a function embedded in MATLAB. Figure 4.5 shows the noise reduction in one video frame using the Wiener filter with different Gaussian noise variances (σ). Then, object tracking was performed by detecting the two brightest areas of the striker using the image intensity thresholding. These brightest areas are shown with red circles in Figure 4.3 and they are the reflections of the light used to illuminate T2. The centroid of the two areas was found in each frame and tracked.

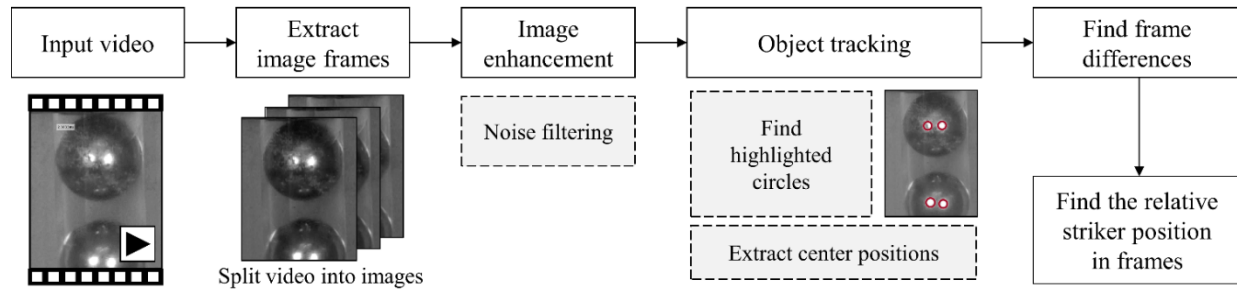


Figure 4.3 – Video processing algorithm used to track the striker.

For the sensor disk (Figure 4.4), each video was fragmented into individual frames and each frame was rotated 3° clockwise to adjust the image orientation. The motion of the disk was tracked using the Canny edge detection technique [182], also embedded in MATLAB. The results of the application of Canny edge detection to a frame are presented in Figure 4.4. Then, the horizontal sensor edges were extracted (shown in red color in Figure 4.4) and the sensor center line was detected as the middle line passing through the sensor horizontal edges. Using this algorithm, the position of the sensor center was found in each image frame and sensor relative position was obtained by finding the differences between subsequent frames.

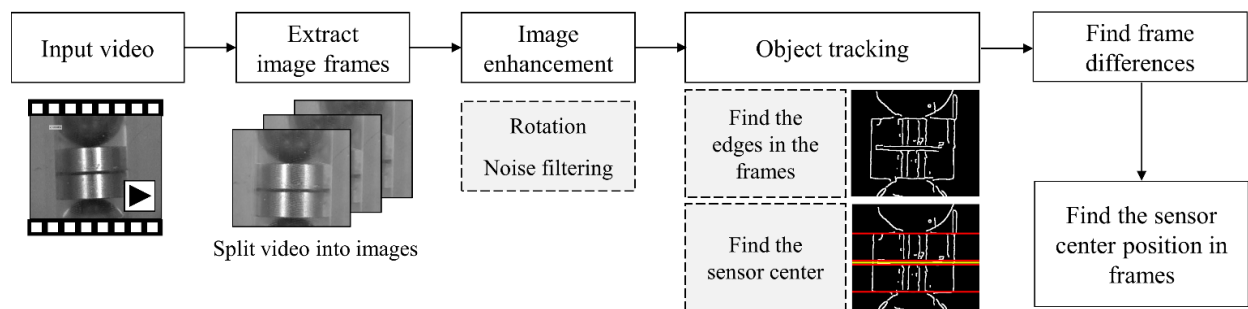


Figure 4.4 - Video processing algorithm used to detect the vibration of the sensor disk.

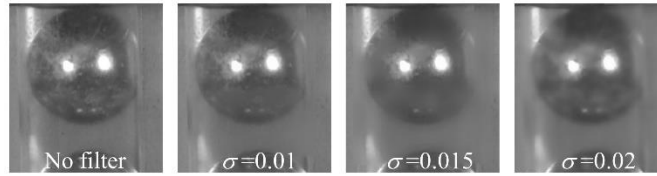


Figure 4.5 – Image noise reduction using the Wiener filter with different Gaussian noise variances (σ).

4.5 Results and Discussion

4.5.1 Repeatability: Analyzing the 6-day Test Results

Figure 4.6 presents the mean of all the 4320 solitary waves recorded by each transducer. The incident and the reflected waves are clearly visible. The peak amplitude of the ISW was 4.97 V, 4.73 V, and 4.24 V, for T1, T2, and T3, respectively, which means that the amplitude of T3 was about 17% higher than T1. These discrepancies have many concurrent causes: slight differences in the falling height of the striker, energy loss due to the friction with the inner wall, different dielectric constants of the PZTs, differences in the manual assembly of the disks, and slight rotation of the disk with respect to the longitudinal direction of the wave. As most, if not all, of these causes are hard to be controlled manually, the outcome is that the amplitude of the waves cannot be considered as is as a damage-sensitive feature for NDE/SHM applications, but normalization is suggested.

Figure 4.6a shows a negative voltage spike trailing the incident wave. Although its origin is unclear, it could be related by a temporary lack of static compression on the PZT, or a flaw in the assembly of the sensor disk. In all three transducers, the ISW is trailed by a small hump, which is

caused by the Hertzian contact between the spherical particle and the disk-shaped sensor. The discrete modeling results show that this small pulse is the result of the rebound between the sensor disk and the adjacent particles as the contact stiffness between the sensor disk and the adjacent spheres is higher than the contact stiffness between two spheres. Therefore, the solitary wave propagation speed locally increases at the sensor disk. As the ISW passes through the sensor disk and arrives at the next particle, the disk and the particle separate, yielding to a momentary zero interaction force at the sensor disk. Then, owing to its higher momentum, the sensor disk strikes the following particle again, yielding to the small hump.

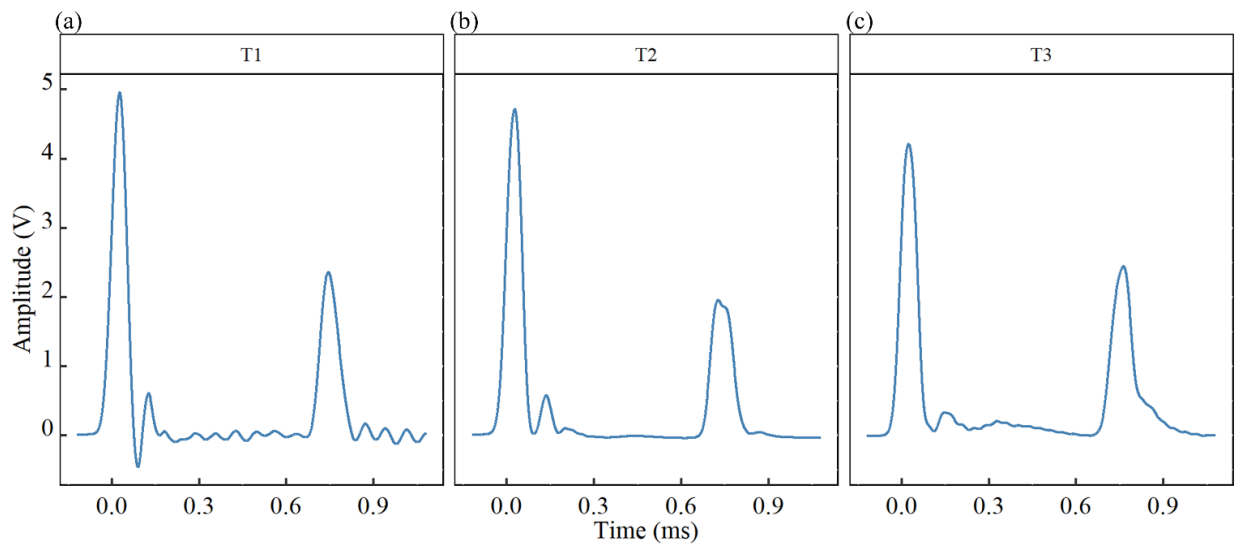


Figure 4.6 – Experimental time waveforms obtained by averaging the single waveforms collected throughout the whole experiment. (a) Transducer 1. (b) Transducer 2. (c) Transducer 3.

The amplitude of the reflected wave was also not the same across the three transducers. Besides the reasons mentioned for the striker, the variations seen for the PSW are to be attributed to small variations of the boundary conditions under the plate, i.e. around the point of contact between the chain and the plate.

Owing to the variabilities detected with Figure 4.6, it is important to identify features that prove to be independent from transducer-to-transducer difference and dependent only on the mechanical and geometric properties of the structure to be inspected or monitored over time. Four wave characteristics were considered, namely the amplitude of the incident wave, the time of flight, the normalized amplitude, and the correlation coefficient. The time of flight is the time delay at the sensor disk between the incident and the reflected wave. The normalized amplitude, hereinafter referred to as the amplitude ratio, is the ratio between the amplitude of the reflected wave to the amplitude of the incident wave. Finally, the correlation coefficient, defined as [183]

$$r = \frac{\sum_i (x_i - \bar{x})(y_i - \bar{y})}{\sqrt{\sum_i (x_i - \bar{x})^2 \sum_i (y_i - \bar{y})^2}} \quad (4.1)$$

measures the similarity between two time-waveforms, one of which is a reference signal. In Eq. (4.1), x_i and y_i are the i^{th} values of the two signals, and \bar{x} and \bar{y} are the mean value of the two signals. The correlation coefficient is equal to 1 if the two signals are identical, 0 if they are completely uncorrelated, and -1 if they are anti-correlated. In addition, the ISW correlation coefficient and the PSW correlation coefficients were determined by comparing segments of signals that isolate the ISW and the PSW.

Figure 4.7 presents the values of the features extracted for each transducer. Each data point represents the average of the 10 recordings collected every 20 minutes. Overall, the features do not show any trend in agreement with the fact that the properties of the plate remained constant. The following additional considerations can be made. The amplitude of the ISW varied visibly within the same transducer as much as 25% (T1). The time of flight is the most repeatable feature, and the coefficient of variation is comprised between 2% and 3%. As the time of flight has the least variability, it can be considered the most reliable parameter for solitary wave-based NDE applications. The values of the amplitude ratio within each transducer are scattered and the

associated coefficient of variation ranges between 12% and 13%. Such variation is caused by the random occurrence of twin reflected solitary waves, as will be discussed later in section 5.3. According to [9], the twin reflected solitary waves could be caused by low static pre-compression in the chain. Striker motions and sensor vibrations could also be the contributing factors in the variations of the amplitude of the incident wave. For the correlation coefficients, the analysis of the whole-time waveforms and the analysis of the individual pulses, i.e. ISW and PSW, were carried out. The coefficient related with the whole waveforms spanned between 0.8 and 1. The range is much narrower when the individual pulses were considered. The incident wave remained nearly identical in shape throughout the experiment, whereas the coefficient of the reflected wave was as low as 0.9 when a twin wave was generated at the interface. For instance, the lower PSW correlation coefficients obtained from the second transducer between 70 hours and 100 hours after the start of the test are associated with twin PSWs.

The average value of the time of flight, amplitude ratio, and correlation coefficients relative to each transducer is presented in Table 4.1. Transducers 1 and 2 are very similar to each other whereas transducer 3 had slightly higher average time of flight and amplitude ratio values. As discussed earlier, such small discrepancy can be attributed to different energy losses due to friction with the frames or other assembly differences that are difficult to control. Table 4.1 shows that the average ISW correlation coefficient was higher than 0.995 for all the transducers, showing the repeatability of the generated ISWs over the experiment.

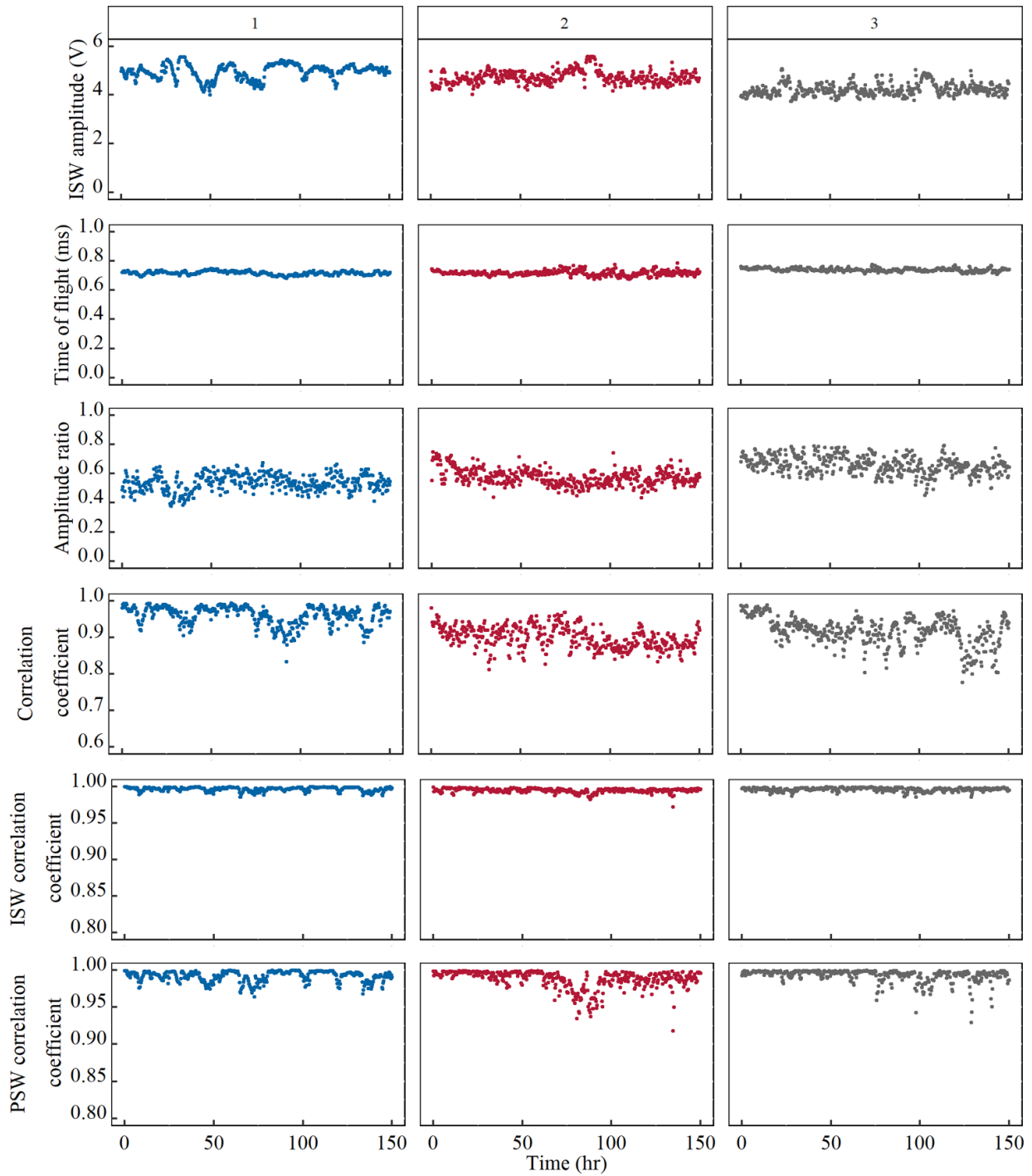


Figure 4.7 – The solitary wave features extracted from the time-waveforms recorded with the sensor disk. Each dot represents the average value of the ten measurements collected every 20 minutes. (Left column) Transducer 1. (Center column) Transducer 2. (Right column) Transducer 3.

Table 4.1– Time waveforms analysis. Average value of the time of flight, amplitude ratio, correlation coefficient, ISW correlation coefficient, and PSW correlation coefficient associated with the three solitary wave transducers.

Transducer	Time of flight (ms)	Amplitude ratio	Correlation coefficient	ISW correlation coefficient	PSW correlation coefficient
1	0.720	0.54	0.961	0.997	0.992
2	0.720	0.58	0.901	0.995	0.988
3	0.737	0.66	0.917	0.996	0.993

4.5.2 Estimating the Plate Young’s Modulus: Using Solitary Wave Features

To explain how the technology could be used for the noninvasive characterization of materials, this section describes the approach to estimate the elastic modulus of the plate using the experimental data discussed in the previous section. First, a model of the setup was created using the discrete element model presented in section 4.3. The plate placed on an optical table was assumed to behave as a semi-infinite solid. Noteworthy the model is not strictly accurate, as the transducers sit on a bi-layer system one of which has a rectangular grid of tapped holes. The density and the Poisson’s ratio of the body were assumed to be equal to 7800 kg/m^3 and 0.3, respectively. The solitary wave features were obtained for different values of the Young modulus, which is the main factor affecting the solitary wave features [127].

Figure 4.8 presents the numerically predicted relationship between the elastic modulus and the time of flight. Six cases were modeled. Three models (Figure 4.8a) assume a 4 mm free-fall of the striker and dissipation coefficients equal to 0, 4.5 N·m/s, and 25 N·m/s. The remaining models (Figure 4.8b) considered three falling heights, namely 4 mm, 4.5 mm, and 5 mm with the dissipation coefficient equal to 4.5 N/m·s. The vertical lines overlapped to Figure 4.8 identifies the experimental average time of flight presented in Table 4.1, namely 0.720 ms (transducers 1

and 2) and 0.737 ms (transducer 3). Both figures demonstrate that the time of flight increases as the Young's modulus of the material to be characterized becomes softer. This occurs because the acoustic energy carried by the solitary pulse increases the deformation of the material surface, delaying the rebound of the pulse. The gradient of the curves is steeper for stiffer materials, for which a small change of the time of flight yields to a large change of the predicted modulus. As such, the characterization of stiff materials requires an accurate model and an accurate instrument, because small errors in the measurements may yield to large error in the estimation of the elastic modulus. Figure 4.8a shows that at a given Young's modulus, the time of flight is directly proportional to the energy dissipation consistent with the fact that weaker incident wave travels at lower speed. However, the effect of dissipation on the time of flight seems to be small. On the contrary, Figure 4.8b demonstrates that small differences in the free fall of the striker have a significant effect on the prediction of the elastic modulus, especially for stiff materials. For example, when the recorded time of flight is 0.737 ms, the elastic modulus associated with the 4 mm falling height is about 100 GPa, but it doubles if the falling height was 5 mm. Figure 4.8b shows that larger fall induces faster waves in agreement with the fact that stronger impacts induce higher amplitudes and therefore faster waves.

Under the reasonable assumption that the dissipation was absent or small, the measurement performed with T3 yields to an estimated Young's modulus equal to ~ 200 GPa, whereas the estimation performed with T1 and T2 does not match the numerical estimations. Despite 0.737 ms is only 2% higher than 0.720 ms, the difference in the estimation of the modulus is quite significant. To overcome such limitation, the diameter and the material of the particles should be modified in order to shift the gradient of the curves. Assuming that striker falling height was 5 mm in transducers 1 and 2 yields to an estimated Young's modulus equal to ~ 220 GPa. Therefore, the

lower average time of flight and higher ISW amplitude in transducer 1 and 2 could be caused by a higher striker falling height due to a flaw in manufacturing or assembly of those transducers.

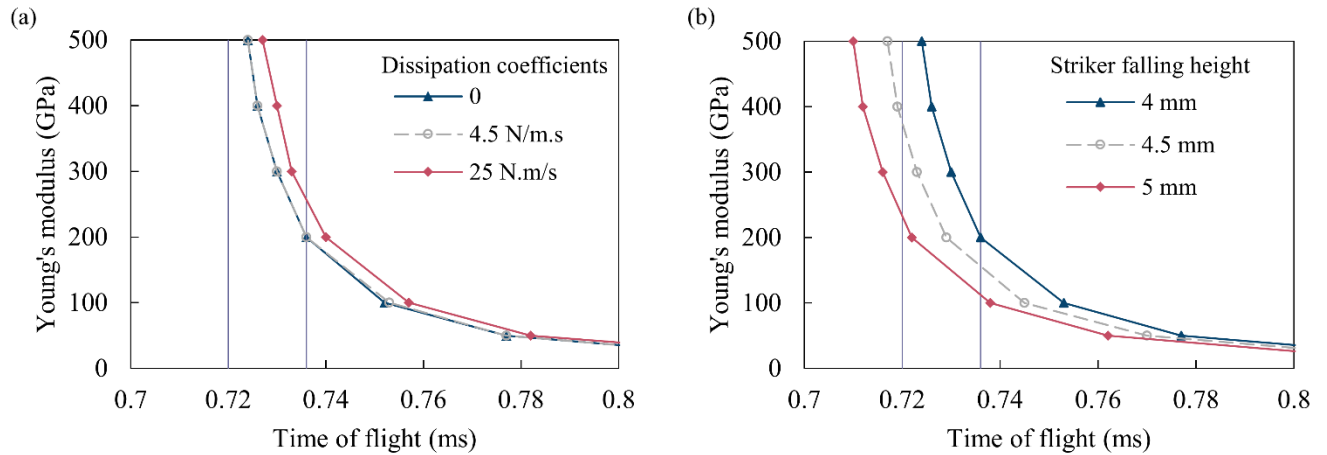


Figure 4.8 – Numerical relationship between the elastic modulus of the plate modeled as a semi-bulky material and the time of flight associated with the primary reflected wave. (a) Striker fall equal to 4 mm and different dissipation coefficients. (b) Dissipation coefficient equal to 4.5 N/m.s and different striker falling heights.

4.5.3 Video Processing Results

To gain more insights about the dynamics associated with the generation and detection of HNSWs, 16 solitary wave strikes were randomly recorded with the two high-speed cameras and processed with the two video processing techniques discussed in section 4.4. First, Figure 4.9 presents the ISW amplitude, time of flight, and normalized ratio measured from the time waveforms associated with those 16 events. The amplitude of the ISW varied between 4.2 V and 5.1 V, the time of flight varied between 0.707 ms and 0.737 ms, and the normalized amplitude spanned from 0.53 to 0.74. The observations agree with what discussed in section 4.5.1. To investigate the step between strikes #7 and #8, which occurred about three hours apart. Figure 4.17

shows the associated time waveforms. The shape of the two ISWs is identical but the peak amplitude of strike #8 is about 15% higher. The two PSWs are instead different in shape and therefore also in amplitude.

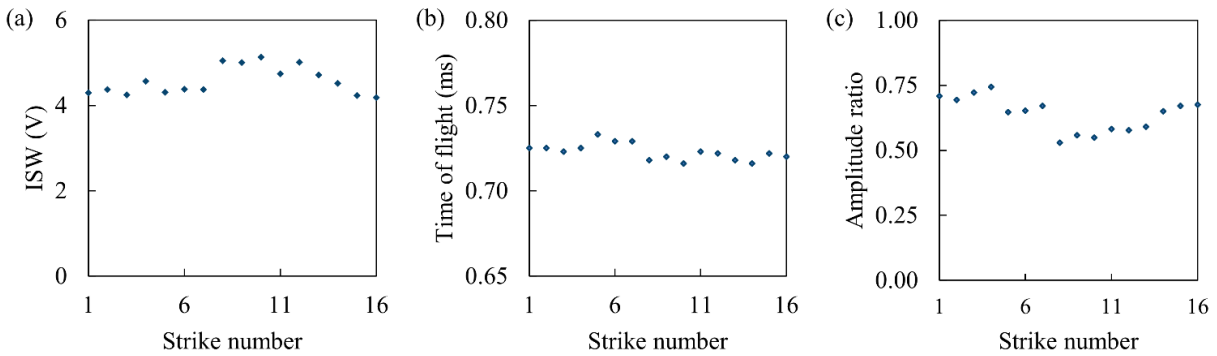


Figure 4.9 – Analysis of the sixteen videos collected with the two high-speed cameras. Solitary wave features extracted from the time waveforms collected with the sensor disk. (a) Peak amplitude of the incident wave, (b) time of flight associated with the primary reflected wave, and (c) normalized amplitude of the reflected wave.

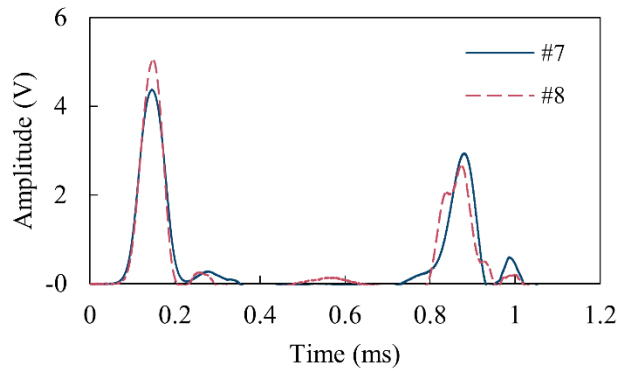


Figure 4.10 - Time waveforms measured by the sensor disk associated with strikes number 7 and 8.

Figure 4.11 shows five frames relative to one of the 16 strikes. The position of the striker is shown at different positions, labeled with the parameter h . The value equal to 1 identifies the striker in contact with the electromagnet (Figure 4.11a). The value equal to 0 represents the striker in contact with the second particle of the chain (Figure 4.11e). The bright areas circled in red were detected by the image intensity thresholding. The horizontal line passing through the center of the circles were used to determine the relative height of the striker. The positions $h = 1$ and $h = 0$ were 72 pixels apart and given that the striker fall was 4 mm, the camera resolution is 18 pixels per mm, equivalent to $56 \mu\text{m}$. As the frame rate of the cameras was 960 fps, the time intervals between the video frames are almost 1 ms. It can be shown that the maximum striker displacement between the video frames which could be missed due to the frame rate limitations is less than $150 \mu\text{m}$.

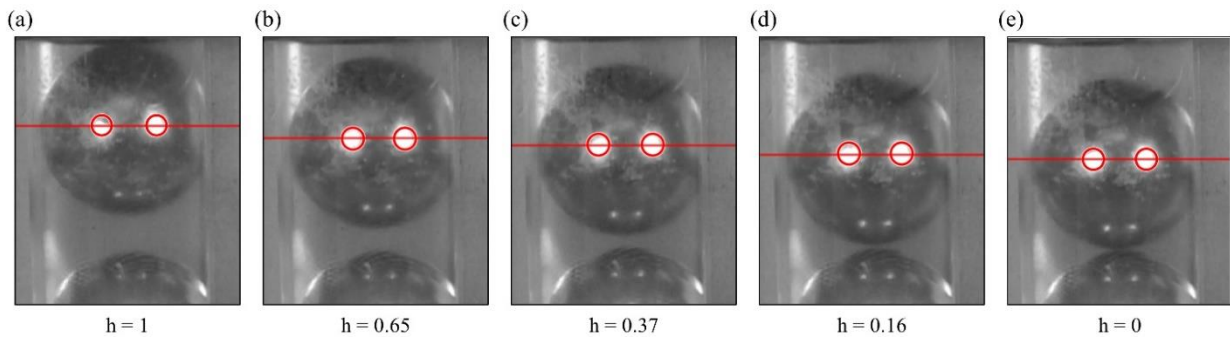


Figure 4.11 – Snapshots relative to one of the sixteen frames. The value of h indicates the relative position of the striker.

Figure 4.12a shows h as a function of time. The duration of the first fall was about 28 ms, equivalent to the time necessary to a body to fall from a height of 4 mm. The figure reveals that the striker hit the chain about five times, and the time interval between the first and the second hit was about 36 ms, which is much longer than the time interval necessary to observe the propagation

of the solitary waves. This implies that the second impact does not interfere with the propagation of solitary waves that is used for NDE and SHM applications. A close-up view of Figure 4.12a is presented in Figure 4.12b and shows that the first impact of the striker with the second particle of the chain did not occur at the same time. This is because the camera were manually activated with a remote shutter whereas the electromagnet was controlled by the PXI. Figure 4.12b shows also that apparently some impacts never occurred, i.e. there are no data points with $h = 0$. This is because the impact occurred in between two consecutive frames, which are about 1 ms apart. The curve relative to strikes #7 and #8 are presented in Figure 4.12c. Surprisingly, the two graphs are quite similar and therefore unable to shed light about the reasons for the differences noted in Figure 4.9 and Figure 4.10.

To investigate a relationship between the amplitude of the incident wave and the strength of the impact, the peak amplitude of the ISW is plotted against the normalized height h (Figure 4.13a) and the effective distance between the striker and the second particle of the chain (Figure 4.13b). The labels indicate the strike number while the dashed line represent a linear regression fit. Overall, the amplitude of the ISW is proportional to the height of the first rebound. However, such dependence is not as evident as expected. As a matter of fact, a close-up view of the graph shows that the strike with the highest amplitude (strike #10) did not correspond with the highest rebound. Conversely, one of the lowest rebound heights (strike #13) did not correspond to one of the lowest wave amplitudes. The reasons associated with such discrepancies are unclear and only in part can be associated with the resolution of the videos, for which each pixel represents $56 \mu\text{m}$, equivalent to 0.014 relative rebound height.

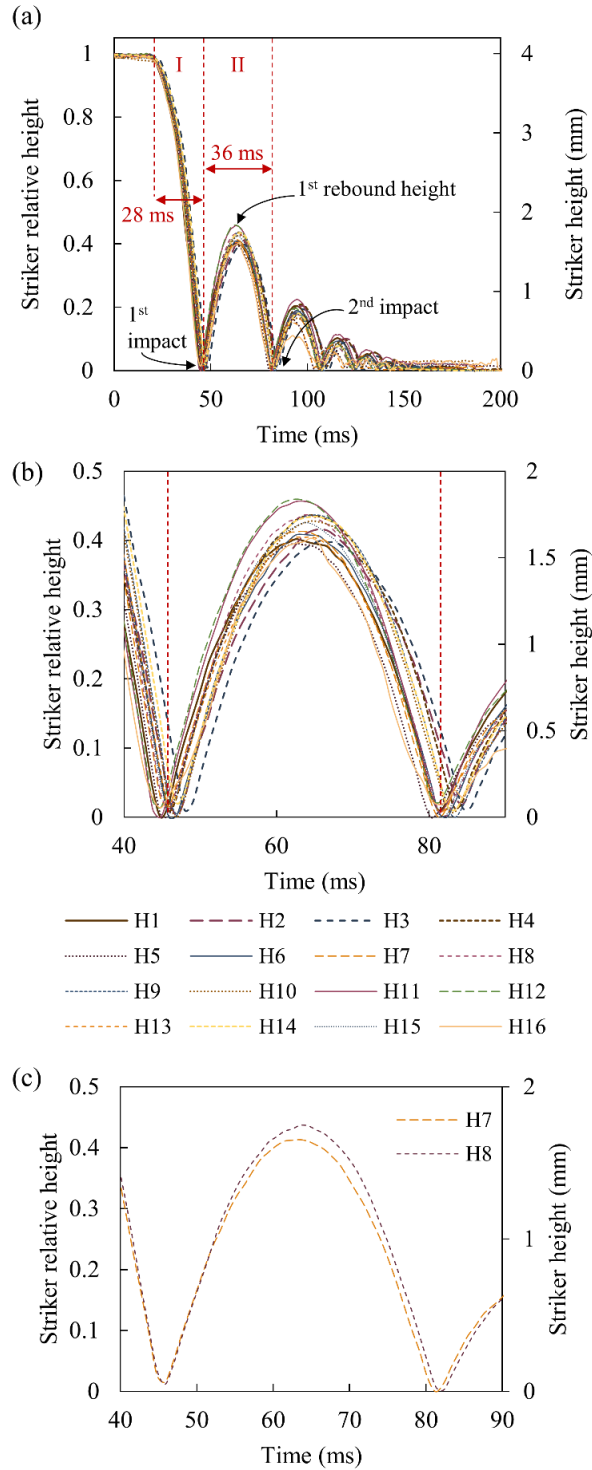


Figure 4.12 – Video processing analysis of the striker motion. (a) Vertical position of the striker for all 16 strikes for the whole duration of the motion. (b) Close-up view of the motion relative to the first and the second impacts on the chain. (c) As of (b) but relative to strikes #7 and #8.

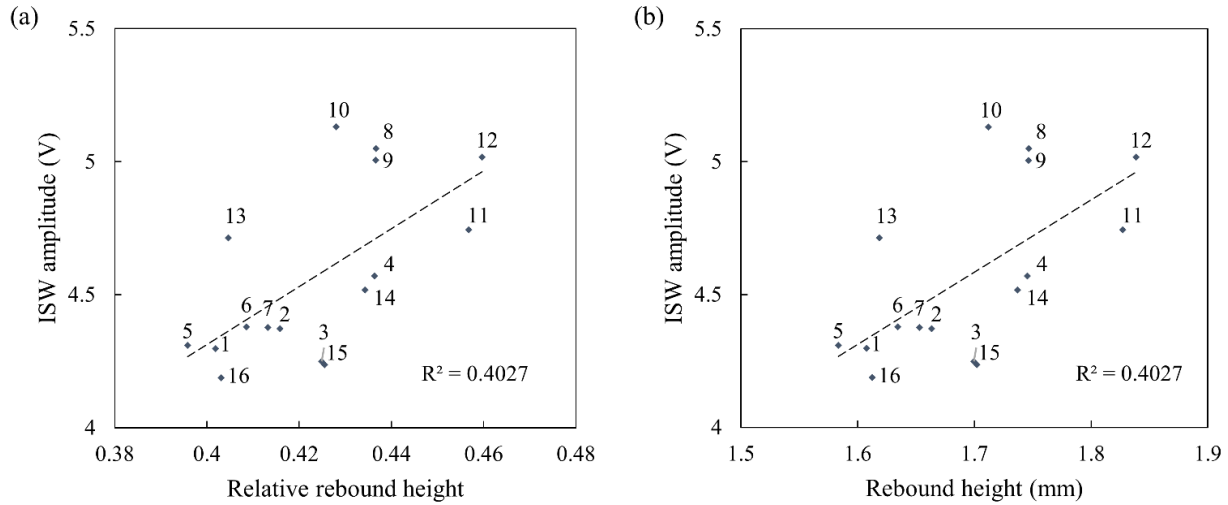


Figure 4.13 – Video processing analysis of the striker motion. Peak amplitude of the incident wave recorded with the sensor disk and the corresponding (a) relative rebound height, (b) rebound height.

In order to investigate the dynamic response of the sensor disk, the edges of the disk (Figure 4.14) were tracked during the analysis of each frame. The top and the bottom edge of the disk, shown with red lines, were 273 pixels apart. As the sensor disk (composed of two steel disks, PZT, and Kapton tape) was about 12.4 mm thick, the video resolution was about 22 pixels/mm, i.e., each pixel was 45 μm . The sensor center line in each frame was also obtained by finding the middle horizontal line passing through the detected sensor edges. The analysis unveiled that the disk rolled as much as 4 pixels, equivalent to 0.180 mm, whereas there was no evidence of pitch motion.

The left column of Figure 4.15 presents a waterfall chart of the rolling vibration in the 16 recorded videos. The oscillations occurred between 50 ms and 150 ms consistent with what observed in Figure 4.12. Interestingly, the oscillations seems to have started a few milliseconds after the impact of the striker. As the recordings were started manually, the start of the oscillation varied slightly. The right column of Figure 4.15 presents the time waveforms of different strikes H7, H8, and H10. The peak-to-peak amplitude of the three strikes are different, as well as their

arrival. The latter may be caused by asynchronization from strike to strike although we may not exclude that the oscillations are not strictly triggered by the crossing of the solitary wave but rather to a general vibration of the whole transducer generated by the impact of the striker. A cross-comparison between these waveforms and Figure 4.13 shows that the largest peak-to-peak amplitude (H10) does correspond to the highest ISW amplitude but not the highest rebound height. It is shown that the magnitude of the sensor vibrations varies in different solitary wave incidences. Despite the rebound heights of the striker for H7 and H8 are nearly identical, and therefore it can be assumed that the impact force was nearly the same, the oscillation of the sensor disk for the same event are quite different.

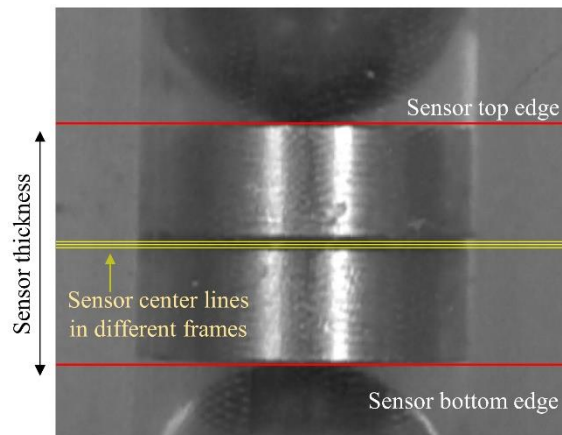


Figure 4.14 – Video processing of the sensor disk. Individual frame and pre-processing. The edges and center lines of the sensor disk identified using the video processing algorithm adopted in this study.

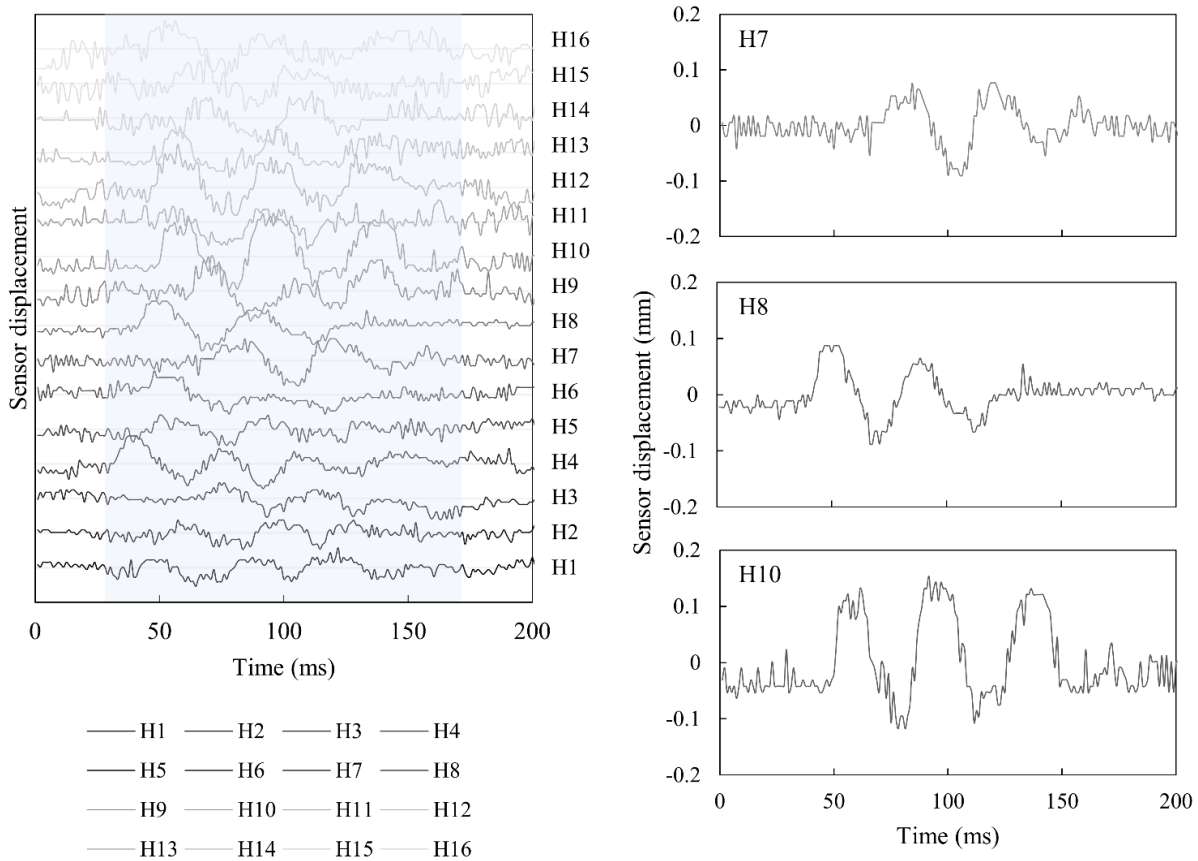


Figure 4.15 - Video processing of the sensor disk. (Left column) Time history of the disk vibrations. Note that the position of the sensor center line was obtained by averaging the position of 4 horizontal edges associated with the sensor disk. As such, the sensor displacements were discretized in steps of 0.25 pixel. Therefore, the minimum sensor displacement obtained from the videos is about 0.011 mm. (Right column) Close-up view of strikes 1, 8, and 10.

Finally, Figure 4.16 shows the magnitude of the oscillations sensor vibrations in colors in order to emphasize the differences among the 16 strikes. Figure 4.17 shows the peak-to-peak sensor displacement obtained from the videos as a function of the associated ISW amplitude. The results confirm that that stronger ISW induced large oscillations.

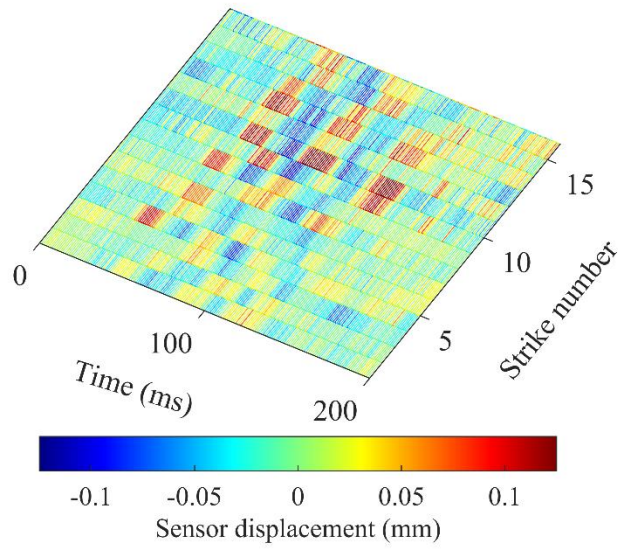


Figure 4.16 - The sensor vibrations detected in the videos in colormap format.

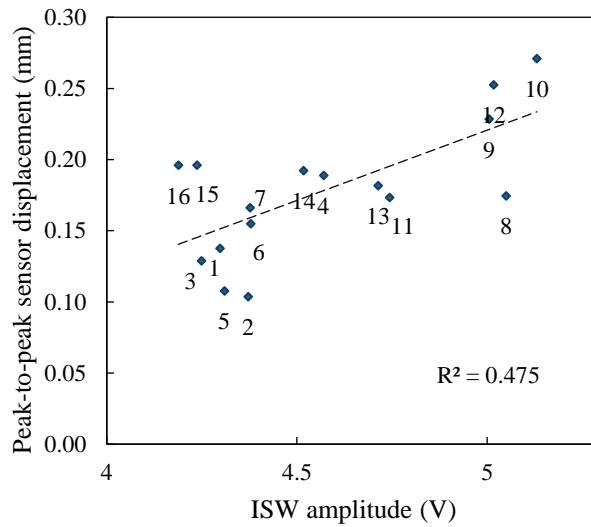


Figure 4.17 – Peak-to-peak sensor displacement as a function of the associated incident solitary wave amplitudes.

4.6 Conclusion

In this chapter, the long-term performance of three solitary wave transducers was investigated by placing the transducers above a test object monitored for a week while the transducers triggered and detected thousands of waves. The variability of the stress waves, mechanically induced by the impact of the striker, was quantified by extracting simple features such as amplitude and time of flight. In addition, sixteen measurements were captured with short videos at ~1,000 fps. The results of the study demonstrate that the traveling time of the solitary waves is the most reliable parameter for long-term monitoring with the lowest variability and the least susceptibility to physical changes within the array. When the NDE applications are targeted to the characterization of the material, the results demonstrate that an accurate model of the dynamic interaction between solitary waves and material is needed in order to obtain reliable predictions of the elastic modulus of the material to be characterized. While acoustic leakage in the form of dissipation seems to be non-critical for such predictions, the precise control of the free-fall of the striker and the elastic deformation of the material underneath the chain is pivotal. The fact that the features selected in the study were overall constant, suggest that the HNSW transducer can be used for damage detection. The findings of this study suggest revisiting the design of the sensing system and in particular to consider valid alternatives to the PZT bonded in between two thick disks.

5.0 Application of Granular Crystals to Control Mechanical Waves

This chapter investigates the asymmetric propagation of acoustic waves in a one-dimensional chain of spherical particles coupled with asymmetric intruders. The chain passes acoustic waves along one direction (forward configuration) whereas partially blocks the acoustic energy propagating along the opposite direction (reverse configuration). A numerical analysis is conducted to investigate this asymmetric propagation by simulating a statically compressed chain of particles interacting via Hertzian contact and subjected to small amplitude periodic displacements at one end. The amount of acoustic energy transmitted through the chain in both configurations is studied and quantified in terms of the acoustic energy transfer ratio, defined as the ratio of the acoustic power at the last particle to the acoustic power at the first particle. The effect of the applied frequency and number of particles in the chain on the transfer ratio is investigated. In addition, a parametric study is performed to evaluate the effects of geometric and material properties on the efficiency of asymmetric acoustic wave propagation in the proposed system. The results show that the proposed design supports asymmetric propagation of low frequency acoustic waves.

This chapter is written based on the following article:

Jalali, H., Rizzo, P., Nasrollahi, A., “Asymmetric propagation of low-frequency acoustic waves in a granular chain using asymmetric intruders.” *Journal of Applied Physics*, 126(7), 2019.

5.1 Introduction

Granular media, in the form of arrays of closely packed particles interacting via nonlinear contact forces, have shown promising applications as acoustic metamaterials [3, 4]. The dynamic behavior of these arrays is categorized as strongly nonlinear, weakly nonlinear, and linear regimes [3-5]. Strongly nonlinear arrays are typically in the form of uncompressed chains, which do not support tensile restoring forces between particles when they are separated from each other. These systems are shown to support the formation and propagation of highly nonlinear solitary waves. Strongly nonlinear chains are also known as sonic vacuum, since they do not support a characteristic sound speed [3-5]. In linear and weakly nonlinear regimes, granular chains provide filtering properties, which originate from internal reflections of waves by the periodic structure or Bragg scattering [3, 19, 55]. Diatomic chains, made of alternating particles of different masses, also show frequency bandgaps [3, 7, 27, 52, 184], which are frequency ranges in which acoustic waves are filtered.

Granular media present unique features such as wave speed tunability by changing static compression [5, 34, 35]. The dynamic response of the granular materials can be controlled by changing the grains' shape and dimension [33-38], material properties [33-35], and grains configuration and arrangement [3, 34, 35]. In addition, the filtering properties can be tuned by changing the structural design [52], the amplitude of applied vibrations [55], or by using electric [56] or magnetic fields [52, 57]. These features have led to various applications for the control of wave propagation including impact mitigation and energy harvesting [28, 170], discrete breathers [7, 52, 60, 184, 185], acoustic lens [24], acoustic switches and logic gate [119], and acoustic diodes [19, 20, 93, 186].

Similar to their electrical counterparts, acoustic diodes (ADs) break the reciprocity of the propagation of acoustic waves and allow the transmission of waves in one direction only. ADs have potential use in a variety of applications, including the improvement of the accuracy of ultrasound imaging in nondestructive evaluation and medical applications [61, 62]. For example, they may provide brighter and clearer ultrasound-based images by preventing disturbance between incident ultrasound waves and backtracking waves traveling in the opposite direction. Other potential applications are unidirectional impact mitigation, vibration isolation, and noise insulation [61, 62]. ADs acting as noise barriers can be helpful in reducing environmental noise annoyance and enhancing human comfort, health, and efficiency.

The first AD was proposed by Liang *et al.* and consisted of a superlattice of glass and water layers coupled with a nonlinear medium (ultrasonic contrast agent made of suspension of microbubbles) acting as a frequency convertor [61, 62]. If an acoustic wave of a particular frequency is applied from the superlattice side, it is blocked by the system. On the other hand, if it is applied from the nonlinear medium side, acoustic energy will be partially transmitted through the system. This stems from the fact that the incident wave is partially converted to a secondary wave of a different frequency in the nonlinear medium, and the superlattice acts as a filter that blocks the propagation of the original wave but allows the propagation of the secondary wave. Consequently, the asymmetric propagation of acoustic waves is achieved within specific frequency ranges.

This innovative design has been followed by other researchers who proposed granular media as frequency convertors and frequency filters to enhance the efficiency of the nonreciprocal wave propagation and broaden the working frequency band [20, 186]. Fu *et al.* for example, used 1-D chain of masses connected by tension-compression asymmetric bilinear springs and linear springs,

acting as frequency convertor and frequency filter, respectively [186]. Boechler *et al.* reported a non-reciprocal acoustic transmission in a 1-D granular chain containing a defect particle [19]. The defect particle creates a localized mode, which allows transmission of waves with frequency values above the chain cutoff frequency in one direction. The drawback of using nonlinearity in the design of ADs is the frequency distortion of the applied wave, and the amplitude dependence of the AD performance.

Li *et al.* proposed an AD made of an asymmetric 2D lattice of steel rods [21] to achieve asymmetric propagation of acoustic waves with breaking spatial symmetry in a linear system. The original wave frequency is preserved as the wave pass through the linear system. Other designs for the asymmetric acoustic wave transmission include water-immersed asymmetric gratings [187] and plates [188]. These ADs are based on one-way diffraction of high frequency acoustic waves using subwavelength-scaled asymmetric patterns and cannot provide asymmetric transmission of low frequency waves (below 1 kHz) in small-sized structures due to the wavelength limitations in wave diffraction.

Cui *et al.* demonstrated the nonreciprocal propagation of acoustic waves by breaking geometrical symmetry in a granular chain. This AD was based on the amplitude-dependent bandgaps in a compressed granular chain coupled with a conical rod [65]. The conical rod was used to change the amplitude of the incident wave, activating the bandgaps only in one direction.

Other innovative AD designs consisted of resonant ring cavities filled with circulating fluid [189], Helmholtz resonators combined with a straight channel [190], and a piezoelectric membrane coupled with a non-linear electronic circuit which allows active control or tunability of the system's acoustic properties [191].

Most of the aforementioned AD designs provide unidirectional propagation of acoustic waves only for a single frequency or within a narrow band of frequencies. In addition, to the best of the authors' knowledge, these designs work for high frequency values, i.e. are not effective at shielding low frequency sound, which is the most common and pervasive source of noise affecting human health [192-195]. Therefore, little has been done to investigate the ability of ADs as efficient noise barriers for indoor and/or outdoor applications.

To address this gap, the study presented in this chapter examined numerically a novel AD design based on asymmetric intruders in a statically compressed 1-D chain of spherical particles. The intruders restrict particles movement in one direction, resulting in partial attenuation of acoustic waves. However, the design allows the transmission of acoustic waves in the opposite direction as the vibration of particles does not interact with the intruders. This design follows the work of Li and Rizzo, in which asymmetric intruders in a chain of particles were used to achieve unidirectional propagation of solitary waves [23]. A solitary pulse was generated in the chain by applying an initial velocity to the first particle. It was shown that the intruders prevent the propagation of the solitary wave by restraining the displacement of the particles along one direction; but allow the propagation along the opposite direction.

Although the system was proven effective under impact loading, its performance under periodic loadings was not considered. The present numerical study aimed at studying the design performance as an acoustic barrier under periodic excitations. Since sound waves are composed of a series of sinusoidal waves of various amplitudes and frequencies, it was necessary to examine the efficiency of the AD subjected to sinusoidal loadings. A few computational models were implemented in MATLAB software to investigate the transient response of the proposed AD along the opposite directions for different frequencies. The efficiency of the AD was evaluated by

comparing acoustic power transition along the opposite directions. The results provide evidence that using this asymmetric geometry in a linear chain allows asymmetric propagation of low-frequency acoustic waves (below 300 Hz) which has not been realized in the previous designs. This may pave the way to the development of unidirectional sound walls for shielding low-frequency noises as the most annoying and persistent components in traffic and industrial noise.

The novelty of the study presented in this chapter is two-fold. First, an innovative AD design is presented using asymmetric intruders in granular media. The dynamic behavior of this asymmetric configuration subjected to periodic vibrations has not been studied to date. Second, it is shown that the proposed diode can provide asymmetric transmission of low frequency acoustic waves (below 300 Hz), which has not been achieved by the previous AD designs.

This chapter is organized as follows. Section 5.2 presents the design of the proposed AD and the numerical simulation used in this study. The dynamic response of the AD is presented in time and frequency domains in section 5.35.3. This section illustrates the efficiency of the AD subjected to noise induced vibrations. The frequency bandwidth and efficiency of the diode is then compared to previous diodes' designs found in the literature. Additionally, the effect of vibrations' amplitude, number of intruders, and material properties on the performance of the proposed AD is investigated. Section 5.4 ends the chapter with some concluding remarks.

5.2 Acoustic Diode Design and Numerical Setup

Figure 5.1 shows the initial scheme of the proposed AD. A statically compressed 1-D chain of forty 20 mm in diameter particles is enclosed by two rods. In the initial design, the spheres are

made of stainless steel to resemble the configuration studied in [23]. As shown in Figure 5.1a, part of the chain contains asymmetric stainless-steel intruders and is identified as the potential barrier zone (PBZ). The intruders are attached to the upper rod shown in Figure 5.1a. In contrast, the neutral zone (NZ) does not contain any intruder. The particles in the NZ are not restricted, and can move along both directions, carrying any acoustic energy induced by the vibration of the membrane. Asymmetric acoustic propagation is achieved with the prismatic intruders that are in contact with the spheres on one side. The contact surface of the intruders is assumed to be at 45 degrees with respect to the chain axis.

In the forward configuration (Figure 5.1b), acoustic wave and static precompression are applied by the actuator positioned on the left side of the chain, and the structural support to the whole system is provided by a plate on the right side of the chain. In this configuration, applying precompression causes the particles to move toward right initially. Therefore, there is a gap between the particles and the corresponding intruders initially (Figure 5.1b), and the particles oscillate around the point equilibrium induced by the static pre-compression. Because the amplitude of the vibration is smaller than initial static deformation δ_0 , the particles in the PBZ never get in contact with the intruders in the forward configuration. Therefore, the intruders do not affect particles vibration along the forward configuration.

In the reverse configuration (Figure 5.1c), the actuator is positioned on the right side of the chain, and the wall is on the left side of the chain. In this configuration the particles in the PBZ are in contact with the intruders since the precompression causes the particles to move toward the intruders. So, the particles' vibrations are restricted by the intruders. In fact, the design allows interaction between the asymmetric intruders and the particles only in the reverse configuration. As a result, the diode enables the transmission of the acoustic energy in the forward direction but

prevents it in the reverse direction. The acoustic barrier would be attained with the configuration of Figure 5.1c in which the acoustic energy is prevented from reaching the plate.

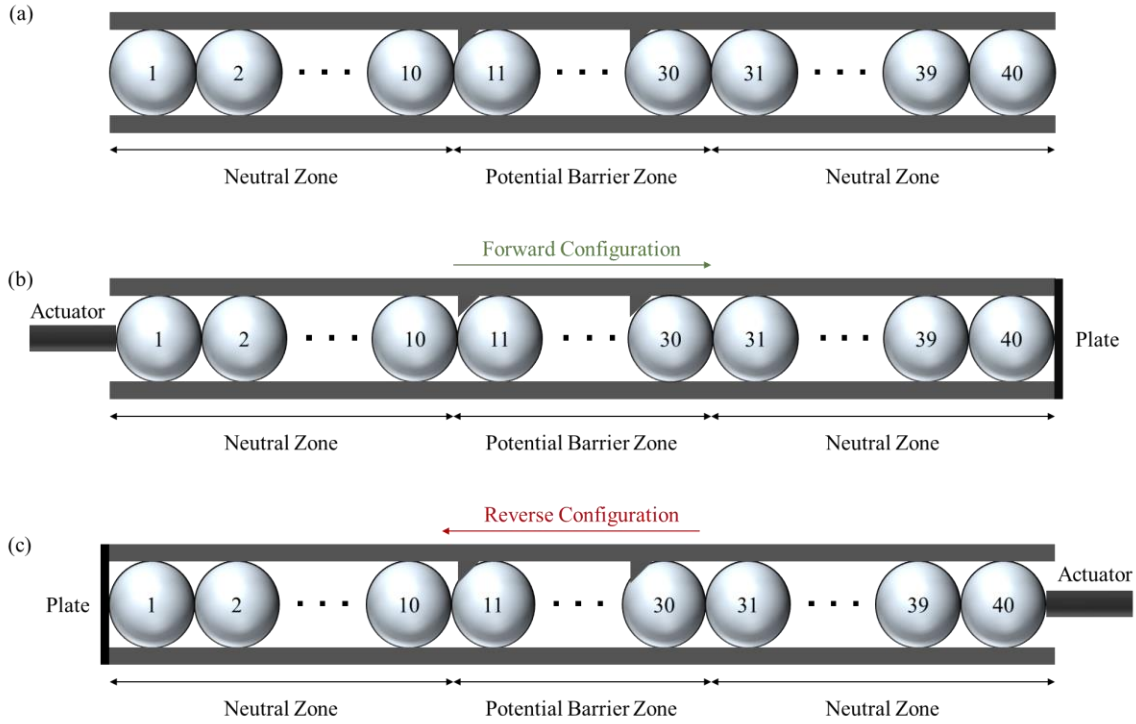


Figure 5.1 – (a) Design of the proposed 1-D acoustic diode. (b) Forward configuration, which allows the propagation (from left to right) of acoustic waves, since there is a gap between the particles and the intruders after applying the static compression. (C) Reverse configuration, in which the acoustic energy (propagating from left to right) is blocked by multiple reflections in the PBZ.

In both configurations, it is assumed that the acoustic energy is completely absorbed by the ending wall to avoid interference between the incident and the reflected waves from the wall. Noise induced vibrations are simulated by triggering the first particle of the chain (lattice site number 1) with a harmonic excitation $A\sin(2\pi ft)$. The amplitude A of the excitation was initially set to $0.5 \mu\text{m}$. This is compatible to deformation induced by typical loud traffic noise. The propagation of

the sound waves is studied by assuming that the amplitude of the particle's displacement caused by the vibration of the membrane is smaller than the initial static deformation (δ_0) induced by the pre-compressive force. As such, the granular chain is in the linear regime.

To illustrate the effect of the intruders in the reverse configuration, the force-displacement relationship associated with the interaction between the particles and the intruders in the PBZ ($1 \leq i \leq 30$) is shown in Figure 5.2. The dashed line represents the interaction between the i^{th} particle and the $i+1^{\text{th}}$ particle as a function of the dynamic displacement u_i of the i^{th} particle, modeled using the Hertzian contact law $F = k \delta^{3/2}$. For simplicity, the displacement of the $i+1^{\text{th}}$ particle is assumed zero. Positive and negative values of u_i indicate rightward and leftward displacements, respectively. For $u_i = 0$, the interaction force acting on the i^{th} particle equals to the static compression (F_0). It is supposed that this static force is applied by the adjacent particle. The interaction force between the i^{th} particle and the intruder activates when the i^{th} particle moves toward right (positive values of u_i). The dotted line presents the interaction force acting on the i^{th} particle from the intruder. This force increases nonlinearly as the particle moves toward right (positive values of u_i) but is equal to zero for negative values (leftward displacement of the i^{th} particle). The solid red line represents the sum of the interaction forces acting on the i^{th} particle from the particle $i+1$ and the intruder as a function of u_i . The interaction stiffness is increased in the reverse configuration for positive values of u_i (as the particle moves to right) as a consequence of the presence of the intruders. For $u_i < \delta_0$, the particles are detached from each other, and there is no interaction force between them. The amplitude of the dynamic displacements of the particles is less than the static deformation (δ_0), which means the particles are not separated while vibrating.

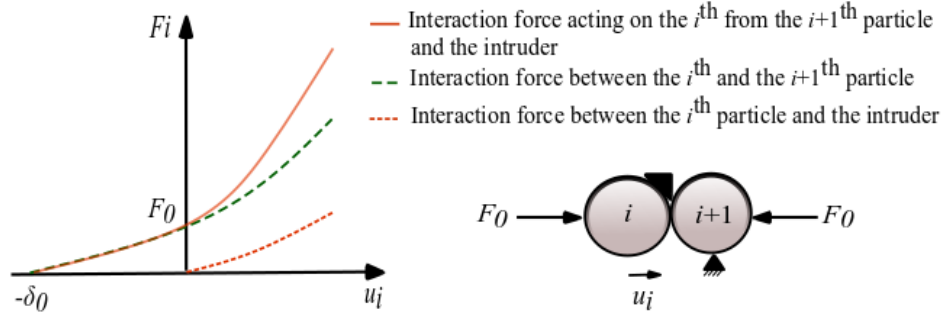


Figure 5.2 - Effect of asymmetric intruders on the interaction force acting on the i^{th} particle in the PBZ in the reverse configuration.

The equation of motion of the particles in the forward configuration is:

$$m\ddot{u}_i = k[\delta_0 + u_{i-1} - u_i]_+^{3/2} - k[\delta_0 + u_i - u_{i+1}]_+^{3/2} \quad (5.1)$$

where m is the mass of the particles, u_i is the displacement of the i^{th} particle, k is the contact stiffness between two particles, defined as $k = \frac{E\sqrt{2R}}{3(1-\nu^2)}$ in a chain composed of identical elastic spherical particles of radius R , Young's modulus of E , and Poisson's ratio of ν_i , and $\delta_0 = (F_0/k)^{2/3}$ is the static overlap caused by static compression F_0 . The bracket $[s]_+$ denotes $\max(s, 0)$. It is noteworthy that the argument in the bracket is always positive in the linear regime, since the static overlap is much greater than the amplitude of associated with the dynamic displacements.

In the reverse configuration, the equation of motion of the particles in the NZ is the same of Eq. (5.1), where the equation of motion of the particles in the PBZ ($11 \leq i \leq 30$) is defined as:

$$m\ddot{u}_i = k[\delta_0 + u_{i-1} - u_i]_+^{3/2} - k[\delta_0 + u_i - u_{i+1}]_+^{3/2} - 2k_p([u_i]_+ \cos 45^\circ)^{3/2} \cos 45^\circ \quad (5.2)$$

where k_p is the contact stiffness between the particles and the intruders defined as $4\sqrt{R}/3 \left[(1-\nu^2)/E + (1-\nu_i^2)/E_i \right]$. The parameters E_i and ν_i represent the Young's modulus and

the Poisson's ratio of the intruders, respectively. Energy dissipation in the chain is neglected in this simulation. The described discrete particle model is solved using the MATLAB solver ode45 for a time period of 100 ms and time step of 1 μ s.

To mimic the vibration of airborne sound, the first particle of the diode was excited with a harmonic displacement centered at a single frequency. Owing to the initial static compression the granular chain acts as a low-pass acoustic filter [3, 19, 27], and the cutoff frequency f_c depends on the geometric and material properties of the particles. In an infinite 1-D chain of identical particles, f_c is determined by [3]:

$$f_c = \left(\sqrt{4K_2/m} \right) / 2\pi \quad (5.3)$$

where $K_2 = 3/2 k \delta_0^{1/2}$ and k is the Hertzian stiffness. In non-infinite 1-D chains, the existence of bandgaps has been predicted numerically and observed experimentally [27, 184]. For illustrative purposes Table 5.1 lists the cutoff frequency associated with three different particles materials and diameters. Overall, the increase of the size lowers the cutoff frequency. For example, the 20 mm PTFE chain provides a cutoff frequency of 2377 Hz.

In this study, stainless steel and aluminum particles were considered for a diode subjected to a static pre-compression of 20 N. First, the existence of the cutoff frequency was investigated to validate the numerical simulation against Eq. (5.3). Then, the response of the diode to several discrete (in the frequency domain) excitations below the cutoff frequency was studied. The efficiency of the AD in providing unidirectional acoustic wave propagation was determined as a function of the applied frequency. The analysis was conducted for vibrations of different amplitudes, namely 1 μ m, 0.5 μ m, and 0.1 μ m. It is noted here that these amplitudes are smaller than the static overlap induced by the pre-compression.

Table 5.1 – Static overlap and cutoff frequency of compressed monatomic granular chains.

Material	Material properties			Static compression (N)	Diameter (mm)	Static overlap (μm)	Cutoff frequency (Hz)
	Young modulus (GPa)	Poisson ratio	Density (kg/m^3)				
Stainless steel	200	0.30	7800	20	10	1.95	19519
					20	1.55	7746
					30	1.35	4511
PTFE	1.5	0.46	2200	5	10	18.4	5990
					20	14.6	2377
					30	12.7	1384
Aluminum	70	0.33	2700	20	10	3.88	23544
					20	3.08	9344
					30	2.69	5441

5.3 Results and Discussion

To check the accuracy of the model, the low-pass filtering of an array made with either stainless steel or PTFE particles in the forward configuration was investigated. The results are presented in Figure 5.3. Figure 5.3a shows the displacement measured in the first and last particle of the stainless-steel chain when the excitation frequency was 1 kHz, and the peak-to-peak amplitude was 1 μm . Positive and negative displacement values represent rightward and leftward displacement of the particles, respectively. The plot shows that the wave propagated undisturbed through the array without attenuation. When the excitation signal was 8 kHz, the displacement amplitude at the lattice site 40 (Figure 5.3b) was heavily attenuated, in agreement with Eq. (5.3), that predicts a cutoff frequency at 7746 Hz.

From Figure 5.3b, the energy transfer ratio was found to be 9×10^{-4} corresponding to ~ 30 dB. This attenuation is due to the reflections of acoustic waves in the periodic structure [3]. It should be noted that the time duration of the input signal does not affect the transient response of the system, and the same results would be achieved if a longer or a shorter input signal was applied.

Similarly, Figure 5.3c and Figure 5.3d present the results associated with PTFE particles. Here, the excitation frequencies were 1 kHz and 3 kHz, the latter one being above the theoretical cutoff of 2377 Hz. The chain has transmitted the 1 kHz vibration without changing the frequency and amplitude of that; however, the 3 kHz vibration is filtered, and the frequency and amplitude of the applied wave are converted to lower values as the wave propagates through the chain. From Figure 5.3d the attenuation at particle 40 is about 37 dB.

Now that the accuracy of the numerical model was verified, the dynamic response of the stainless-steel diode subjected to a 100 ms long 125 Hz sinusoidal excitation with peak-to-peak amplitude of $1.0 \mu\text{m}$ is discussed by presenting in Figure 5.4 and Figure 5.5. Figure 5.4a and Figure 5.4b show the displacement of particles #1, #10, #30, and #40 as a function of time in the forward and the reverse configurations, respectively. While the acoustic wave propagates undisturbed along the forward configuration (Figure 5.4a), the amplitude decreases in the reverse configuration (Figure 5.4b), because the particles' movement is restricted by the asymmetric intruders in the PBZ. The negative or leftward displacement of the particles in the reverse configuration remains constant through the chain because the intruders do not affect the leftward displacement. For convenience, a zoom-in of the plots is presented in Figure 5.4c and Figure 5.4d, respectively.

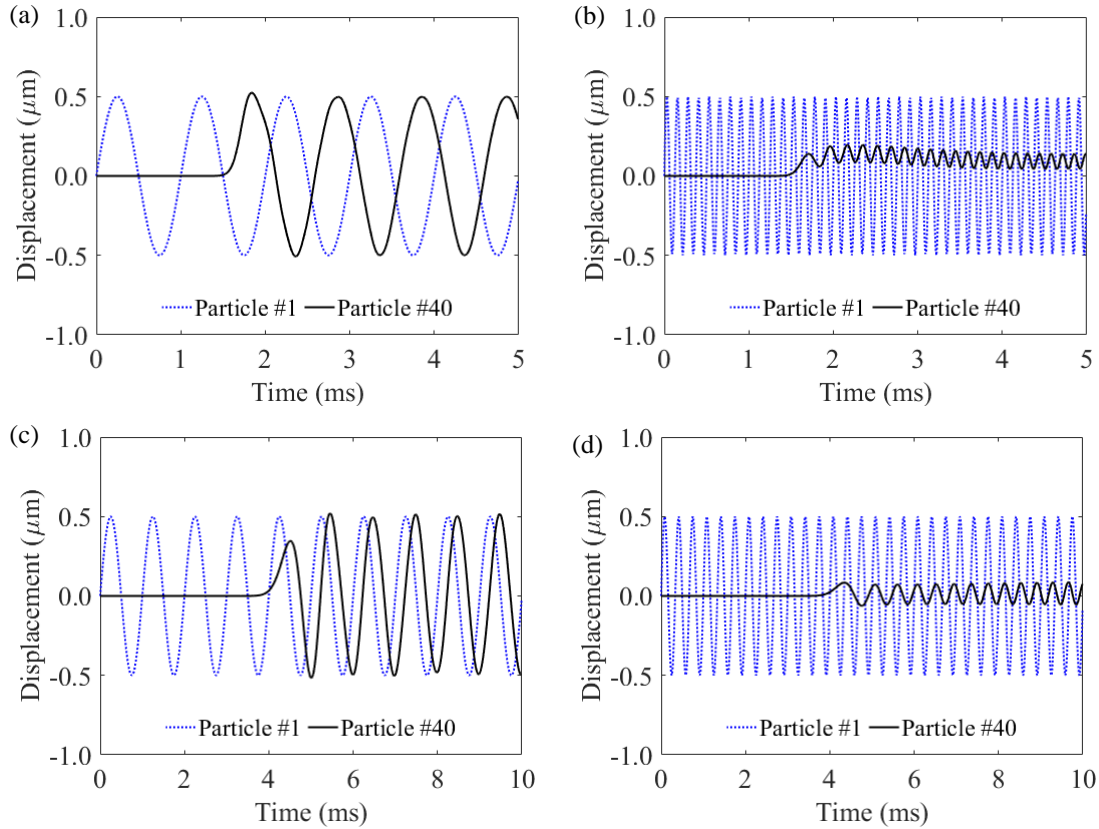


Figure 5.3 – Validation of the numerical model of the acoustic diode. (a, b) Displacement of the 1st and 40th particles when the diode made of stainless-steel particles is subjected to a sinusoidal excitation along the forward configuration at (a) 1000 Hz and (b) 8000 Hz. (c, d) Displacement of 1st and 40th PTFE particles when the diode is subjected to a sinusoidal excitation of (c) 1000 Hz and (d) 3000 Hz along the forward configuration.

Figure 5.4b reveals some attenuation in the neutral zone between the 1st and the 10th particle in the reverse configuration where there is no intruder. This is related to the fact that the wave period of the applied vibration ($T = 1/f$) is much longer than the time during which the vibration propagates from the first particle to the PBZ. The wave period of 125 Hz vibrations is equal to 8 ms while the wave arrives at the PBZ (particle #11) after 0.4 ms. It means that when the vibrations arrive at particle #11 ($t = 0.4$ ms), all the first 10 particles are moving in the same direction; therefore, the displacement of the first 10 particles is affected by their following

particles. Since the rightward displacement of particle #11 is restricted by intruders, the displacement of particle #10 is also partially restricted by particle #11. In other words, the interaction between intruders and the particles in PBZ affects the particles movements in the first NZ segment. This provides the partial attenuation observed in the NZ.

Figure 5.5a compares the time waveforms at lattice site 40 in the forward (dotted line) and in the reverse (solid line) configurations. Clearly, the signal is attenuated by the interaction of the particles with the intruders. Figure 5.5b compares instead the force at the same site, and shows that the force oscillates around 20 N, which is the static pre-compression applied to the chain. The amplitude of the oscillations is much smaller than the static compression, thus confirming the assumption that the chain behaves within the linear regime. According to Figure 5.5a and Figure 5.5b the particles' displacement is restricted in the reverse configuration, however the force amplitude has not changed significantly due to the equilibrium in the chain.

The Fourier transform of the waveforms displayed in Figure 5.5a are presented in Figure 5.5c. While the spectrum associated with the forward configuration has a single peak at 125 Hz, the transform relative to the reverse configuration reveals the presence of higher harmonics. These harmonics are common in vibration of nonlinear systems subjected to harmonic excitations and have been reported in previous studies relative acoustic metamaterial designs using nonlinear media [64, 119]. In the diode investigated in the present study, nonlinearity originates from the asymmetric increase of interaction stiffness in the reverse configuration due to the presence of asymmetric intruders (Figure 5.2).

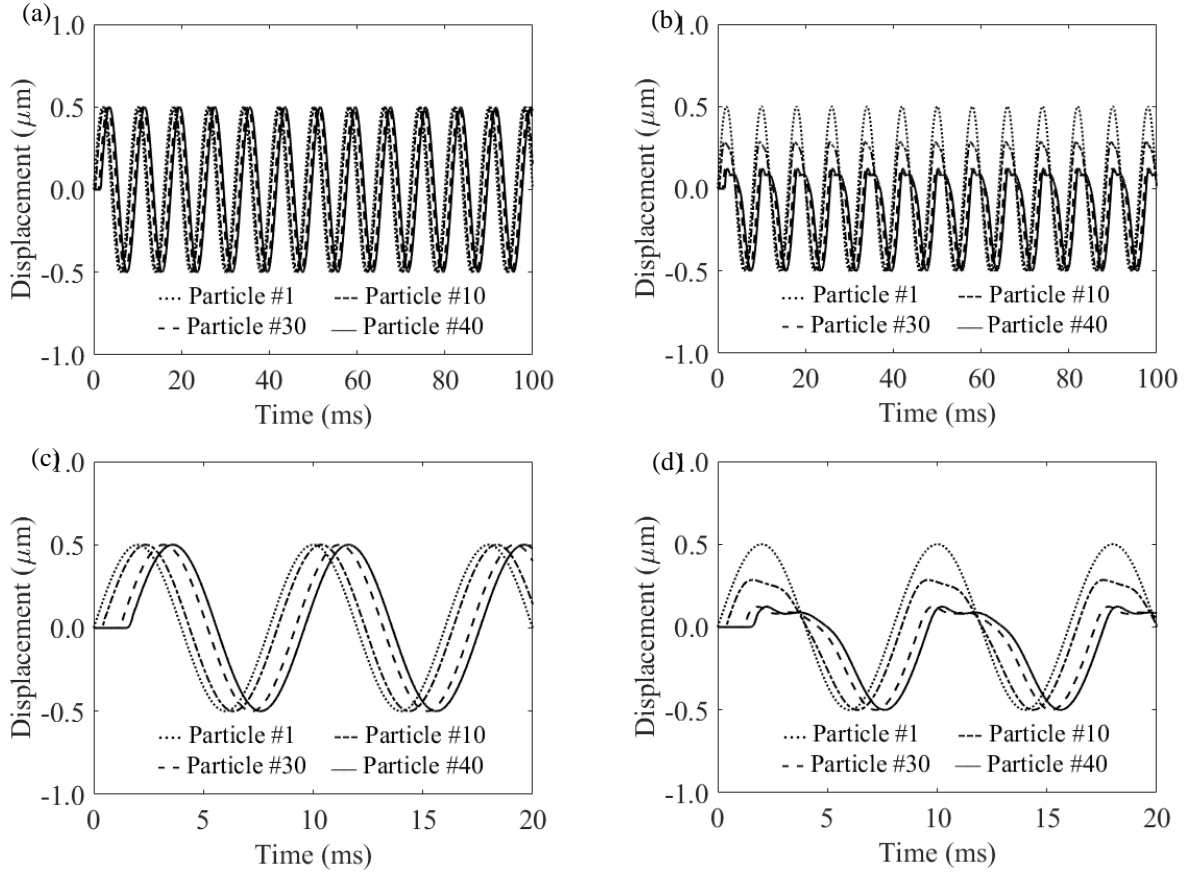


Figure 5.4 – Dynamic response of the stainless-steel diode subjected to a 1 μm peak-to-peak, 125 Hz, 100 ms sine wave. Displacement of the particles #1, #10, #30, and #40 in the (a) forward and (b) reverse configuration. (c) close-up view of (a); (d) close-up view of (b).

To examine the efficiency of the proposed diode, the energy transfer ratio at each particle was calculated by dividing the acoustic power measured at a given particle to the acoustic power at the first particle where the power was defined as the area integral under the frequency spectrum diagram such as the one shown in Figure 5.5c. The results are presented in Figure 5.5d for all the 40 lattice sites. The vertical lines identify the boundaries of the PBZ. The acoustic energy transfer ratio is equal to 1 across the particles of the forward configuration. However, this ratio decreases to 0.48 close to the end of the PBZ in the reverse configuration. This implies that 52% of the acoustic energy is blocked by the intruders in the reverse configuration.

The rectifying ratio, defined as the ratio of the transmitted energy in the forward configuration to the reverse configuration is equal to 2.08 for this configuration. The performance of the diode can also be quantified in terms of the contrast ratio (R_C), defined as [21]:

$$R_C = \frac{T_p - T_n}{T_p + T_n} \quad (5.4)$$

where T_p and T_n are the transmitted power (area under frequency spectrum) in the forward and reverse configurations, respectively. An ideal diode would have $R_C = 1$, which corresponds to acoustic power transmission ratios of 1 and 0 in the forward and reverse configurations, respectively. The results presented in in Figure 5.4 and Figure 5.5 show a contrast ratio of 0.35 for the case studied. Sound power level reduction in the reverse configuration, expressed in dB, was also calculated as the logarithmic ratio of the transmitted acoustic energy to applied acoustic energy. Here, a 3.2 dB reduction of sound power levels is achieved in the reverse configuration. In terms of sound insulation, 3.2 dB noise reduction is not easily perceptible by human ear, even if it corresponds to about 50% reduction of sound energy [193].

To evaluate the performance of the diode across a wider spectrum of frequencies, 2-D maps of the energy transfer ratio in the reverse configuration are presented in Figure 5.6 as a function of the frequency and lattice site. The case relative to 1 μm peak-to-peak amplitude excitations is presented. Figure 6a refers to the range from 25 Hz to 1000 Hz, with a frequency step of 20 Hz. Figure 5.6b extends the analysis to 10 kHz, at steps of 40 Hz. The ratio becomes zero above 7745 Hz, in agreement with the cut-off frequency (7746 Hz) predicted analytically by Eq. (5.3) and listed in Table 5.1.

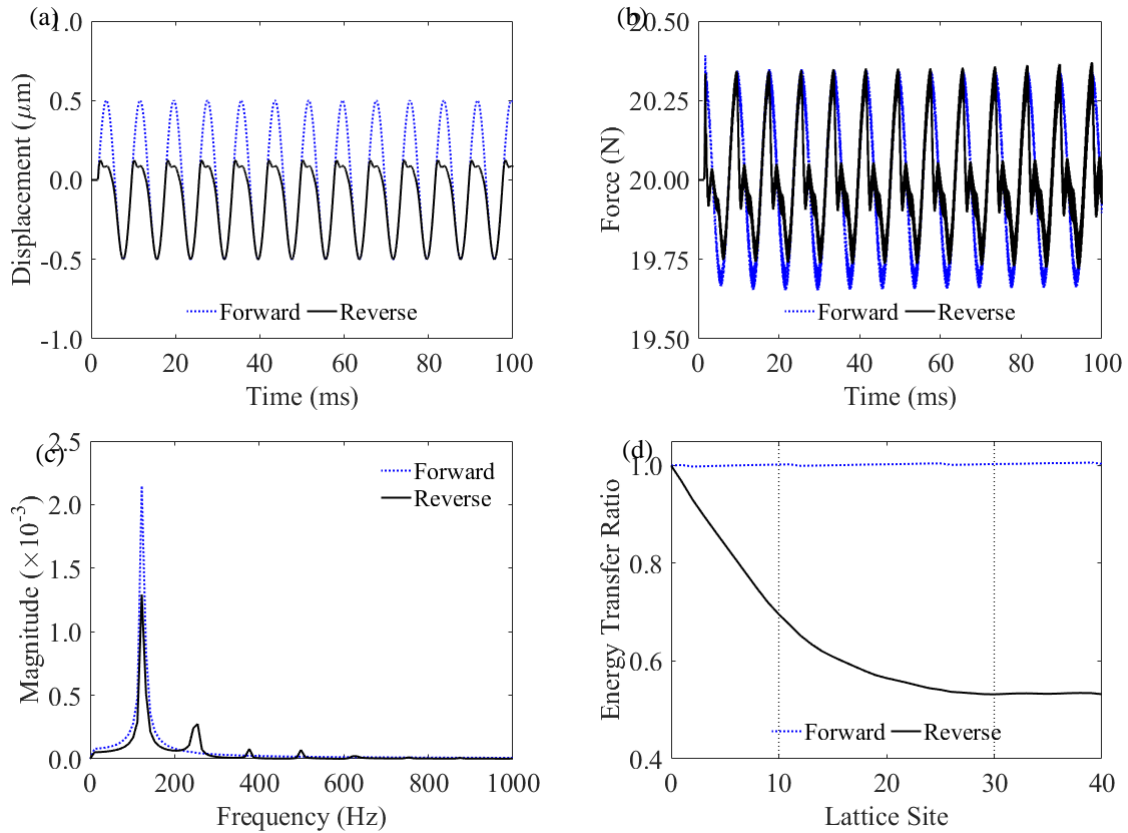


Figure 5.5 – Dynamic response of the stainless-steel AD subjected to a 1 μm peak to peak amplitude, 125 Hz, 100 ms sine wave (a) Displacement of particle #40 as a function of time in both configurations. (b) Force of particle #40 as a function of time in both configurations. (c) Power distribution over frequency for the transmitted wave at particle #40 in both configurations (d) Energy transfer ratio as the wave propagates through the chain in both configurations.

Figure 5.6c and Figure 5.6d represent a close-up view of the range 25-300 Hz. The results suggest that the diode acts as high-pass filter by forbidding the propagation of the acoustic energy below 300 Hz. A minimum energy transmission ratio of 0.47 is achieved in this frequency range, corresponding to a contrast ratio of 0.36. To compare the performance the proposed diodes to other diodes, Table 5.2 is presented. It summarizes the bandwidth and efficiency of passive diode designs found in the literature. The efficiency is presented in terms of contrast ratio or rectifying

ratio. According to the table, the previous AD designs provide asymmetric propagation of mechanical waves in the kHz range (mostly ultrasonic); however, the asymmetric propagation of low frequency waves (below 300 Hz) is not reported before.

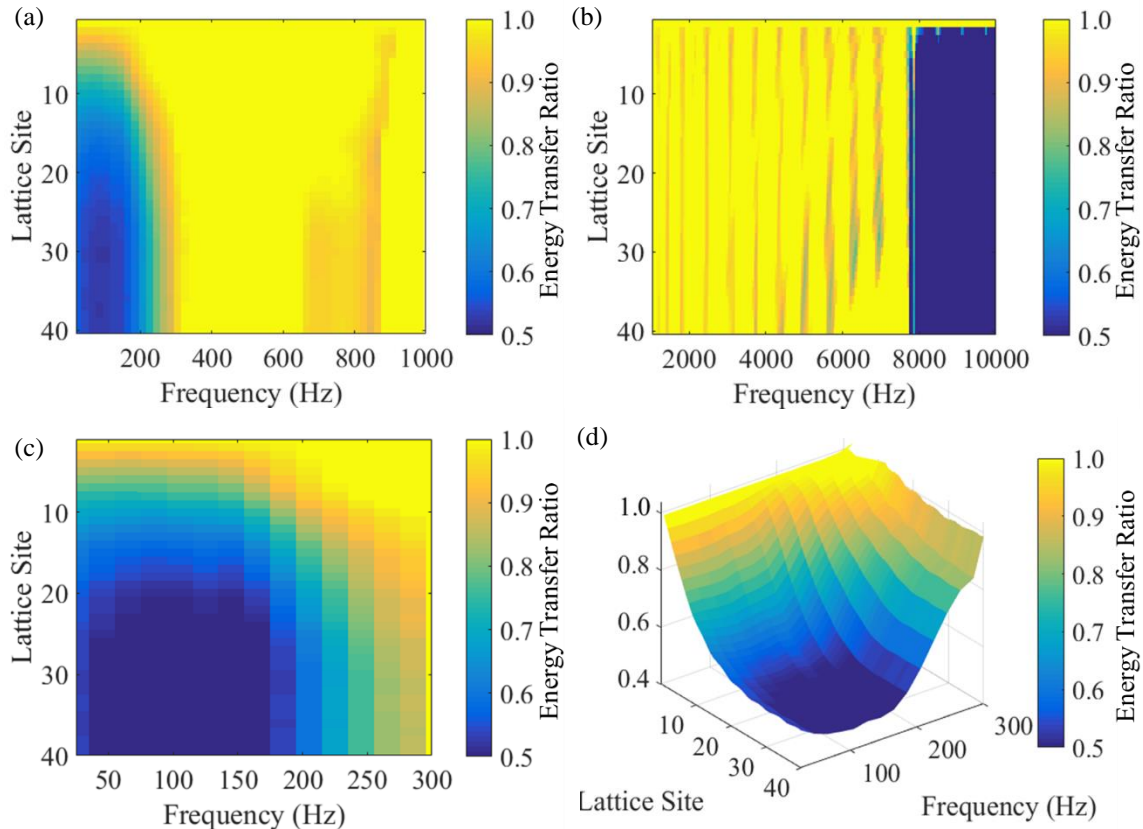


Figure 5.6 – Reverse configuration. Energy transfer ratio as a function of lattice site and frequency, where the peak-to-peak amplitude of the input signal is equal to $1 \mu m$. (a) from 25 Hz to 1000 Hz with a frequency step of 20 Hz, and (b) from 1000 Hz to 7000 Hz with a frequency step of 40 Hz. (c) 2D map for frequencies between 25 Hz and 250 Hz. (d) 3D plot for frequencies between 25 Hz and 250 Hz.

Table 5.2 – Bandwidth and efficiency of passive acoustic diodes designs available in the scientific literature.

Design description	Reference	Operating bandwidth	Efficiency	
			Contrast ratio	Rectifying ratio
Nonlinear media as a frequency converter, coupled with a frequency filter	[20]	1 - 11 kHz		$\approx 10^5$
	[64]	$f_c - 2 f_c^*$ 2.4 f_c - 3.2 f_c^* 850 – 930 kHz		$\approx 10^5$
	[62]	1000 – 1090 kHz		$\approx 10^3$
Asymmetric geometry	[21]	16 - 23 kHz 36 - 47 kHz	0.9	
	[187]	250 – 500 kHz		2-5
	[188]	350 – 630 kHz	0.2 - 0.75	
	[65]	1.35 – 1.44 kHz	0.9	
Other	[189]	0.8 kHz		$\approx 10^4$
	[37]			
	[190]	3.4 – 3.6 kHz		6 - 10

* f_c : Cutoff frequency of the selection component which is equal to 4.2 Hz in the presented design.

Based on Figure 5.6, the energy transfer ratio above 300 Hz is close to one even in the reverse configuration. This implies that the initial design of the proposed AD is effective only below 300 Hz. To understand the presence of these passing bands, Figure 5.7a and Figure 5.7b present the time waveforms measured at the 40th particle in both configurations relative to 300 Hz and 500 Hz excitations, respectively. According to these figures, the magnitude of the negative (leftward) displacement of the last vibrating particle in the reverse configuration is greater than 0.5 μm , which is the amplitude of the applied vibration at the first particle. The magnitude of negative displacement of the 40th particle in the reverse configuration increases to 0.55 μm and 0.8 μm , when it is subjected to 300 Hz (Figure 5.6a) and 500 Hz vibrations (Figure 5.6b), respectively. It means that the equilibrium position of the particles subjected to high frequency vibrations in the

reverse configuration has shifted slightly to left due to the interaction between the particles and the intruders. As a result, the overall dynamic displacement amplitude of the particles is not mitigated significantly in the reverse configuration, allowing acoustic energy transmission of high frequency vibrations in this configuration. In other words, the shift of the particles' equilibrium position allows them to transmit the high frequency vibrations despite the presence of the intruders.

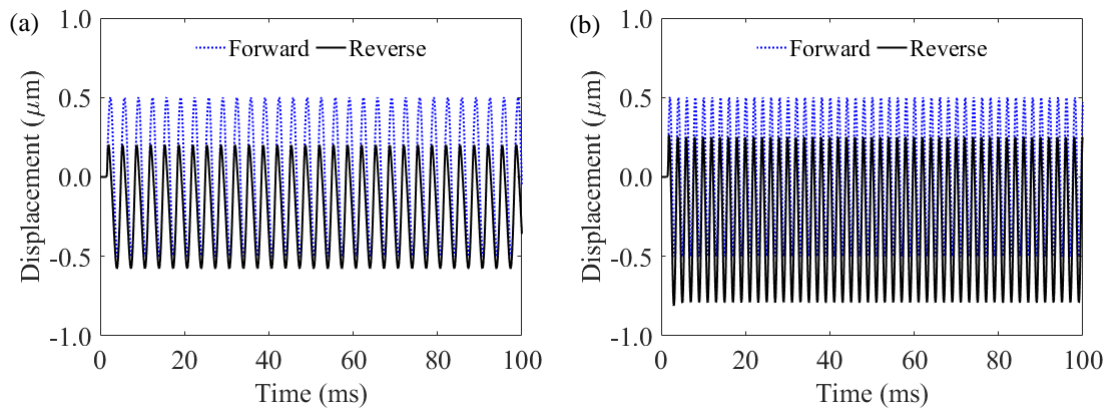


Figure 5.7 – Time domain response of the stainless-steel diode at the 40th particle, under 1 μm peak-to-peak amplitude and frequency of (a) 300 Hz, and (b) 500 Hz.

To evaluate the effect of the noise amplitude on the response of the diode, Figure 5.8 shows the energy transfer ratio in the reverse configuration for peak-to-peak amplitudes equal to 0.2 μm and 2 μm between 25 Hz and 300 Hz. The graphs reveal that the diode is more efficient with the increase of the signal strength. The quantitative comparison of the energy transfer ratio at particle #40 is provided in Figure 5.8c. Across the 25-300 Hz range, the ratio decreases with the increase of the amplitude of the sine wave. This means that the louder is the airborne sound, the more efficient is the diode. This stems from the nonlinearity in the interaction between particles and intruders. In fact, the interaction forces between particles in the PBZ and barriers increases

nonlinearly as the amplitude of vibrations increases. Consequently, the proposed AD provides higher efficiency in non-reciprocal propagation of the acoustic waves as the amplitude of applied vibration increases. Since the amplitude of vibrations induced noise depends on the sound level, the AD performance improves as the sound level increases.

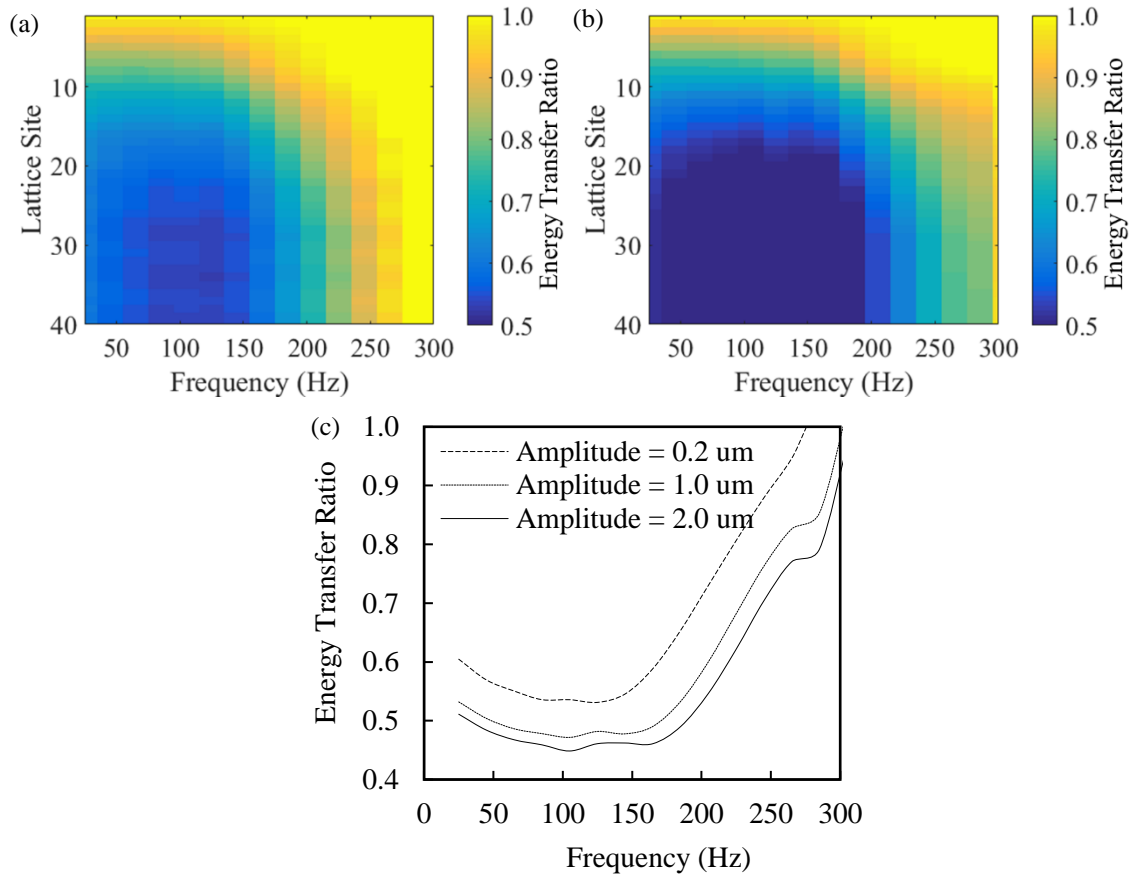


Figure 5.8 –Energy transfer ratio as a function of lattice site and frequency in the reverse configuration, where the peak-to-peak amplitude was (a) $0.2 \mu m$ and (b) $2 \mu m$. (c) Comparison of energy transfer ratio at particle #40 in the reverse configuration.

Figure 5.9 evaluates the effect of the number of particles in the PBZ on the AD performance. Figure 5.9a and Figure 5.9b present a 2D map of the energy transfer ratio where the PBZ contains

10 and 30 particles, respectively. The analysis is conducted for 1 μ m peak-to peak amplitude vibration. Figure 5.9c provides the quantitative analysis the site #40 for the three lengths of the diode. Interestingly, the energy ratio is not always inversely proportional to the number of particles in the BPZ. As a matter of fact, above 220 Hz, a shorter diode is more efficient. This implies that increasing the number of particles in the PBZ leads to a narrower bandwidth of the diode. The motivation behind this behavior is associated with the shift in the equilibrium position of the particles, demonstrated in Figure 5.6. In fact, the longer PBZ provides more space for the shift in the equilibrium position of particles in the reverse configuration, and the shift can be gradually cumulated along the PBZ in this configuration. Therefore, the longer PBZ adversely affects the working frequency band. Overall, it can be concluded that increasing the number of particles in the PBZ leads to improving the efficiency (contrast ratio) of the AD but decreases the working band width.

The effect of the particles' material was studied next. Aluminum, for example, would provide a lighter diode. The 2D map of the energy transfer ratio in the reverse configuration of a diode made of 20 mm aluminum particles is presented in Figure 5.10a. The comparison with the stainless-steel design is shown Figure 5.10b and shows that the is less efficient than the steel one. This is because steel is stiffer than aluminum, which results in a stiffer interaction between the particles and the intruders. The softer interaction between the particles and intruders in the aluminum chain leads to less reduction of vibration amplitudes compared to the stainless-steel chain. Therefore, aluminum diode provides a higher energy transfer ratio in the reverse configuration. Similarly, PTFE provides a lower stiffness at the interaction between particles and barriers in the reverse configuration due to its low stiffness. Figure 5.11 presents the time domain response of the last particle in a PTFE chain subjected to a 125 Hz vibration with amplitude of

0.5 μm . As it can be seen, the amplitude of vibrations is not decreased significantly in the reverse configuration compared to the forward configuration. It can be concluded that using stiffer materials leads to better performance of the proposed AD.

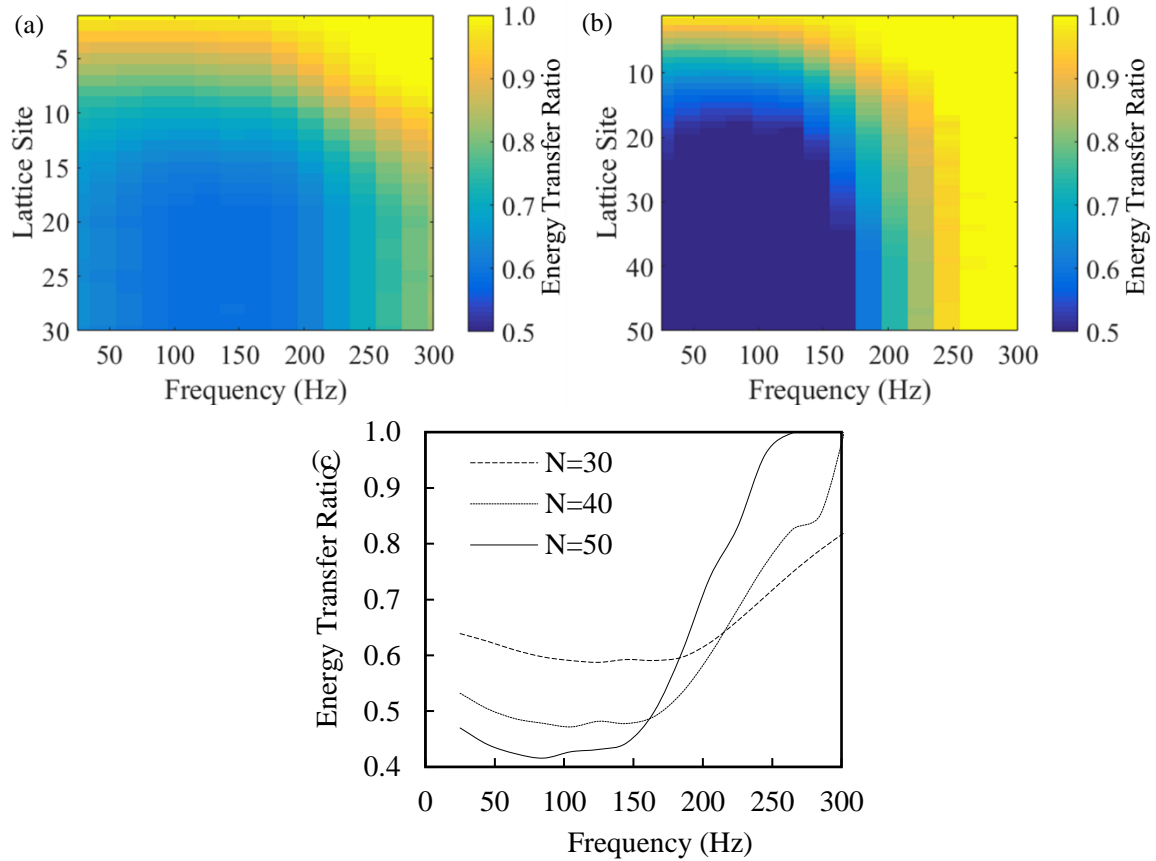


Figure 5.9 – Reverse configuration. Energy transfer ratio as a function of lattice site and frequency, where the peak-to-peak amplitude is equal to 1 μm and the diode contains (a) 30 and (b) 50 particles. (c) Comparison of energy transfer ratio at the last particle in diodes with 30, 40, and 50 particles.

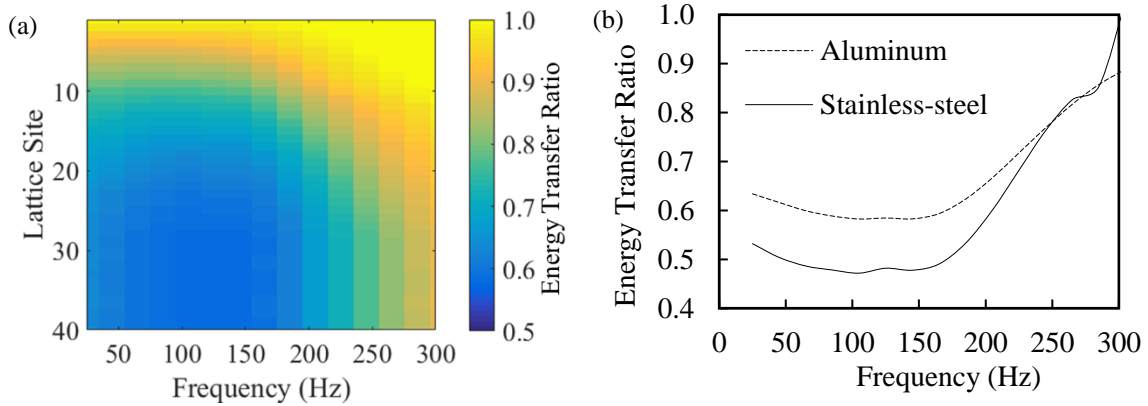


Figure 5.10 – (a) Energy transfer ratio as a function of lattice site and frequency, where the peak-to-peak amplitude is equal to $1 \mu\text{m}$ in the aluminum diode. (b) Comparison of energy transfer ratio at the last particle in stainless-steel and aluminum diodes.

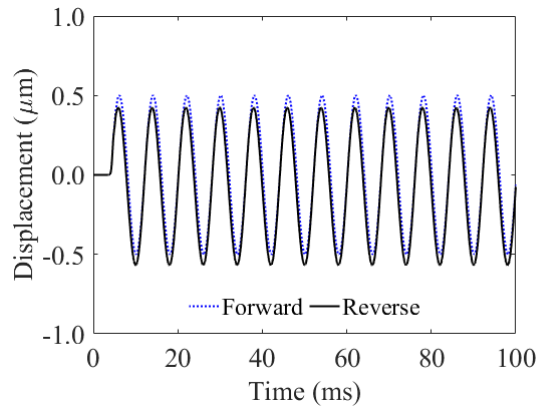


Figure 5.11 - Time domain response of the PTFE AD in the forward and reverse configurations. Displacement of the 40th particle, when the chain is subjected to a periodic vibration with peak-to-peak amplitude of $1 \mu\text{m}$ and frequency of 125 Hz.

5.4 Conclusions

In this chapter, the design of a new acoustic diode to shield low frequencies ($<1000 \text{ Hz}$) was presented. The diode on its simplest form consists of a statically pre-compressed one-dimensional

chain of mono-periodic particles with asymmetric rigid intruders. The performance of this diode at shielding acoustic waves was investigated by triggering harmonic vibrations at one end of the chain and by measuring the amplitude of such vibration at the opposite end. Arrays subjected to three different harmonic amplitudes and made of three different particles materials were considered. The study was conducted numerically, and the results showed that the proposed diode can yield unidirectional transmission of low frequency acoustic waves. In addition, the results showed that the diode possesses a wider working frequency band and higher contrast ratio as the amplitude of the applied vibrations increases. The efficiency of the can be improved by increasing the number of particles in the potential barrier zone, i.e., in the zone containing the intruders; however, such an increase makes the working bandwidth narrower. Finally, the results suggest that using stiffer materials improves the performance of the studied AD.

Future studies shall look at the experimental validation of the design as well as the expansion of the study to consider 3D walls made of such diodes.

6.0 Summary and Conclusions

This chapter presents a summary of this dissertation and a brief list of the main findings of the present research. The chapter ends with some recommendations for future research.

6.1 Overview of the Dissertation

This dissertation investigated new NDE applications of granular crystals. This technique is based on the propagation and detection of highly nonlinear solitary wave through an uncompressed 1-D monophasic array of spherical particles in which one end of the array is in contact with the material/structure to be inspected, and the particle at the opposite end induces the waves by a mechanical impact. This study delved into the application of solitary waves for the detection of localized corrosion in plate-like structures and the examination of anisotropy in rock materials. For this purpose, numerical and experimental studies were conducted. Furthermore, the long-term performance of the developed HNSW transducers was investigated.

In Chapter 2.0, the study on the application of solitary waves for the detection of localized corrosion was presented. Coupled discrete element/finite element models were used to study the dynamic interaction between solitary waves and steel plates in pristine and corroded conditions. In addition, two experiments were conducted to monitor localized corrosion in two steel plates of different thicknesses using the solitary wave transducers. Both the numerical and the experimental results showed that solitary waves are affected by the progress of localized corrosion in steel plates. Therefore, this study provides evidence that the solitary wave-based NDE method can be used as

an effective method for the detection of localized corrosion. Furthermore, it was shown that the solitary wave-based NDE method is more sensitive to localized corrosion in thinner plates. The results of this study will aid in the development of a local thickness monitoring technique that can be employed remotely in high-temperature environments.

In chapter 3.0, the application of solitary waves for characterizing transversely isotropic geomaterials was investigated. Numerical and experimental methods were used to examine the interaction of solitary waves with sandstone and slate samples in different conditions. The experimental data were analyzed using multivariate outlier detection. It was shown that the method was effective in detecting anisotropy and providing insight into the mechanical features of the rock samples.

In chapter 4.0, the long-term performance of the developed solitary wave transducers was investigated in a one-week-long test. In addition, sixteen solitary wave measurements were captured with short videos at ~1,000 fps. The results of the study demonstrated that the traveling time of the solitary waves is the most reliable parameter for long-term monitoring with the lowest variability and the least susceptibility to physical changes within the array. The fact that the solitary wave features were overall constant suggests that the solitary waves can be used for damage detection. However, an accurate model of the dynamic interaction between solitary waves and material is needed to obtain reliable predictions of the properties of the material/structure to be characterized. While acoustic leakage in the form of dissipation seems to be non-critical for such predictions, the precise control of the free-fall of the striker and the accurate prediction of elastic deformations in the inspecting medium is essential. Furthermore, the findings of this study suggested revisiting the design of the sensing system embedded in the solitary wave transducers.

Finally, chapter 5.0 investigated the dynamic response of a compressed 1D granular crystal coupled with asymmetric rigid intruders. The performance of this design at shielding mechanical vibrations was investigated numerically. It was shown that the proposed design can yield unidirectional transmission of low-frequency acoustic waves. In addition, the results showed that the diode possesses a wider working frequency band and higher efficiency in shielding mechanical waves as the amplitude of the applied vibrations increases. Furthermore, the efficiency can be improved by increasing the number of particles in the potential barrier zone, i.e., in the zone containing the intruders; however, such an increase makes the working bandwidth narrower. Finally, the results suggested that using stiffer materials improves the performance of the studied design.

The findings of the present study will aid in the development of granular crystal-based engineering devices. The results demonstrate that the effectiveness of the solitary wave-based NDE method for localized NDE applications. In addition, the study provides new insights into the behavior of solitary waves and their interaction with boundaries. The dissertation also provides insight into the potential modifications for the design of HNSW transducers.

6.2 Main Novel Findings

The following provides a list of the main findings of this dissertation:

- Solitary waves interacting with a thin plate are sensitive to the presence of localized corrosion defects in the plate. Therefore, solitary waves can be used as an effective and efficient method for corrosion detection in plates.

- The traveling time and the amplitude of the reflected solitary waves are strongly affected when the depth of corrosion defects exceeds 50% of the plate thickness.
- The solitary wave-based NDE method is more sensitive to localized corrosion in thinner plates.
- The sensitivity of the solitary wave-based NDE method to corrosion can be improved by using larger, heavier, and stiffer particles.
- The length of the granular chain and the position of the sensor particle do not affect the properties of the reflected solitary waves significantly. However, in high-temperature environments using longer granular chains and keeping the sensor away from the monitoring object can be beneficial to isolate the vulnerable sensing systems from hot zones. In addition, using thermally insulating materials like silicon nitride is advantageous in high-temperature environments.
- The solitary wave-based NDE is also effective for characterizing transversely isotropic geo-materials.
- Application of multivariate outlier analysis was shown effective in analyzing the data obtained from solitary wave-based NDE and detecting structural anomalies
- In the solitary wave-based NDE, an accurate numerical model of the dynamic interaction between solitary waves and inspection medium is essential for a reliable prediction of the properties of materials/structures to be characterized. In particular, the accurate prediction of elastic deformations in the inspecting medium is essential.
- The propagation of vibrations in a statically compressed one-dimensional chain of mono-periodic particles can be partially blocked using asymmetric rigid intruders.

- The propagation of mechanical waves in a compressed one-dimensional chain of mono-periodic particles coupled with asymmetric rigid intruders results in the generation of higher harmonics in the chain.

6.3 Limitations of the Solitary Wave-based NDE

The application of the solitary wave NDE method is limited to localized monitoring purposes. This method can provide information about the mechanical properties and the geometry of the inspection medium only at the vicinity of the contact area between the granular chain and the inspection medium. Therefore, the method could not be employed for global monitoring purposes. It can be concluded that the solitary wave-based NDE can be employed in combination with other NDE methods used for inspecting broader areas.

It should be noted that this dissertation only provided evidence that solitary waves are effective for detecting corrosion defects. However, the method might not be effective for quantifying the corrosion damages and providing accurate information about the width and the depth of corrosion defects. Furthermore, the sensitivity of the solitary wave-based NDE method for corrosion monitoring might decrease in cases with different boundary conditions, initial thicknesses, or material properties.

6.4 Suggestions for Future Studies

The following provides a list of suggestions for future studies:

- Further studies are needed to investigate the effectiveness of the solitary wave-based NDE under different conditions like with different sizes and boundary conditions of the inspection medium. It is essential to define a characteristic length for the effect of boundaries on the reflected solitary waves.
- The design of the sensing system embedded in the solitary wave transducers needs to be improved to achieve less susceptibility to physical changes within the array.
- The numerical modeling of the propagation of solitary waves through granular chains can be improved by using elastoplastic contact models to capture more accurately energy dissipation in the chain that originates from the plastic deformation in the particles.
- The performance of different configurations of solitary wave transducers, e.g., L-shaped and J-shaped granular chains, need to be investigated for application of the solitary wave-based NDE in areas where the straight solitary wave transducers are not suitable.
- The performance of the solitary wave NDE method in high temperature environments need to be investigated experimentally.
- The application of the solitary wave-based NDE in industrial fields needs further investigation.

Bibliography

1. Hertz, H., *On the contact of elastic solids*. Z. Reine Angew. Mathematik, 1881. **92**: p. 156-171.
2. Johnson, K.L. and K.L. Johnson, *Contact mechanics*. 1987: Cambridge university press.
3. Deymier, P.A., *Acoustic metamaterials and phononic crystals*. Vol. 173. 2013: Springer Science & Business Media.
4. Nesterenko, V., *Dynamics of heterogeneous materials*. 2013: Springer Science & Business Media.
5. Daraio, C., V. Nesterenko, E. Herbold, and S. Jin, *Tunability of solitary wave properties in one-dimensional strongly nonlinear phononic crystals*. Physical Review E, 2006. **73**(2): p. 026610.
6. Wang, Y.-S., W. Chen, B. Wu, Y.-Z. Wang, and Y.-F. Wang, *Tunable and Active Phononic Crystals and Metamaterials*. Applied Mechanics Reviews, 2020. **72**(4).
7. Boechler, N., J. Yang, G. Theocharis, P. Kevrekidis, and C. Daraio, *Tunable vibrational band gaps in one-dimensional diatomic granular crystals with three-particle unit cells*. Journal of Applied Physics, 2011. **109**(7): p. 074906.
8. Ni, X. and P. Rizzo, *Use of highly nonlinear solitary waves in nondestructive testing*. Materials evaluation, 2012. **70**(5).
9. Nasrollahi, A., P. Rizzo, and M.S. Orak, *Numerical and experimental study on the dynamic interaction between highly nonlinear solitary waves and pressurized balls*. Journal of Applied Mechanics, 2018. **85**(3).

10. Ni, X. and P. Rizzo, *Highly nonlinear solitary waves for the inspection of adhesive joints*. Experimental mechanics, 2012. **52**(9): p. 1493-1501.
11. Kim, E., F. Restuccia, J. Yang, and C. Daraio, *Solitary wave-based delamination detection in composite plates using a combined granular crystal sensor and actuator*. Smart Materials and Structures, 2015. **24**(12): p. 125004.
12. Yang, J., C. Silvestro, S.N. Sangiorgio, S.L. Borkowski, E. Ebrahimzadeh, L. De Nardo, and C. Daraio, *Nondestructive evaluation of orthopaedic implant stability in THA using highly nonlinear solitary waves*. Smart Materials and Structures, 2011. **21**(1): p. 012002.
13. Yang, J., S.N. Sangiorgio, S.L. Borkowski, C. Silvestro, L. De Nardo, C. Daraio, and E. Ebrahimzadeh, *Site-specific quantification of bone quality using highly nonlinear solitary waves*. Journal of biomechanical engineering, 2012. **134**(10).
14. Rizzo, P., A. Nasrollahi, W. Deng, and J.M. Vandenbossche, *Detecting the presence of high water-to-cement ratio in concrete surfaces using highly nonlinear solitary waves*. Applied Sciences, 2016. **6**(4): p. 104.
15. Singhal, T., E. Kim, T.-Y. Kim, and J. Yang, *Weak bond detection in composites using highly nonlinear solitary waves*. Smart Materials and Structures, 2017. **26**(5): p. 055011.
16. Nasrollahi, A. and P. Rizzo, *Axial stress determination using highly nonlinear solitary waves*. Journal of the Acoustical Society of America, 2018. **144**(4): p. 2201-2212.
17. Nasrollahi, A. and P. Rizzo, *Numerical Analysis and Experimental Validation of an Nondestructive Evaluation Method to Measure Stress in Rails*. Journal of Nondestructive Evaluation, Diagnostics and Prognostics of Engineering Systems, 2019. **2**(3).
18. Nasrollahi, A., *On the application of highly nonlinear solitary waves for nondestructive evaluation*. 2019, University of Pittsburgh.

19. Boechler, N., G. Theocharis, and C. Daraio, *Bifurcation-based acoustic switching and rectification*. Nature Materials, 2011. **10**(9): p. 665-668.
20. Devaux, T., V. Tournat, O. Richoux, and V. Pagneux, *Asymmetric acoustic propagation of wave packets via the self-demodulation effect*. Physical review letters, 2015. **115**(23): p. 234301.
21. Li, X.-F., X. Ni, L. Feng, M.-H. Lu, C. He, and Y.-F. Chen, *Tunable unidirectional sound propagation through a sonic-crystal-based acoustic diode*. Physical review letters, 2011. **106**(8): p. 084301.
22. Liu, C., Z. Du, Z. Sun, H. Gao, and X. Guo, *Frequency-preserved acoustic diode model with high forward-power-transmission rate*. Physical Review Applied, 2015. **3**(6): p. 064014.
23. Li, K. and P. Rizzo, *Nonreciprocal propagation of solitary waves in granular chains with asymmetric potential barriers*. Journal of Sound and Vibration, 2016. **365**: p. 15-21.
24. Spadoni, A. and C. Daraio, *Generation and control of sound bullets with a nonlinear acoustic lens*. Proceedings of the National Academy of Sciences, 2010. **107**(16): p. 7230-7234.
25. Hussein, M.I., M.J. Leamy, and M. Ruzzene, *Dynamics of Phononic Materials and Structures: Historical Origins, Recent Progress, and Future Outlook*. Applied Mechanics Reviews, 2014. **66**(4).
26. Hladky-Hennion, A.-C., G. Allan, and M. de Billy, *Localized modes in a one-dimensional diatomic chain of coupled spheres*. Journal of applied physics, 2005. **98**(5): p. 054909.

27. Boechler, N., G. Theocharis, S. Job, P. Kevrekidis, M.A. Porter, and C. Daraio, *Discrete breathers in one-dimensional diatomic granular crystals*. Physical review letters, 2010. **104**(24): p. 244302.
28. Daraio, C., V. Nesterenko, E. Herbold, and S. Jin, *Energy trapping and shock disintegration in a composite granular medium*. Physical Review Letters, 2006. **96**(5): p. 058002.
29. Hladky-Hennion, A.-C. and M.d. Billy, *Experimental validation of band gaps and localization in a one-dimensional diatomic phononic crystal*. The Journal of the Acoustical Society of America, 2007. **122**(5): p. 2594-2600.
30. Boechler, N.S., *Granular Crystals: Controlling Mechanical Energy with Nonlinearity and Discreteness*. 2011: California Institute of Technology.
31. Nesterenko, V., *Propagation of nonlinear compression pulses in granular media*. J. Appl. Mech. Tech. Phys.(Engl. Transl.);(United States), 1984. **24**(5).
32. Lazaridi, A. and V.F. Nesterenko, *Observation of a new type of solitary waves in a one-dimensional granular medium*. Journal of Applied Mechanics and Technical Physics, 1985. **26**(3): p. 405-408.
33. Sen, S., J. Hong, J. Bang, E. Avalos, and R. Doney, *Solitary waves in the granular chain*. Physics Reports, 2008. **462**(2): p. 21-66.
34. Rosas, A. and K. Lindenberg, *Pulse propagation in granular chains*. Physics Reports, 2018.
35. Chong, C., M.A. Porter, P.G. Kevrekidis, and C. Daraio, *Nonlinear coherent structures in granular crystals*. J Phys Condens Matter, 2017. **29**(41): p. 413003.

36. Khatri, D., D. Ngo, and C. Daraio, *Highly nonlinear solitary waves in chains of cylindrical particles*. Granular Matter, 2011. **14**(1): p. 63-69.
37. Ngo, D., S. Griffiths, D. Khatri, and C. Daraio, *Highly nonlinear solitary waves in chains of hollow spherical particles*. Granular Matter, 2013. **15**(2): p. 149-155.
38. Ngo, D., D. Khatri, and C. Daraio, *Highly nonlinear solitary waves in chains of ellipsoidal particles*. Phys Rev E Stat Nonlin Soft Matter Phys, 2011. **84**(2 Pt 2): p. 026610.
39. Coste, C., E. Falcon, and S. Fauve, *Solitary waves in a chain of beads under Hertz contact*. Physical review E, 1997. **56**(5): p. 6104.
40. Yang, J., C. Silvestro, D. Khatri, L. De Nardo, and C. Daraio, *Interaction of highly nonlinear solitary waves with linear elastic media*. Physical Review E, 2011. **83**(4): p. 046606.
41. Job, S., F. Melo, A. Sokolow, and S. Sen, *How Hertzian solitary waves interact with boundaries in a 1D granular medium*. Physical review letters, 2005. **94**(17): p. 178002.
42. Yang, J., D. Khatri, P. Anzel, and C. Daraio, *Interaction of highly nonlinear solitary waves with thin plates*. International Journal of Solids and Structures, 2012. **49**(13): p. 1463-1471.
43. Cai, L., P. Rizzo, and L. Al-Nazer, *On the coupling mechanism between nonlinear solitary waves and slender beams*. International Journal of Solids and Structures, 2013. **50**(25-26): p. 4173-4183.
44. Schiffer, A. and T.-Y. Kim, *Modelling of the interaction between nonlinear solitary waves and composite beams*. International Journal of Mechanical Sciences, 2019. **151**: p. 181-191.

45. Schiffer, A., A.I. Alkhaja, J. Yang, E.N. Esfahani, and T.Y. Kim, *Interaction of highly nonlinear solitary waves with elastic solids containing a spherical void*. International Journal of Solids and Structures, 2017. **118-119**: p. 204-212.
46. Yang, J., F. Restuccia, and C. Daraio. *Highly nonlinear granular crystal sensor and actuator for delamination detection in composite structures*. in *International workshop on structural health monitoring, Stanford, CA*. 2011.
47. Berhanu, B., P. Rizzo, and M. Ochs, *Highly nonlinear solitary waves for the assessment of dental implant mobility*. Journal of applied mechanics, 2013. **80**(1): p. 011028.
48. Nasrollahi, A., P. Rizzo, and M.S. Orak, *Numerical and experimental study on the dynamic interaction between highly nonlinear solitary waves and pressurized balls*. Journal of Applied Mechanics, 2018. **85**(3): p. 031007.
49. Nasrollahi, A., R. Lucht, and P. Rizzo, *Solitary waves to assess the internal pressure and the rubber degradation of tennis balls*. Experimental Mechanics, 2019. **59**(1): p. 65-77.
50. Nasrollahi, A., M.S. Orak, A. James, L. Weighardt, and P. Rizzo, *A Nondestructive Evaluation Approach to Characterize Tennis Balls*. Journal of Nondestructive Evaluation, Diagnostics and Prognostics of Engineering Systems, 2019. **2**(1): p. 011004.
51. Nasrollahi, A. and P. Rizzo, *Axial stress determination using highly nonlinear solitary waves*. The Journal of the Acoustical Society of America, 2018. **144**(4): p. 2201-2212.
52. Herbold, E., J. Kim, V. Nesterenko, S. Wang, and C. Daraio, *Tunable frequency band-gap and pulse propagation in a strongly nonlinear diatomic chain*. arXiv preprint arXiv:0806.4225, 2008.
53. Li, F., D. Ngo, J. Yang, and C. Daraio, *Tunable phononic crystals based on cylindrical Hertzian contact*. Applied Physics Letters, 2012. **101**(17): p. 171903.

54. Yang, J. and C. Daraio, *Frequency-and amplitude-dependent transmission of stress waves in curved one-dimensional granular crystals composed of diatomic particles*. *Experimental Mechanics*, 2013. **53**(3): p. 469-483.
55. Narisetti, R.K., *Wave propagation in nonlinear periodic structures*. 2010, Georgia Institute of Technology.
56. Yeh, J.-Y., *Control analysis of the tunable phononic crystal with electrorheological material*. *Physica B: Condensed Matter*, 2007. **400**(1-2): p. 137-144.
57. Robillard, J.-F., O.B. Matar, J. Vasseur, P.A. Deymier, M. Stippinger, A.-C. Hladky-Hennion, Y. Pennec, and B. Djafari-Rouhani, *Tunable magnetoelastic phononic crystals*. *Applied Physics Letters*, 2009. **95**(12): p. 124104.
58. Theocharis, G., M. Kavousanakis, P. Kevrekidis, C. Daraio, M.A. Porter, and I. Kevrekidis, *Localized breathing modes in granular crystals with defects*. *Physical Review E*, 2009. **80**(6): p. 066601.
59. Man, Y., N. Boechler, G. Theocharis, P. Kevrekidis, and C. Daraio, *Defect modes in one-dimensional granular crystals*. *Physical Review E*, 2012. **85**(3): p. 037601.
60. Theocharis, G., N. Boechler, P. Kevrekidis, S. Job, M.A. Porter, and C. Daraio, *Intrinsic energy localization through discrete gap breathers in one-dimensional diatomic granular crystals*. *Physical Review E*, 2010. **82**(5): p. 056604.
61. Liang, B., B. Yuan, and J.C. Cheng, *Acoustic diode: rectification of acoustic energy flux in one-dimensional systems*. *Phys Rev Lett*, 2009. **103**(10): p. 104301.
62. Liang, B., X.S. Guo, J. Tu, D. Zhang, and J.C. Cheng, *An acoustic rectifier*. *Nat Mater*, 2010. **9**(12): p. 989-92.

63. Liang, B., X.-y. Zou, B. Yuan, and J.-c. Cheng, *Frequency-dependence of the acoustic rectifying efficiency of an acoustic diode model*. Applied Physics Letters, 2010. **96**(23).
64. Fu, C., B. Wang, T. Zhao, and C.Q. Chen, *High efficiency and broadband acoustic diodes*. Applied Physics Letters, 2018. **112**(5).
65. Cui, J.-G., T. Yang, and L.-Q. Chen, *Frequency-preserved non-reciprocal acoustic propagation in a granular chain*. Applied Physics Letters, 2018. **112**(18): p. 181904.
66. Administration, P.a.H.M.S., *Pipeline Significant Incident 20 Year Trend*. 2019, US DOT.
67. Wood, M.H., A.V. Arellano, and L. Van Wijk, *Corrosion related accidents in petroleum refineries*. European Commission Joint Research Centre, report no. EUR, 2013. **26331**.
68. Sharma, S. and A. Mukherjee, *Ultrasonic guided waves for monitoring corrosion in submerged plates*. Structural Control and Health Monitoring, 2015. **22**(1): p. 19-35.
69. Gallion, J.R. and R. Zoughi, *Millimeter-Wave Imaging of Surface-Breaking Cracks in Steel With Severe Surface Corrosion*. IEEE Transactions on Instrumentation and Measurement, 2017. **66**(10): p. 2789-2791.
70. Sedaghati, A., F. Honarvar, and A.N. Sinclair, *Lamb wave-based experimental and numerical studies for detection and sizing of corrosion damage in metallic plates*. Proceedings of the Institution of Mechanical Engineers, Part C: Journal of Mechanical Engineering Science, 2018: p. 0954406218781965.
71. Honarvar, F., F. Salehi, V. Safavi, A. Mokhtari, and A.N. Sinclair, *Ultrasonic monitoring of erosion/corrosion thinning rates in industrial piping systems*. Ultrasonics, 2013. **53**(7): p. 1251-1258.

72. Cheong, Y.-M., K.-M. Kim, and D.-J. Kim, *High-temperature ultrasonic thickness monitoring for pipe thinning in a flow-accelerated corrosion proof test facility*. Nuclear Engineering and Technology, 2017. **49**(7): p. 1463-1471.
73. Cawley, P., F. Cegla, and A. Galvagni, *Guided waves for NDT and permanently-installed monitoring*. Insight-Non-Destructive Testing and Condition Monitoring, 2012. **54**(11): p. 594-601.
74. Rao, J., M. Ratassepp, D. Lisevych, M. Hamzah Caffoor, and Z. Fan, *On-line corrosion monitoring of plate structures based on guided wave tomography using piezoelectric sensors*. Sensors, 2017. **17**(12): p. 2882.
75. Shen, G. and T. Li, *Infrared thermography for high-temperature pressure pipe*. Insight-Non-Destructive Testing and Condition Monitoring, 2007. **49**(3): p. 151-153.
76. Bagavathiappan, S., B. Lahiri, T. Saravanan, J. Philip, and T. Jayakumar, *Infrared thermography for condition monitoring—A review*. Infrared Physics & Technology, 2013. **60**: p. 35-55.
77. Cadelano, G., A. Bortolin, G. Ferrarini, B. Molinas, D. Giantin, P. Zonta, and P. Bison, *Corrosion detection in pipelines using infrared thermography: experiments and data processing methods*. Journal of Nondestructive Evaluation, 2016. **35**(3): p. 49.
78. Cheng, W., *Pulsed eddy current testing of carbon steel pipes' wall-thinning through insulation and cladding*. Journal of Nondestructive evaluation, 2012. **31**(3): p. 215-224.
79. Angani, C., D. Park, G. Kim, C. Kim, and Y. Cheong, *Differential pulsed eddy current sensor for the detection of wall thinning in an insulated stainless steel pipe*. Journal of Applied Physics, 2010. **107**(9): p. 09E720.

80. Xu, Z., X. Wu, J. Li, and Y. Kang, *Assessment of wall thinning in insulated ferromagnetic pipes using the time-to-peak of differential pulsed eddy-current testing signals*. NDT & E International, 2012. **51**: p. 24-29.
81. Safizadeh, M. and M. Hasanian, *Gas pipeline corrosion mapping using pulsed eddy current technique*. International Journal of Advanced Design and Manufacturing Technology, 2011. **5**(1): p. 11.
82. Xie, S., Z. Chen, T. Takagi, and T. Uchimoto, *Quantitative non-destructive evaluation of wall thinning defect in double-layer pipe of nuclear power plants using pulsed ECT method*. NDT & E International, 2015. **75**: p. 87-95.
83. Schmarje, N., J. Saillant, K. Kirk, and S. Cochran, *Imaging with lithium niobate/epoxy composites*. Ultrasonics, 2004. **42**(1-9): p. 439-442.
84. Zhang, S., R.E. Eitel, C.A. Randall, T.R. Shrout, and E.F. Alberta, *Manganese-modified Bi Sc O 3–Pb Ti O 3 piezoelectric ceramic for high-temperature shear mode sensor*. Applied Physics Letters, 2005. **86**(26): p. 262904.
85. McNab, A., K. Kirk, and A. Cochran, *Ultrasonic transducers for high temperature applications*. IEE Proceedings-Science, Measurement and Technology, 1998. **145**(5): p. 229-236.
86. Megriche, A., L. Lebrun, and M. Troccaz, *Materials of Bi4Ti3O12 type for high temperature acoustic piezo-sensors*. Sensors and Actuators A: Physical, 1999. **78**(2-3): p. 88-91.
87. Baba, A., C.T. Searfass, and B.R. Tittmann, *High temperature ultrasonic transducer up to 1000 C using lithium niobate single crystal*. Applied Physics Letters, 2010. **97**(23): p. 232901.

88. Cegla, F.B., P. Cawley, J. Allin, and J. Davies, *High-temperature (> 500 C) wall thickness monitoring using dry-coupled ultrasonic waveguide transducers*. IEEE transactions on ultrasonics, ferroelectrics, and frequency control, 2011. **58**(1): p. 156-167.
89. Dixon, S., C. Edwards, and S. Palmer, *High accuracy non-contact ultrasonic thickness gauging of aluminium sheet using electromagnetic acoustic transducers*. Ultrasonics, 2001. **39**(6): p. 445-453.
90. Kruger, S., M. Lord, and J.P. Monchalin. *Laser ultrasonic thickness measurements of very thick walls at high temperatures*. in *AIP Conference Proceedings*. 2006. AIP.
91. Lee, J.-H. and S.-J. Lee, *Application of laser-generated guided wave for evaluation of corrosion in carbon steel pipe*. Ndt & E International, 2009. **42**(3): p. 222-227.
92. Job, S., F. Melo, A. Sokolow, and S. Sen, *How hertzian solitary waves interact with boundaries in a 1D granular medium*. Phys Rev Lett, 2005. **94**(17): p. 178002.
93. Nesterenko, V.F., C. Daraio, E.B. Herbold, and S. Jin, *Anomalous wave reflection at the interface of two strongly nonlinear granular media*. Phys Rev Lett, 2005. **95**(15): p. 158702.
94. Daraio, C., V. Nesterenko, E. Herbold, and S. Jin, *Strongly nonlinear waves in a chain of Teflon beads*. Physical Review E, 2005. **72**(1): p. 016603.
95. Porter, M.A., C. Daraio, E.B. Herbold, I. Szelengowicz, and P. Kevrekidis, *Highly nonlinear solitary waves in periodic dimer granular chains*. Physical Review E, 2008. **77**(1): p. 015601.
96. Job, S., F. Melo, A. Sokolow, and S. Sen, *Solitary wave trains in granular chains: experiments, theory and simulations*. Granular Matter, 2007. **10**(1): p. 13-20.

97. Carretero-González, R., D. Khatri, M.A. Porter, P. Kevrekidis, and C. Daraio, *Dissipative solitary waves in granular crystals*. Physical review letters, 2009. **102**(2): p. 024102.
98. Yang, T., L. Tham, C. Tang, Z. Liang, and Y. Tsui, *Influence of heterogeneity of mechanical properties on hydraulic fracturing in permeable rocks*. Rock mechanics and rock engineering, 2004. **37**(4): p. 251-275.
99. Wojtowicz, M. and M. Jarosiński, *Reconstructing the mechanical parameters of a transversely-isotropic rock based on log and incomplete core data integration*. International Journal of Rock Mechanics and Mining Sciences, 2019. **115**: p. 111-120.
100. Asaka, M. and R.M. Holt, *Anisotropic Wellbore Stability Analysis: Impact on Failure Prediction*. Rock Mechanics and Rock Engineering, 2020: p. 1-23.
101. Alabbad, A., J. Dvorkin, Y. Altowairqi, and Z.F. Duan, *Rock Physics Based Interpretation of Seismically Derived Elastic Volumes*. Frontiers in Earth Science, 2021. **8**: p. 728.
102. Maxwell, S., *Microseismic imaging of hydraulic fracturing: Improved engineering of unconventional shale reservoirs*. 2014: Society of Exploration Geophysicists.
103. Kanitpanyacharoen, W., R. Vasin, H.-R. Wenk, and D.N. Dewhurst, *Linking preferred orientations to elastic anisotropy in Muderong Shale, Australia*. Geophysics, 2015. **80**(1): p. C9-C19.
104. Wang, Z., *Seismic anisotropy in sedimentary rocks, part 1: A single-plug laboratory method*. Geophysics, 2002. **67**(5): p. 1415-1422.
105. Riazi, N., C. Clarkson, A. Ghanizadeh, A. Vahedian, S. Aquino, and J. Wood, *Determination of elastic properties of tight rocks from ultrasonic measurements: Examples from the Montney Formation (Alberta, Canada)*. Fuel, 2017. **196**: p. 442-457.

106. Vishnu, C., M.A. Mamtani, and A. Basu, *AMS, ultrasonic P-wave velocity and rock strength analysis in quartzites devoid of mesoscopic foliations—implications for rock mechanics studies*. *Tectonophysics*, 2010. **494**(3-4): p. 191-200.
107. Přikryl, R., T. Lokajíček, Z. Pros, and K. Klíma, *Fabric symmetry of low anisotropic rocks inferred from ultrasonic sounding: Implications for the geomechanical models*. *Tectonophysics*, 2007. **431**(1-4): p. 83-96.
108. Leiss, B. and K. Ullemeyer, *Texture characterisation of carbonate rocks and some implications for the modeling of physical anisotropies, derived from idealized texture types*. *Zeitschrift der deutschen geologischen Gesellschaft*, 1999: p. 259-274.
109. Mokhtari, M., M.M. Honarpour, A.N. Tutuncu, and G.N. Boitnott, *Characterization of elastic anisotropy in Eagle Ford Shale: Impact of heterogeneity and measurement scale*. *SPE Reservoir Evaluation & Engineering*, 2016. **19**(03): p. 429-439.
110. Sayers, C., *The elastic anisotropy of shales: Journal of Geophysical Research*, 99, no. 1994, B1.
111. Ivankina, T., H. Kern, and A. Nikitin, *Directional dependence of P-and S-wave propagation and polarization in foliated rocks from the Kola superdeep well: Evidence from laboratory measurements and calculations based on TOF neutron diffraction*. *Tectonophysics*, 2005. **407**(1-2): p. 25-42.
112. Ivankina, T., I.Y. Zel, T. Lokajicek, and H. Kern. *Elastic anisotropy of layered rocks: Texture-based theoretical predictions (effective media modeling) versus ultrasonic measurements of gneiss*. in *52nd US Rock Mechanics/Geomechanics Symposium*. 2018. American Rock Mechanics Association.

113. Cummer, S.A., J. Christensen, and A. Alù, *Controlling sound with acoustic metamaterials*. Nature Reviews Materials, 2016. **1**(3): p. 1-13.
114. Brillouin, L., *Wave propagation and group velocity*. Vol. 8. 2013: Academic Press.
115. Duan, F. and J. Guojun, *Introduction To Condensed Matter Physics: Volume 1*. Vol. 1. 2005: World Scientific Publishing Company.
116. Daraio, C., V.F. Nesterenko, E.B. Herbold, and S. Jin, *Energy trapping and shock disintegration in a composite granular medium*. Phys Rev Lett, 2006. **96**(5): p. 058002.
117. Li, K. and P. Rizzo, *Energy harvesting using an array of granules*. Journal of Vibration and Acoustics, 2015. **137**(4): p. 041002.
118. Spadoni, A. and C. Daraio, *Generation and control of sound bullets with a nonlinear acoustic lens*. Proc Natl Acad Sci U S A, 2010. **107**(16): p. 7230-4.
119. Li, F., P. Anzel, J. Yang, P.G. Kevrekidis, and C. Daraio, *Granular acoustic switches and logic elements*. Nat Commun, 2014. **5**: p. 5311.
120. Nesterenko, V.F., *Propagation of nonlinear compression pulses in granular media*. J. Appl. Mech. Tech. Phys.(Engl. Transl.);(United States), 1984. **24**(5).
121. Chatterjee, A., *Asymptotic solution for solitary waves in a chain of elastic spheres*. Physical Review E, 1999. **59**(5): p. 5912.
122. Rosas, A. and K. Lindenberg, *Pulse propagation in granular chains*. Physics Reports, 2018. **735**: p. 1-37.
123. Hasan, M.A. and S. Nemat-Nasser, *Basic properties of solitary waves in granular crystals*. Journal of the Mechanics and Physics of Solids, 2017. **101**: p. 1-9.
124. Hong, J. and A. Xu, *Nondestructive identification of impurities in granular medium*. Applied physics letters, 2002. **81**(25): p. 4868-4870.

125. Sen, S., M. Manciu, and J.D. Wright, *Solitonlike pulses in perturbed and driven Hertzian chains and their possible applications in detecting buried impurities*. Physical Review E, 1998. **57**(2): p. 2386.
126. Yang, J., C. Silvestro, D. Khatri, L. De Nardo, and C. Daraio, *Interaction of highly nonlinear solitary waves with linear elastic media*. Phys Rev E Stat Nonlin Soft Matter Phys, 2011. **83**(4 Pt 2): p. 046606.
127. Deng, W., A. Nasrollahi, P. Rizzo, and K. Li, *On the reliability of a solitary wave based transducer to determine the characteristics of some materials*. Sensors, 2016. **16**(1): p. 5.
128. Schiffer, A., R. Alia, W.J. Cantwell, D. Lee, E. Kim, and T.-Y. Kim, *Elastic interaction between nonlinear solitary waves in granular chains and composite beams: Experiments and modelling*. International Journal of Mechanical Sciences, 2020. **170**: p. 105350.
129. Villacreses, J.P., B. Caicedo, S. Caro, and F. Yépez, *Feasibility of the use of nonlinear solitary waves for the nondestructive measurement of Young's modulus of rocks and compacted materials*. Transportation Geotechnics, 2021. **26**: p. 100437.
130. Jalali, H., Y. Zeng, P. Rizzo, and A. Bungler, *Help-HighlyNonlinearSolitaryWavestoEstimateOrientationandDegreeofAnisotropyinRocks*. Materials Evaluation, 2021. **79**(10).
131. Ni, X., P. Rizzo, J. Yang, D. Katri, and C. Daraio, *Monitoring the hydration of cement using highly nonlinear solitary waves*. NDT & E International, 2012. **52**: p. 76-85.
132. Nasrollahi, A., W. Deng, P. Rizzo, A. Vuotto, and J.M. Vandenbossche, *Nondestructive testing of concrete using highly nonlinear solitary waves*. Nondestructive Testing and Evaluation, 2017. **32**(4): p. 381-399.

133. Schiffer, A., A. Alkhaja, J. Yang, E. Esfahani, and T.-Y. Kim, *Interaction of highly nonlinear solitary waves with elastic solids containing a spherical void*. International Journal of Solids and Structures, 2017. **118**: p. 204-212.
134. Yoon, S., A. Schiffer, W.J. Cantwell, and T.-Y. Kim, *Detection of core-skin disbonds in honeycomb composite sandwich structures using highly nonlinear solitary waves*. Composite Structures, 2021. **256**: p. 113071.
135. Jalali, H. and P. Rizzo, *Highly nonlinear solitary waves for the detection of localized corrosion*. Smart Materials and Structures, 2020. **29**(8): p. 085051.
136. Jalali, H. and P. Rizzo, *Numerical investigation of the interaction of highly nonlinear solitary waves with corroded steel plates*. International Journal of Mechanical Sciences, 2021. **208**: p. 106676.
137. Zheng, B., P. Rizzo, and A. Nasrollahi, *Outlier analysis of nonlinear solitary waves for health monitoring applications*. Structural Health Monitoring, 2020. **19**(4): p. 1160-1174.
138. Berhanu, B., P. Rizzo, and M. Ochs, *Highly nonlinear solitary waves for the assessment of dental implant mobility*. Journal of applied mechanics, 2013. **80**(1).
139. Yoon, S., A. Schiffer, I.G. Jang, S. Lee, and T.-Y. Kim, *Predictions of the elastic modulus of trabecular bone in the femoral head and the intertrochanter: a solitary wave-based approach*. Biomechanics and Modeling in Mechanobiology, 2021: p. 1-17.
140. Yoon, S., A. Schiffer, J.J. Kim, I.G. Jang, S. Lee, and T.-Y. Kim, *Numerical predictions of the interaction between highly nonlinear solitary waves and the microstructure of trabecular bone in the femoral head*. Journal of the Mechanical Behavior of Biomedical Materials, 2020. **109**: p. 103805.

141. Nasrollahi, A. and P. Rizzo, *Modeling a new dynamic approach to measure intraocular pressure with solitary waves*. Journal of the mechanical behavior of biomedical materials, 2020. **103**: p. 103534.
142. Dervilis, N., E. Cross, R. Barthorpe, and K. Worden, *Robust methods of inclusive outlier analysis for structural health monitoring*. Journal of Sound and Vibration, 2014. **333**(20): p. 5181-5195.
143. Worden, K., *Structural fault detection using a novelty measure*. Journal of Sound and vibration, 1997. **201**(1): p. 85-101.
144. Worden, K., G. Manson, and N.R. Fieller, *Damage detection using outlier analysis*. Journal of Sound and Vibration, 2000. **229**(3): p. 647-667.
145. Worden, K., G. Manson, and D. Allman, *Experimental validation of a structural health monitoring methodology: Part I. Novelty detection on a laboratory structure*. Journal of sound and vibration, 2003. **259**(2): p. 323-343.
146. Worden, K. and G. Manson, *The application of machine learning to structural health monitoring*. Philosophical Transactions of the Royal Society A: Mathematical, Physical and Engineering Sciences, 2007. **365**(1851): p. 515-537.
147. Rizzo, P., M. Cammarata, D. Dutta, and H. Sohn, *An unsupervised learning algorithm for fatigue crack detection in waveguides*. Smart Materials and Structures, 2009. **18**(2): p. 025016.
148. Zhu, X.P., P. Rizzo, A. Marzani, and J. Bruck, *Ultrasonic guided waves for nondestructive evaluation/structural health monitoring of trusses*. Measurement Science and Technology, 2010. **21**(4): p. 045701.

149. Rizzo, P., E. Sorri, F.L. di Scalea, and E. Viola, *Wavelet-based outlier analysis for guided wave structural monitoring: application to multi-wire strands*. Journal of Sound and Vibration, 2007. **307**(1-2): p. 52-68.
150. Pistone, E., K. Li, and P. Rizzo, *Noncontact monitoring of immersed plates by means of laser-induced ultrasounds*. Structural Health Monitoring, 2013. **12**(5-6): p. 549-565.
151. Mariani, S., T. Nguyen, R.R. Phillips, P. Kijanka, F. Lanza di Scalea, W.J. Staszewski, M. Fateh, and G. Carr, *Noncontact ultrasonic guided wave inspection of rails*. Structural Health Monitoring, 2013. **12**(5-6): p. 539-548.
152. Zheng, B., P. Rizzo, and A. Nasrollahi, *Outlier analysis of nonlinear solitary waves for health monitoring applications*. Structural Health Monitoring, 2019: p. 1475921719876089.
153. Schiffer, A., D. Lee, E. Kim, and T.-Y. Kim, *Interaction of highly nonlinear solitary waves with rigid polyurethane foams*. International Journal of Solids and Structures, 2018. **152**: p. 39-50.
154. Gr, L. and Q. SS, *The Finite Element Method: A Practical Course*. 2003, Butterworth-Heinemann.
155. Zener, C., *The intrinsic inelasticity of large plates*. Physical Review, 1941. **59**(8): p. 669.
156. Sondergaard, R., K. Chaney, and C. Brennen, *Measurements of solid spheres bouncing off flat plates*. Journal of Applied Mechanics, 1990. **112**(3): p. 694-699.
157. Boettcher, R., A. Russell, and P. Mueller, *Energy dissipation during impacts of spheres on plates: Investigation of developing elastic flexural waves*. International Journal of Solids and Structures, 2017. **106**: p. 229-239.

158. Dubuc, B., A. Ebrahimkhanlou, and S. Salamone, *Stress monitoring of prestressing strands in corrosive environments using modulated higher-order guided ultrasonic waves*. Structural Health Monitoring, 2019: p. 1475921719842385.
159. Frankel, G., *Pitting corrosion of metals: a review of the critical factors*. Journal of the Electrochemical society, 1998. **145**(6): p. 2186.
160. Eslami, A., B. Fang, R. Kania, B. Worthingham, J. Been, R. Eadie, and W. Chen, *Stress corrosion cracking initiation under the disbonded coating of pipeline steel in near-neutral pH environment*. Corrosion Science, 2010. **52**(11): p. 3750-3756.
161. Sokolow, A., J.M. Pfannes, R.L. Doney, M. Nakagawa, J.H. Agui, and S. Sen, *Absorption of short duration pulses by small, scalable, tapered granular chains*. Applied physics letters, 2005. **87**(25): p. 254104.
162. Hong, J., *Universal power-law decay of the impulse energy in granular protectors*. Physical review letters, 2005. **94**(10): p. 108001.
163. Doney, R. and S. Sen, *Decorated, tapered, and highly nonlinear granular chain*. Physical review letters, 2006. **97**(15): p. 155502.
164. Melo, F., S. Job, F. Santibanez, and F. Tapia, *Experimental evidence of shock mitigation in a Hertzian tapered chain*. Physical Review E, 2006. **73**(4): p. 041305.
165. Nakagawa, M., J.H. Agui, D.T. Wu, and D.V. Extramiana, *Impulse dispersion in a tapered granular chain*. Granular Matter, 2003. **4**(4): p. 167-174.
166. Doney, R.L., J.H. Agui, and S. Sen, *Energy partitioning and impulse dispersion in the decorated, tapered, strongly nonlinear granular alignment: a system with many potential applications*. Journal of applied physics, 2009. **106**(6): p. 064905.

167. Breindel, A., D. Sun, and S. Sen, *Impulse absorption using small, hard panels of embedded cylinders with granular alignments*. Applied Physics Letters, 2011. **99**(6): p. 063510.
168. Przedborski, M.A., T.A. Harroun, and S. Sen, *Localizing energy in granular materials*. Applied Physics Letters, 2015. **107**(24): p. 244105.
169. Li, K., P. Rizzo, and A. Bagheri, *A parametric study on the optimization of a metamaterial-based energy harvester*. Smart Materials and Structures, 2015. **24**(11): p. 115019.
170. Li, K. and P. Rizzo, *Energy harvesting using arrays of granular chains and solid rods*. Journal of Applied Physics, 2015. **117**(21): p. 215101.
171. Li, K. and P. Rizzo, *Energy harvesting using an array of granules*. Journal of Vibration and Acoustics, 2015. **137**(4).
172. Li, K., P. Rizzo, and X. Ni, *Alternative designs of acoustic lenses based on nonlinear solitary waves*. Journal of Applied Mechanics, 2014. **81**(7).
173. Rizzo, P. and K. Li, *Analysis of the geometric parameters of a solitary waves-based harvester to enhance its power output*. Smart Materials and Structures, 2017. **26**(7): p. 075004.
174. Lu, G., E. Gordeliy, R. Prioul, G. Aidagulov, E.C. Uwaifo, Q. Ou, and A.P. Bungler, *Time-Dependent Hydraulic Fracture Initiation*. Journal of Geophysical Research: Solid Earth, 2020. **125**(3): p. e2019JB018797.
175. StructX. *Typical properties for various rocks*. 2020; Available from: https://structx.com/Soil_Properties_010.html.
176. Cardarelli, F., *Materials handbook*. 2018: Springer.
177. Schlumberger. *Oilfield Glossary*. 2021 [cited 2021; Available from: <https://www.glossary.oilfield.slb.com/en/>].

178. Daraio, C., V.F. Nesterenko, E.B. Herbold, and S. Jin, *Tunability of solitary wave properties in one-dimensional strongly nonlinear phononic crystals*. Phys Rev E Stat Nonlin Soft Matter Phys, 2006. **73**(2 Pt 2): p. 026610.
179. Jalali, H., Y. Zeng, P. Rizzo, and A. Bungler, *Help-Highly Nonlinear Solitary Waves to Estimate Orientation and Degree of Anisotropy in Rocks*. Materials Evaluation, 2021. **79**(10).
180. Misra, R., H. Jalali, S.J. Dickerson, and P. Rizzo, *Wireless Module for Nondestructive Testing/Structural Health Monitoring Applications Based on Solitary Waves*. Sensors, 2020. **20**(11): p. 3016.
181. Wiener, N., *Extrapolation, interpolation, and smoothing of stationary time series: with engineering applications*. Vol. 8. 1964: MIT press Cambridge, MA.
182. Canny, J., *A computational approach to edge detection*. IEEE Transactions on pattern analysis and machine intelligence, 1986(6): p. 679-698.
183. Lee Rodgers, J. and W.A. Nicewander, *Thirteen ways to look at the correlation coefficient*. The American Statistician, 1988. **42**(1): p. 59-66.
184. Hladky-Hennion, A.C. and M. de Billy, *Experimental validation of band gaps and localization in a one-dimensional diatomic phononic crystal*. J Acoust Soc Am, 2007. **122**(5): p. 2594-600.
185. Boechler, N., G. Theocharis, S. Job, P.G. Kevrekidis, M.A. Porter, and C. Daraio, *Discrete breathers in one-dimensional diatomic granular crystals*. Phys Rev Lett, 2010. **104**(24): p. 244302.
186. Fu, C., B. Wang, T. Zhao, and C. Chen, *High efficiency and broadband acoustic diodes*. Applied Physics Letters, 2018. **112**(5): p. 051902.

187. He, Z., S. Peng, Y. Ye, Z. Dai, C. Qiu, M. Ke, and Z. Liu, *Asymmetric acoustic gratings*. Applied Physics Letters, 2011. **98**(8).
188. Li, C., M. Ke, Y. Ye, S. Xu, C. Qiu, and Z. Liu, *Broadband asymmetric acoustic transmission by a plate with quasi-periodic surface ridges*. Applied Physics Letters, 2014. **105**(2): p. 023511.
189. Fleury, R., D.L. Sounas, C.F. Sieck, M.R. Haberman, and A. Alù, *Sound isolation and giant linear nonreciprocity in a compact acoustic circulator*. Science, 2014. **343**(6170): p. 516-519.
190. Li, Y., C. Shen, Y. Xie, J. Li, W. Wang, S.A. Cummer, and Y. Jing, *Tunable asymmetric transmission via lossy acoustic metasurfaces*. Physical review letters, 2017. **119**(3): p. 035501.
191. Popa, B.I. and S.A. Cummer, *Non-reciprocal and highly nonlinear active acoustic metamaterials*. Nat Commun, 2014. **5**: p. 3398.
192. Hubbard, H.H. and H. HH, *Noise induced house vibrations and human perception*. 1982.
193. Ouis, D., *Annoyance from road traffic noise: a review*. Journal of environmental psychology, 2001. **21**(1): p. 101-120.
194. Can, A., L. Leclercq, J. Lelong, and D. Botteldooren, *Traffic noise spectrum analysis: Dynamic modeling vs. experimental observations*. Applied Acoustics, 2010. **71**(8): p. 764-770.
195. Waye, K.P., *Effects of low frequency noise and vibrations: Environmental and occupational perspectives*. 2011.